Molecular simulation of nanoporous materials

Application to metal-organic frameworks, zeolites, and cyclodextrins

Erdös, M.

DOI
10.4233/uuid:13c4cd9c-a386-49f8-a68b-ab9ef4d65ab6

Publication date
2022

Document Version
Final published version

Citation (APA)
Erdös, M. (2022). *Molecular simulation of nanoporous materials: Application to metal-organic frameworks, zeolites, and cyclodextrins*. [Dissertation (TU Delft), Delft University of Technology]. https://doi.org/10.4233/uuid:13c4cd9c-a386-49f8-a68b-ab9ef4d65ab6

Important note
To cite this publication, please use the final published version (if applicable).
Please check the document version above.

MOLECULAR SIMULATION OF NANOPOROUS MATERIALS

APPLICATION TO METAL-ORGANIC FRAMEWORKS, ZEOLITES, AND CYCLODEXTRINS

MOLECULAR SIMULATION OF NANOPOROUS MATERIALS

APPLICATION TO METAL-ORGANIC FRAMEWORKS, ZEOLITES, AND CYCLODEXTRINS

Dissertation

for the purpose of obtaining the degree of doctor
at Delft University of Technology
by the authority of the Rector Magnificus, Prof.dr.ir. T.H.J.J. van der Hagen,
chair of the Board for Doctorates to be defended publicly on
Monday 13 June 2022 at 12:30 o'clock

by

Máté ERDŐS

Master of Science in Chemical Engineering,
Delft University of Technology, The Netherlands
born in Gyula, Hungary.

This dissertation has been approved by the promotors.

Composition of the doctoral committee:

Rector Magnificus,	chairperson
Prof. dr. ir. T. J. H. Vlugt	Delft University of Technology, promotor
Dr. O. A. Moultos	Delft University of Technology, copromotor
Independent members:	
Prof. dr. A. Urakawa	Delft University of Technology, The Netherlands
Prof. dr. T.S. van Erp	Norwegian University of Science and Technology, Norway
Prof. dr. D.N. Theodorou	National Technical University of Athens, Greece
Prof. dr. J.M. Thijssen	Delft University of Technology, The Netherlands
Prof. dr. B.P. Tighe	Delft University of Technology, The Netherlands, reserve member
Other members:	
Prof. dr. I. Economou	Texas A&M University at Qatar, Qatar

The research reported in this thesis was carried out at the Process & Energy Department, Faculty of Mechanical, Maritime and Materials Engineering, Delft University of Technology. This work was sponsored by NWO Domain Science for the use of supercomputer facilities. T. J. H. V. acknowledges NWO-CW (Chemical Sciences) for a VICI grant.

Keywords: Porous materials, Molecular Simulation, Adsorption, Diffusion, Computational Screening

Printed by: TBD

Front & Back: Cover design by M. Erdős.

ISBN 000-00-0000-000-0 TBD

An electronic version of this dissertation is available at
http://repository.tudelft.nl/.

So long, and thanks for all the fish.

Douglas Adams

CONTENTS

1

INTRODUCTION

1.1. POROUS MATERIALS

POROUS materials are widely used in numerous fields such as separation [1–6], catalysis [7–10], energy storage [11–14] *etc.* With the discovery of the adsorption capabilities of zeolites, research on porous materials gained momentum in the late 19th century [15]. This made zeolites promising candidates for catalytic processes in the oil and gas industry [15, 16]. Zeolites are nanoporous materials consisting of tetrahedral SiO_4 and AlO_4 units connected to each other by shared oxygen atoms [17] (Figure 1.1a). As discovered over the years, the pore structure of zeolites varies significantly with the different secondary building units formed by the tetrahedral units, such as 4-, 6-, or 8-member rings *etc.* [18]. Based on the topology of the framework, zeolites can be distinguished in various types, which are commonly denoted with a three letter code *e.g.*, MFI, LTA *etc.* [18]. To date, 253 experimentally synthesized [18] and more than 5 million theoretical [19–21] zeolite topologies have been reported. The different types of pore structures with varying pore sizes gave rise to the application of zeolites as molecular sieves [22]. However, only a few types of frameworks *e.g.*, MFI, LTA, MOR, CHA, FAU, LEV [23, 24] are used on an industrial scale. Another important characteristic of zeolites is the ratio of the number of Si to Al atoms (Si/Al ratio) present in the framework which determines the hydrophilicty of the structure [1, 25–27]. The Al content of zeolites leads to charge imbalance which is compensated by the presence of exchangeable nonframework cations, usually alkali or alkaline ions, located in the cavities of the framework [17]. The properties of zeolites, namely the well-defined pore structure, exchangeable cations, and tuneable hydrophilicity are exploited in several industrial processes such as catalysis [7–9, 28], separation technology [3, 4, 29–38], wa-

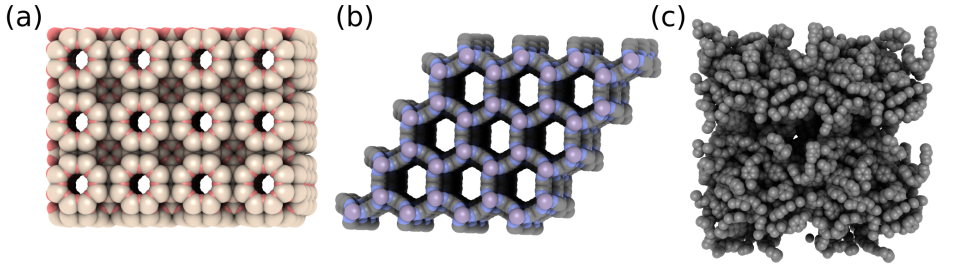

Figure 1.1: Schematic representation of (a) LTA-type zeolite, (b) the FAKMAH MOF structure consisting of Mn^{6+} metal clusters and $[C_{12}H_4N_4]^{-4}$ organic linkers, and (c) a hyper-cross-linked activated carbon polymer. The graphical representations are created with iRASPA [45].

ter purification [1, 2, 39, 40], and energy storage [11, 12, 41].

Until the end of the 20th century, zeolites dominated the research on porous materials [16]. In the past two decades, new classes of porous materials with a wide-range of physico-chemical properties, *i.e*, porosity, surface area, hydrophilicity, surface charge *etc*. have been synthesized [10, 42]. Such classes are for example Covalent-Organic Frameworks (COFs) [43], Metal-Organic frameworks (MOFs) [10], Zeolitic Imidazolate Frameworks (ZIFs) [44] and Porous Polymer Networks (PPNs) [42]. COFs are a class of porous materials with highly ordered crystal structure and permanent porosity [43]. One important feature of COFs is that the composition of the structure can be precisely controlled through the selection of the right organic precursors [43]. MOFs are crystalline porous materials consisting of metal ions or inorganic clusters (nodes) connected by organic linkers [10, 46] (Figure 1.1b). One of the main advantages of MOFs is that they are highly tunable [47]. By changing the organic linkers and/or metal clusters, specific properties such as the porosity, pore size, surface area, hydrophilicity *etc*. can be altered or embedded to MOFs [46]. Therefore, tailor-made structures with desired properties can be obtained for several technological applications [5, 6, 10, 13, 14]. One drawback of MOFs is that some frameworks can loose structural stability because of the exposure to the water. During the last decade, 90 000 different MOF structures have been experimentally synthesized [48–50], which is only a tiny fraction of the millions of possible MOFs that could be potentially synthesized [16, 51, 52]. ZIFs are a class of MOFs which have the same topological structure as zeolites [44, 53]. ZIFs are composed of metal-ions with tetrahedral coordination (*e.g.* Fe, Co, *etc*.) and imidazolate linkers [44, 53]. PPNs are organic polymers which are assembled from different building blocks, commonly small organic molecules [54] (Figure 1.1c). PPNs are synthesized through irreversible cross-linking reactions typically yielding amorphous structures [54, 55]. Similarly to MOFs, PPNs are also highly tunable through the change or functionalization of the used building blocks [54, 55].

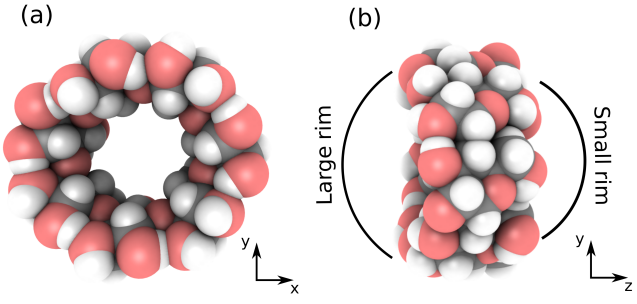

Figure 1.2: (a) and (b) show the atomistic representation of a β-cyclodextrin molecule. The graphics are created with iRASPA [45].

One promising building block of PPNs are cyclodextrins (CDs) which are cyclic oligosaccharides comprising D-glucopyranoside units linked through $\alpha-1,4$ glycosidic bonds [56]. The most common cyclodextrins contain 6, 7, and 8 glucopyranoside units and are commonly denoted as α-, β-, and γ-CD, respectively [56]. CDs have a hollow truncated cone shape with a hydrophobic inner and hydrophilic outer surface [56]. Due to this unique structure, the cavity of CDs can encapsulate other molecules by forming inclusion complexes. Upon inclusion complex formation, the physicochemical characteristics of the guest molecule (*e.g.* solubility, thermal stability, bioavailability, membrane permeability *etc.*) can be altered, and thus, CDs can be used in a wide variety of applications [57–60]. These applications include, but are not limited to, drug delivery [57, 58, 61, 62], catalysis [57, 63, 64], food [57, 65, 66] and separation technologies [57, 67, 68].

The highly-tunable nature of zeolites, COFs, ZIFs, MOFs and PPNs makes them very attractive to create tailor-made structures for particular applications [16, 52, 54]. Due to the vast variety of available building blocks, the number of conceivable structures is almost unlimited [16, 54, 69]. Although in theory this creates endless possibilities, in practice, only a small fraction of possible materials can be synthesized and tested for a particular application due to the required resources [70–74]. To minimize the number of necessary experiments for identifying optimal building blocks, the understanding of the molecular level behavior of the system is essential. Since most of the physico-chemical phenomena occur inside the pores of the structure, obtaining a molecular level understanding of the involved processes by using only experimental techniques can be a challenging task [75]. Simulations in which all atoms and bonds of the molecules are considered, can be used to obtain information at the molecular scale. These simulations are referred to as molecular simulations and are discussed in the next section of this chapter.

1

1.2. MOLECULAR SIMULATION OF POROUS MATERIALS

Molecular simulations can be used to obtain detailed insight into molecular level phenomena which are often not accessible from experimental measurements [75]. For a comprehensive description of molecular simulation techniques the reader is referred to the appropriate text books [76–78]. The two main types of molecular simulation are Molecular Dynamics (MD) and Monte Carlo (MC) simulations [76, 77, 79]. In MD simulations, the time evolution of a system consisting of interacting particles or molecules is modelled by the numerical integration of Newton's equations of motion [76]. One of the limitations of MD simulations is the relatively short time scale that can be reached. With the currently available computational resources, the evolution of a realistic system with 10^4-10^5 atoms typically can be only followed on a timescale of milliseconds [77]. In MC simulations, different configurations (system states) of interacting particles or molecules present in the system are generated by performing so-called trial moves (*e.g.*, translation or rotation of molecules) which are accepted or rejected based on the imposed probability distribution of system states, and random numbers [76]. Unlike in MD simulations, the dimension of time is not present in MC simulations (unless it is put in through a "backdoor" [80]). Due to this difference in the two methods, MD and MC simulations are used to predict dynamic and static properties of molecular systems, respectively. However, it is important to note that the calculated properties from the time and ensemble averages in MD and MC simulations, respectively, are identical (ergodicity hypothesis) [76, 77].

The application areas of MC and MD simulations range from testing theories on simplistic models [81–84] to predicting thermodynamic and transport properties of complex, realistic systems [76, 85–88]. Molecular simulations can be also used for predicting the properties of materials which would require to carry out experiments at difficult conditions *e.g.* high pressure, temperature, using toxic substances *etc.* For porous materials, MC simulations are most commonly used to gain a fundamental understanding of the adsorption of fluids on porous structures [79, 89, 90]. By performing MC simulations in different ensembles, the heat of adsorption, Henry coefficient, the adsorption loading at a given pressure, and location of adsorption sites can be predicted [76]. MD simulations are typically used to predict the transport properties of molecules inside porous structures [77]. For example the diffusion of fluids inside the pores [76, 79]. The properties calculated by performing MC and MD simulations can be used to design new or improve existing technologies involving the adsorption of fluids on porous materials [91–94].

In the past decades, molecular simulations have been extensively used to obtain molecular understanding of the adsorption of fluids on porous materials [87, 88, 91,

95–98] and to identify optimal structures for specific applications [74, 99–104]. High-throughput screening studies have been carried out to identify promising MOFs, zeolites, and PPNs for the storage of CH_4 [20, 52, 54, 99, 105], H_2 [106–108], and CO_2 [74, 109, 110], and for the separation of numerous binary and ternary gas mixtures (*i.e.*, CO_2/CH_4 [101, 111], N_2/CH_4 [112], hexane isomers [102], $SO_2/CO_2/CO$ [113] *etc.* [103, 114]).

To conduct a high-throughput computational screening study, a database of computation-ready structures (*e.g.*, solvent free, no disordered atoms) is required. The database can consist of already synthesized or hypothetical structures. To date, most of the reported screening studies considered hypothetical structures [51, 52, 99, 106, 107, 115]. In the past decade, several databases containing hypothetical structures have been reported. Wilmer *et al.* [99] reported a database containing c.a. 138 000 hypothetical MOFs which were built by the combination of 102 building blocks derived from already existing MOFs. In case of zeolites, the hypothetical zeolite database [19] contains more than 5 million zeolite structures. A database containing c.a. 18 000 hypothetical PPNs was also reported by Martin *et al.* [54]. Databases of hypothetical structures can contain an almost unlimited number and types of structures which provides the opportunity to derive unknown structure-property relationships [104]. Newly discovered structure-property relationships can be used to guide the experimental synthesis effort toward structures with properties that are likely to yield improved performance for the application in interest. Screening studies can also help to identify the performance limit of different classes of materials for certain applications [51, 52]. For example, to assess the feasibility of the target set by the Advanced Research Project Agency-Energy (ARPA-E) for natural gas storage [116], Simon *et al.* [52] investigated more than 650 000 materials including MOFs, zeolites, and PPNs for the storage of CH_4. It was concluded that the target defined by ARPA-E is probably not reachable by using the investigated classes of materials [52]. As demonstrated by Simon *et al.* [52], high-throughput computational screening studies using hypothetical databases with hundreds of thousands of structures can be powerful tools for finding structure-property relationships and identifying upper application limits of materials which might not be possible if only a small number materials are studied. Moreover, performing screening studies on hypothetical databases can lead to the conclusion that investing in new types of synthesis methods of specific structures or type of materials is not recommended. Since hypothetical materials might turn out to be very complicated or impossible to synthesize, using databases with hypothetical structures for discovering new materials may not be the optimal option. Therefore, to identify promising structures for a specific application, the use of a database with already synthesized (or shown to be synthesizable) materials is preferred. The choice of the database can have a large influence on the out-

come of the screening study depending on the assumptions made during the creation of the database [117, 118]. Since the atomic coordinates of already synthesized materials are derived based on experimental measurements, the reported structures can contain solvents in the pores, have missing hydrogen atoms, structural defects, and may have overlapping atoms [117]. These features might be meaningful in crystallographic studies but can cause problems in molecular simulations, and thus, have to be dealt with. During the creation of a computation-ready database these issues can be handled using different approaches. For example, in the computational-ready experimental (CoRE) MOF database [119] all bound and unbound solvent molecules are removed from the experimental structures. In the Cambridge Structural Database non-disordered MOF subset (CSDSS) database [48] only unbound solvents are removed. Moghadam *et al.* [48] showed that the adsorption loading of H_2 and CH_4 on several MOFs that are present in both of these databases is significantly different. This finding highlights that the assumptions made at the creation of the database should be carefully considered in the screening study. Ideally, the identified structures should be synthesized and tested for the application in interest, however, this has been done only in very few studies [99].

Besides screening studies, molecular simulations are widely used to obtain molecular level understanding of the adsorption mechanism and diffusion of molecules in the pores of porous materials [76, 79, 87, 88, 91, 93, 95–98, 120–123]. In addition to predicting macroscopic properties such as adsorption isotherms and heats of adsorption, information on the microscopic level such as preferred adsorption sites, energetic interactions between atoms, and the adsorption mechanism of components can also be obtained from molecular simulations. In porous materials, preferred adsorption sites can be identified using several approaches. It can be done for example based on potential energy maps representing the interaction strength of the adsorbate and adsorbent at different positions inside the structure or by calculating the density distribution of adsorbates inside the structure based on the configurations generated throughout a simulation. By identifying the preferred adsorption sites at different conditions *e.g.*, pressures, temperatures, the relative importance of individual adsorption sites can also be determined. Ultimately, information about the adsorption mechanism of compounds can be obtained which can support the understanding of experimental measurements or the design of new materials [124]. For example, Walton *et al.* [124] used MC simulations to show that the step-wise adsorption isotherm of CO_2 on MOFs is caused by pore filling effects due to the strong electrostatic interactions between CO_2 and not by the change in the MOF crystal structure. Düren *et al.* [125] identified the interplay of factors influencing methane adsorption based on the characteristic properties of three MOFs, two zeolites, and four carbon nanotubes. Using

the obtained results, Düren *et al.* [125] proposed IRMOFs that have not been previously synthesized. The new structures showed substantially higher methane uptake than the already synthesized ones.

In the past decade, the adsorption of numerous compounds on zeolites, MOFs, and PPNs have been studied using molecular simulation techniques [52, 54, 101–103, 105, 106, 110]. The effect of different properties of zeolites such as Si/Al ratio, flexibility, location and type of exchangable cation *etc.* on the adsorption of variety of compounds have been studied using molecular simulation techniques [26, 95, 98, 126–128]. For specific applications of zeolites and MOFs, the transport properties and preferred adsorption sites of molecules inside the pores of the structures were also studied by molecular simulation techniques [75, 88, 127–129].

Despite being a powerful approach, molecular simulation of porous materials also faces challenges and limitations. A fundamental limitation is the unavailability of accurate transferable force fields. There are numerous force fields available which are usually fitted to reproduce the behavior of specific systems and have limited accuracy for others [26, 130–133]. Force fields used to model physico-chemical phenomena in porous materials have to be able to accurately describe the (1) adsorbate-adsorbate, (2) adsorbate-framework, and (3) framework-framework interactions [130]. The main difficulty arises in the derivation of the parameters for the adsorbate-framework and framework-framework interactions. In case of the adsorbate-framework interactions, the long range van der Waals and electrostatic interactions play a crucial role for physico-chemical phenomena especially for adsorption and diffusion [130]. Parameters to describe long-range interactions can be fitted using experimental data or ab initio level calculations. However, fitting Van der Waals parameters based on ab intio level calculations can be challenging due to its accuracy and difficulty to map the classical force field parameters onto the calculated potential energy surface [130]. Therefore, Van der Waals parameters are usually fitted to experimental data which are often not readily available and not always consistent [130]. Another challenge of molecular simulations for porous materials is the description of framework flexibility. Although the flexibility of the framework can affect the diffusion and adsorption of adsorbates on porous materials [95], in most studies rigid frameworks are used [95]. This assumption is usually adopted for two reasons: flexible models of porous materials significantly increase the required computational time which becomes unfeasible, or no force field is available for the system which can account for the flexibility of the framework. In case of zeolites, it is shown that framework flexibility does not have a significant effect on the adsorption of CO_2 [134], argon [135], *n*-alkanes [95], and cyclohexanes [136]. However, Caro-Ortiz *et al.* [137] showed that the adsorption of aromatic molecules such as ethylbenzene and xylene is affected by the flexibility of the zeolite framework. The

flexibility of the framework can also have considerable effect on the diffusion of guest molecules in porous materials [75]. It is shown for example that the diffusion coefficient of aromatic molecules in rigid and flexible zeolites can differ by orders of magnitude [138].

MOFs can be inherently more flexible than zeolites [139, 140]. In MOFs, the interactions which connect the metals or inorganic clusters with the organic linkers can range from strong covalent bonds to weak coordination bonds. Depending on the type of interaction between nodes and linkers, and the flexibility of the linkers, MOFs can be highly flexible materials, so called "soft porous crystals" [140, 141]. The flexibility of the framework can be also related to its mechanical stability [142]. The varying degree of flexibility poses many challenges to derive a transferable force field for MOFs which can account for the flexibility of the framework. Recently, a couple of general force fields have been reported for MOFs which include the flexibility of the frameworks. Bureekaew *et al.* [143] reported the MOF-FF force field which was derived for a variety of MOF-families (ZnO_4, $Zr_6O_4(OH)_4$, copper and zinc paddle-wheel) based on ab initio calculations. Coupry *et al.* [144] extended the UFF force field with additional atom types found in the CoRE database. Vanduyfhuys *et al.* [145] reported a software package which can be used to derive flexible force field parameters for MOFs based on ab initio calculations. Heinen *et al.* [146] reported a new approach to fit the functional forms and the corresponding force field parameters to the elastic tensor of the framework computed from ab initio calculations. The main advantage of this new approach proposed by Heinen *et al.* [146] is that the missing functional forms of the derived force field can be identified based on components of the elastic tensor. It can be seen that there are several models available to include the flexibility of framework in molecular simulations. However, these methods are computationally expensive and not applicable to all systems.

Due to their very versatile nature, porous materials are expected to be used in more and more applications in the future. Molecular simulation is a very powerful tool for identifying porous materials for applications or for providing insight into the molecular level phenomena inside porous materials. In this thesis, computational studies are carried out to both ends. *In silico* screening of MOFs and zeolites are carried to identify new structures for specific applications. Zeolites, cyclodextrins and theoretical systems are studied to understand the molecular phenomena occurring inside the pores of the structures.

1.3. OUTLINE OF THIS THESIS

In this thesis, specific applications of porous materials are studied using molecular simulations. Zeolites, MOFs, and cyclodextrins (CDs) are studied for waste water treat-

ment and energy related applications. The purpose of the presented studies is twofold: (1) to identify the best performing materials for a specific application from a large pool of structures, and (2) to obtain molecular insight into the molecular phenomena involved in a specific application. These studies aim to provide guidance for experimentalist in finding new, better performing materials, and a more detailed understanding of the involved phenomena. The first chapter of this thesis discusses the importance of porous materials, the role of molecular simulations in the discovery of new type of materials, and the outline of this thesis. In Chapter 2, the pressure of fluids in nanoporous materials is investigated based on the theory reported by Galteland *et al.* [147]. The pressure of a nanoconfined fluid is one of the most important thermodynamic properties which is needed for an accurate description of for example the flow rate and diffusion coefficient of fluids in porous materials. Two different pressures are needed to account for confinement effects in nanoporous materials: the differential pressure P, and the integral pressure $\hat{p}$. The relation between the differential and integral pressure is investigated by performing Monte Carlo (MC) simulations of Lennard-Jones fluids. It is shown that the differential and integral pressure are different for small pores and become equal as the pore size increases. Our findings indicate that the integral pressure (size dependent pressure) should be used in the computation of thermodynamic properties of fluids in nanopores. Besides testing theories of porous materials, molecular simulations can be also used to identify new materials to improve the performance of specific applications. In Chapters 3 and 4, two computational screening studies of Metal-Organic Frameworks (MOFs) and zeolites are presented for adsorption driven chillers (ACs) and high-pressure H_2 drying applications, respectively. In Chapter 3, a computational screening study of 2 930 already synthesized MOFs is carried out for adsorption driven heat pumps/chiller (AHP/AHCs) applications. 12 MOF structures are identified as promising candidates for AC application. The deliverable working capacities of these MOFs are considerably higher (> 0.6 ml ml^{-1}) than the previously reported highest value (> 0.45 ml ml^{-1}) in literature [148]. In Chapter 4, the performance of 218 zeolite structures is investigated for high-pressure H_2 drying. High-pressure H_2 gas is considered a promising energy carrier especially in case of vehicular applications. However, in many cases the water content of the high-pressure H_2 gas exceeds the 5 ppm limit which ensures that the water remains in the gas phase, thus, preventing ice formation upon expansion, and corrosion of the metallic parts of the storage vessel. Therefore, finding efficient drying methods such as selective adsorption of water by nanoporous materials is necessary to enable the use of high-pressure H_2 in vehicular applications. The 6 most promising structures are identified. The identified zeolites can be used to dry up to 8 000 times their own volume of H_2 gas. Our findings indicate that zeolites can be potential candidates for high-pressure H_2 drying applications. Be-

sides looking for better performing structures from a large pool of candidates, the efficiency of applications can also be improved by understanding the involved processes and fine tuning of current materials. In Chapters 5, 6, and 7, zeolites and cyclodextrins are investigated for waste water treatment related applications. In Chapter 5, the adsorption mechanism of 2,4,6-trichlorophenol (TCP) from aqueous solutions on FAU-type zeolites with different Al content is studied by performing MC simulations. The computational results are compared to experimental measurements. It is shown that simulations can capture the effect of the Si/Al ratio on the adsorption of the TCP. It is concluded that the S-shaped adsorption isotherm of TCP is caused by lateral interactions of the TCP molecules. In Chapter 6, the inclusion complex formation of β-CD with 6 environmentally relevant OMPs is studied. The binding free energy and enthalpy of the 6 inclusion complexes are reported with comparisons to experimental data and the contributions of the different interactions to the inclusion complex formation are discussed. Our findings show that MD simulations can adequately describe the inclusion complex formation of β-CD with OMPs. In Chapter 7, the diffusivity of CDs in aqueous solutions is investigated. The calculated self-diffusion coefficients using different water force fields are compared with experimental measurements and the effect of the water force field on the diffusivity of CDs is discussed. Our findings show that MD simulation can be used to provide reasonable diffusivity predictions, and to obtain molecular-level understanding useful for industrial applications of CDs.

2

FLUIDS IN CONFINEMENT: RELATION BETWEEN THE DIFFERENTIAL AND INTEGRAL PRESSURES

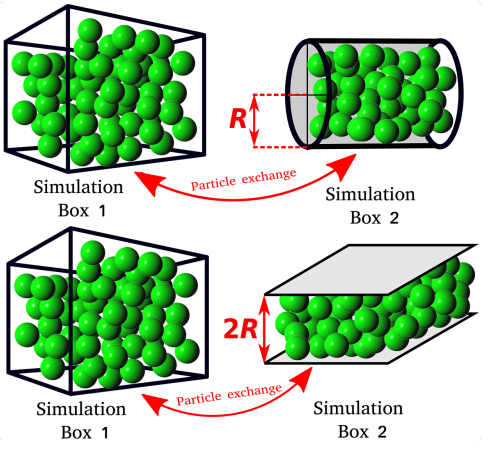

This chapter is based on the following publication: M. Erdős, O. Galteland, D. Bedeaux, S. Kjelstrup, O. A. Moultos, and T. J. H. Vlugt, Gibbs ensemble Monte Carlo simulation of fluids in confinement: Relation between the differential and integral pressures, *Nanomaterials* **10**, 293 (2020).

2.1. INTRODUCTION

The widespread application of nanoporous materials in several fields such as chromatography, membrane separation, catalysis, *etc.*, has led to a growing interest in the accurate description of the thermodynamic behavior of fluids confined in nanopores [49, 83, 149–152]. The pressure of a nanoconfined fluid is one of the most important thermodynamic properties which is needed for an accurate description of the flow rate, diffusion coefficient, and the swelling of the nanoporous material [153–156]. Various approaches for calculating the pressure of a fluid in a nanopore have been proposed [83, 84, 147, 157]. The main difficulty of the pressure calculation arises from the ambiguous definition of the pressure tensor inside porous materials due to the presence of curved surfaces and confinement effects [153, 158, 159]. Traditional thermodynamic laws and concepts such as Gibbs surface dynamics, Kelvin equation, *etc.*, may not be applicable at the nano-scale [160]. In the past decade, several methods were reported using different simulation techniques i.e. classical density functional theory [161, 162], equation of state modelling [163] *etc.*, to model the behaviour of fluids in confinement.

Recently, Galteland *et al.* [147] reported a new approach for the calculation of pressure in nanoporous materials using Hill's thermodynamics for small systems [164]. In this approach, two different pressures are needed to account for confinement effects in nanoporous materials: the differential pressure P, and the integral pressure $\hat{p}$. In an ensemble of small systems, the differential pressure times the volume change of the small systems is equal to the work exerted on the surroundings by the volume change. The differential pressure corresponds to the macroscopic pressure and does not depend on the size of the system. The addition of a small system to an ensemble of small systems exerts work on the surroundings which is equal to the integral pressure times the volume of the added small system. The differential and integral pressures are different for small systems and become equal in the thermodynamic limit. For a small system with volume V, the two pressures are related by [147, 164]:

$$P(V) = \left(\frac{\partial(\hat{p}(V)V)}{\partial V}\right)_{T,\mu} = \hat{p}(V) + V\left(\frac{\partial(\hat{p}(V))}{\partial V}\right)_{T,\mu} \tag{2.1}$$

As shown in this equation, the two pressures are different only when the integral pressure $\hat{p}$ depends on the volume of the system. Galteland *et al.* [147] performed equilibrium and non-equilibrium molecular dynamics simulations of LJ fluids in a face-centered lattice of spherical grains representing a porous medium. Using Hill's thermodynamics of small systems [164] and the additive property of the grand potential, Galteland *et al.* [147] defined the compressional energy ($\hat{p}V$) of the representative elementary volume (REV) in the simulations as follows:

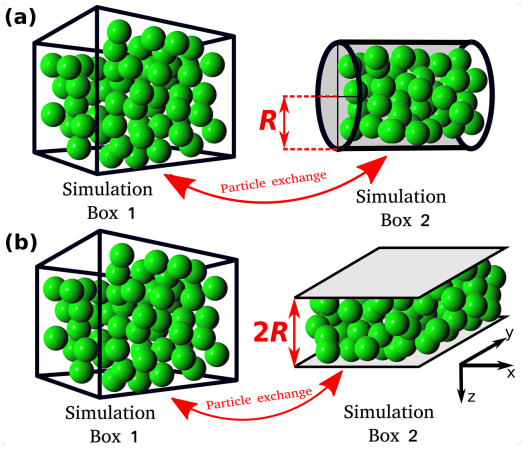

Figure 2.1: Schematic representation of the Monte Carlo simulation scheme. Simulation box 1 represents the bulk fluid with differential pressure P and uses periodic boundary conditions in each direction. Simulation box 2 contains the confined fluid with (average) integral pressure $\langle\hat{p}\rangle$. In simulation box 2, periodic boundary condition is applied only along the x-axis. In subfigures (a) and (b), the two investigated systems are shown where the bulk fluid is in equilibrium with the nanoconfined fluid in a cylinder and in a slit pore, respectively. Due to the particle exchange, the chemical potential of the two boxes are equal, but in general $P \neq \langle\hat{p}\rangle$.

$$\hat{p}V = \hat{p}^{\mathrm{f}}V^{\mathrm{f}} + \hat{p}^{\mathrm{r}}V^{\mathrm{r}} - \hat{\gamma}^{\mathrm{fr}}\omega^{\mathrm{fr}} \tag{2.2}$$

where $\hat{p}$ is the integral pressure of volume V, $\hat{p}^{\mathrm{f}}$ and V^{f} are the integral pressure and volume of the fluid, $\hat{p}^{\mathrm{r}}$ and V^{r} are the integral pressure and volume of the grain particles, and the $\hat{\gamma}^{\mathrm{fr}}$ and ω^{fr} are the integral surface tension and surface area between the fluid and grain particles. Galteland *et al.* [147] carried out Molecular Dynamics (MD) simulations of a single spherical grain in a pore and then of a face centered lattice of spherical grains in a pore. The authors computed the integral rock pressure, surface tension, and the pressure of the representative volume. Based on the obtained results it was concluded that the definition of two pressures is needed to calculate the pressure of the fluid in nanoporous medium.

In this chapter, the theory proposed by Galteland *et al.* [147] is investigated by performing MC simulations of Lennard-Jones fluids. The simulations are carried out in a modified Gibbs ensemble, using two simulation boxes in equilibrium with each other. One box represents the bulk fluid, while the other simulation box represents the nanoconfined system, including walls that interact with the fluid particles, as shown in Figure 2.1.

The effect of confinement on the integral pressure is investigated by considering different fluid-wall interaction strengths and pore geometries, namely, a cylinder and a slit pore. To investigate the relation between the differential and integral pressure, the

difference of the two pressures, $P - \langle \hat{p} \rangle$, and the ratio of driving forces for mass transport, $\frac{d\langle \hat{p} \rangle}{dP}$, are computed. In Section 2.2, the devised ensemble and the equations used to calculate the pressure and energy of the system are presented. In Section 2.3, a rigorous derivation of the expression used to compute the ratio of driving forces is shown. In Section 2.4, the results for the different differential pressures and pore geometries are shown. In Section 2.5, our conclusions are summarized.

2.2. SIMULATION DETAILS

All MC simulations are carried out using an in-house simulation code. The MC simulations consist of two simulation domains, simulation box 1 and simulation box 2 (see Figure 2.1). Throughout this chapter, the terms simulation box 1 and 2 are used to refer to the two domains. The total number of particles in the system, N_T, is fixed and particles can be exchanged between the simulation boxes. box 1 is cubic and has periodic boundary conditions imposed in all directions. box 1 represents a bulk fluid. The differential pressure, P, and temperature, T, in simulation box 1 are imposed, while the volume, V_1, and the number of particles, N_1, can fluctuate. Simulation box 2 is either a cylinder or a slit pore with a fixed volume V_2. The size of the cylinder and the slit pore are defined by the radius, R, and by the distance between the two parallel planes, $2R$, respectively (Figure 2.1). In box 2, periodic boundary conditions are applied only in the axial direction for the cylinder and in the x and y directions for the slit pore (see Figure 2.1). box 2 represents the confined fluid which has an integral pressure $\hat{p}$. In simulation box 2 the volume, V_2, and temperature T are imposed while the number of particles N_2 can fluctuate by exchanging particles with box 1. The instantaneous integral pressure fluctuates, and by definition [164] its ensemble average, $\langle \hat{p} \rangle$, will be equal to P only for macroscopic systems ($R \to \infty$). The ensemble used is a variation of the NPT-Gibbs ensemble [165]. The main difference between the ensemble used in this work and the conventional NPT-Gibbs ensemble is that in our simulations the volume of box 2 is fixed [165]. Essentially, box 2 corresponds to the grand-canonical ensemble with the reservoir explicitly modelled in box 1. This computational setup was also used in other studies, i.e. studied by A. Z. Panagiotopoulos et. al. [165], P. Bai et. al. [166] *etc.*

In the MC simulations, three types of trial moves are used: translations, volume changes, and particle exchanges. The translation and particle exchange trial moves are used in both simulation boxes while volume change trial moves are only performed in simulation box 1. The acceptance rules of the trial moves can be found elsewhere [76]. The particle exchange trial moves, ensure that box 1 and box 2 are in chemical equilibrium, i.e., the chemical potentials of the two boxes are equal ($\mu_1 = \mu_2$). The chemical potentials of the boxes are defined as the sum of the ideal and excess chemical poten-

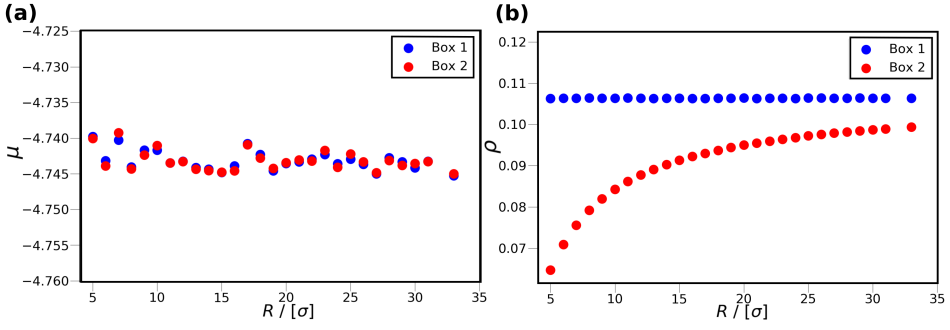

Figure 2.2: The chemical potential and density of the bulk, box 1, and confined fluids, box 2, as a function of the cylinder radius, R, at $P = 0.2$ (in simulation box 1). The blue and red colors represent box 1 and box 2, respectively. The temperature is fixed at $T = 2$. All of the values are presented in reduced units. The errorbars are smaller than the symbol sizes.

tials of the fluid in the respective box ($\mu_1 = \mu_1^{\mathrm{id}} + \mu_1^{\mathrm{ex}}, \mu_2 = \mu_2^{\mathrm{id}} + \mu_2^{\mathrm{ex}}$). The ideal gas chemical potentials ($\mu_1^{\mathrm{id}}, \mu_2^{\mathrm{id}}$) are calculated based on the density and temperature of the fluid ($\mu_1^{\mathrm{id}} = k_{\mathrm{B}} T \log(\rho)$). The excess chemical potential ($\mu_1^{\mathrm{ex}}, \mu_2^{\mathrm{ex}}$) can be calculated using different methods, i.e. Widom's test particle insertion method [76], Continuous Fractional Component Monte Carlo method [85, 89, 167], Bennet acceptance ratio method [168] *etc.* Although the Bennet acceptance ratio method is computationally more efficient than Widom's test particle insertion method, Widom's test particle method is sufficient for the systems considered in this chapter. For calculating the excess chemical potential with Widom's test particle insertion method the following relation is used:

$$\mu^{\mathrm{ex}} = -k_{\mathrm{B}} T \ln \left\langle \exp \left[- \frac{E_{\mathrm{i}}}{k_{\mathrm{B}} T} \right] \right\rangle \tag{2.3}$$

, where $\langle\rangle$ denotes the averages of all insertions, and E_{i} represents the potential energy of the inserted particle. Separate simulations are carried out using different cylinder radii R while imposing $P = 0.2$ (in reduced units) in box 1. In Figure 2.2, the chemical potential of box 1 and box 2 (Figure 2.2a), and the density of box 1 and box 2 (Figure 2.2b) are shown as a function of the cylinder radius at $P = 0.2$. As can be seen from Figure 2.2a, the chemical potentials of box 1 and box 2 are equal within the uncertainties of the simulations.

In all simulations, the total potential energy, U, is calculated using the 12-6 Lennard-Jones interaction potential:

$$U = U_{\mathrm{fluid-fluid}} + U_{\mathrm{fluid-wall}} \tag{2.4}$$

where $U_{\mathrm{fluid-fluid}}$ is the potential energy due to interaction between the fluid particles, and $U_{\mathrm{fluid-wall}}$ represents the potential energy contribution from the interactions be-

tween the fluid particles and the wall of box 2. $U_{\text{fluid-fluid}}$ in both simulation boxes is calculated according to:

$$U_{\text{fluid-fluid}} = \begin{cases} \sum_{i<j} \left[4\epsilon_{\text{fluid}} \left(\left(\frac{\sigma_{\text{fluid}}}{r_{ij}} \right)^{12} - \left(\frac{\sigma_{\text{fluid}}}{r_{ij}} \right)^{6} \right) - U_{\text{shift}} \right] & r_{ij} < 2.5\sigma_{\text{fluid}} \\ 0, & \text{otherwise} \end{cases} \tag{2.5}$$

where r_{ij} is the distance of particle i and j, U_{shift} makes the interaction potential continuous at the cut-off distance ($2.5\sigma_{\text{fluid}}$), and ϵ_{fluid}, σ_{fluid} are the Lennard-Jones parameters. In the past, several studies were reported using different types of interaction potentials to model the fluid-solid interactions in confined spaces [166, 169, 170]. Since the aim of this chapter is to show the difference between the differential and integral pressures and not to simulate some specific adsorption system, only two types of interaction potentials are considered for the interaction of fluid particles with the wall in simulation box 2. In the first case, the wall has only repulsive interactions with the fluid particles. The potential energy contribution of this type is calculated based on the Weeks-Chandler-Andersen potential [171]:

$$U_{\text{fluid-wall}} = \begin{cases} \sum_{i=0}^{N_2} \left[4\epsilon_{\text{fw}} \left(\left(\frac{\sigma_{\text{fw}}}{r_{wi}} \right)^{12} - \left(\frac{\sigma_{\text{fw}}}{r_{wi}} \right)^{6} \right) + 1 \right] & r_{\text{w}i} < 2^{1/6}\sigma_{\text{fw}} \\ 0, & \text{otherwise} \end{cases} \tag{2.6}$$

where N_2 is the number of particles in box 2, $r_{\text{w}i}$ is the closest distance of particle i from the walls, ϵ_{fw} and σ_{fw} are the Lennard-Jones parameters for the interaction between the wall and the fluid particles. In the second case, the attractive interactions between the wall and fluid particles are taken into account using the traditional form of the 12-6 Lennard-Jones interaction potential:

$$U_{\text{fluid-wall}} = \begin{cases} \sum_{i=0}^{N_2} \left[4\epsilon_{\text{fw}} \left(\left(\frac{\sigma_{\text{fw}}}{r_{wi}} \right)^{12} - \left(\frac{\sigma_{\text{fw}}}{r_{wi}} \right)^{6} \right) - U_{\text{shift-fw}} \right] & r_{\text{wi}} < 2.5\sigma_{\text{fw}} \\ 0, & \text{otherwise} \end{cases} \tag{2.7}$$

where $U_{\text{shift-fw}}$ makes the interaction potential continuous at the cut-off distance, and ϵ_{fw} and σ_{fw} are the LJ parameters.

The expression for calculating the integral pressure in box 2 is as follows [77]:

$$\hat{p} = \frac{N_2}{V_2} k_{\text{B}} T + \hat{p}_{\text{fluid-fluid}} + \hat{p}_{\text{fluid-wall}} \tag{2.8}$$

where $\hat{p}_{\text{fluid-fluid}}$ represents the contribution of the fluid-fluid interaction to the integral pressure, k_B is the Boltzmann constant, and $\hat{p}_{\text{fluid-wall}}$ represents the contribution of the fluid-wall interaction to the integral pressure. The $\hat{p}_{\text{fluid-fluid}}$, and $\hat{p}_{\text{fluid-wall}}$

terms represent the virial contributions of the integral pressure. The terms are calculated based on the virial theorem [153], i.e. using the derivative of the potential energy function respect to r. The pressure term $\hat{p}_{\text{fluid-fluid}}$ is calculated as follows [153]:

$$\hat{p}_{\text{fluid-fluid}} = \frac{48}{3V_2}\epsilon_{\text{fluid}} \sum_{i<j} \left(\left(\frac{\sigma_{\text{fluid}}}{r_{ij}} \right)^{12} - 0.5 \left(\frac{\sigma_{\text{fluid}}}{r_{ij}} \right)^{6} \right) \tag{2.9}$$

The third term in Equation 2.8 represents the pressure contribution related to the interactions of the LJ particles with the wall of box 2. The term $\hat{p}_{\text{fluid-wall}}$ for the repulsive wall potential is derived based on Equation 2.6 [153]. The following expression is obtained:

$$\hat{p}_{\text{fluid-wall}} = \begin{cases} \sum_{i=1}^{N_2} \frac{24}{3V_2}\epsilon_{\text{fw}} \left(\left(\frac{\sigma_{\text{fw}}}{r_{wi}} \right)^{12} - 0.5 \left(\frac{\sigma_{\text{fw}}}{r_{wi}} \right)^{6} \right) & r_{wi} < 2^{1/6}\sigma_{\text{fw}} \\ 0, & \text{otherwise} \end{cases} \tag{2.10}$$

The following expression is used to calculate the $\hat{p}_{\text{fluid-wall}}$ when the wall has also attractive interactions with the fluid [153]:

$$\hat{p}_{\text{fluid-wall}} = \begin{cases} \sum_{i=1}^{N_2} \frac{24}{3V_2}\epsilon_{\text{fw}} \left(\left(\frac{\sigma_{\text{fw}}}{r_{wi}} \right)^{12} - 0.5 \left(\frac{\sigma_{\text{fw}}}{r_{wi}} \right)^{6} \right) & r_{wi} < 2.5\sigma_{\text{fw}} \\ 0, & \text{otherwise} \end{cases} \tag{2.11}$$

By comparing Equations 2.10, 2.11 and 2.9, it can observed that the multiplication factor 48 in Equation 2.9 is replaced by the factor 24 in Equations 2.10 and 2.11. This difference means that only 50 % of the fluid-wall interactions are taken into account at the calculation of the $\hat{p}_{\text{fluid-wall}}$ term [153]. In the MC simulations, Equations 2.8, 2.9, 2.10 and 2.11 yield instantaneous values from which ensemble averages are computed, i.e., $\langle \hat{p} \rangle$.

In this chapter, all of the reported parameters are in dimensionless units. In all simulations, the LJ parameters of the fluid particles are $\epsilon_{\text{fluid}} = 1$, $\sigma_{\text{fluid}} = 1$ and the cut-off radius is $r_{\text{cut}} = 2.5\sigma_{\text{fluid}}$ for the fluid-fluid interactions. Regardless of the type of interaction potential used to calculate the interaction of the fluid particles and the wall in simulation box 2, the LJ parameter, $\sigma_{\text{fw}} = 1$ is used. In the case of the purely repulsive wall potential the LJ parameter $\epsilon_{\text{fw}} = 1$ is used. In case of the attractive wall potential, five different values for the ϵ_{fw} LJ parameters are considered: $\epsilon_{\text{fw}} = 0.3, 0.5, 0.7, 1.0, 1.5$. The LJ interactions are truncated and shifted (i.e., no tail corrections are applied). To avoid phase transitions, the temperature is fixed at $T = 2$ [172, 173] which is higher than the critical temperature of the LJ fluid (c.a. 1.3 with tail corrections [172, 173]).

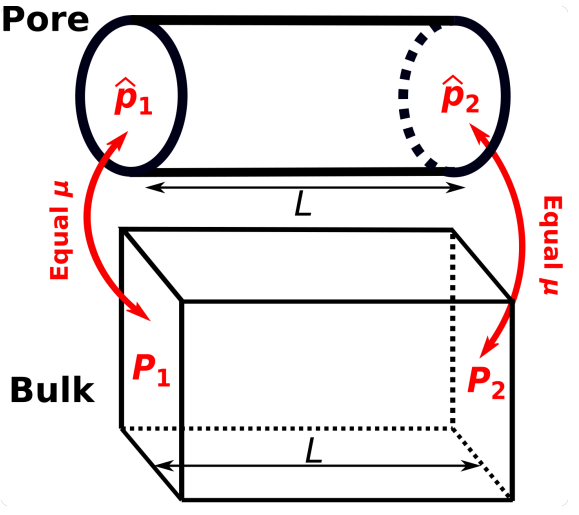

Figure 2.3: Schematic representation of a bulk fluid in equilibrium with a nanoconfined fluid in a pore. The concept of the ratio of driving forces for mass transport, $\frac{d\langle\hat{p}\rangle}{dP}$, can be introduced based on the definition of ratio of driving forces in the two systems, $\frac{d\langle\hat{p}\rangle}{dL}$ and $\frac{dP}{dL}$.

2.3. THEORY

Mass transport of fluids can happen through diffusion, convection, and migration. Since the driving force for both diffusion and convection depends on the pressure of the fluid, to accurately model the behavior of fluids in nanopores, the description of the pressure of the fluid is crucial. To investigate the difference between the differential and integral pressures, the ratio $\frac{d\langle\hat{p}\rangle}{dP}$ is calculated. The term $\frac{d\langle\hat{p}\rangle}{dP}$ is the ratio of the pressure gradient for mass transport in the bulk phase, $\frac{dP}{dL}$, and in the confined space $\frac{d\langle\hat{p}\rangle}{dL}$ (see Figure 2.3). Essentially, the ratio of driving forces, $\frac{d\langle\hat{p}\rangle}{dP}$, equals the ratio of transport coefficients when either P or $\hat{p}$ is used as driving force for mass transport in the corresponding transport equation. $\frac{d\langle\hat{p}\rangle}{dP}$ is referred to as the ratio of driving forces throughout this work. One possible approach to compute the ratio of driving forces is to perform simulations at different imposed differential pressures and calculate the difference in the differential and integral pressures. To avoid the necessity of performing several simulations, in this chapter the ratio of driving forces is calculated based on the fluctuation theory. Using this approach the ratio of driving forces can be obtained by performing a single simulation.

To obtain an expression for $\frac{d\langle\hat{p}\rangle}{dP}$, the partition function of the system is needed [76]:

$$Q = C \sum_{N_1=0}^{N_T} \frac{V_2^{N_T-N_1}}{N_1!\,(N_T-N_1)!} \int_0^\infty \mathrm{d}V_1\; V_1^{N_1}\; e^{-\beta P V_1} \int \mathrm{d}r^{N_T}\; e^{-\beta U} \tag{2.12}$$

where C is a constant, $\beta = \frac{1}{k_B T}$, N_1 is the number of particles in box 1, N_T is total number of particles in the simulation, V_1 is the volume of box 1, V_2 is the volume of box 2, and U is the potential energy. The ensemble average of a thermodynamic property X can be obtained using:

$$\langle X \rangle = \frac{\sum_{N_1=0}^{N_T} \frac{V_2^{(N_T-N_1)}}{N_1!\,(N_T-N_1)!} \int_0^\infty \mathrm{d}V_1\; V_1^{N_1}\; e^{-\beta P V_1} \int \mathrm{d}r^{N_T}\; e^{-\beta U} X}{\sum_{N_1=0}^{N_T} \frac{V_2^{(N_T-N_1)}}{N_1!\,(N_T-N_1)!} \int_0^\infty \mathrm{d}V_1\; V_1^{N_1}\; e^{-\beta P V_1} \int \mathrm{d}r^{N_T}\; e^{-\beta U}} \tag{2.13}$$

Therefore, to obtain the expression for $\frac{\mathrm{d}\langle \hat{p} \rangle}{\mathrm{d}P}$, the following relation is used:

$$\frac{\mathrm{d}\langle \hat{p} \rangle}{\mathrm{d}P} = \frac{\mathrm{d}}{\mathrm{d}P} \frac{\sum_{N_1=0}^{N_T} \frac{V_2^{(N_T-N_1)}}{N_1!\,(N_T-N_1)!} \int_0^\infty \mathrm{d}V_1\; V_1^{N_1}\; e^{-\beta P V_1} \int \mathrm{d}r^{N_T}\; e^{-\beta U} \hat{p}}{\sum_{N_1=0}^{N_T} \frac{V_2^{(N_T-N_1)}}{N_1!\,(N_T-N_1)!} \int_0^\infty \mathrm{d}V_1\; V_1^{N_1}\; e^{-\beta P V_1} \int \mathrm{d}r^{N_T}\; e^{-\beta U}} \tag{2.14}$$

By switching the order of the integration and differentiation the following expression is obtained:

$$\begin{aligned}
&\frac{\mathrm{d}\langle \hat{p} \rangle}{\mathrm{d}P} = \\
&\frac{\left(\sum_{N_1=0}^{N_T} \int_0^\infty \mathrm{d}V_1 \int \mathrm{d}r^{N_T}\; \frac{V_2^{(N_T-N_1)}\, V_1^{N_1}}{N_1!\,(N_T-N_1)!}\; (-\beta\, V_1) e^{-\beta P V_1}\; e^{-\beta U} \hat{p} \right)}{\left(\sum_{N_1=0}^{N_T} \int_0^\infty \mathrm{d}V_1 \int \mathrm{d}r^{N_T}\; \frac{V_2^{(N_T-N_1)}\, V_1^{N_1}}{N_1!\,(N_T-N_1)!}\; e^{-\beta P V_1}\; e^{-\beta U} \right)^2} \\
&\times \left(\sum_{N_1=0}^{N_T} \int_0^\infty \mathrm{d}V_1 \int \mathrm{d}r^{N_T}\; \frac{V_2^{(N_T-N_1)}\, V_1^{N_1}}{N_1!\,(N_T-N_1)!}\; e^{-\beta P V_1}\; e^{-\beta U} \right) \\
&- \frac{\left(\sum_{N_1=0}^{N_T} \int_0^\infty \mathrm{d}V_1 \int \mathrm{d}r\; \frac{V_2^{(N_T-N_1)}\, V_1^{N_1}}{N_1!\,(N_T-N_1)!}\; (-\beta\, V_1) e^{-\beta P V_1}\; e^{-\beta U} \right)}{\left(\sum_{N_1=0}^{N_T} \int_0^\infty \mathrm{d}V_1 \int \mathrm{d}r^{N_T}\; \frac{V_2^{(N_T-N_1)}\, V_1^{N_1}}{N_1!\,(N_T-N_1)!}\; e^{-\beta P V_1}\; e^{-\beta U} \right)^2} \\
&\times \left(\sum_{N_1=0}^{N_T} \int_0^\infty \mathrm{d}V_1 \int \mathrm{d}r^{N_T}\; \frac{V_2^{(N_T-N_1)}\, V_1^{N_1}}{N_1!\,(N_T-N_1)!}\; e^{-\beta P V_1}\; e^{-\beta U} \hat{p} \right) \\
&= \langle -\beta V_1 \hat{p} \rangle - (\langle -\beta V_1 \rangle \langle \hat{p} \rangle) = \beta(\langle V_1 \rangle \langle \hat{p} \rangle - \langle V_1 \hat{p} \rangle) = \frac{\langle V_1 \rangle \langle \hat{p} \rangle - \langle V_1 \hat{p} \rangle}{k_b T}
\end{aligned} \tag{2.15}$$

The final expression in Equation 2.15 is essentially the cross correlation between V_1 and $\hat{p}$. In this chapter, this expression is used to calculate the ratio of driving forces.

2.4. RESULTS AND DISCUSSION

In this work, the difference between the differential and integral pressure, $P - \langle \hat{p} \rangle$, and the ratio of driving forces $\frac{\mathrm{d}\langle \hat{p} \rangle}{\mathrm{d}P}$, are investigated. Two different pore geometries, a cylinder and a slit pore, are studied with varying fluid-wall interaction potentials. The effect of confinement is investigated for gas ($\rho \approx 0.1$) and liquid ($\rho = 0.58, 0.8$) phases, corresponding to $P = 0.2$, 2.0, 6.0, respectively.

2.4.1. DIFFERENCES BETWEEN THE DIFFERENTIAL AND INTEGRAL PRESSURES

In Figure 2.4, the difference between the differential, P, and the ensemble average of the integral pressure, $\langle \hat{p} \rangle$, is shown as a function of the inverse radius, R^{-1}, of box 2 for the cylindrical and slit pore cases for the two types of wall potentials. As can be seen in Figure 2.4, as R^{-1} decreases, the difference between the differential and integral pressure decreases in all cases. The data are fitted to $AR^{-1}+B$, where A and B are constants. The coefficient of determination of the fitted lines is above 0.99 showing that the relation between the R^{-1} and $P - \langle \hat{p} \rangle$ is indeed linear. For large radii ($R > 30\sigma$), where the fluid in box 2 behaves like in the bulk, $P - \langle \hat{p} \rangle$ approaches 0 which is also indicated by the fitted lines.

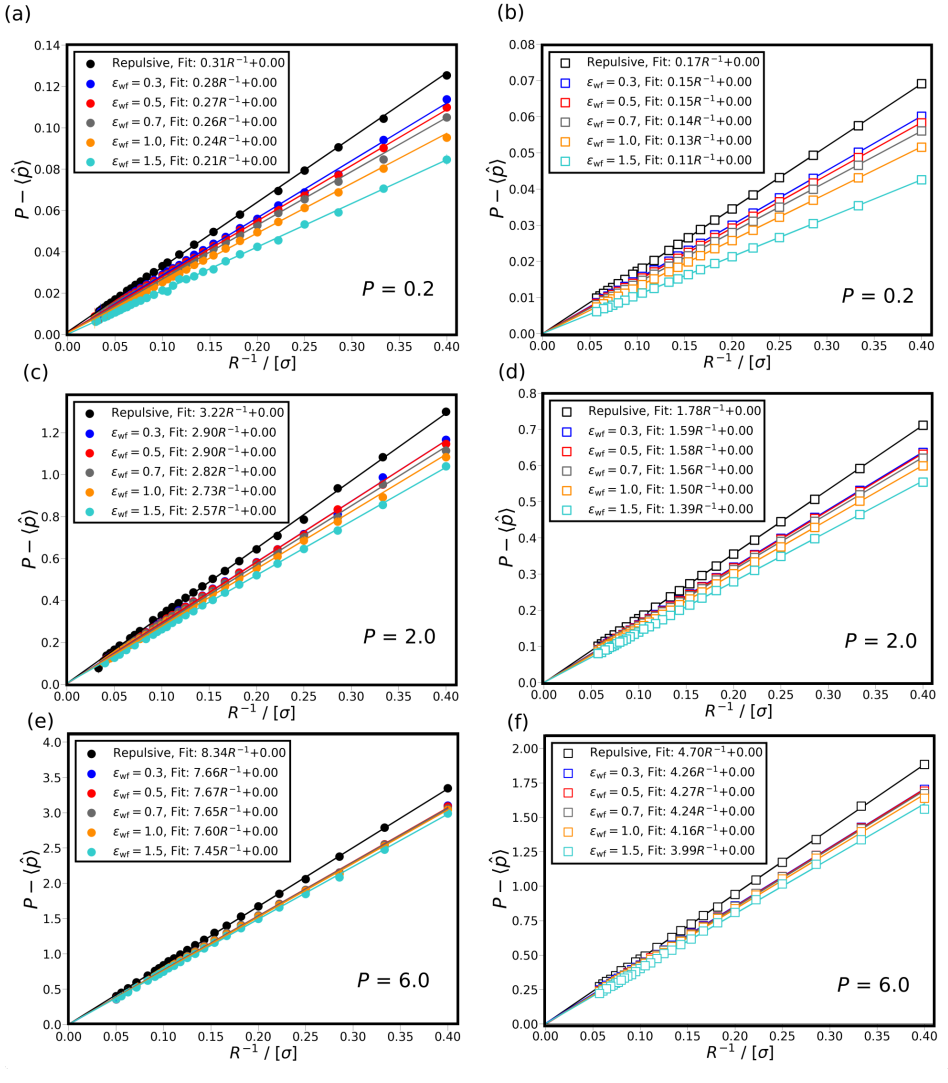

Figure 2.4: The difference between the differential, P, and the ensemble average of integral pressure, $\langle\hat{p}\rangle$, is shown as a function of the inverse radius R^{-1} of box 2 at $P = 0.2$, 2.0, and 6.0 for cylindrical and slit pores with fluid-wall interactions. In subfigures (a), (c), and (e), the pressure difference is shown for cylindrical pores at differential pressure $P = 0.2$, 2.0, and 6.0, respectively. In subfigures (b), (d), and (f), the pressure difference is shown for slit pores at differential pressure $P = 0.2$, 2.0, and 6.0, respectively. The simulation results are shown with symbols, while the lines are fits to the data points. The equation used for the fitting is $AR^{-1} + B$, where A and B are constants. The colors denote the different level of attraction between the wall of box 2 and the fluid, repulsive wall potential (black), $\epsilon_{\text{wf}} = 0.3$ (blue), 0.5 (red), 0.7 (gray), 1.0 (orange), and 1.5 (cyan). The results for the cylindrical pore are shown with closed circles and for the slit pores with open rectangles. The temperature of both boxes is set to $T = 2$. The average densities of box 1 are $\rho \approx 0.10$, 0.58, and 0.8 at $P = 0.2$, 2.0, and 6.0, respectively.

In Figures 2.4a, 2.4c, 2.4e the difference between the two pressures are shown for the cylindrical pore. In 2.4b, 2.4d, 2.4f, the difference in the pressures are shown for the slit pore. By comparing the magnitude of $P - \langle \hat{p} \rangle$ for the cylindrical and slit pore cases, it can be seen that the pressure difference is larger in the cylindrical pore than in the slit pore. The larger value of $P - \langle \hat{p} \rangle$ for the cylindrical pores can be attributed to the stronger confinement effects compared to the slit pore. The stronger confinement effects are also indicated by the steeper slopes (constant A in the fitted lines) of the cylindrical pore compared to the slit pore. It can also be observed that by increasing the interaction strength between the wall of box 2 and the fluid, ϵ_{wf}, the difference between the differential and integral pressure at the same pore size decreases. By comparing the calculated values of $P - \langle \hat{p} \rangle$ for $P = 0.2$ and $P = 6.0$, it can be seen that the effect of the interaction strength between the wall in box 2 and the fluid, ϵ_{wf}, is considerably larger at the lower differential pressure. For example, in the case of the slit pore the ratio of slopes of the fitted line for $\epsilon_{\text{wf}} = 1.0$ and $\epsilon_{\text{wf}} = 1.5$ at $P = 0.2$ is 0.88, see Figure 2.4b, and at $P = 6.0$ is 0.96, see Figure 2.4f. This can be caused by the different number of particles inside the pore at the two differential pressures. In the case of $P = 0.2$, by increasing the interaction strength, more particles can enter the pore which results in larger integral pressures, while at $P = 6.0$ the pore is practically saturated for all ϵ_{wf} and therefore the interaction strength has a lower effect on the integral pressure.

Based on the work of Galteland *et al.* [147], the slope of the fitted line can also be related to the effective surface tension between the fluid particles and the wall in box 2, i.e. $P - \langle \hat{p} \rangle \sim \frac{\hat{\gamma}^{\text{fr}}_{\text{effective}}}{R}$. The linear relation between $P - \langle \hat{p} \rangle$ and R^{-1} shows that the effective surface tension does not depend on the curvature of the wall. In Figure 2.4, it can be observed that the effective surface tension decreases as the fluid-wall interactions become more attractive. In Figures 2.4a-b, 2.4c-d and 2.4e-f, it can be seen that the ratio of the effective surface tensions (slopes of the fitted lines) for the same ϵ_{wf} with the slit and cylindrical pore is nearly constant. For example, at $\epsilon_{\text{wf}} = 0.5$ and $P = 2.0$ the ratio of the slope of the fitted lines for the slit and cylindrical pore is ~ 0.54, see Figure 2.4c-d, and at $\epsilon_{\text{wf}} = 0.3$ and $P = 0.2$ the ratio of the two slopes is also ~ 0.54, see Figure 2.4a-b. The ratio of the effective surface tensions between the slit and cylindrical pores are in the range of ~0.52-0.56 and considered constant since it is within the uncertainties of simulations. The constant ratio of effective surface tension between the slit and cylindrical pore also indicates the larger confinement effects in the cylindrical pore.

2.4.2. RATIO OF DRIVING FORCES

In Figure 2.5, the ratio of driving forces for mass transport, $\frac{\mathrm{d}\langle \hat{p} \rangle}{\mathrm{d}P}$, is shown as a function of the inverse radius of box 2, R^{-1}, at three different pressures, $P = 0.2, 2.0, 6.0$,

for both the slit and cylindrical pores. From Figure 2.5, it can be observed that $\frac{d\langle\hat{p}\rangle}{dP}$ is considerably smaller than 1 for small pore sizes.

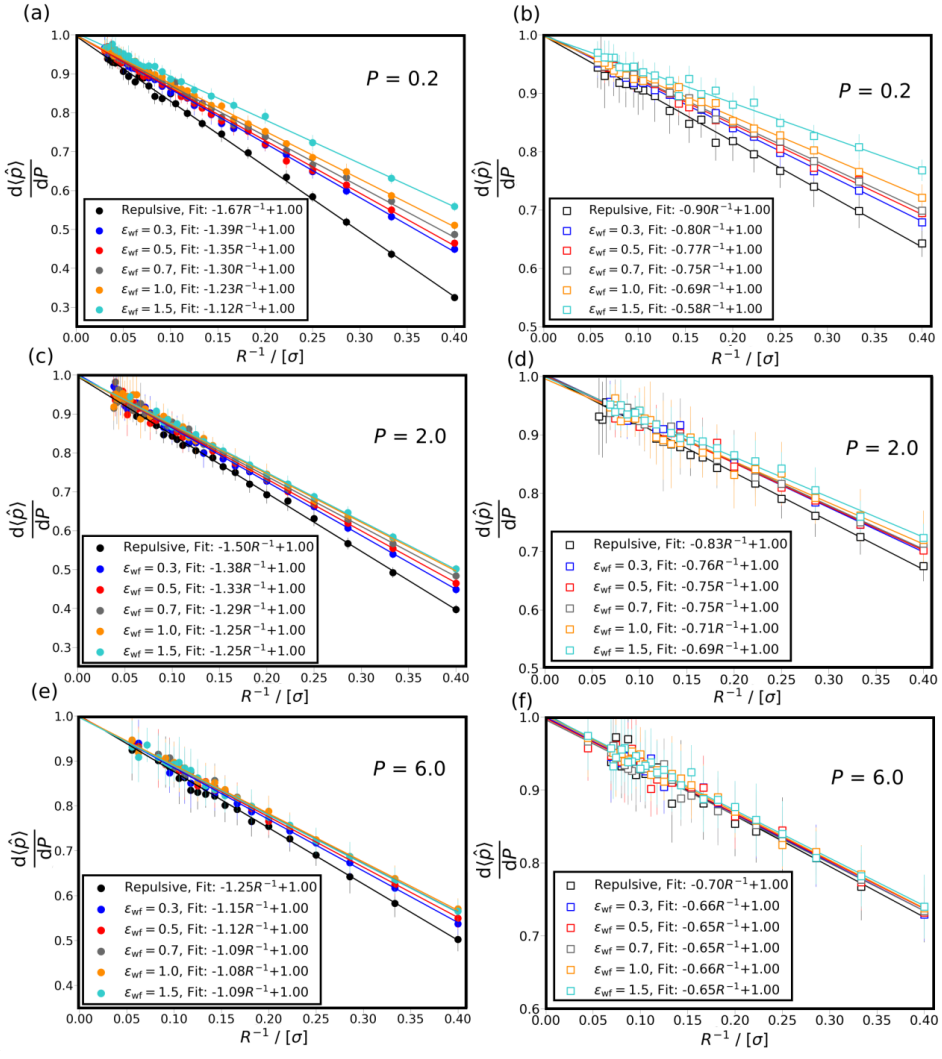

Figure 2.5: The ratio of driving forces, $\frac{d\langle\hat{p}\rangle}{dP}$, is shown as a function of the inverse radius, R^{-1}, of box 2 at $P = 0.2, 2.0$, and 6.0 for the cylindrical and slit pore cases with repulsive and attractive wall potentials. In subfigures (a), (c), and (e), $\frac{d\langle\hat{p}\rangle}{dP}$ is shown for cylindrical pores at differential pressure $P = 0.2$, 2.0, and 6.0, respectively. In subfigures (b), (d), and (f), $\frac{d\langle\hat{p}\rangle}{dP}$ is shown for slit pores at differential pressures $P = 0.2$, 2.0, and 6.0, respectively. The simulation results are shown with symbols, while the lines are fits to the data points. The equation used for the fitting is $AR^{-1} + B$, where A and B are constants. The results for the cylindrical pore are shown with closed circles and for the slit pores with open rectangles. The colors denote the different wall potential used in box 2, repulsive wall potential (black), $\epsilon_{wf} = 0.3$ (blue), $\epsilon_{wf} = 0.5$ (red), $\epsilon_{wf} = 0.7$ (gray), $\epsilon_{wf} = 1.0$ (orange), and $\epsilon_{wf} = 1.5$ (cyan). The temperature of both boxes is set to $T = 2$. The average densities of box 1 are $\rho \approx 0.10$, 0.58, and 0.8 at $P = 0.2$, 2.0, and 6.0, respectively.

This means that a change in the differential pressure, P, of box 1 results in a smaller change in the integral pressure, $\langle\hat{p}\rangle$, of box 2. This difference underlines the effect of the confinement on the pressure of the fluid in nanopores and shows the difference in driving forces in the bulk and confined fluid. As R increases, $\frac{d\langle\hat{p}\rangle}{dP}$ approaches 1, i.e., the fluid in the pore behaves more like a bulk fluid. As can be seen in Figure 2.5, $\frac{d\langle\hat{p}\rangle}{dP}$ is larger for the slit pore than for the cylindrical pore at the same conditions. This means that in case of the slit pore a change in the differential pressure, P, results in a larger difference in the integral pressure, $\langle\hat{p}\rangle$, than for the cylindrical pore. The larger change in the integral pressure indicates that the confinement effects are weaker in the slit pore. In Figures 2.5a and 2.5b, it can be observed that by increasing the interaction strength between the wall of the pore and the fluid particles, the ratio of the driving forces decreases. At higher differential pressures the decrease in the ratio of driving forces due to the increasing fluid-wall interaction strength becomes less pronounced, see Figure 2.5c-d and 2.5e-f. The smaller influence of the interaction strength, ϵ_{fw}, on the ratio of driving forces may be caused by the increasing contribution of the fluid-fluid interactions to the integral pressure due to the larger number of fluid particles in the pore at higher differential pressure. In Figure 2.5a-b, 2.5c-d and 2.5e-f the ratio of driving force is shown for the slit and cylindrical pores at the same differential pressure. It can be seen that the ratio of the slopes of the fitted lines for the same value of ϵ_{wf} with the slit and cylindrical pore is constant within the uncertainties of the simulations. The ratio of the slopes is in the range of ~0.52-0.58 which indicates that the confinement effects in the cylindrical pore are almost twice as strong as in the slit pore.

2.5. CONCLUSIONS

In this chapter, the difference between the differential and integral pressure are investigated by performing MC simulations. The simulations are carried out in a variation of the Gibbs ensemble with two simulation boxes in chemical equilibrium. One of the simulation boxes represents the bulk fluid with differential pressure P, and the other a slit or cylindrical pore with repulsive or attractive wall interaction potential. In case of the attractive wall potentials, several scenarios are considered for the strength of the interaction between the wall and the fluid particles. The effect of confinement is investigated for three differential pressures $P = 0.2, 2.0, 6.0$, corresponding to gas ($\rho \approx 0.1$) and liquid phases ($\rho = 0.58, 0.8$). It is concluded that the difference between the differential and integral pressure $P - \langle\hat{p}\rangle$, for all studied cases approaches 0 when $R \to \infty$. It is shown that the increase in the interaction strength between the wall and the fluid particles has smaller effect on the difference in the pressures $P - \langle\hat{p}\rangle$, as the differential pressure increases. Based on the work of Galteland *et al.* [147], the difference of the differential and integral pressure is related to the effective surface tension between

the fluid particles and wall of the pore. It is shown that the effective surface tension does not depend on the curvature of the wall. It is found that by considering a bulk fluid in equilibrium with a cylindrical or slit nanopore, the ratio of driving forces for mass transport in the bulk phase is larger than in the nanopore ($\frac{\mathrm{d}\langle\hat{p}\rangle}{\mathrm{d}P} << 1$) for small pore sizes. As R increases, $\frac{\mathrm{d}\langle\hat{p}\rangle}{\mathrm{d}P}$ approaches 1, i.e., the fluid in the pore behaves more like a bulk fluid. This clearly shows that the approximation that $\hat{p} \approx P$ does not hold on the nanoscale. Our findings and the findings of Galteland *et al.* [147], and Rauter *et al.* [174] imply that the integral pressure should be incorporated in the modeling fluids in nanopores. For example the different pressures should be considered in the Navier-Stokes equation during the modeling of a fluid flow through a nanopore.

3

IN SILICO SCREENING OF METAL-ORGANIC FRAMEWORKS FOR ADSORPTION DRIVEN HEAT PUMPS AND CHILLERS

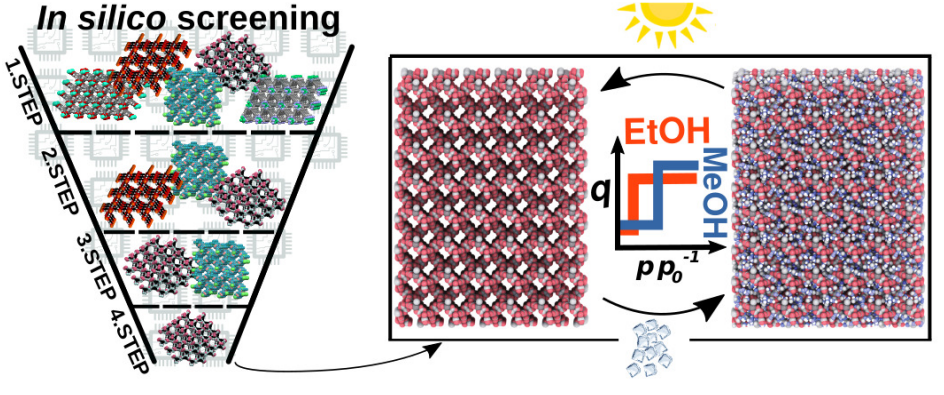

This chapter is based on the following publication: M. Erdős, M. F. de Lange, F. Kapteijn, O. A. Moultos, and T. J. H. Vlugt, In silico screening of metal–organic frameworks for adsorption-driven heat pumps and chillers, *ACS Applied Materials & Interfaces* **10**, 27074 (2018).

3.1. INTRODUCTION

Energy consumption worldwide is continuously rising and is predicted to reach approximately 150% of the current level in 2040 [175]. One fifth of the total [175] and 50% [176] of the European Union's energy demand is attributed to hot water production and space heating/cooling of buildings [177]. Although more and more energy is produced from clean low carbon sources for heating/cooling, 75% of it is still acquired by using fossil fuels [176]. To tackle the problems of the increasing energy consumption and the considerable use of fossil fuels in energy production, the European Union has set several targets, such as improving the energy efficiency by 20% and to produce 20% of the total energy consumption from renewable energy sources by 2020 [176]. To ameliorate the dependence on fossil fuels and increase energy efficiency, several technologies have emerged recently, utilizing renewable energy sources for heating/cooling applications [178, 179]. Thermally driven heaters and coolers are promising candidates due to the use of thermal energy instead of electricity [180]. The working principles of these technologies are based on absorption [181, 182], chemical reaction [183] or adsorption [184, 185]. In absorption driven heat pumps, heat is generated or taken up by the working fluids (working pair) through absorption, evaporation, condensation, and desorption [186, 187]. The most common working pairs are water/LiBr and water/ammonia [186, 187]. In chemical reaction based heat pumps, the endothermic/exothermic nature of a reversible chemical reaction is exploited to take up or generate heat for cooling or heating purposes [186]. In adsorption driven heat pumps/chillers (AHP/ACs), the heating/cooling is achieved by the adsorption and desorption of a working fluid on a solid adsorbent [188]. In AHP/ACs, environmentally friendly working fluids, such as water, methanol or ethanol can be used [188, 189]. One of the advantages of adsorption driven heat pumps/chillers (AHP/ACs) is the applicability of low temperature (<373K) heat sources (*e.g.*, solar, industrial waste heat) as the driving force [190, 191]. To operate AHP/ACs, no moving parts are necessary unlike in other thermally driven heat pumps [192]. A drawback of AHP/ACs systems is the lower performance compared to heat pumps based on absorption or chemical reactions [188].

One possible way to improve the energy efficiency of AHP/ACs is by finding adsorbents with enhanced adsorption and thermophysical properties. To this extent, several types of materials have been already reported in literature as possible adsorbents in AHP/ACs applications. Such materials are zeolites, silica gels, activated carbons, composite adsorbents and MOFs [190, 193–197]. Several MOFs have stepwise adsorption isotherms which provides the possibility to operate AHP/ACs over a small pressure range. The high porosity, surface area, exchangeable linkers of the structure and possible stepwise adsorption behavior make MOFs promising candidates as adsorbents in

adsorption driven heat pumps and chillers [188].

In conjunction with the application of MOFs as adsorbents, alcohols (methanol, ethanol) can be used as promising adsorbates [198]. It is shown that several MOFs lose structural stability after prolonged exposure to water, an issue that seems to be more severe in the case of ammonia [91, 188, 199–201]. By using methanol or ethanol as adsorbate, degradation of the structure is not observed [198, 202].

Due to the relatively high triple point temperature of water (273.16 K) [203], it cannot be used for cooling applications below 0 °C. Methanol and ethanol have lower triple point temperatures (methanol: 175 K, ethanol: 150 K) [204, 205] and are applicable below 0 °C [198]. Since alcohols have higher vapor pressures than water the adsorption-desorption cycle is expected to be more efficient [206]. At the operating conditions of AHP/ACs, alcohols have lower enthalpy of evaporation (at 303 K and 1 bar: methanol ~0.90 kJ ml^{-1}, ethanol ~0.65 kJ ml^{-1}) [207] compared to water (at 303 K and 1 bar: ~2.30 kJ ml^{-1}) [207]. Therefore, the allocatable amount of heat/cold with the same volume of adsorbed material is lower for alcohols. Although alcohols possess several advantageous properties compared to other adsorbates, adsorbents with higher alcohol adsorption capacity (>0.45 ml working fluid per 1 cm^3 structure) [148, 198] have to be developed for more efficient application of alcohols in AHP/ACs [198].

To identify MOFs with promising alcohol adsorption properties for more efficient AHP/ACs, a computational screening study can be carried out. At the operating conditions of AHP/ACs with MOFs, pore condensation can occur which causes the stepwise adsorption behavior. Pore condensation involves first order phase transition of the adsorbate. To the best of our knowledge there is no reported computational screening study of MOFs involving the phenomenon of pore condensation.

To conduct the computational screening study of MOF-alcohol working pairs, a database of computation-ready structures (*e.g.*, solvent free, no disordered atoms) with accurate point charges is desirable. The CoRE MOF database [119] has been extended, for most of the MOFs (~ 3 000), with accurate point charges, computed by the Density Derived Electrostatic Charges (DDEC) method [208] (referred to as DDEC database). The availability of accurate point charges enables the calculation of electrostatic interactions, which plays a crucial role for polar adsorbates, such as alcohols [208]. Here, MC simulations are performed in various statistical ensembles to select the best MOFs from the DDEC database for ACs application. For both methanol and ethanol, 4 screening steps are carried out leading to the best 6 structures, from the initial ~2930, at the end of the screening process. The selected 12 structures (6 for each adsorbate) show diverse adsorption step locations and promisingly high deliverable working capacities (~0.6 ml ml^{-1}) compared to the experimentally reported highest

values (~0.45 ml ml^{-1}) [148]. These materials are promising candidates as adsorbents for AHP/ACs since the diverse adsorption step location allows for different operational conditions and the high working capacities provide an opportunity for more allocatable heat/cold per working cycle.

This chapter is structured as follows. In Section 3.2, the chosen database and the devised screening process are explained in details. In Section 3.3, the details of the performed simulations are reported. In Section 3.4, the results of the screening steps with explanation are presented. In Section 3.5, the conclusions of the screening study is presented.

3.2. DATABASE AND SCREENING METHODOLOGY

3.2.1. DATABASE

In this chapter, a database of already experimentally synthesized structures is used. In the past decade, several versions of the CoRE database has been reported. In 2014, Chung *et al.* [119] reported the first CoRE database with ca. 4 700 already synthesized structures which can be directly used for simulations. In 2019, Chung *et al.* [117] reported a newer version of the CoRE database with c.a. 14 000 MOF structures. In the computation of adsorption isotherms of polar molecules in MOFs, electrostatic interactions play a major role. Electrostatic interactions are calculated using partial charges provided for each atom. While polarization effects can play a crucial role in the simulation of polar adsorbate adsorption in MOFs [209, 210], there is no transferable polarizable force field available for MOFs. Since the derivation of a polarizable force field for each structure would require a considerable amount of CPU time, the polarizability of the system is usually not considered in high-throughput screening studies of MOFs. All assigned partial charges are static in each simulation. The first version of the CoRE MOF database has been extended for most of the MOFs (~ 3 000) with point charges computed by the Density Derived Electrostatic Charges (DDEC) method [208]. The structures investigated in this screening study are taken from the DDEC database [208]. There are several duplicates in the database, such as CuBTC which appears ~60 times with slightly different structures, but more than ca. 2 000 structures are unique [208]. The large structural diversity of the database can be seen by considering that there are more than ~50 types of metal clusters present in the database [208]. The structures have pore limiting diameters (PLD) ranging from ~1 Å to ~23 Å and largest cavity diameters (LCD) from ~2 Å to ~24 Å. There are only 3 structures in the database with LCD larger than ~16 Å and the rest of the structures mostly have LCD below ~9 Å. One of the unfavorable phenomena in AHP/ACs is the irreversible capillary condensation of the adsorbate which causes high desorption temperature. This phenomenon does not occur below a critical pore diameter (D_C) which can be different for each adsorbate,

for example for methanol D_C = 35 Å and for ethanol D_C = 43 Å [188]. Hence, by considering the available pore diameter range in the database, it becomes apparent that the critical pore diameters for methanol and ethanol are larger than the highest LCD value in the database. Therefore, irreversible capillary condensation can be neglected during the screening process.

3.2.2. SCREENING METHODOLOGY

The objective of this screening study is to select the best performing MOFs for ACs application, from the structures available in the DDEC database, in the least amount of computational time possible. Desirable structures should have a very steep adsorption step within the relative pressure ($P\ P_0^{-1}$, where P_0 is the saturation pressure of the adsorbate) interval $0.05 < P\ P_0^{-1} < 0.4$ and, as high as possible deliverable working capacity. A very steep uptake step is desired to ensure the highest thermodynamic efficiency in AHP/ACs application [185, 188]. Since the deliverable working capacity determines the maximum amount of allocatable heat per working cycle, it should be as high as possible. In efficient AC applications a high regeneration (desorption) temperature is unfavorable since it decreases the efficiency of the cooler. An adsorption step at low relative pressure ($P\ P_0^{-1} < 0.05$) can indicate high adsorption affinity which requires high temperature for regenerating the adsorbent. To avoid high desorption temperatures, the adsorption step should occur at a relative pressure higher than $P\ P_0^{-1} = 0.05$ [185]. With the adsorption step occurring at higher relative pressures the temperature difference between the low (evaporator) and intermediate (adsorber/condenser) temperature sides (temperature lift) decreases resulting in lower efficiency [188]. To realize a sufficiently high temperature lift, the uptake step should take place below $P\ P_0^{-1} = 0.4$ [185]. Hence, the desired relative pressure range for methanol and ethanol (for other working fluids the interval can differ) is $0.05 < P\ P_0^{-1} < 0.4$.

Since the calculation of one uptake value of a methanol adsorption isotherm can take days, the simulation of detailed isotherms for ~3 000 structures is not practical. A screening methodology consisting of subsequent steps is devised. In each step, the structures are narrowed down to promising ones, based on more and more relevant properties for AC application. After carrying out the 4 steps, 6 MOFs for each adsorbate are chosen as the best performing structures for ACs applications. A schematic representation of the screening process is shown in Figure 3.1. In the screening process, all isotherms are calculated at 303 K since this is a commonly used adsorption temperature in AC applications [188].

Based on previous studies [188, 198], methanol and ethanol are expected to show similar adsorption properties. This can be understood by considering the similar structural and chemical properties (*e.g.*, size, -OH group *etc.*) of the two adsorbates. To reduce the computational cost, the results obtained for methanol are also used

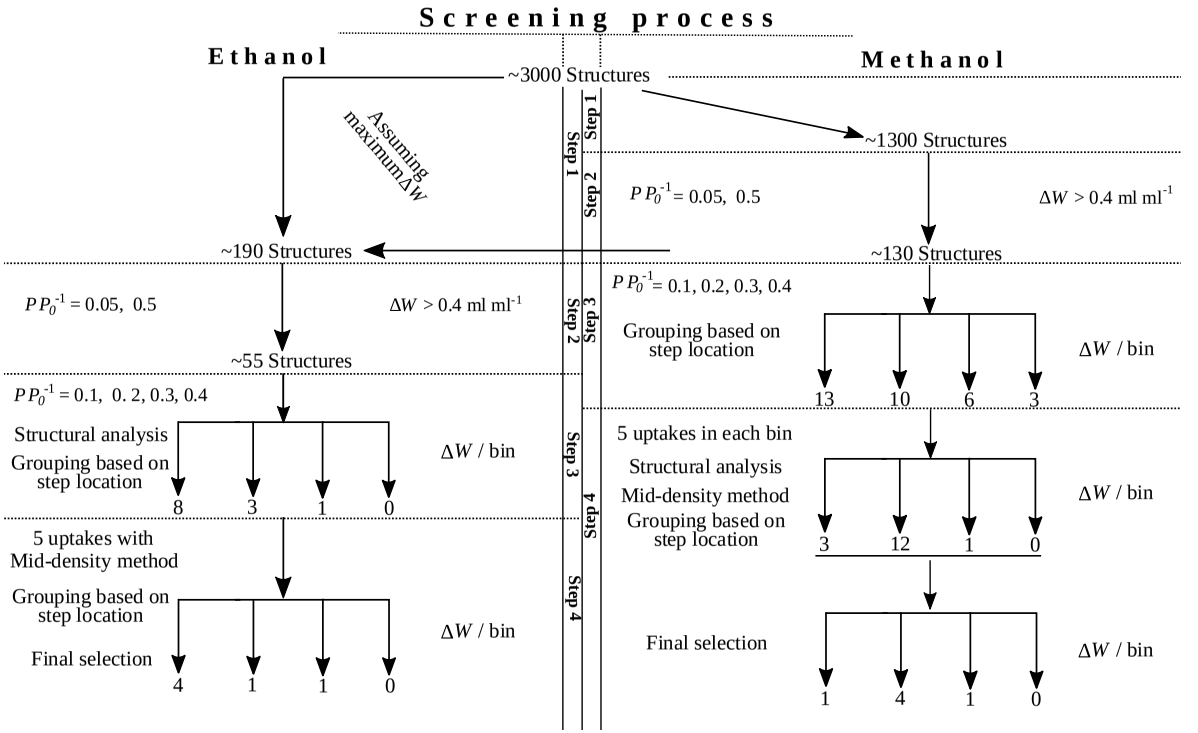

Figure 3.1: Overview of the devised screening process with methanol and ethanol. For each adsorbate, four subsequent steps are carried out. In the first step with ethanol as working fluid, the results of the first and second steps with methanol are used to select structures for ethanol. The number of selected structures at the end of each step are shown for each adsorbate. The performed tasks (left side of the step) and the selection criterion (right side of the step) are also shown for each step.

in the screening process with ethanol. Therefore, methanol is considered first as adsorbate. After performing the second screening step, the investigation for ethanol is commenced by using the results obtained from the first and second screening steps of methanol screening. The detailed description of the screening methodology is presented below.

Since all steps, except for the first, are identical for both adsorbates, the screening process is presented for methanol and only the first step is presented for the screening with ethanol.

Methanol - Step 1: Based on the physical properties of the structures and methanol, several MOFs can be excluded. One selection criterion is determined by the kinetic diameter of methanol which is approximately 3.6 Å. During the adsorption-desorption process molecules have to diffuse into the pores (enter and leave). Hence, structures with pore limiting diameter less than 4 Å are not considered further.

Step 2: For the remaining structures after the first step, two data points of the adsorption isotherm are calculated to determine the difference in the amount of adsorbed working fluid at the two relative pressures (working capacity). Since the adsorption step should take place at the relative pressure window of $0.05 < P\ P_0^{-1} < 0.4$ [188], the two uptakes are calculated at relative pressure $P\ P_0^{-1} = 0.05$ and $P\ P_0^{-1} = 0.5$.

Since a significant drawback of the current AHP/ACs is the considerably large size of these devices [188], it is desired to find adsorbents that can store more working fluid per unit volume of adsorbent. Therefore, in this work the loadings are calculated as volume of adsorbed material per unit volume of the structure instead of per unit mass. The selection criteria are also defined in this form. To calculate the volume of the structures, the crystallographic densities of the MOFs are used as reported in the database. In case of the adsorbed material its volume is approximated by using its liquid phase density. The loading q, in units of ml adsorbed material per 1 ml of adsorbent, can be expressed as:

$$q = \frac{q_{\text{mol}}\ M_{\text{MeOH}}\ \rho_{\text{struc}}}{\rho_{\text{MeOH}}^{\text{liq}}} \tag{3.1}$$

where q_{mol} is the loading expressed in units of mol kg^{-1}, ρ_{struc} is the crystallographic density of the framework, $\rho_{\text{MeOH}}^{\text{liq}}$ is the liquid density of methanol (at T = 303 K and P = 1 bar, $\rho_{\text{MeOH}}^{\text{liq}}$ = 781.77 kg m^{-3}) [211], and M_{MeOH} is the molecular weight of methanol (M_{MeOH} = 32.04 g mol^{-1}).

Structures are selected based on the loading difference between the two calculated points (working capacity - ΔW). Since the aim of this chapter is to contribute to the development of better adsorbents for ACs application, the selection criterion is set to $\Delta W > 0.4$ ml ml^{-1} which is almost the highest already reported working capacity

for MOFs (~0.45 ml ml^{-1}) [148].

Step 3: To predict the location of the assumed adsorption step another set of uptakes are calculated for the previously selected structures. The new data points are computed at relative pressures 0.1, 0.2, 0.3 and 0.4 for every structure. From the uptakes the deliverable working capacity (ΔW_{del}) is calculated. ΔW_{del} is defined as the highest difference in loading between two adjacent relative pressure points. Relative pressure intervals, where the assumed adsorption step occurs, can be defined by considering the deliverable working capacities. Based on the position of the assumed adsorption step the structures are grouped into four bins:

- First bin: ΔW_{del} is in the range $0.05 \leq P\,P_0^{-1} \leq 0.1$
- Second bin: ΔW_{del} is in the range $0.1 < P\,P_0^{-1} \leq 0.2$
- Third bin: ΔW_{del} is in the range $0.2 < P\,P_0^{-1} \leq 0.3$
- Fourth bin: ΔW_{del} is in the range $0.3 < P\,P_0^{-1} \leq 0.4$

Since the evaporator temperature in AHP/AC application depends on the location of the adsorption step, the structures in different bins can be considered for different working conditions in AHP/AC. For example, if the adsorption step occurs at lower relative pressure $P\,P_0^{-1}$, a lower evaporator temperature can be applied. Hence, the selection is performed by comparing the deliverable working capacities of the structures in the same bin.

Step 4: In this step, initially the structures are assessed based on structural properties (in case of ethanol this information is already used in Step 3). The considered properties are the cluster type, ligand type, functional groups, presence of coordinatively unsaturated sites, and pore dimensionality. MOFs with expensive, difficult synthesis routes or with potentially harmful building blocks are not desirable for the application. The flexibility of the structure can cause desorption hysteresis [188], which increases the desorption temperature and lowers efficiency. Therefore, frameworks with expensive/difficult synthesis, potentially harmful building blocks or flexibility are not considered further. To determine the presence and location of the adsorption step, five more uptake values of the isotherm are calculated for the above selected structures at relative pressures linearly distributed over the interval of the bin assigned to the structure. In these simulations, the mid-density scheme [212] (briefly explained in Section 3.3) is applied to accurately locate the adsorption step.

Using the results of these simulations the final selection is made. The six best structures are selected based on the deliverable working capacity and the location of the adsorption step.

Ethanol - Step 1: As mentioned earlier, the first selection criterion in case of ethanol differs from methanol. By considering the similar adsorption behavior of methanol and ethanol and using the results obtained for methanol adsorption (Step

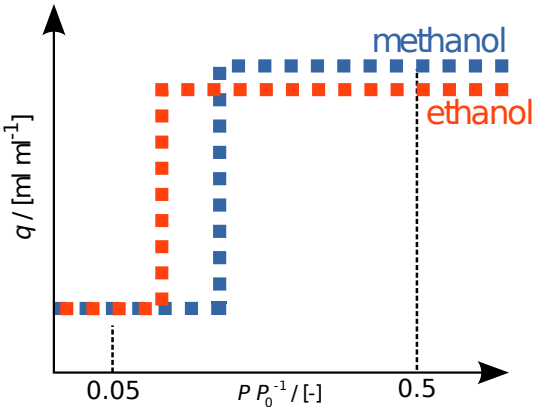

Figure 3.2: Schematic representation of the adsorption behavior of methanol and ethanol. If methanol shows a stepwise adsorption isotherm with a MOF, then ethanol behaves alike and the adsorption step also occurs for ethanol but at a lower relative pressure.

1 and 2), a significant amount of computational time can be saved. In case of ethanol adsorption the following groups of structures can be distinguished:

- Low uptake at $P\,P_0^{-1}$ =0.05, high uptake at $P\,P_0^{-1}$ =0.5
- High uptake at $P\,P_0^{-1}$ =0.05, high uptake at $P\,P_0^{-1}$ =0.5
- Low uptake at $P\,P_0^{-1}$ =0.05, low uptake at $P\,P_0^{-1}$ =0.5

The groups which contain structures with potentially high working capacity for ethanol can be identified by assuming similar adsorption behavior for the two working fluids. This assumption is that if methanol shows a stepwise adsorption behavior, then ethanol behaves alike and the adsorption step also occurs for ethanol but at a lower relative pressure (Figure 3.2 shows the schematic representation of this assumption). The validity of this assumption is based on the experimental work reported in Ref. [198] and by considering the stronger confinement effects caused by the larger size of the ethanol molecules [198]. Based on this assumption the group of structures which can be suitable for ethanol adsorption is identified.

In the case of the first group, the structures have an adsorption step for methanol with working capacity higher than 0.4 ml ml^{-1}. This means that for ethanol the adsorption step also occurs and shifts to lower relative pressure. Therefore, these structures are considered as potential candidates for ethanol adsorption as well. The third group can also contain structures with high working capacity, based on the assumption that the adsorption step of these structures for methanol would occur at higher relative pressures than 0.5 and would shift to lower relative pressures in case of ethanol. Therefore, these structures can be favorable with ethanol. Since the structures in the

second group are already saturated at $P\,P_0^{-1} = 0.05$, these MOFs are not desirable in the screening with ethanol. Based on the working capacity values, structures in the second and third group cannot be distinguished. To select the promising structures from these groups, the highest achievable working capacity with ethanol as working fluid is approximated. By examining the results obtained for methanol (Figure 3.5) and based on the kinetic diameter of (~2.6 Å) and methanol (~ 3.6 Å) the following assumptions are made: 85% of the calculated helium void fraction can be used for alcohols as free volume for adsorption. The free space left after methanol adsorption at the highest simulated relative pressure is calculated as follows:

$$E_v = 0.85\phi_{He} - q_{0.5}^{MeOH} \tag{3.2}$$

where E_v is the empty void volume after methanol adsorption at $P\,P_0^{-1} = 0.5$, ϕ_{He} is the helium void fraction of the structure, and $q_{0.5}^{MeOH}$ is the methanol uptake at a relative pressure $P\,P_0^{-1} = 0.5$. The highest possible working capacity with ethanol as working fluid is calculated as follows:

$$\Delta W_{max}^{EtOH} = \Delta W^{MeOH} + E_v \tag{3.3}$$

This equation is used to predict the highest achievable working capacity with ethanol as adsorbate, for all of the structures considered in the second step of the screening with methanol. The selection is carried out by considering the predicted maximum ethanol working capacity of the structures which are selected for the second screening step with methanol. Structures with higher predicted working capacity than 0.4 ml ml^{-1} are chosen for the subsequent screening step (Step 2).

3.3. SIMULATION DETAILS

All Monte Carlo simulations are carried out with the RASPA software package [79, 90]. The force field parameters for adsorbates are taken from the TraPPE force field [213]. The adsorbates (methanol, ethanol) are simulated as flexible molecules in which the bond lengths are fixed but bond bending angles and dihedrals are used. The Lennard-Jones (LJ) parameters of the MOFs are primarily taken from the DREIDING force field [214] and for the parameters which are not available the parameters reported in the UFF force field [215] are used. Short range Van der Waals interactions are taken into account by the (12-6) Lennard-Jones potential. Long range electrostatic interactions are considered by the Ewald summation method with a relative precision of 10^{-6} [216]. For the LJ interactions, a cut-off radius of 14 Å with analytic tail corrections are applied. The mixed pair potentials are calculated using the Lorentz-Berthelot mixing rules [77, 217]. In all MC simulations periodic boundary conditions are imposed in ev-

ery direction. The atomic charges of the structures are taken from the crystallographic files published in the aforementioned database. All LJ parameters are shown in Table SA.1-SA.2 of the Appendix.

The size of the simulation box is determined by the number and size of the unit cells. In each simulation the number of unit cells per simulation box is chosen based on the defined cut off radius. The length of the simulation box in each direction is at least twice the cut off radius. In all simulations, the frameworks are considered rigid. This approach is often applied in simulations of nanoporous materials to prevent the necessity of excessive computational efforts [95, 218, 219].

To obtain the adsorption isotherms of methanol and ethanol in the different MOF structures, Configurational-Bias Monte Carlo (CBMC) simulations [76, 220, 221] in the grand-canonical (GC) ensemble [76] is used. In these simulations the temperature, chemical potential, which can be related to pressure (for example by using the Peng-Robinson (PR) equation of state (EoS) [222]), and the volume of the simulation box are kept constant. The following types of trial moves are used: translations (~18%), rotations (~18%), reinsertions (~10%), partial reinsertions/deletions (~18%) and molecule exchanges with the reservoir (~36%).

To create initial configurations with a predefined state (*e.g.*, amount of adsorbates in the framework) for the GCMC simulation, the CBMC simulation technique in the canonical ensemble (NVT) is used. In these simulations the temperature, the volume and the number of particles are kept constant. The following types of trial moves were applied: translations (20%), rotations (20%), reinsertions (20%), partial reinsertions (20%) and Widom's test particle insertions (20%).

All simulations started with an equilibration period of 50 000 to 500 000 cycles in which ensemble averages are not calculated. In a cycle the number of MC steps is equal to the number of molecules in the simulation box with a minimum of 20 MC steps per cycle. In this chapter, to obtain sufficiently accurate results each simulation is restarted until the standard deviation of the number of adsorbed molecules (μVT) or the total energy of the system (NVT) becomes smaller than 5%. Hence, the number of cycles is not specified in this description because it can differ from structure to structure and also for pressures. In general, 50 000 to 500 000 cycles are applied in the simulations.

Certain geometric properties of the structures are required to conduct the screening study. The helium void fraction for each MOF structure is calculated with the Widom insertion method [90]. The pore limiting diameter (PLD), largest cavity diameter (LCD) and the Volumetric Surface Area (VSA) of each structure are calculated in the first step of the screening study. These simulations are performed by using the Zeo++ software package [223, 224]. The saturation pressure of methanol and ethanol are calculated using the Antoine-equation. The parameters for the equation are taken

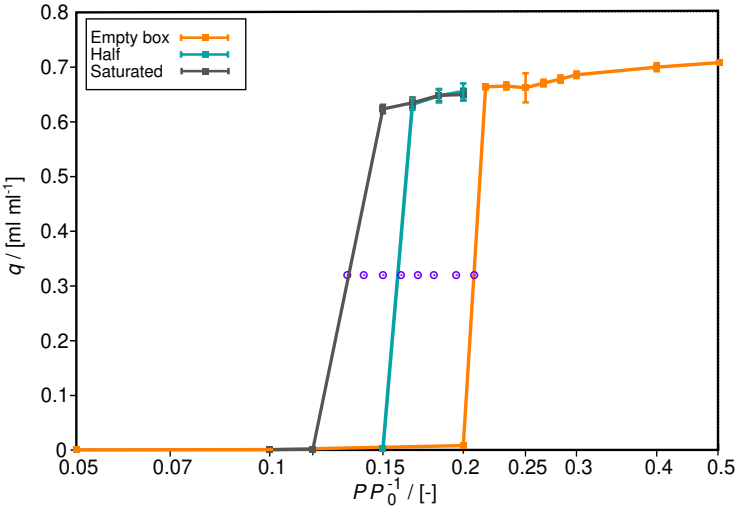

Figure 3.3: Schematic representation of the mid-density scheme [212] through the adsorption isotherms of methanol on the PEVQEO structure. The orange, blue, and gray symbols represent the equilibrium adsorption loading starting from an empty, half saturated, and fully saturated structure, respectively. The lines are there for guiding the eye. The purple symbols represent the loading which correspond to the half saturated state.

from the NIST database [225, 226]. The calculated saturation pressures of methanol and ethanol as a function of temperature are shown in Table A.3.

3.3.1. MID-DENSITY SCHEME

At relative pressures close to a high change in the density of the adsorbed phase (such as close to a steep adsorption step) the simulation of uptakes can be difficult due to the presence of metastable states. To determine the accurate location of the equilibrium phase transition, in principle, thermodynamic integration of the grand potential can be used [227–229]. In the thermodynamic integration method, several states along a path crossing the metastable state of the fluid are calculated. However, this method is computationally expensive. To overcome this problem, a computationally cheaper method, the mid-density scheme [212] can be applied to determine the accurate location of the equilibrium phase transition.

In this method, three isotherms are calculated. One isotherm with an empty (considered as default initial configuration in this chapter), one with a saturated and one with a "half" saturated simulation box as initial configuration. In Figure 3.3, the schematic representation of mid-density scheme [212] is shown through the adsorption isotherms of methanol on the PEVQEO structure. After obtaining the first two isotherms (from empty and saturated initial box) usually a hysteresis can be observed.

In case of a hysteresis, for one relative pressure two states are found. One of the states is a metastable state and the another is a stable state. These two states are separated by free energy barrier (a saddle point in the number of particles - relative pressure space). To identify the stable state, the simulations are started with the average loading. For each average number of adsorbed molecules a NVT simulation is performed. The results of these NVT simulations are used as new initial configurations (half box) in GCMC simulations performed at the corresponding relative pressures where the two calculated loading values (from initially empty and saturated) differ from each other. The obtained isotherm from the simulations with the half saturated box as initial configuration is considered to represent the accurate adsorption step.

3.4. RESULTS AND DISCUSSION

Since there is no specific and transferable force field for alcohol adsorption in MOFs, the applicability of the chosen force field has to be tested. To validate the force field, experimentally measured isotherms of methanol and ethanol are compared with the isotherms obtained from the simulations. In the database six structures with available experimental adsorption data for either methanol or ethanol exist. Therefore, these structures are used for the validation of the force field. In the DDEC database the naming of the structures is mixed. Most of the structures are referred to with a combination of six letters (for example DOTSOV) and some of the frameworks are reported with common names *e.g.* ZIF-8, ZIF-90. For consistency, the exact reported names in the database are used here. In Figure 3.4, the experimentally measured and simulated adsorption isotherms with methanol and ethanol as adsorbates at 288K and 298K are shown for ZIF-8. The experimentally measured and simulated isotherms for the other five structures are shown in the Supporting Information of Ref. [152]. Although the applied generic force field has not been specifically fitted to reproduce these experiments, the experimental and simulation results are in reasonable agreement. Based on the results obtained for the six structures used in the validation, it is concluded that the location of the adsorption step (if present) and the uptake values are properly captured by the proposed force field.

3.4.1. SCREENING WITH METHANOL

In this section, the results of each screening step with methanol are presented. By excluding structures with PLD < 4 Å (Step 1), approximately 1300 from the original 2930 structures are selected for Step 2.

In Figure 3.5, the adsorbed amounts of methanol at relative pressures $P\,P_0^{-1} = 0.05$ and 0.5, and the working capacity are plotted as a function of the helium void fraction for the selected ca. 1300 structures (Step 2). The color code represents the largest cavity diameters of the structures. In Figure 3.5a and 3.5b, methanol adsorption values

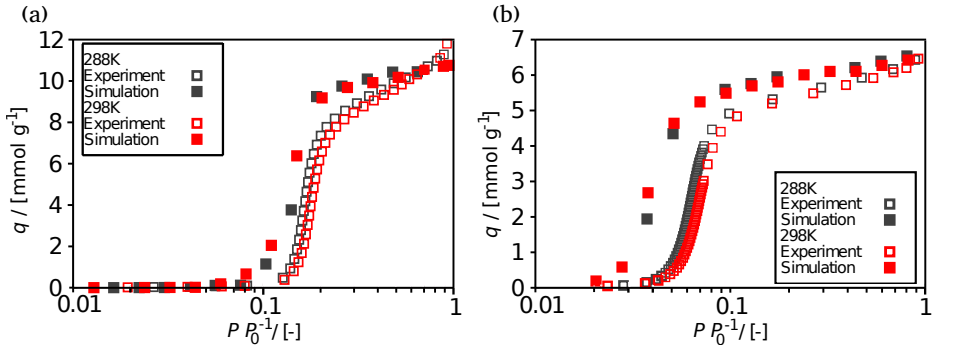

Figure 3.4: Excess amount of adsorbed methanol (a) and ethanol (b) are shown as a function of relative pressure, $P\ P_0^{-1}$ (where P_0 is the saturation pressure of the adsorbate), for ZIF-8 at 288 K (for methanol P_0 = 9.80 kPa, for ethanol P_0 = 4.28 kPa) [230] and 298 K (for methanol P_0 = 16.81 kPa, for ethanol P_0 = 7.82 kPa) [230]. Closed symbols represent simulation results and open symbols are experimental data [198].

at the lower ($P\ P_0^{-1}$ = 0.05) and higher ($P\ P_0^{-1}$ = 0.5) relative pressures are shown, respectively. Most of the structures with lower LCD than ~10 Å are already saturated at $P\ P_0^{-1}$ = 0.05. Almost all structures are nearly or fully saturated at $P\ P_0^{-1}$ = 0.5 (Figure 3.5b). The structures showing high working capacities are mainly the ones with higher LCD (> 10Å) (Figure 3.5c). The finding indicates the strong correspondence between the adsorption uptake value at the lower relative pressure and the working capacity of the structure. It is observed (Figure 3.5) that for structures with pore diameters smaller than ca. 16 Å, the most critical parameter determining the working capacity is the uptake of the structure at $P\ P_0^{-1}$ = 0.05. Unfortunately, the DDEC database contains only three structures with LCDs higher than 16 Å. Therefore, the possibilities to investigate the effect of the pore dimensions on the adsorption uptake are limited.

Based on the calculated working capacities of the structures, 159 MOFs fulfill the selection criterion ($\Delta W > 0.4$ ml ml^{-1}). For this selection of structures, there are multiple structures which are practically the same (chemical composition, underlying topology *etc.*) with slight differences in the atomic positions. These structures are referred to as duplicates and most of those are excluded from the screening. A few duplicates are used in this chapter to investigate the sensitivity of the method to small structural differences. Some of these duplicates are shown in Table 3.1 and Figures S8-S18 in the Supporting Information of Ref. [152]. Consequently, the number of structures selected for the subsequent step is 130.

The 4 additional points of the isotherm are calculated for each selected structures. Based on the obtained results the structures are grouped according to the defined "bin" system. The cardinality of the first, second, third and fourth bin are 69, 31, 26 and 4, respectively. The obtained adsorption isotherms, are shown in the Supporting Infor-

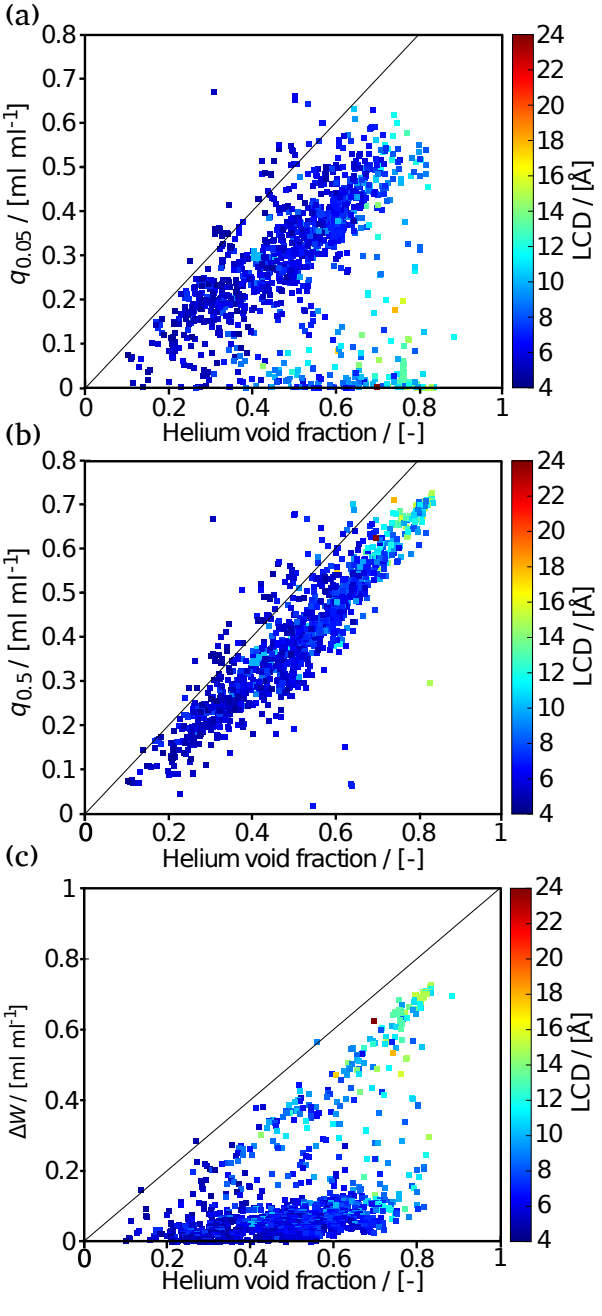

Figure 3.5: Excess adsorption uptake at relative pressure $p\ p_0^{-1}$ = 0.05 (a), $p\ p_0^{-1}$ = 0.5 (b) and working capacity (c) with methanol as a function of the helium void fraction for the ca. 1300 structures considered in the second step at 303K (where P_0 is the saturation pressure of the adsorbate, P_0 = 21.70 kPa) [230]. The coloring represents the largest cavity diameter (LCD) of the structures.

Table 3.1: Summary of structural analysis of the best 25 structures with methanol including largest cavity diameter (LCD), pore limiting diameter (PLD), helium void fraction (ϕ_{He}), volumetric surface area (VSA), cluster type, ligands, coordination, functional groups, dimensionality, presence of coordinatively unsaturated sites (CUS) and the references (Ref.) to the publications reporting the original MOF structures.

Name	Common name	Ref.	PLD / [Å]	LCD / [Å]	Φ_{He} / [-]	VSA / [$m^2\ cm^{-3}$]	α^a / -	ΔW_{del}	Cluster-type	Ligand 1	Ligand 2	Coordination	Functional groups	CUS	Dim.
XAMDUM01	HKUST-1	231	6.72	13.18	0.76	1861	0.05	0.532	$[Cu_2]^{4+}$	$[H_3C_9O_6]^{3-}$	-	C3L(1)4	-	Yes	3D
ZIGFEC	Cr-BTC	232	6.84	12.81	0.76	1905	0.07	0.525	$[Cr_2]^{4+}$	$[H_3C_9O_6]^{3-}$	-	C3L(1)4	-	Yes	3D
YUGLES	-	233	6.78	10.9	0.81	2207	0.08	0.559	$[Cu_2]^{4+}$	$[H_6C_18O_8]^{4-}$	-	CL(1)	-	Yes	3D
LUYHAP[b]	PCN-46	234	6.74	12.06	0.83	2193	0.1	0.562	$[Cu_2]^{4+}$	$[H_6C_20O_8]^{4-}$	-	CL(1)	-	Yes	3D
RUVKAV[b]	PCN-46	234	7.15	11.95	0.83	2149	0.11	0.613	$[Cu_2]^{4+}$	$[H_6C_20O_8]^{4-}$	-	CL(1)	-	Yes	3D
ANUGIA	UMCM-152	235	6.76	13.85	0.86	2137	0.11	0.598	$[Cu_2]^{4+}$	$[H_14C_28O_8]^{4-}$	-	CL(1)	-	Yes	3D
SUKYIH	-	236	7.09	9.65	0.82	2271	0.11	0.545	$[Cu_2]^{4+}$	$[H_16C_29O_8]^{4-}$	-	CL(1)	-	Yes	3D
FUNCEX	-	237	12.48	13.22	0.81	1873	0.16	0.57	$[Zn_2]^{4+}$	$[H_16O_8C_34Br_2]^{4-}$	$[H_8N_6C_12]$	CL(1)L(2)	(C)-Br	No	3D
XEBHOC[d]	Cu_2(TCPPDA)	238	9.91	12.08	0.86	2170	0.16	0.635	$[Cu_2]^{4+}$	$[H_20O_34N_2O_8]^{4-}$	-	CL(1)	-	Yes	3D
HAFTOZ	-	239	7.52	15.37	0.81	2005	0.16	0.623	$[Ni_8]^{12+}$	$[H_4C_10N_4]^{1-}$	-	CL(1)12	-	No	3D
PEVQEO[c]	IRMOF-1	240	7.95	14.86	0.84	2184	0.16	0.63	$[Zn_4O]^{6+}$	$[H_4C_8O_4]^{2-}$	-	CL(1)3	-	No	3D
XAWVUN[d]	Cu_2(TCPPDA)	238	9.22	10.79	0.86	2177	0.16	0.611	$[Cu_2]^{4+}$	$[H_20O_34N_2O_8]^{4-}$	-	CL(1)	-	Yes	3D
IRMOF-6	IRMOF-6	240	6.71	15.04	0.77	2079	0.16	0.544	$[Zn_4O]^{6+}$	$[H_6C_10O_4]^{2-}$	-	CL(1)3	-	No	3D
LAWGEW[c]	IRMOF-1	240	7.94	15.07	0.83	2200	0.19	0.635	$[Zn_4O]^{6+}$	$[H_4C_8O_4]^{2-}$	-	CL(1)3	-	No	3D
SAHYOQ03[c]	IRMOF-1	240	7.94	15.11	0.84	2192	0.19	0.615	$[Zn_4O]^{6+}$	$[H_4C_8O_4]^{2-}$	-	CL(1)3	-	No	3D
GUNFAW01	-	241	7.34	9.61	0.74	2301	0.24	0.594	$[CrMn]^{6+}$	$[C_2O_4]^{2-}$	-	CL(1)3	-	Yes	3D
BEPRIZ	MCF-18(L2,Co)	242	6.04	10.21	0.7	1933	–[e]	0.436	$[Co_3O]^{6+}$	$[H_11C_19NO_4]^{2-}$	-	CL(1)3	-	No	3D
VEXVAW	-	243	5.86	9.77	0.67	1917	–[e]	0.381	$[Fe_3O]^{6+}$	$[H_11C_19NO_4]^{2-}$	-	CL(1)3	-	No	3D
AGAXOV	MOF-107	244	5.31	7.05	0.74	2449	–[e]	0.362	$[Cu_2]^{4+}$	$[H_2C_6SO_4]^{2-}$	-	CL(1)2	(C)-S-(C) {L1}	Yes	2D
FUNBEW	-	237	9.19	11.16	0.78	1922	–[e]	0.393	$[Zn_2]^{4+}$	$[H_16O_8C_34Br_2]^{4-}$	$[H_8N_2C_10]$	CL(1)L(2)	(C)-Br	No	3D
MOF-1-Dybtsev	-	245	7.58	9.36	0.65	1761	–[e]	0.424	$[Zn_2]^{4+}$	$[H_4C_8O_4]^{2-}$	$[H_12C_6N_2]$	CL(1)2L(2)	-	No	3D
MOYYIJ	-	246	9.38	12.42	0.72	2078	–[e]	No step	$[Cu_2]^{4+}$	$[H_6C_16O_8]^{4-}$	-	CL(1)	-	Yes	3D
YIWPEZ	-	247	5.15	6.79	0.52	1754	–[e]	No step	$[Cd_2]$	-	-	-	-	-	
YURJUR	-	248	8.48	13.69	0.76	1956	–[e]	0.404	$[Ce_3]^{12+}$	$[H_6C_14O_6S]^{2-}$	-	CL(1)6	(C)2-S-O2 {L1}	No	3D
ZnBDCdabco	-	245	7.58	9.36	0.65	1761	–[e]	0.414	$[Zn_2]^{4+}$	$[H_4C_8O_4]^{2-}$	$[H_12C_6N_2]$	CL(1)2L(2)	-	No	3D

[a] - α represents the relative pressure value where the loading is equal to the half of the possible maximum loading of the structure. [b] are duplicate structures of each other. [c] are duplicate structures of each other. [d] are duplicate structures of each other. [e] The location of the step is not accurate. The mid-density analysis is not carried out for the structure because the deliverable working capacity is lower than 0.5 ml ml^{-1}.

The pore limiting diameter (PLD), largest cavity diameter (LCD), and volumetric surface area (VSA) are calculated using the Zeo++ software package [223, 224]. The helium void fraction of the structures are calculated with Widom test particle insertion method implemented in the RASPA software package [90]. The deliverable working capacity (ΔW_{del}) is calculated as the difference in loadings before and after the adsorption step.

mation of Ref. [152]. There are 40 structures with lower deliverable working capacity than the desired 0.4 ml ml^{-1}. This is an indication for a non-stepwise adsorption behavior and these structures are not considered for further investigation. For the next screening step, thirteen structures from the first bin, ten from the second, six from the third and three structures from the fourth bin with the highest deliverable working capacities are selected. Since it is not straightforward how to handle duplicated structures, in each case the duplicate with highest and with the lowest deliverable working capacities are chosen to investigate the difference.

Based on the structural assessment of the selected structures, several structures are discarded. The BICDAU, ECOLEP and HIGRIA structures have chiral ligands, which makes the synthesis of these frameworks difficult and expensive. Therefore, these MOFs are excluded. The MOCKAR and PEVQAK structures are discarded because defects are encountered (two carbon atoms overlapping instead of double bond and hydrogen atoms are missing) in the Crystallographic Information files (CIFs). In the PETWOC structure the inorganic cluster is $[U_6O_8]^{12+}$, which contains a radioactive metal so this structure is also excluded. The structural properties of the MOFs and the results for the mid-density method (Step 4) are shown in Table 3.1. The adsorption isotherms obtained by using the mid-density method for each structure are shown in the Supporting Information of Ref. [152].

There are 3 different sets of duplicate structures indicated by superscripts in Table 3.1. As mentioned in the previous sections, the treatment of these duplicates is not straightforward. Based on the obtained results it becomes apparent that the corresponding duplicate structures have similar values for the properties (ΔW_{del}, LCD, PLD, adsorption step location) shown in Table 3.1.

Based on the assessed structural properties of the structures, MOFs with unfavorable properties (*e.g.*, difficult/expensive synthesis *etc.*) are already discarded. The final selection criteria for choosing the best MOFs are the deliverable working capacity and the location of the adsorption step. The selection is performed by considering the structures in the defined relative pressure intervals (bins) to obtain MOFs for distinctive operating conditions for ACs applications. The number of structures in the bins varies greatly. Most of the structures are in the second bin ($0.1 > P\,P_0^{-1} > 0.2$) and there is just one in the third ($0.2 > P\,P_0^{-1} > 0.3$). There are 3 structures in the first bin ($0.05 > P\,P_0^{-1} > 0.1$): XAMDUM01 (HKUST-1), YUGLES and ZIGFEC (Cr-BTC). The YUGLES structure is chosen because it has the highest deliverable working capacity. The second bin contains 12 structures. Due to the high cardinality of this bin, several structures are chosen with diverse adsorption step locations. The ANUGIA (UMCM-152), SUKYIH and RUVKAV (PCN-46) structures have similar adsorption step locations and RUVKAV has the highest deliverable working capacity of these, so this structure is

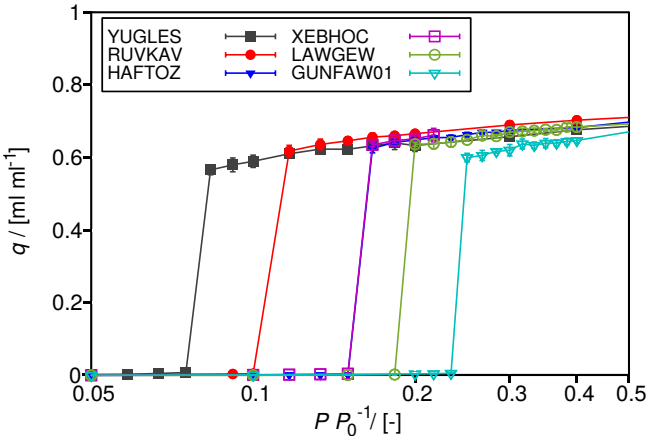

Figure 3.6: Methanol adsorption isotherms of the six best structures after applying the mid-density method to locate the step location. The excess amounts of adsorbed methanol are shown as a function of relative pressure, $P\,P_0^{-1}$ (where P_0 is the saturation pressure of the adsorbate), at 303 K (P_0 = 21.70 kPa) [230] for each structure. The error bars indicate the 95% confidence intervals. The following MOFs can also be referred to with common names: RUVKAV (PCN-46), XEBHOC (Cu_2(TCPPDA)), and LAWGEW (IRMOF-1).

selected. The FUNCEX, HAFTOZ, IRMOF-6 and XEBHOC (Cu_2(TCPPDA)) structures have also similar step locations. Regarding these frameworks, the HAFTOZ and XEBHOC structures have the highest deliverable working capacity, so these are selected from those 5 structures. The adsorption uptake step of PEVQEO (IRMOF-1), LAWGEW and SAHYOQ03 occurs also at similar relative pressures, which is expected since these are duplicates. However, the LAWGEW structure has a slightly higher working capacity, thus this MOF is selected. In the highest bin, there is just one structure (GUNFAW01) to be selected. The finally selected MOFs are the following: YUGLES(Cu), RUVKAV(Cu), XEBHOC(Cu), HAFTOZ(Ni), LAWGEW(Zn), and GUNFAW01(Cr, Mn). The methanol isotherms for the six best structures with using the mid-density method are shown in Figure 3.6.

3.4.2. SCREENING WITH ETHANOL

In this section, the results of each screening step with ethanol is presented. The calculated methanol and predicted ethanol working capacities (Step 1 - ethanol) are compared and it is observed that for most of the structures these values are equal. There are 32 additional structures with high predicted working capacity (> 0.4 ml ml^{-1}) for ethanol, which do not have a high working capacity for methanol (Figure S44 in the Supporting Information of Ref. [152]). The structures with predicted working capacity higher than 0.4 ml ml^{-1} are selected for the subsequent screening step. The number of promising structures is reduced to 191 from the initial 2930 without performing any

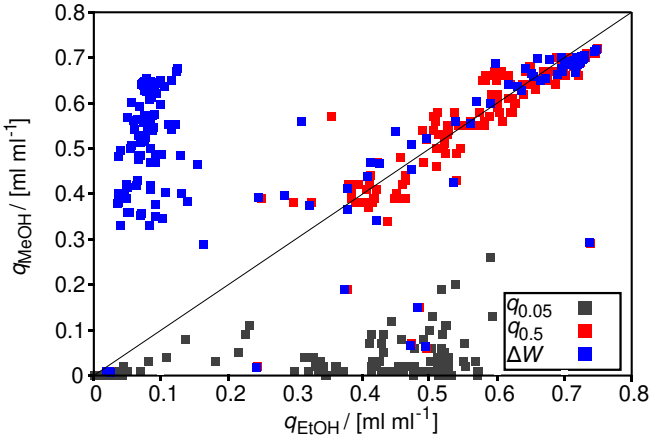

Figure 3.7: Excess methanol uptakes as a function of excess ethanol uptakes for the ca. 190 structures selected in the first screening step with ethanol. The color code represents the uptake at 0.05 (black) and 0.5 (red) relative pressures, and the working capacity (blue) of the structures.

additional simulations.

In Figure 3.7, the results of the second screening step with both adsorbates are shown. The methanol uptakes are shown as a function of the ethanol uptakes. The similar adsorption behavior of the two working fluids can be observed in Figure 3.7. A large number of structures show high ethanol and low methanol uptakes at $P\,P_0^{-1}$ = 0.5. These structures are identified as the ones placed in the first bin during the third screening step with methanol. As assumed the adsorption step for these structures with ethanol is shifted to lower relative pressure which results in a high uptake value at $P\,P_0^{-1} = 0.05$. Consequently, these structures have a low working capacity for ethanol while showing high working capacity for methanol (top left part of Figure 3.7). At this step (Step 2), 55 structures are selected ($\Delta W > 0.4$ ml ml^{-1}) for further investigation.

Four more points of the isotherm are calculated for the 55 selected structures at relative pressures 0.1, 0.2, 0.3 and 0.4. The structures are grouped according to the above defined bin system. The obtained results also support the assumed similar adsorption behavior of the adsorbates. It is observed that several structures which are assigned to the third bin with methanol, are placed in the second bin with ethanol. Similarly, there is a significant overlap for the structures in the second bin with methanol and the first with ethanol.

The lack of a steep adsorption step can also be observed with ethanol. After obtaining the additional isotherm points, the deliverable working capacity becomes lower than the desired 0.4 ml ml^{-1} for 10 structures. These structures are not considered further.

Based on structural properties, MOFs with unfavorable attributes (*e.g.*, difficult or expensive synthesis, containing potentially harmful building blocks, flexibility of the framework *etc.*) for application in ACs are discarded. Since the flexibility of the framework can cause desorption hysteresis [188], the flexible MIL-88c-open structure is not considered for further investigation. Furthermore, the RONZID, JUTCUW and PIYZAZ structures contain cyanide, which is a potentially harmful substance, these MOFs are discarded. The VUSJUP structure is excluded because of a defect in the reported structure (CIF). From the selection of chosen structures, there are numerous duplicates from which the one with the highest deliverable working capacity is selected. After the structural analysis and the selection based on deliverable working capacity are performed (Step 3) the number of remaining structures is 12. 8 structures are selected from the first, 3 from the second, 1 from the third and 0 from the fourth bin.

The structural properties and results after performing the mid-density analysis with the 5 additional adsorption uptakes (Step 4) are shown in Table A.4 of the Appendix. The structures are regrouped because of the shift in the location of the adsorption step and structures with high deliverable working capacity are chosen from the distinctive bins. The ANUGIA and RUVKAV structures show the adsorption step below the lower limit of the first bin. The deviation from the lower limit is small compared to the size of the bin (10%). Hence, based on the deliverable working capacity values, the RUVKAV structure is considered as a promising candidate. From the first bin the FUNBOG, XEBHOC and PEVQEO structures are chosen because of their high working capacity and diverse step location. In the second and third bin only 1 structure is placed at the last selection step. Both of these structures are considered promising frameworks. Therefore, the finally selected frameworks are the following: RUVKAV(Cu), FUNBOG(Zn), XEBHOC(Cu), PEVQEO(Zn), HAFTOZ(Ni), and GUNFAW01(Cr, Mn). The ethanol isotherms for the best 6 structures after applying the mid-density method are shown in Figure 3.8.

By conducting 4 subsequent screening steps, 6 structures with both working fluids are selected. The selected structures show considerably high deliverable working capacities and diverse adsorption step locations with both working fluids. For the two working fluids five of the selected structures are the same (PEVQEO and LAWGEW are duplicates) which supports the assumption for the similar adsorption behavior of the two working fluids. The sixth best performing candidate selected is YUGLES for methanol and FUNBOG for ethanol. Since all structures in the database are experimentally synthesized, the synthesis route and characterization of the most promising MOFs are available in literature [233, 234, 237–241]. For most of the selected structures, experimentally measured adsorption isotherms with several adsorbates (*e.g.* H_2,

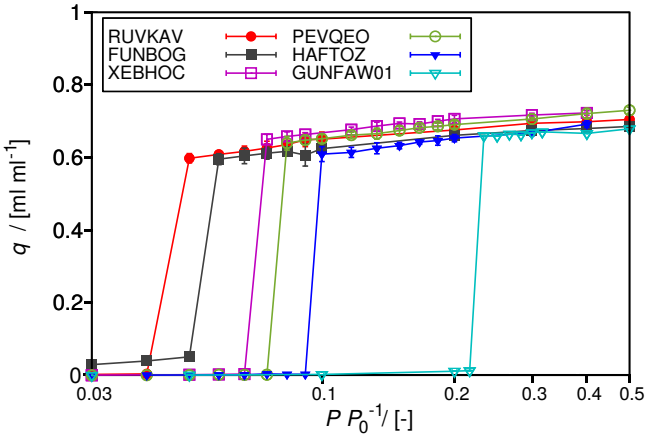

Figure 3.8: Ethanol adsorption isotherms of the six best structures after applying the mid-density method to locate the step location. The excess amounts of adsorbed ethanol are shown as a function of relative pressure, $P\,P_0^{-1}$ (where P_0 is the saturation pressure of the adsorbate), at 303 K (P_0 = 10.38 kPa) [230] for each structure. The error bars indicate the 95% confidence intervals. The following MOFs can also be referred to with common names: RUVKAV (PCN-46), XEBHOC (Cu_2(TCPPDA)), and PEVQEO (IRMOF-1).

N_2, CO_2 *etc.*) are reported [233, 234, 238, 240, 249–252].

It can be seen that the selected structures have diverse cluster and linker types with several types of metal ions (Cu, Zn, Ni, Cr, Mn). The atomistic representation of the 7 different selected MOFs are shown in Figure 3.9. Despite the differences in cluster and linker types, the selected structures have several similar physical properties. All frameworks have high helium void fractions, volumetric surface areas and similar pore dimensions as shown in Table 3.1 and Table A.4 of the Appendix. In Figures S46-S47 in the Supporting Information of Ref. [152], the deliverable working capacity of the best 25 structures with methanol are shown as a function of volumetric surface area (VSA) and helium void fraction. It can be observed that with increasing VSA and helium void fraction the deliverable working capacity increases, however, a correlation based on only these properties cannot be established. In Figure 3.5c, several structures with high helium void fraction and low maximum working capacity are shown which suggests that considering only the physical properties (helium void fraction, surface area, pore dimension) of the structures is not sufficient to predict the deliverable working capacity of the framework. Since electrostatic interactions play a major role in the adsorption of polar adsorbates in MOFs, the polarity of the linkers also needs to be taken into account at the assessment of MOFs for ACs application.

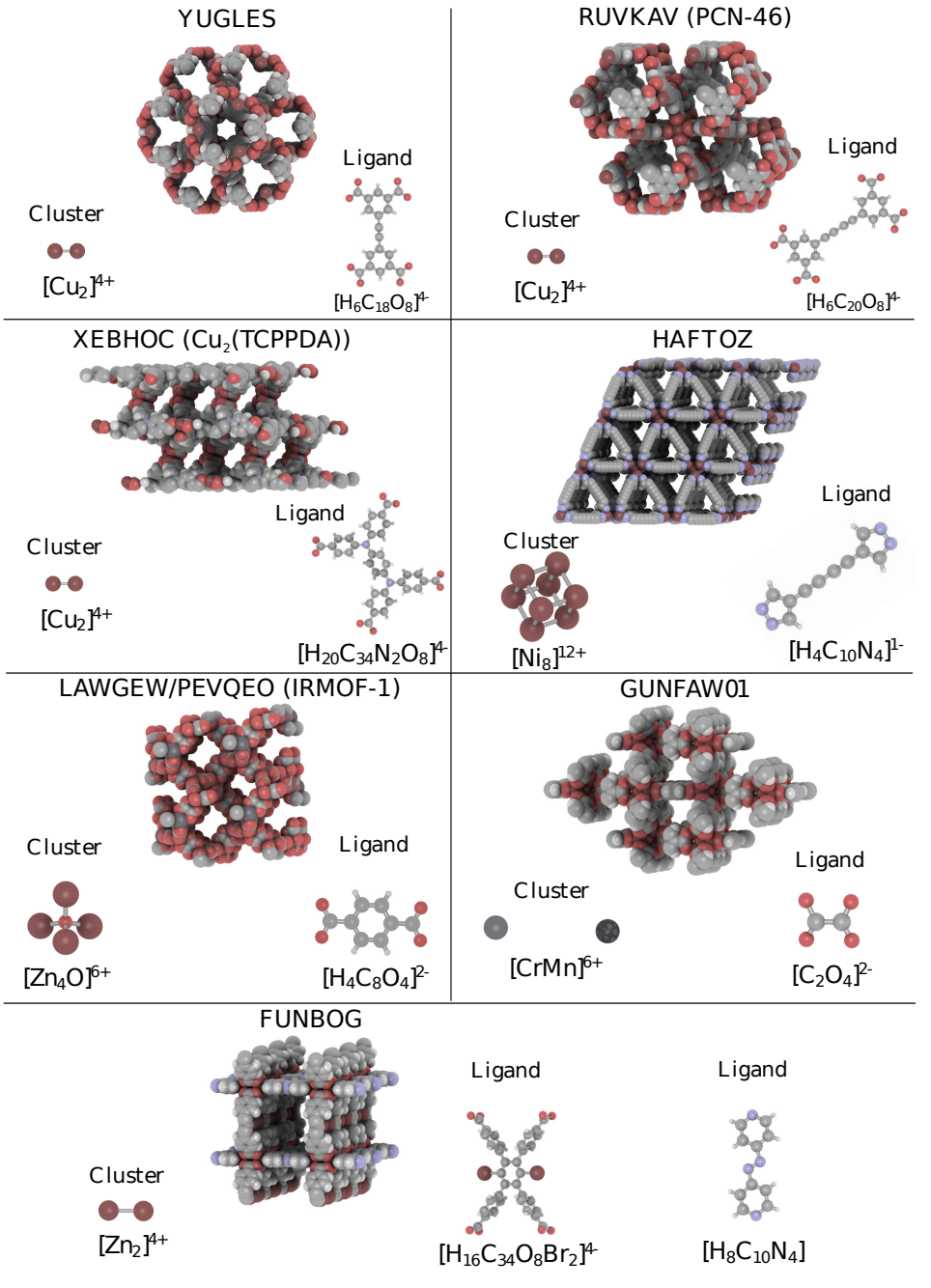

Figure 3.9: Atomistic representation of the finally selected structures. The super cell, cluster and linker are shown for each finally selected MOF. Since the LAWGEW and PEVQEO structures are duplicates, this MOF is only shown once. The following MOFs can also be referred to with common names: RUVKAV(PCN-46), XEBHOC(Cu_2(TCPPDA)), and LAWGEW(IRMOF-1). The graphical representations are created with iRASPA. [45]

The YUGLES(Cu) and RUVKAV(Cu) structures differ only in the length of the linkers connecting the metal clusters. While the small difference in the length of the linkers (2 carbon atoms) does not have a significant effect on the polarity of the pores, it leads to a larger pore size for the RUVKAV framework. Therefore, the two structures have similar adsorption affinity but the RUVKAV framework can accommodate a higher amount of working fluid. For the RUVKAV structure the adsorption step occurs at a higher relative pressure because more working fluid is required for pore condensation. It is expected that by further increasing the size of the linker, without the incorporation of polar functionalities, the volumetric working capacity of the framework would be reduced due to the weaker interaction between the MOF and the working fluid. Although the incorporation of polar functionalities can increase the volumetric working capacity, it also increases the adsorption affinity, which may lead to stronger interactions between the framework and adsorbate. This may cause undesirably high desorption temperatures. Our results indicate that the pore dimensions and the polarity of linkers have a combined effect on the adsorption of polar adsorbates in MOFs. Nevertheless, for establishing rigorous correlations between these properties and the deliverable working capacity, further research is necessary.

3.5. CONCLUSIONS

A computational screening of ~2 930 experimentally synthesized Metal-Organic Frameworks is performed to find the best performing structures for AC applications with methanol and ethanol as working fluids. To the best of our knowledge, this is the first reported computational screening study of MOFs involving the phenomenon of pore condensation to date. The screening procedure with methanol is performed in four subsequent steps. Based on the obtained results in the first three screening steps for methanol it is concluded that for the investigated pore size range the adsorbents can be assumed to be saturated at a relative pressure $P\,P_0^{-1}$= 0.5. Therefore, the loading at relative pressure $P\,P_0^{-1}$= 0.05 determines the maximum working capacity for AC application. It is observed that the helium void fraction of the structure is a reasonable descriptor of the maximum working capacity. In the fourth step of the screening process, the mid-density scheme [212] is applied to efficiently and accurately locate the position of the adsorption step (equilibrium phase transition). By using the results obtained in the first and second steps of the screening with methanol the screening process for ethanol is commenced. It is found that by assuming similar adsorption behavior for methanol and ethanol a significant amount of calculations can be avoided. Without performing any additional simulations and just by considering the results obtained for methanol, the number of possible candidate structures is reduced from 2930 to ca. 190. In a similar manner as for methanol four subsequent steps are

carried out for ethanol. At the end of the screening procedure the six most promising structures are selected based on the location of the adsorption step and deliverable working capacity with both working fluids (see Figure 3.6 and Figure 3.8). These structures are considered promising for AHP/ACs application since the deliverable working capacities are considerably higher ($\sim$ 0.6 ml ml^{-1}) than the previously reported highest value ($\sim$ 0.45 ml ml^{-1}) in literature [148]. It is shown that the screening of MOFs with methanol and ethanol for AHP/AC applications is a challenging task but it can be performed with a reasonable amount of computational effort. These results can provide fundamental guidance for experimental and computational investigations of new MOFs for AHP/ACs applications.

4

IN SILICO SCREENING OF ZEOLITES FOR HIGH-PRESSURE HYDROGEN DRYING

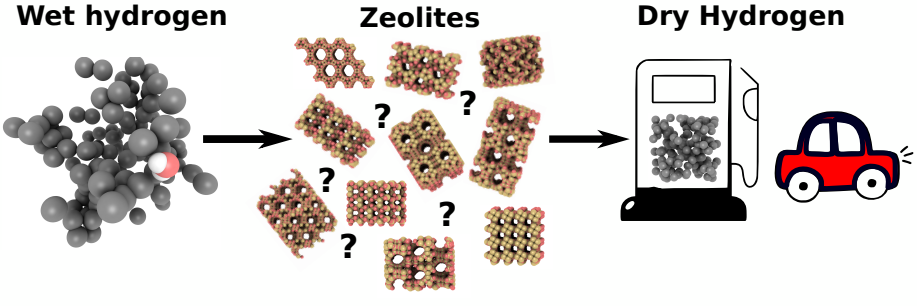

This chapter is based on the following publication: M. Erdős, D. F. Geerdink, A. Martin-Calvo, E. Pidko, L. J. P. van den Broeke, S. Calero, T. J. H. Vlugt, and O. A. Moultos, In silico screening of zeolites for high-pressure hydrogen drying, *ACS Applied Materials & Interfaces* **13**. 8383-8394 (2021).

4.1. INTRODUCTION

H_2 is considered a promising energy carrier which can be used in fuel cells and in combustion engines [253–259]. H_2 can be produced in a sustainable way via water electrolysis using renewable energy sources [260–263]. Due to its low volumetric energy density, to efficiently use H_2, it has to be compressed to high-pressures i.e., 350 - 700 bar [258, 264–266]. Conventionally, hydrogen is compressed using mechanical compressors [265, 267, 268]. The most-commonly used mechanical compressor types for H_2 compression are piston, compressed air, ionic and diaphragm compressors [265].

In the past decade, electrochemical H_2 compressors (EHCs) have been developed [269, 270] as an alternative to mechanical compressors. Compared to mechanical compressors, EHCs do not have moving parts which can be damaged during the operation of the device [268, 269]. Additionally, due to the isothermal compression process, EHCs can be more energetically efficient compared to mechanical compressors based on adiabatic compression [267]. HyET Hydrogen BV. [270] has developed an EHC that can compress H_2 from ambient pressures to 1 000 bar in a single step [270]. The working principle of EHC is similar to proton exchange membrane (PEM) based fuel cells [271]. In the EHC stack, a PEM is placed between the anode and the cathode allowing only to protons to permeate from the anode to the cathode side. On the cathode, protons are reduced to molecular H_2 at elevated pressures [270, 271]. Since EHCs rely on the presence of water for the transport of protons through the PEM, the outgoing high-pressure H_2 stream has a water content which exceeds the quality requirements of the ISO 14687—2:2019 standard [272]. According to this standard, the water content of H_2 fuel used in transportation and stationary applications should not exceed 5 ppm (throughout this chapter mole based ppm values are reported). This limit ensures that at high-pressures (*e.g.*, P >700 bar) and close to ambient temperatures, the water remains in the gas phase, thus, preventing the ice formation upon expansion, and the corrosion of the metallic parts of the storage vessel [273]. The presence of water in high-pressure H_2 also influences the thermodynamic properties of the H_2 gas [274].

Rahbari *et al.* [86] investigated the solubility of water in H_2 at high-pressures (P = 10 - 1 000 bar) for a wide range of temperatures (T = 283 - 423 K) using molecular simulation and equation of state (EoS) modelling. Additionally, an overview of all available experimental data on the solubility of water in high-pressure H_2 was reported [86]. It was shown that at the investigated pressure and temperature range, the equilibrium content of water in the gas phase is significantly higher than 5 ppm (molar) (i.e. ISO standard requirement [272]). At the lowest temperature (T = 283 K) and highest pressure (P = 1 000 bar) investigated in this chapter, the computed water content of the H_2 gas was 29 ppm [86]. This suggests that achieving 5 ppm water content by using

conventional drying methods, i.e. based on cooling or pressure swing adsorption, can be very energy intensive.

As an alternative drying method, selective adsorption of water on porous materials can be considered. Porous materials such as Metal-Organic frameworks (MOFs), activated carbons, zeolites *etc.* have been investigated for the drying of different gas streams [275–278]. In particular, zeolites are promising candidates for the selective adsorption of water from high-pressure H_2 streams due to their high water adsorption capacity, tunable hydrophilicity, and high thermal stability which ensures easy regeneration of the structure by heating [87, 91, 279].

The adsorption of pure water and pure H_2 on zeolites has been studied by several research groups both by simulation [51, 87, 88, 92, 96, 97, 108, 280] and experimental techniques [87, 88, 92, 97, 280]. In these studies, it was shown that depending on the Si/Al ratio of the framework, zeolites can have either high water or H_2 loading capacities. However, to the best of our knowledge there is no reported work on the adsorption of binary H_2/water mixtures at high-pressures.

In this chapter, a computational screening study is carried out to identify potential zeolite frameworks for the drying of high-pressure H_2 streams. To simulate the adsorption of water/H_2 mixtures on zeolites, MC simulations are performed. We show that the adsorption selectivity for water increases as the Si/Al ratio decreases. Since a high adsorption selectivity for water is desirable for the drying of high-pressure H_2, the Al content of the zeolites available in the zeolite database of the International Zeolite Association (IZA) is adjusted to obtain structures with the lowest possible Si/Al ratio while obeying Löwenstein's rule [281] which states that the formation of Al-O-Al bonds is prohibited in zeolites. To identify promising zeolites for the drying of high-pressure H_2 gas at conditions relevant to vehicular applications, H_2O/H_2 mixture with a water content of 12.3 ppm (molar) at 875 bar and 310 K is considered in this chapter. The selected operating pressure is based on the conditions typically used at refueling stations for vehicles, where H_2 should be stored at P = 875 bar (or higher) to be able to fuel a vehicle within 3-5 minutes [265, 282]. According to HyET Hydrogen BV. [270], the water content of H_2 compressed to 875 bar using EHC is ca. 12.3 ppm. To obtain a better understanding of the effect of pressure and water content on the adsorption selectivity of zeolite structures, additional water/H_2 mixtures with 12.3 ppm and 478 ppm of water at 400 bar and 310 K are considered. The value of 478 ppm is an estimation of the equilibrium solubility of water in H_2 at 400 bar and 310 K based on the study of Rahbari *et al.* [86]. Promising zeolites for high-pressure H_2 drying are identified based on the computed adsorption selectivity for water, the pore limiting diameter (PLD), and volume of the H_2 gas that can be dried by 1 dm^3 of zeolite. The proposed zeolites can be used to dry 400 - 8 000 times their own volume of H_2 gas depending on the

operating conditions. Our findings strongly indicate that zeolites with high Al content are potential candidates for the drying of high-pressure H_2 gas. To date, most types of zeolites have not been synthesized with the highest possible Al content yet [283]. For example, MFI-type zeolite can be synthesized with Si/Al ratio 9.3 [284] which is considerably higher than the theoretical minimum (Si/Al ratio = 2). Our findings indicate that the development of new synthetic pathways allowing for the creation of zeolites with high Al content would be beneficial for high-pressure H_2 drying.

The remainder of the chapter is structured as follows: In Section 4.1, details of the simulation methods are explained. In Section 4.3, the effects of the Si/Al ratio, pressure and water content on the adsorption selectivity, and the selection procedure of the most promising zeolites for high-pressure H_2 drying are reported. In Section 4.4, the conclusions of this chapter are summarized.

4.2. SIMULATION METHODOLOGY AND COMPUTATIONAL DETAILS

4.2.1. FORCE FIELDS

In all simulations, the (12-6) LJ potential is used for van der Waals interactions between guest-guest and guest-host. The LJ potential is truncated and shifted at 12 Å. No tail-corrections are used. The force field parameters reported by Castillo *et al.* [87] are used to model the zeolite frameworks, and the interactions between water and the zeolite atoms. In that study, the guest-host force field parameters were fitted using the rigid, five-site TIP5P/Ew [285] water model. Therefore, the TIP5P/Ew force field is used in all our simulations. In the study by Castillo *et al.* [87] the LJ parameters for the interactions between water and the framework atoms were fitted to experimentally measured water adsorption isotherms for the LTA4A structure [87]. It is important to note that our choice to use these force fields was based on the fact that no transferable force fields for the simulation of the adsorption of water on Al containing zeolites are currently available (mainly because the relevant experimental data are largely lacking). To model H_2 and the interactions of H_2 with Si and O atoms of the framework, the parameters reported by Deeg *et al.* [97] are used. These parameters were fitted to experimentally measured H_2 adsorption isotherms on pure Si zeolites.

The LJ parameters for the interactions of H_2 with the Al and Na^+ atoms of the framework were fitted to an experimentally measured H_2 adsorption isotherm on the LTA4A structure [286]. The calculated and experimentally measured adsorption isotherms of H_2 are shown in Figure 4.1.

It can be observed that the computed isotherm is in good agreement with the experiments. The diffusion of H_2 molecules inside the zeolite is also investigated us-

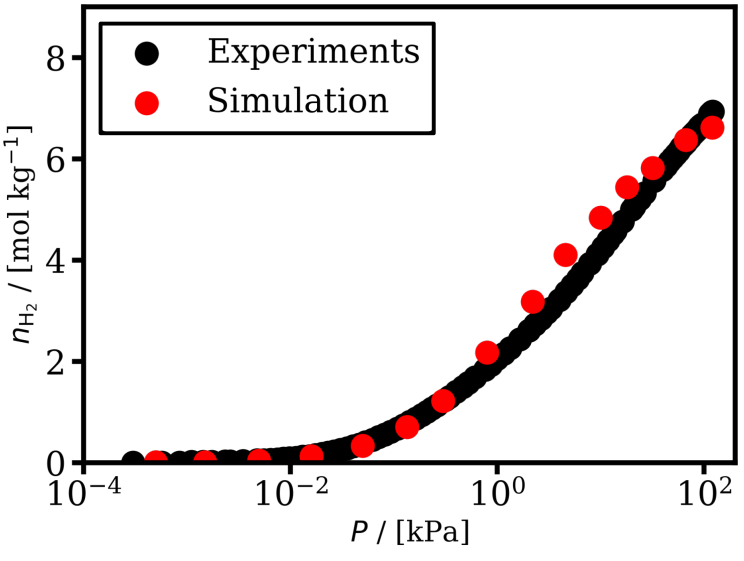

Figure 4.1: Amount of adsorbed hydrogen on the LTA4A as a function of pressure at T = 77 K. The red and black symbols represent computational and experimentally measured [286] results, respectively.

ing these force field parameters. The calculated mean square displacement of H_2 as a function of time in LTA4A is shown in Figure 4.2. It can be observed that hydrogen molecules have limited displacement inside the zeolite with the fitted force field parameters, as indicated by the almost flat MSD curve. Based on the computed MSD, diffusivity of H_2 inside the LTA4A is lower than c.a. 8×10^{-13} m^2 s^{-1}. To the best of our knowledge, no experimental diffusion data of H_2 on LTA4A is available, thus it is unclear whether or not our force field can accurately describe the mass transport of hydrogen in zeolite frameworks with non-framework Na^+ cations. Ideally, we would like to develop a transferable force field that is applicable to all zeolite structures. However, fitting a transferable force field that can describe both dynamics and adsorption thermodynamics requires a large number of experimental data, which are largely lacking. For this reason, and because the focus of our work is on high-pressure hydrogen drying, we feel that the development of such a transferable force field is beyond the scope of this chapter.

For interactions between unlike interaction sites, the Lorentz-Berthelot combining rules [77] are used. In all simulations, electrostatic interactions are described by fixed point charges. The long range electrostatic interactions are calculated using the Ewald method with a relative precision of 10^{-6} [76]. All force field parameters are listed in Tables A.5 and A.6 of the Appendix.

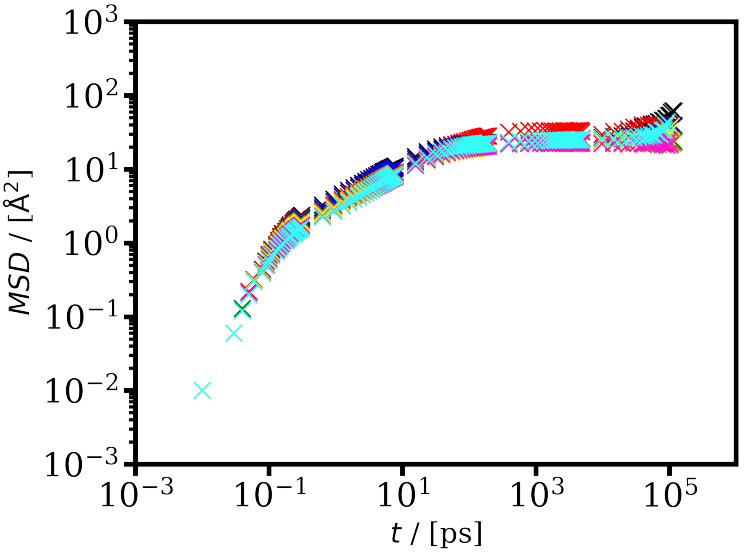

Figure 4.2: Mean squared displacement of H_2 in LTA4A as a function of time at $T = 77$ K. The colors represent simulations with different number of H_2 molecules in the alpha cages of the LTA4A. The black, red, blue, green, orange, yellow, magenta and cyan colors represent the simulations with 1, 2, 3, 4, 5, 6, 7, and 8 H_2 molecules per alpha cage, respectively.

4.2.2. SIMULATION DETAILS

The MC simulations for the calculation of the adsorption isotherms were performed using the RASPA software package [79, 90]. The atomic positions of the zeolite structures were taken from crystallographic files (CIF) of the IZA database [18] implemented in the iRASPA visualization package [45]. In this database, 231 zeolite structures are included. 13 structures contain Si atoms coordinated by only 3 oxygen atoms instead of 4. These zeolites were excluded from the screening study. The zeolite structures were considered rigid in all simulations. This is a common practice in simulations of adsorption of small molecules on nanoporous materials because it significantly reduces the CPU time [95, 152]. Nevertheless, it has been shown that for small non-aromatic molecules, framework flexibility has a small effect on adsorption properties [95]. The Al containing zeolites were created by randomly exchanging the Si atoms of the original zeolite structure for Al, while obeying Löwenstein's rule [281]. As shown in literature [129, 287, 288], the distribution of Al atoms in certain types of zeolites can affect the adsorption properties such as the adsorption loading, diffusion *etc.* However, at very high Al content (i.e. Si/Al ratio < 3) the effect of the distribution of Al atoms is expected to be small. The structures with the lowest possible Si/Al ratio were created by using the following MC scheme: Initially, half of the Si atoms are exchanged for Al (i.e.,

Si/Al = 1). Consequently, identity changes are carried out during which the Al atoms violating Löwenstein's rule are exchanged with randomly selected Si atoms which are connected to at least one other Si atom via an oxygen atom. If no structure obeying Löwenstein's rule is obtained after 100 000 attempts then a new structure with one Al atom less is created (i.e., Si/Al > 1) and the exchange of the Al atoms is started again. This procedure is performed until a structure obeying Löwenstein's rule is obtained. CIF files containing the obtained structures with the lowest Si/Al ratio are provided as separate files in the Supporting Information of Ref. [289].

The charge imbalance of the framework due to the presence of the Al atoms is compensated by the insertion of nonframework Na^+ cations. In principle, the nonframework cations should be placed to the experimentally measured crystallographic positions [98, 128]. However, the crystallographic positions of Na^+ are not available for most zeolites. Therefore, in this chapter, the cations are inserted randomly in the framework and their positions are equilibrated by performing simulations in the canonical (NVT) ensemble at 1 000 K. In these simulations, translation (50%) and random reinsertion (50%) trial moves are used. To obtain an equilibrated structure, 500 000 cycles are carried out. A cycle consists of as many MC steps as the number of molecules in the system. A minimum of 20 MC steps are carried out per cycle. Due to the random insertions, cations may be placed in positions which should not be accessible, in so-called pockets. The Zeo++ software package [223, 224] provides the functionality to identify pockets which should be blocked for a sphere with a certain radius (i.e, probe size). This approach was tested for LTA- and FAU-type zeolites. We observed that by using the ionic radius of Na^+ (r_{Na^+} = 1.16 Å) as probe size, the sodalite cages are blocked in both structures. Based on the reported crystallographic positions of Na^+, the sodalite cages should be accessible for Na^+ in FAU-type zeolite [290] but not in LTA-type zeolite [291]. This shows that by using blocking spheres, the inaccessible pockets for Na^+ cannot be clearly identified without experimental data. Therefore, in this chapter, blocking spheres are only used for LTA-type zeolite in which the location of Na^+ cations (sodalite cages) are reported experimentally. Since the kinetic diameters of water (2.65 Å) and H_2 (2.89 Å) are similar to the window size of most zeolites, for these molecules no blocking spheres are used, in accordance with other studies [87, 108, 280].

To calculate the adsorption isotherms of H_2/water binary mixture on zeolites, MC simulations in the grand-canonical ensemble (μVT) are performed. In these simulations, the following trial moves are used for the cations: translations (50%) and random reinsertions (50%). For the H_2 and water molecules, the following trial moves are carried out: translations (20%), rotations (20%), random reinsertions (20%), and particle exchanges with the reservoir (40%). For all structures, 200 000 equilibration cycles are

performed which ensures that the equilibrium loading of the components is reached. Using the equilibrated configuration, 5 independent simulations of 100 000 production cycles are carried out to obtain accurate ensemble averages.

In the RASPA software package [79, 90], the imposed chemical potential is calculated from the fugacity of the fluid. The fugacity coefficients of the components are predicted by the Peng-Robinson Equation of State (PR EoS) [222]. Recently, Rahbari *et al.* [86] compared the performance of the PR EoS and MC simulations for predicting the fugacity coefficients of water and H_2 at a wide pressure range (10 - 1 000 bar). It was shown that the PR EoS yields inaccurate fugacity coefficients at high-pressures ($P > 400$ bar), while the fugacity coefficients computed by MC simulations are in reasonable agreement with the experimentally measured data. Therefore, in this chapter, the fugacity coefficients of water and H_2 are calculated by performing MC simulations in the continuous fractional component NPT (CFCNPT) ensemble [89] implemented in the BRICK-CFCMC software package [292, 293]. In CFCMC simulations, special types of molecules, the so-called fractional molecules are used. The LJ and electrostatic interactions of these molecules with the rest of the system are scaled by a parameter $\lambda \in [0,1]$, where $\lambda = 0$ means that the fractional molecule does not interact with other molecules and $\lambda = 1$ means that the fractional molecule has the same interactions as other molecules of the same type. For calculating fugacity coefficients, it is assumed that the water is infinitely diluted in H_2 since only a few ppm of water are present in the H_2 gas. The simulation box consists of 512 H_2 and 1 fractional molecule of each component which enables the calculations of the excess chemical potential that can be related to the fugacity coefficient. The detailed derivation of the relations between the fugacity coefficients and the excess chemical potential are presented elsewhere [86, 89]. The trial moves used in the CFCNPT simulations are selected with the following probabilities: 35 % translations, 30 % rotations, 1 % volume changes, 17 % λ changes, and 17 % identity changes of the fractional molecule. The simulations consist of 100 000 equilibration and 500 000 production cycles. The calculated fugacity coefficients of the components are shown in Table A.7 of the Appendix. The uncertainity of ensemble averages were calculated as the standard deviation of the mean from five independent simulations.

To identify potential zeolite structures for the drying of high-pressure H_2 streams, the adsorption selectivity (S_{H_2O,H_2}) is used as a criterion. In this work, the adsorption selectivity is defined as the percentage of water adsorbed on the zeolite:

$$S_{H_2O,H_2} = \frac{q_{H_2O}}{q_{H_2} + q_{H_2O}} \times 100\% \tag{4.1}$$

where q_{H_2O} and q_{H_2} are the numbers of water and H_2 molecules adsorbed per unit cell. The adsorption selectivities are computed for water/H_2 mixtures with 12.3 ppm

and 478 ppm water content. The value of 478 ppm is an estimation of the equilibrium solubility of water in H_2 at 400 bar and 310 K based on the study of Rahbari *et al.* [86]. In that study, the solubility of water at T = 323, 366, and 423 K was reported for various water force fields, i.e. TIP3P [294], TIP4P/2005 [295], and TIP5P/Ew [285], while at T = 310 K the authors used only TIP3P. Since in this chapter the TIP5P/Ew force field is used at T = 310 K, the solubility of water is estimated based on the solubilities reported with TIP3P. In particular, we assume that the ratio of solubilities computed with the TIP3P and TIP5P/Ew force fields at the same pressure is independent of the temperature. Thus, the ratio of the solubilities predicted with the two force fields at T = 423 K is calculated (i.e, ca. 0.62) and assumed to be equal with the ratio at T = 310 K. Using the available solubility data reported by Rahbari *et al.* [86], we estimate the solubility of water in H_2 at T = 310 K and P = 400 bar with the TIP5P/Ew model to be 478 ppm.

The helium void fraction (ϕ_{He}) of each zeolite is calculated using the Widom's test particle insertion method [76] using the RASPA software package [79, 90]. In this chapter, the reported helium void fractions are computed for zeolites with the lowest Si/Al ratio in the presence of Na^+ cations. The geometrical properties of the zeolite structures i.e., PLD, LCD, accessible surface area (ASA) are calculated using the Zeo++ software package [223, 224].

4.3. RESULTS AND DISCUSSION

4.3.1. EFFECT OF THE SI/AL RATIO

In Figure 4.3, the adsorption selectivities of the FAU-, MOR-, MFI-, FER-, CHA-, and LTA-type zeolites for water is shown for a water/H_2 mixture with 12.3 ppm water content at P = 875 bar and T = 310 K as a function of the Si/Al ratio of the framework. As expected, for all structures the adsorption selectivity is increasing as the Si/Al ratio decreases. This is due to the increasing hydrophilicity of the structure. The FAU-, CHA-, and LTA-type zeolites show preferential adsorption for water ($S_{H_2O,H_2} > 50\%$) only for relatively high Al contents, i.e., Si/Al < 4. Figure 4.3 also shows that the difference in the adsorption selectivities of MFI-type zeolites that can be experimentally synthesized (i.e., Si/Al = 9.3 [284]) with the theoretical ones having low Si/Al ratios (> 8) can be as high as 60%. This clearly indicates that progress in the synthesis techniques of zeolites allowing for the creation of structures with high Al content would be beneficial for high-pressure H_2 drying.

To obtain a better understanding of the adsorption mechanism, the preferred adsorption sites of water and H_2 are identified based on the computed density plots. The simulation box is divided into a 3D grid and the number of H_2O, H_2, and Na^+ at the grid points is calculated from 200 simulation snapshots. The number of occurrences of each species in the snapshots are summed along the z-axis of the grid and normalized

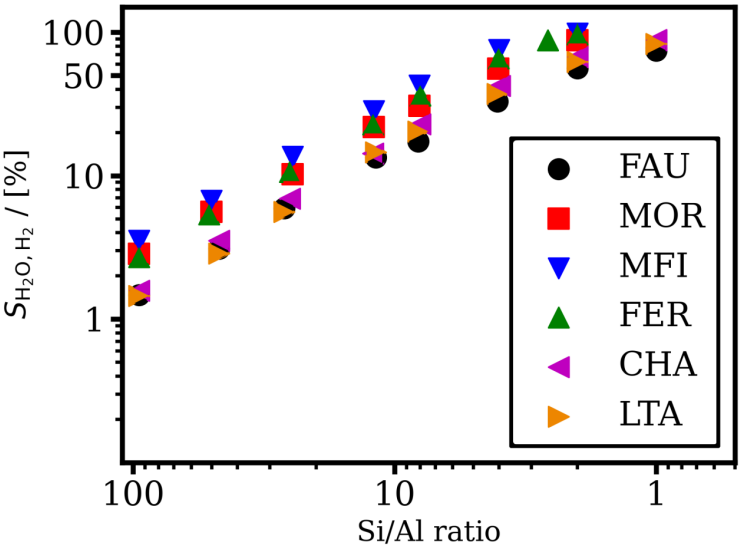

Figure 4.3: The adsorption selectivity of FAU-, MOR-, MFI-, FER-, CHA-, and LTA-type zeolites for water from a water/H_2 mixture with 12.3 ppm water content as a function of the Si/Al ratio of the framework, at P = 875 bar and T = 310 K. The error bars are smaller than the symbol size.

to a [0, 1] interval. The obtained 2D grid of the normalized occurrences is referred to as the normalized density corresponding to the relative probability of finding the species at a grid point. In Figures 4.4a and 4.4b, the normalized densities of H_2O, H_2, and Na^+ on MFI-type zeolite without Al, and with the lowest possible Si/Al ratio, respectively, are shown on the xy plane for a system at P = 875 bar, T = 310 K, and y_{H_2O} = 12.3 ppm. MFI-type zeolites consist of straight and zig-zag channels connected via intersections. These characteristics can be identified in Figure 4.4c: the straight channels are perpendicular to the xz plane and the zigzag channels are located in the xz plane [18]. From Figure 4.4a (Si/Al ratio $\rightarrow \infty$), it becomes clear that practically only H_2 (black color) is adsorbed on the zeolite. This is caused by the highly hydrophobic nature of the pores due to the absence of Al atoms. As shown clearly, H_2 molecules are absorbed in all pores, having a slightly higher occurrence at the center of the intersection of the straight and zigzag channels than at the other parts of the zeolite. From Figure 4.4b (Si/Al ratio = 2), it can be observed that practically only water molecules (red color) are adsorbed. This is expected due to the high Al content of the structure. In Figure A.1 of the Appendix, the radial distribution functions (RDFs) are shown for the oxygen atoms of the water molecules with the Na^+ cations on MOR-, MFI-, LTA-, and FAU-type zeolites having the lowest possible Si/Al ratio. In Figures 4.4b and A.1 of the Appendix, it can be observed that the water molecules are preferentially adsorbed near the wall of

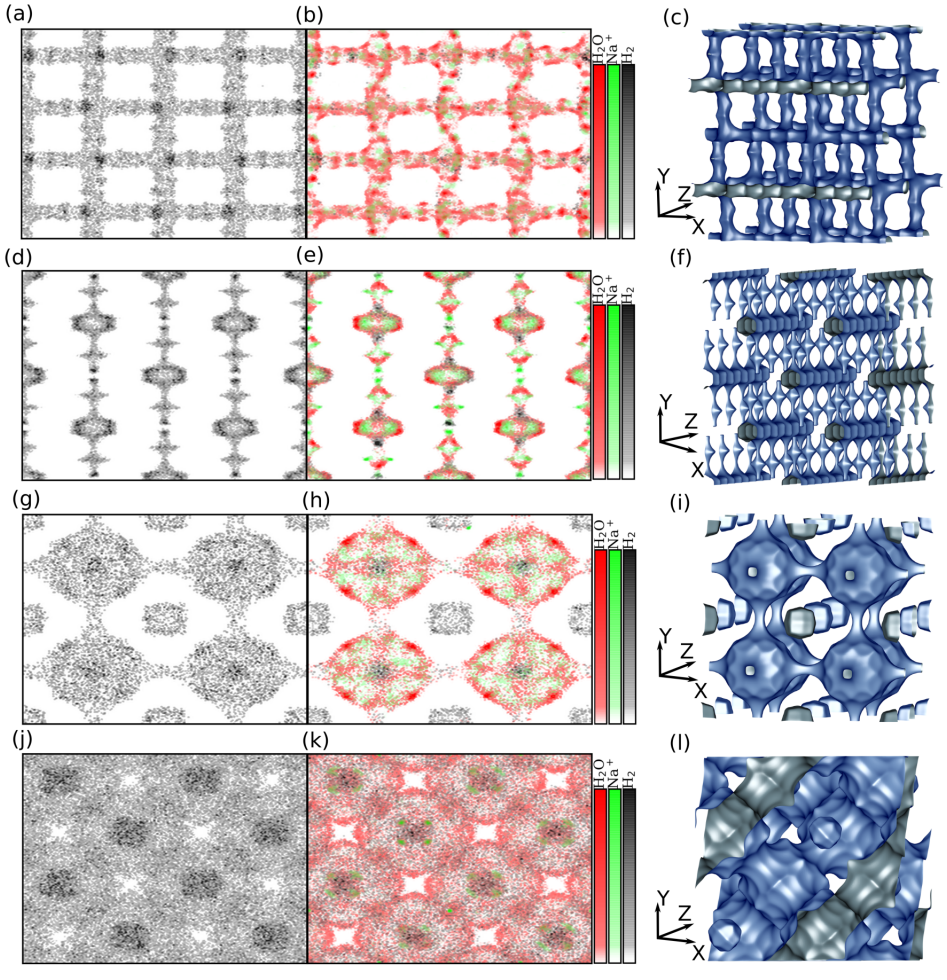

Figure 4.4: The normalized densities of H_2O (red), H_2 (black), and Na^+ (green) on the xy plane for MFI-, MOR-, LTA-, and FAU-type zeolites without and with the maximum amount of Al atoms. (a), (d), (g), and (j) show the normalized densities for the pure silicon MFI-, MOR-, LTA- and FAU-type zeolites, respectively. (b), (e), (h), and (k) show the normalized densities for MFI-, MOR-, LTA- and FAU-type zeolites with the lowest Si/Al ratio, respectively. The pore structures of (c) MFI-, (f) MOR-, (i) LTA-, and (l) FAU-type zeolites represented by the adsorption surface computed with water as a probe molecule. The simulations were carried out at $P = 875$ bar, $T = 310$ K, and $y_{H_2O} = 12.3$ ppm. The representations of the pore structures are created with the iRASPA software package [45]

the zeolite and around the Na^+ cations.

In Figures 4.4d and 4.4e, the normalized densities of H_2O, H_2, and Na^+ on MOR-type zeolite without Al, and with the lowest possible Si/Al ratio are shown, respectively, on the xy plane for a system at $P = 875$ bar, $T = 310$ K, and $y_{H_2O} = 12.3$ ppm. As shown in Figure 4.4f, in MOR-type zeolites two characteristic parts can be identified, i.e., the large main channels formed by the 12-membered rings which are located along the z-

axis, and the small side pockets connected to the main channels by 8-membered rings located along the y-axis. As expected, on the pure Si structure (see Figure 4.4d) only H_2 is adsorbed because of its hydrophobic nature. H_2 molecules are adsorbed throughout the structure with a slightly higher occurrence at the walls of the main channel. As shown in Figure 4.4e, considerably more water than H_2 is adsorbed (S_{H_2O,H_2} = 88 %) on MOR-type zeolite with the lowest Si/Al ratio. The adsorbed H_2 molecules are preferentially located at the intersection of the main channel and at the 8-membered ring connecting the main channels to the side pockets. The different adsorption location of the H_2 molecules is caused by the presence of the water and the Na^+ cations in the structure. The water molecules are clustered around the Na^+ cations which are located at the center of the main channels and side pockets. This is further substantiated from Figure A.1 of the Appendix in which the RDFs are shown for the oxygen atoms of the water molecules with the Na^+ cations on MOR-type zeolite having the lowest Si/Al ratio.

In Figures 4.4g and 4.4h, the normalized densities of H_2O, H_2, and Na^+ on LTA-type zeolite without Al and with the lowest Si/Al ratio are shown on the xy plane at P = 875 bar, T = 310 K, and y_{H_2O} = 12.3 ppm. As shown in Figure 4.4i, the LTA-type zeolite consists of small sodalite cages connected to each other by 4-membered rings. The void space between the sodalite cages is called the alpha cage. The alpha cages are connected to each other by 8-membered rings and are larger than the sodalite cages. Similarly to MFI- and MOR-type zeolites, only H_2 is adsorbed on the pure Si LTA-type zeolite (see Figure 4.4g). The H_2 molecules are adsorbed both at the sodalite and alpha cages of the LTA-type zeolite with a preference towards the center of the alpha cage. As expected, considerably more water than H_2 is adsorbed on the LTA-type zeolite having the lowest Si/Al ratio due to the hydrophilicity of the structure (see Figure 4.4h). From Figure 4.4h, it can be observed that H_2 is preferentially adsorbed at the center of the alpha cage and in the sodalite cages. The water molecules are clustered around the Na^+ ions which are located near the center of the alpha cages. This is further substantiated in the respective RDF shown in Figure A.1 of the Appendix.

In Figures 4.4j and 4.4k, the normalized densities of H_2O, H_2, and Na^+ on FAU-type zeolite without Al, and with the lowest Si/Al ratio are shown on the xy plane for a system at P = 875 bar, T = 310 K, and y_{H_2O} = 12.3 ppm. As shown in Figure 4.4l, similar to LTA-type zeolite, FAU-type zeolite consists of sodalite cages, with the difference that the cages of FAU are connected by 6-membered instead of 4-membered rings. The alpha cages of FAU-type zeolite are similar in size to the LTA-type zeolite but are connected to the each other by 12-membered rings instead of 8-membered rings. Similarly to the other investigated zeolites, only H_2 is adsorbed on the pure Si FAU-type zeolite (see Figure 4.4j). H_2 molecules have the same preferential adsorption site on the

pure Si FAU-type zeolite as on LTA-type zeolite, i.e., at the center of the alpha cage. As expected, considerably more water than H_2 is adsorbed on the FAU-type zeolite with the lowest Si/Al ratio due to the hydrophilicity of the structure (see Figure 4.4k). From Figure 4.4k, it can be observed that H_2 is preferentially adsorbed at the center of the alpha cage. The distribution of water molecules is similar to the one observed in the LTA structures. The clustering of water molecules around the Na^+ ions which are located around the center of the sodalite and alpha cages can be also observed from the respective RDFs shown in Figure A.1 of the Appendix.

MFI- and MOR-type zeolites can be saturated by the adsorption of water around the Na^+ cations leaving no available space for the adsorption of H_2. Due to their higher accessible volume, LTA- and FAU-type zeolites are not saturated by water, and thus, H_2 can be adsorbed at its preferential adsorption location. This shows that the presence of the nonframework Na^+ cations is advantageous for the adsorption selectivity of zeolites for water. The Na^+ cations occupy significant amount of pore space and promote the adsorption of water which further limits the available space for the adsorption of H_2. Therefore, for high-pressure H_2 drying, zeolites with high Na^+ (Al) content are preferred. These findings suggest that the adsorption selectivity of Al containing structures for water is correlated to the available free space in the pores containing nonframework Na^+ cations.

4.3.2. SCREENING OF ZEOLITES FOR HIGH-PRESSURE H_2 DRYING

In Figure 4.5, the computed adsorption selectivities of water (S_{H_2O,H_2}) for each investigated zeolite structure for 12.3 ppm and 478 ppm water contents at P = 400 and 875 bar, and T = 310 K are shown as a function of the helium void fraction (ϕ_{He}). It is clear that structures with low helium void fractions have high adsorption selectivity for water. This finding is in line with the observation that structures with less free space can be saturated with water, which is adsorbed close to the Na^+ cations hindering the adsorption of H_2. By comparing the adsorption selectivities calculated for the water/H_2 mixtures with 12.3 ppm water content at P = 400 (see Figure 4.5a) with the respective selectivities at P = 875 bar (see Figure 4.5c), the effect of the fluid pressure can be observed. The average difference between the adsorption selectivities at the two pressures is ca. 2 %. This means that the pressure of the gas phase has limited effect on the adsorption selectivity. The effect of the water content of the H_2 gas on the adsorption selectivity can be observed in Figures 4.5a and 4.5b, in which the adsorption selectivites are shown for water/H_2 mixtures with 12.3 and 478 ppm water content at P = 400 bar and T = 310 K. The difference between the adsorption selectivities of a structure for the two water fractions can be up to 50 %. Evidently, the effect of the water content is only significant for structures with helium void fractions larger than 0.1. This is caused by the formation of water clusters in the larger pores of the struc-

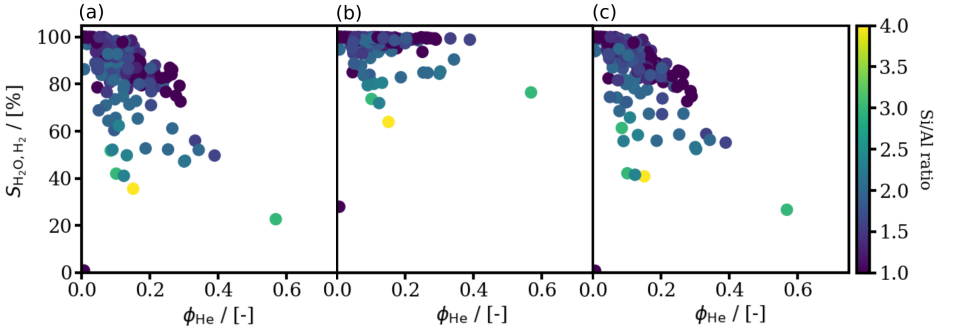

Figure 4.5: The computed adsorption selectivities (S_{H_2O,H_2}) of the 218 zeolite structures for water at (a) P = 400 bar, T = 310, y_{H_2O} = 12.3 ppm, (b) P = 400 bar, T = 310, y_{H_2O} = 478 ppm, and (c) P = 875 bar, T = 310, y_{H_2O} = 12.3 ppm conditions as a function of the helium void fraction of the structures. The helium void fractions are calculated for zeolites containing Na^+ cations using Widom's test particle insertion method [76]. The Si/Al ratio of each framework type is listed in Table S7 in the Supporting Information of Ref. [289]. The colors represent the Si/Al ratio of the structures.

ture. Water cluster formation is inhibited at low y_{H_2O} since the amount of adsorbed water cannot saturate the pores. However, at high y_{H_2O} enough water molecules can be adsorbed from the H_2 gas to fill the larger pores.

In Figure 4.6, RDFs are shown for the oxygen atoms of water molecules, H_2 molecules with Na^+ cations, and oxygen atoms of water molecules with Na^+ cations for FAU-, and BSV-type zeolites with Si/Al ratio = 1 at the three operating conditions: (a) and (d): P = 400 bar and y_{H_2O} = 12.3 ppm, (b) and (e): P = 400 bar and y_{H_2O} = 478 ppm, and (c) and (f): P = 875 bar and y_{H_2O} = 12.3 ppm. In all cases, the water molecules are clustered around the Na^+ cations as indicated by the strong peaks in the RDFs. From Figures 4.6a and 4.6c, it can be observed that the calculated RDFs are almost identical. This observation is in line with our finding presented earlier, i.e. the pressure of the gas phase has a negligible effect on the selectivity of the zeolite for water. By comparing the RDFs calculated for water content of 12.3 ppm and 478 ppm, it can be observed that water molecules are less likely to cluster around Na^+ cations and more probable to form water clusters at higher water content of the gas phase. This phenomenon cannot be observed for BSV-type zeolite (Figures 4.6d, 4.6e, and 4.6f) which has smaller pores than FAU-type zeolite. The RDFs calculated for the BSV-type zeolite are almost identical at all investigated operating conditions (see (Figures 4.6d, 4.6e, and 4.6f)). This is due to the small size of the pores which are saturated with water at all conditions investigated.

Apart from the adsorption selectivity for water, the size of the system used for H_2 drying also plays an important role. Therefore, in this chapter the volume of the H_2 gas that can be dried by 1 dm^3 of zeolite structure (V_{H_2}) is considered as a criterion to identify potential zeolites for the drying of high-pressure H_2 gas. In Figure 4.7, the

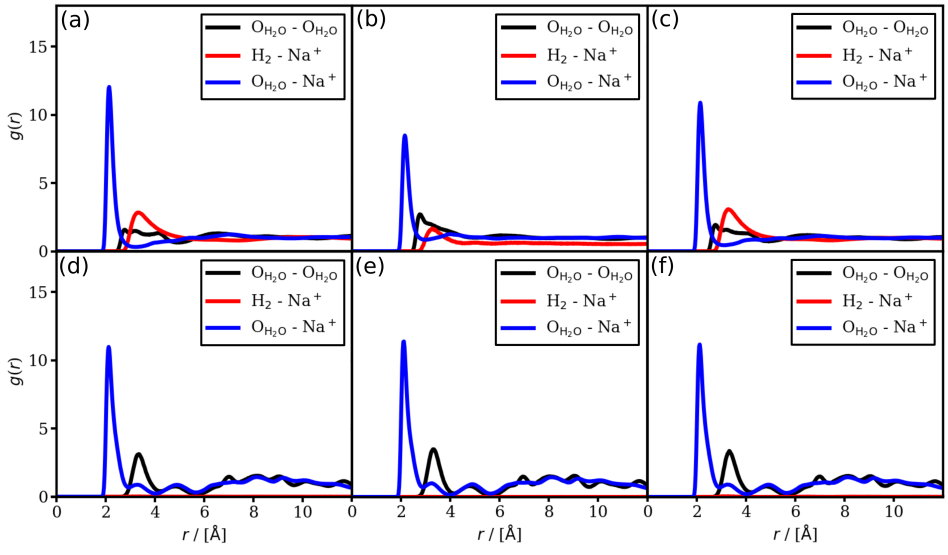

Figure 4.6: The radial distribution functions for the oxygen atoms of water molecules (black), H_2 molecules with Na^+ cations (red), and oxygen atoms of water molecules with Na^+ cations (blue). (a) FAU-type zeolite at P = 400 bar, T = 310 K, and y_{H_2O} = 12.3 ppm, (b) FAU-type zeolite at P = 400 bar, T = 310 K, and y_{H_2O} = 478 ppm, (c) FAU-type zeolite at P = 875 bar, T = 310 K, and y_{H_2O} = 12.3 ppm, (d) BSV-type zeolite at P = 400 bar, T = 310 K, and y_{H_2O} = 12.3 ppm, (e) BSV-type zeolite at P = 400 bar, T = 310 K, and y_{H_2O} = 478 ppm, and (f) BSV-type zeolite at P = 875 bar, T = 310 K, and y_{H_2O} = 12.3 ppm. The Si/Al ratio of BSV- and FAU-type zeolites are 1.0.

volume of H_2 gas that can be dried by 1 dm^3 of zeolite at P = 400 and 875 bar and T = 310 K is shown as a function of the helium void fraction. It can be observed that the V_{H_2} is nearly twice as high at P = 400 bar (see Figure 4.6a) compared to P = 875 bar (see Figure 4.6c). This difference is mainly caused by the different density of H_2 at the two conditions (ρ_{H_2} = 25.2 and 44.6 kg m^{-3}, at T = 310 K and P = 400, and 875 bar, respectively). The amount of H_2 gas that can be dried is increasing with the helium void fraction. However, the adsorption selectivity of the structures with ϕ_{He} > 0.1 tends to be lower than 85 %. This means that a significant amount of H_2 is also adsorbed on the zeolite which is undesirable for H_2 storage applications. To identify promising zeolites for the drying of high-pressure H_2, only structures with adsorption selectivity higher than 99 % are considered. Moreover, to ensure that water molecules can diffuse along the structure and adsorb, only structures with PLDs larger than the kinetic diameter of water ($d_{kinetic}$ = 2.65 Å) are considered. Based on these criteria, the five best performing structures are identified for each studied condition. The identified frameworks for the drying of H_2 with 12.3 ppm water content at P = 400 and P = 875 bar are almost identical, i.e. BSV-, ASV-, PON-, and MFI-type zeolites. Additionally, at P = 400 and P = 875 bar, STO- and the AFN-type zeolites are identified, respectively.

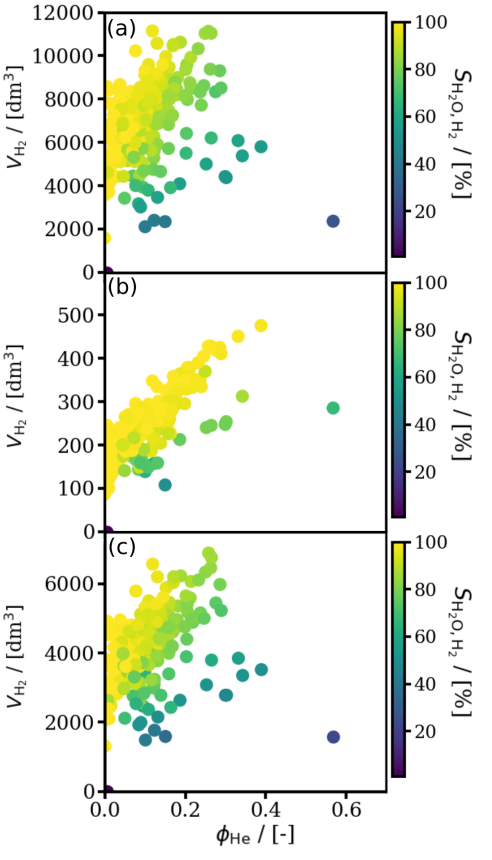

Figure 4.7: The volume of the H_2 gas (V_{H_2}) that can be dried by 1 dm^3 of zeolite structure at (a) P = 400 bar, T = 310, y_{H_2O} = 12.3 ppm, (b) P = 400 bar, T = 310, y_{H_2O} = 478 ppm, and (c) P = 875 bar, T = 310, y_{H_2O} = 12.3 ppm. Data is plotted as a function of the helium void fraction of the framework types. The helium void fractions are calculated for zeolites containing Na^+ cations using Widom's test particle insertion method [76]. The Si/Al ratio of each framework type is listed in Table S7 in the Supporting Information of Ref. [289]. The colors represent the adsorption selectivity of the structure for water.

For drying H_2 gas having 478 ppm water content at P = 400 bar, ITT-, SBE-, SBS-, FAU-, and SBT-type zeolites are found to be the best. In Figure 4.8, atomistic representations of the best performing structures are shown.

In Table 4.1, the 11 best performing structures and their helium void fraction, PLD, LCD, ASA, adsorption selectivities, and the volume of H_2 that 1 dm^3 of structure can dry are listed. The zeolites identified for the drying of H_2 gas with 12.3 ppm water content have helium void fractions in the range from 0.01 to 0.07. In contrast, all of the identified structures at the higher water content have helium void fractions larger than 0.26. This difference is caused by the higher adsorption selectivity of zeolites with more free space ($\phi_{He} > 0.1$) at higher water content (see Figures 4.5a and 4.5b). For example,

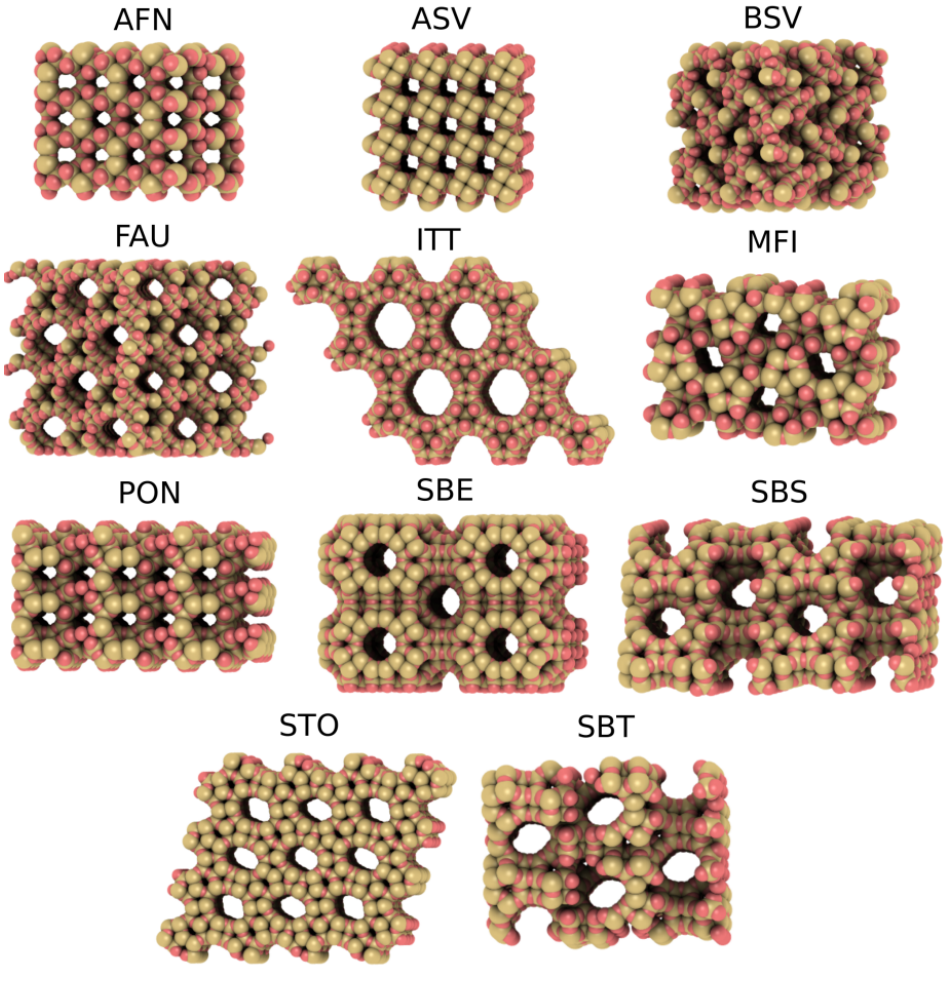

Figure 4.8: Atomistic representations of the 11 best performing zeolite framework types for high pressure H_2 drying. The graphical representation is created with iRASPA [45].

the adsorption selectivity of ITT-type zeolite (which has a $\phi_{He} = 0.33$) for water is 58.8 % at $P = 400$ bar and $y_{H_2O} = 12.3$ ppm while it is 99.4 % at $P = 400$ bar and $y_{H_2O} = 478$ ppm. A similar tendency can be observed for the structures which were identified for the case of $y_{H_2O} = 478$ ppm. The ASA of the structures shows the same trend as the helium void fraction. The structures identified for the case of the lower water content have consistently lower ASA than the ones identified for $P = 400$ bar and $y_{H_2O} = 478$ ppm. It can be also observed that the LCD of the structures identified for the case of higher water content is on average twice as large as of the structures identified for the conditions with the lower water contents. This is in line with the finding that water

clusters can be formed in the larger pores of the zeolites for higher water content. It can be seen that the identified zeolite structures can be used to dry 400 - 8 000 times their own volume of H_2 gas depending on the operating conditions.

Table 4.1: List of zeolites that are identified as the most promising structures for high-pressure H_2 drying. The reported properties are: helium void fraction (ϕ_{He}), pore limiting diameter (PLD), largest cavity diameter (LCD), accessible surface area (ASA), adsorption selectivity (S_{H_2O,H_2}), and the volume of H_2 that 1 dm^3 of structure can dry (V_{H_2}).

Name	Si/Al ratio	ϕ_{He}	PLD/	LCD/	ASA/	P = 400 bar y_{H_2O} = 12.3 ppm		P = 400 bar y_{H_2O} = 478 ppm		P = 875 bar y_{H_2O} = 12.3 ppm	
			[Å]	[Å]	[m^2 cm^{-3}]	S_{H_2O,H_2}/[%]	V_{H_2}/[dm^3]	S_{H_2O,H_2}/[%]	V_{H_2}/[dm^3]	S_{H_2O,H_2}/[%]	V_{H_2}/[dm^3]
BSV	1.0	0.01	3.44	4.77	1367	100	8298	100	247	100	4917
ASV	1.0	0.01	4.03	4.95	1112	100	8166	100	225	100	4702
PON	1.0	0.03	3.9	4.5	1147	100	7629	100	234	100	4383
MFI	2.0	0.06	4.3	5.94	1272	99.4	6896	100	219	99.2	4131
STO	1.5	0.07	5.61	6.4	888	99.5	6475	100	195	99.3	3822
AFN	1.0	0.04	3.08	4.75	1249	99.4	6927	100	228	98.7	4185
ITT	1.6	0.33	11.6	12.77	1598	58.8	5899	99.4	452	56	3852
SBE	1.0	0.26	6.83	12.1	1572	80	9078	99.4	430	84.1	6459
SBS	1.0	0.26	6.87	10.98	1618	85.4	10766	99.8	430	86.9	6887
FAU	1.0	0.29	6.95	10.7	1488	77.1	9008	99.4	427	79.3	5980
SBT	1.0	0.27	6.94	10.4	1629	84.5	10683	99.8	427	86.1	6758

4.4. CONCLUSIONS

The performance of 218 zeolites is investigated for the drying of high-pressure H_2 gas. The effect of the Si/Al ratio on the adsorption selectivity of 6 zeolite structures for water is also studied. We show that structures with the lowest possible Si/Al ratio have the highest adsorption selectivity for water. To obtain a better understanding of the adsorption mechanism, the preferred adsorption sites of H_2 and water on MFI-, MOR-, LTA-, and FAU-type zeolites without Al and with the lowest Si/Al ratio are investigated. It is shown that in the structures with high Al content, water is adsorbed close to the Na^+ cations. For structures with small free space (MFI- and MOR-type zeolites), the structures are saturated by water molecules, thus, hindering the adsorption of H_2. On the structures with larger pores (FAU- and LTA-type zeolites), water cannot saturate the pores, thus, H_2 can also be adsorbed. The adsorption selectivities of the 218 structures with the lowest Si/Al ratio are computed at three operating conditions relevant to high-pressure H_2 drying: (1) P = 400 bar, T = 310 K, y_{H_2O} = 12.3 ppm, (2) P = 400 bar, T = 310 K, y_{H_2O} = 478 ppm, and (3) P = 875 bar, T = 310 K, y_{H_2O} = 12.3 ppm. It is shown that the gas pressure has only limited effect on the adsorption selectivity of zeolites. In sharp contrast, the water content of the H_2 gas has a significant effect on the adsorption selectivity of zeolites with $\phi_{He} > 0.1$. This phenomenon is caused by water clustering in larger pores. The five most promising zeolites based on the volume of H_2 that can be dried by 1 dm^3 of zeolite, the PLD, and the adsorption selectivity of the structure are identified at each studied operating condition. It is shown that at low water concentration in the gas phase, structures with helium void fractions smaller than 0.07 are preferred. The structures identified in case of high water content have helium void fractions larger than 0.26. The structures identified for lower water content have consistently lower accessible surface area than the ones identified for P = 400 bar and y_{H_2O} = 478 ppm. It is also shown that the largest cavity diameters of the structures identified for high water content (478 ppm) are on average twice as large as for the structures identified for low water content (12.3 ppm). Our findings indicate that the volume of H_2 that can be dried by zeolites can be up to 8 000 times the volume of the zeolite framework. To date, most types of zeolites have not been synthesized with the highest possible Al content [283]. For example, MFI-type zeolite can be synthesized [284] for Si/Al ratio 9.3, which is considerably higher than the theoretical minimum (i.e. Si/Al ratio = 2). We show that the difference in the adsorption selectivities of the already synthesized MFI-type zeolites (Si/Al ratio = 9.3) with the ones having low Si/Al ratios can be as high as 60%. Our findings indicate that the development of new synthetic pathways allowing for the creation of zeolites with high Al content would be beneficial for high-pressure H_2 drying.

5

ADSORPTION MECHANISM OF TCP ON HIGH-SILICA ZEOLITES CAUSING S-SHAPED ADSORPTION ISOTHERMS

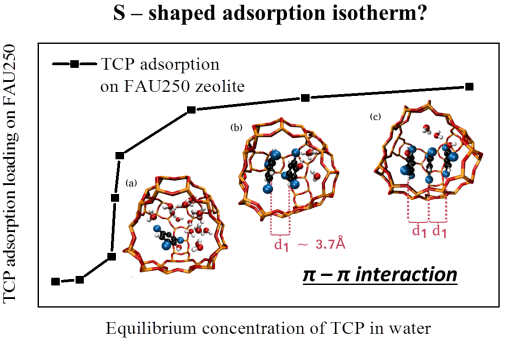

This chapter is based on the following publication: N. Jiang, M. Erdős, O. A. Moultos, R. Shang, T. J. H. Vlugt, S. G. Heijman, and L. C. Rietveld, The adsorption mechanisms of organicmicropollutants on high-silica zeolites causing s-shaped adsorption isotherms: An experimental and Monte Carlo simulation study, *Chemical Engineering Journal* **389**, 123968 (2020).
The experiments presented in this chapter were performed by N. Jiang, R. Shang, S. G. Heijman, and L. C. Rietveld.

5.1. INTRODUCTION

In the process of organic micropollutant (OMP) adsorption from water on solid adsorbents, the adsorption isotherm describes the relation between the equilibrium concentration of OMPs in water and the adsorption loading of OMPs on the solid adsorbents. Giles *et al.* [296] have divided the types of adsorption isotherms into the four groups as shown in Figure 5.1. The C-shaped adsorption isotherm (Figure 5.1a) describes a linear increase of OMP adsorption loading with the equilibrium concentration of OMPs in water, which is often used for a narrow range of OMP concentrations or for very low OMP content, i.e., from a few ng L^{-1} to several µg L^{-1} [297]. When the adsorbent has a limited number of adsorption sites, a plateau in the adsorption isotherm appears after a specific equilibrium concentration of OMPs and above, suggesting the saturation of the adsorbent. This results in the L-shaped (Figure 5.1b) and H-shaped (Figure 5.1c) isotherms. The steeper increase of OMP adsorption loading in the H-shaped isotherms compared to the L-shaped ones indicates that the zeolites exhibiting H-shaped isotherms have a higher affinity for OMPs. In some adsorption processes, the isotherms exhibit a characteristic S- shape (Figure 5.1d) [298]. This shape can be attributed to the higher attraction between OMPs at the surface of the adsorbent or to a complexation reaction of the metallic species of OMPs with ligands in water [297–299]. In general, the occurrence of S-shaped isotherms indicates the unfavorable OMP adsorption at low equilibrium concentrations.

Traditionally, the adsorption of OMPs on adsorbents is mostly obtained from batch experiments. It has been observed in several experimental studies that the adsorption of various OMPs from aqueous solutions on high- silica zeolites results in different types of adsorption isotherms. The adsorption of hydroxycinnamic acids, i.e., p-coumaric acid and ferulic acid, on high-silica zeolites were studied by Simon *et al.* [300]. At the equilibrium concentration range of 0 – 1 g L^{-1}, BEA-type zeolite showed H- shaped isotherms, while FAU-type zeolites gave L-shaped isotherms, indicating that BEA zeolites, having smaller pore sizes, have a higher affinity for the hydroxycinnamic acids than FAU-type zeolites. The plateaus in both isotherms have been attributed to the saturation of the micropores of the zeolites with hydroxycinnamic acids. Zhang *et al.* [301] studied 2,4,6 trichlorophenol (TCP) adsorption on FAU-type zeolites. At an equilibrium concentration of 0 – 30 mg L^{-1}, a C-shaped adsorption isotherm was obtained. TCP is an organic compound widely used for the production of industrial products, *e.g.*, fungicide and herbicide. As a result, TCP has been repeatedly reported to occur in water bodies [302–304] as an important OMP. Although the adsorption experiments can be used to design or optimize zeolite-based adsorbents for the removal of OMPs from water, these experiments do not provide any information on the exact

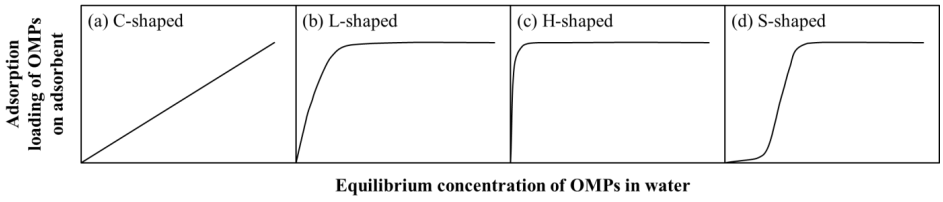

Figure 5.1: The four characteristic types of adsorption isotherms as classified by Giles *et al.* [296]: (a) C-shaped, (b) L-shaped, (c) H-shaped, and (d) S-shaped.

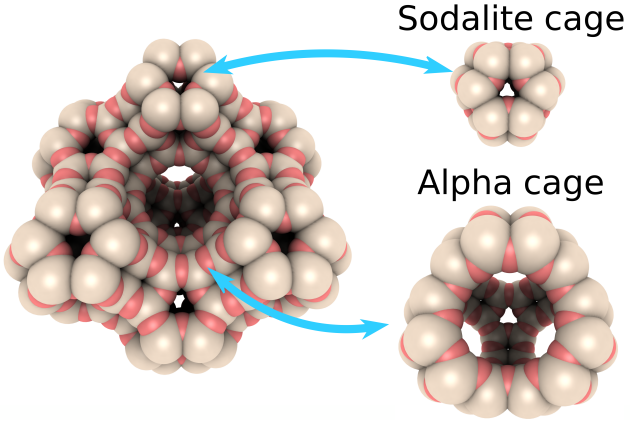

Figure 5.2: The pores in FAU-type zeolites are made of alpha cages and sodalite cages with pore opening diameters 7.4 Å and 2.3 Å, respectively [309, 310].

adsorption mechanisms [305]. To that end, molecular simulation provides the necessary atomistic resolution needed to promote the deeper understanding of the governing physical- chemical mechanisms in adsorption equilibrium, and to further guide adsorption experiments. In this chapter, the adsorption of TCP from water on high-silica FAU-type zeolites is studied by means of both adsorption experiments and MC simulation. FAU-type zeolites were chosen due to their large pore size and amount of micropores, which is shown to have a high adsorption loading for various OMPs [306–308]. The schematic representation of the framework of FAU-type is shown in Figure 5.2.

In batch experiments of TCP adsorption on high-silica FAU-type zeolites, an S-shaped adsorption isotherm was obtained. To the best of our knowledge, this is the first time that an S-shaped isotherm has been reported for the adsorption of OMPs on high-silica zeolites. In this context, MC simulations were carried out to investigate the adsorption mechanisms of the occurring S-shaped isotherm. Moreover, this is also one of the very few MC simulation studies reporting the adsorption of organics from water on high-silica zeolites [311, 312]. To understand the adsorption mechanism, causing

Table 5.1: The physico-chemical characteristics of TCP.

IUPAC name	Chemical formula	Molecular weight / [g mol^{-1}]	Solubility in water / [mg L^{-1}]^{a,c}	Log D at pH = 6^{b,c}
2,4,6-trichlorophenol	$C_6H_3Cl_3O$	197.45	800	3.58

^{a} Estimated by EPIWEB 4.1.
^{b} Estimated by ACD/LABs PhysChem Module (Algorithm Version: 5.0.0.184) [313].
^{c} $T = 298K$

Table 5.2: Information of the high-silica zeolites studied.

Zeolite name^a	Product name	Supplier	Si/Al ratio^b
FAU250	390HUA	Tosoh	250
FAU50	385HUA	Tosoh	50
FAU40	CBV901	Zeolyst	40
FAU30	CBV760	Zeolyst	30

^{a} The names of the zeolites in this chapter were based on the framework type and the Si/Al ratio.
^{b} Si/Al ratio provided by the suppliers.

the S-shaped adsorption isotherm, the experimentally measured and the computed adsorption isotherms were compared qualitatively. The relation between the amount of Al content in FAU-type zeolites and the occurrence of S-shaped isotherms was also discussed.

This chapter is organized as follows: In Section 5.2, the experimental and computational methods for the measurement and computation of the adsorption isotherms are discussed. The experimental work was carried out by Dr. Nan Jiang. In Section 5.3, the experimental and computation results are compared and the adsorption mechanism of TCP is investigated. In Section 5.4, the conclusions of this chapter are summarized.

5.2. MATERIALS AND METHODS

5.2.1. MATERIALS

TCP standards for chromatography analyses were purchased from Sigma- Aldrich, the Netherlands. The basic physico-chemical properties of TCP are listed in Table 5.1.

High-silica zeolite powders of FAU-type framework were provided by suppliers. The names, suppliers and Si/Al ratios of zeolites are listed in Table 5.2.

5.2.2. ADSORPTION EXPERIMENTS

Batch adsorption experiments were conducted in demineralized water. The FAU-type zeolites (30 mg L^{-1}) were dosed in the 100 ml TCP aqueous solution with the TCP concentrations ranging from 0 to 50 µmol L^{-1}. After an equilibrium time of 24h at room temperature (25±1 °C), the zeolites were separated from the TCP solution by membrane filtration (0.2 µm syringe filter, Whatman SPARTANTM). This equilibrium time is expected to be sufficient, as shown by Zhang *et al.* [301], who measured the adsorption of TCP on FAU30.

5.2.3. HIGH PERFORMANCE LIQUID CHROMATOGRAPHY (HPLC) ANALYSIS

The concentration of filtrated TCP solution was determined by HPLC (Shimadzu, Japan) with a C18 column (Phenomenex® KINETEX, 4.6mm) at 30 °. HPLC-grade acetonitrile (Sigma-Aldrich, the Netherlands) and ultra-pure water (Milli-Q ultra-pure water system) were mixed as the mobile phase with a ratio of 65:35 (v:v). The flow rate of the mobile phase was 1.0 ml min^{-1}. The wavelength of the UV detector was set at 280 nm.

5.2.4. MONTE CARLO SIMULATIONS

FORCE FIELDS

The force field parameters for TCP, water and zeolites were taken from the Generalized Amber Force Field (GAFF) [314], Extended Single Point Charge (SPC/E) [315] and Clay Force Field (ClayFF) [316] models, respectively. The choice of these force fields is based on the study by Narasimhan et al. [317] in which it was shown that a similar force field combination was able to reproduce experimental results of the adsorption of paracresol and water onto MFI-type zeolite reasonably well. As discussed earlier, the adsorption isotherms computed from MC simulations were used only to obtain physical insight into the adsorption mechanisms. To this end, no modifications in the force fields or cross interactions parameters between the different species were applied to achieve better agreement with the experimental measurements. Moreover, exhaustive simulations using various other force field combinations was also not the scope of this chapter. All the force field parameters used in this chapter are listed in Tables A.8, A.9, and A.10 of the Appendix.

SIMULATION DETAILS

All MC simulations were carried out using the Cassandra open source software package V1.2 [318]. In the Cassandra software package the chemical potential, which is imposed in the GCMC simulations is shifted with a value containing the isolated molecule partition functions of the molecules which are inserted in the simulation box. To be

able to convert this shifted chemical potential to equilibrium concentration additional simulations are performed. In these simulations the shift in the chemical potential is calculated based on simulations of TCP as an ideal gas in the GC ensemble. To convert the chemical potential to concentration, the excess chemical potential of TCP in water is calculated using the Continuous Fractional Component Monte Carlo (CFCMC) method [89, 274, 292]. The details of the applied method are shown in Section S2 in the Supporting Information of Ref. [1].

Short-range van der Waals interactions were considered by the (12-6) Lennard-Jones potential. For the mixed pair potentials the Lorentz-Berthelot mixing rules [77] were used. Long-range electrostatic interactions were considered by the Ewald summation method [76] with a relative precision of 10^{-5}. For the LJ and electrostatic interactions a cutoff radius of 14 Å with analytic tail correction was applied. In all simulations, 8 unit cells per simulation box (a 2x2x2 supercell) were used and periodic boundary conditions were imposed in all direction. The zeolite framework was considered rigid in all simulations. This approach is often being applied in simulations of nanoporous materials to prevent the necessity of excessive computational efforts [95]. Zeolite frameworks with specified Si/Al ratios were created based on the structures reported by Hriljac *et al.* [281]. The desired Si/Al ratios were achieved by randomly exchanging silicon atoms with aluminum atoms while obeying Löwnestein's rule which states that the Al – O – Al bonds are prohibited in zeolites [281]. The number of sodium atoms were adjusted in accordance to the number of aluminum atoms to ensure the charge-neutrality of the framework. The sodium atoms were fixed at their crystallographic position in order to simplify the simulation scheme. It is important to note that the choice of fixing the sodium or allowing it to move in the zeolite framework may vastly affect the computed adsorption isotherms as shown by Calero *et al.* [98] for alkane adsorption onto FAU-type zeolites. The effect of fixing the sodium ion to the framework has not yet been studied in MC simulations of adsorption from the liquid phase. Thus, further investigation is needed to show the exact magnitude of this effect on the computed adsorption isotherms.

To obtain the adsorption isotherms, Configurational-Bias Monte Carlo (CBMC) simulations in the grand-canonical (μVT) ensemble (GCMC) were performed [76, 77, 90]. The following types of trial moves were used: translations (~12%), rotations (~12%), partial regrowth (~10%) and molecule exchanges with the reservoir (~66%). In all MC simulations, an equilibration period of 5 000 000 MC steps was performed. After the equilibration, production runs of 15 000 000 MC steps were carried out, from which ensemble averages were calculated. The MC simulations were performed for the FAU250, FAU50, FAU40 and FAU30 frameworks. The Si/Al ratios and the number of Al atoms in the framework are listed in Table 5.3. The simulated zeolite frameworks

Table 5.3: The list of the FAU-type zeolite frameworks used in the MC simulations.

Name	Si/Al ratio in simulated box	Number of Al atom in the framework	Number of Super/Sodalite cages
FAU250	255	6	64/64
FAU50	50	30	
FAU40	41	37	
FAU30	30	50	
FAU5	9	156	

cover a wider Si/Al range compared to the batch experiments. The Si/Al in simulations was in the range 5 - 250, while in experiments was in the range 30 - 250.

5.3. RESULTS AND DISCUSSION

5.3.1. TCP ADSORPTION ON FAU-TYPE ZEOLITES: EXPERIMENTAL AND SIMULATION RESULTS

The experimental results of TCP adsorption isotherms on FAU-type zeolites with varying Al content are shown in Figure 5.3. The adsorption isotherms of TCP on FAU250, FAU50 and FAU40 had an S shape, while the adsorption isotherm of FAU30 did not reach a plateau in the experimental concentration range. It is assumed that the observed adsorption isotherm was the beginning stage of S-shaped isotherm and the maximum adsorption loading of TCP on FAU30 will be achieved with the increase of TCP equilibrium concentration. As observed from the adsorption plateaus of S-shaped isotherms, the maximum adsorption loading of TCP on FAU250, FAU50 and FAU40 followed the order FAU250 > FAU50 > FAU40. This indicates that TCP adsorption on FAU-type zeolites, including the TCP loading and the shape of the adsorption isotherms, was driven by the Si/Al ratio of the zeolite. In the studied equilibrium concentration range of 0 – 20 µmol L^{-1} the highest TCP adsorption loading on FAU30 was less than 400 µmol g-1.

In Figure 5.4, the simulated adsorption isotherms of TCP on FAU-type zeolites with varying Al contents are shown. The simulated adsorption isotherms of all five FAU-type zeolites, including FAU5 (which was not tested in batch experiments), were S-shaped. The adsorption loadings of TCP on FAU-type zeolites followed the same order as in the experiments: FAU250 > FAU50 > FAU40 > FAU30 > FAU5. As can be observed in Figure 5.4, the adsorption isotherms for FAU250 and FAU50 computed from MC simulations exhibited almost identical maximum loading to the respective experimentally measured isotherms. By incorporating more Al atoms in the framework, the S-shape of the adsorption isotherms became less pronounced. This is also in line with

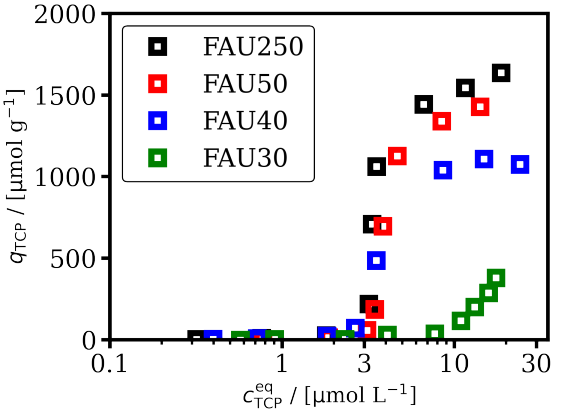

Figure 5.3: The experimentally measured adsorption isotherm of TCP on FAU-type zeolites at T = 298 K.

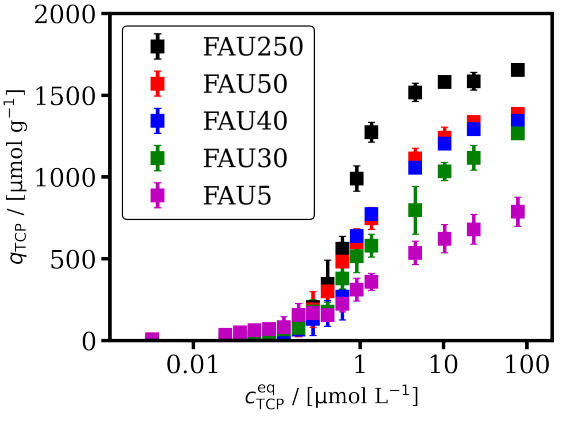

Figure 5.4: The computed adsorption isotherms of TCP on FAU-type zeolites at T = 298 K.

the experimental measurements shown in Figure 5.3, indicating that MC simulations captures the effect of Si/Al ratio on the shape of the adsorption isotherm.

The adsorption loading of TCP on FAU40 was overestimated in the simulation, showing a deviation of ~300 mg g^{-1} from experimental results. The simulated adsorption isotherms of FAU30 zeolites was S-shaped with a maximum TCP loading of ~1200 mg g^{-1} (Figure 5.4), while the adsorption loading of FAU30 obtained from experiments was ~ 400 mg g^{-1}, which is observed from an C-shaped isotherm without adsorption plateau (Figure 5.3). The equilibrium concentration at which the adsorption step occurs in the isotherms computed from MC simulations is not as pronounced as in the experimentally measured ones, and moreover, it seems to deviate quite significantly.

The possible reason for the discrepancies between experiments and MC

simulations is the force fields representing the adsorbent and adsorbates, as well as the fact that sodium ions are fixed in the crystal structure. Since there were no prior MC simulations of the co-adsorption of water and TCP on zeolites, the force fields representing water, TCP and zeolites were chosen based on the study by Narasimhan *et al.* [317], where the adsorption of water and paracresol onto MFI zeolites was studied. As stated earlier, no modification or refitting of the individual force fields was performed here. However, such modifications to improve the accuracy of the simulations, can be realized in several ways: *e.g.*, by optimizing the Lennard-Jones parameters or atomic charges, by explicitly including polarization effects, and by modifying the intermolecular interactions between Al atoms and the adsorbates. Although such modifications may give a better agreement between the simulation and experimental results, their implementation requires significant computational effort which is out of the scope of this chapter.

5.3.2. ADSORPTION MECHANISMS BEHIND THE S-SHAPED ADSORPTION ISOTHERMS

Since the adsorption isotherms for FAU250 computed from MC simulations exhibited almost identical maximum loadings compared to the experimentally measured adsorption isotherms, the MC simulation results of FAU250 were further used to understand the adsorption mechanisms of S-shaped adsorption isotherm. In Figure 5.5, the average number of adsorbed TCP molecules in the alpha cages of FAU250 are plotted as a function of the equilibrium concentration of TCP. The number of adsorbed TCP molecules increased with the increase of TCP equilibrium concentration and the S-shaped curves is observed from Figure 5.5. The S-shaped curves were qualitatively characterized by a division of three stages. At the low coverage range (equilibrium concentration < 0.15 μmol L^{-1}), a minimal amount of TCP molecules (close to 0) were adsorbed on the FAU250 zeolites. There were 0 to 1 TCP molecules adsorbed in the alpha cages. The average number of adsorbed TCPs considerably increased at the transition stage (equilibrium concentration of 0.15 to 10 μmol L^{-1}). At the stage of high coverage (equilibrium concentration > 10 μmol L^{-1}), the maximum number of adsorbed TCP is observed from the plateau.

As shown in Figure 5.5, the S-shaped curves are observed for both alpha cages without Al and alpha cages with Al, while the maximum number of adsorbed TCP in two types of alpha cages varied. An alpha cage provided accommodation to approximately 2 TCP molecules in Al containing cages, and 2.5 TCP molecules in the none-Al containing cage, respectively. In the alpha cages with no Al atom, a maximum of 3 TCP molecules could be adsorbed.

In Figure 5.6, adsorbed TCP and water molecules in an alpha cage without Al are

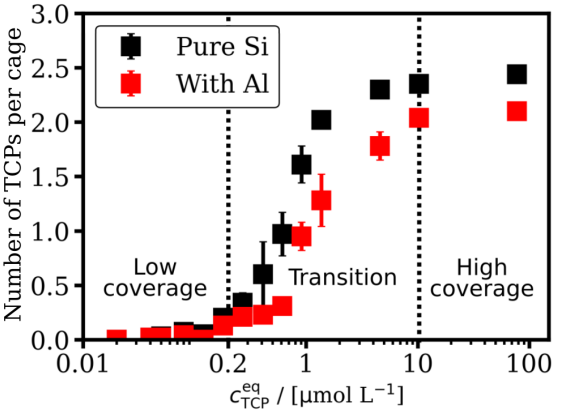

Figure 5.5: The number of adsorbed TCP molecules in the alpha cages of FAU250 zeolite computed from the MC simulations at T = 298 K.

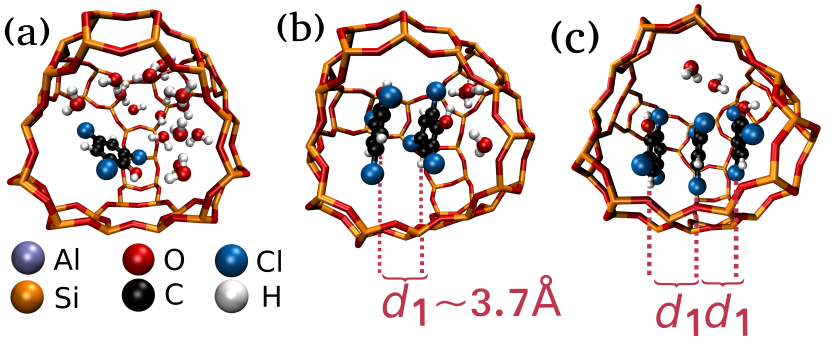

Figure 5.6: The arrangements of TCP and water molecules in the pure Si alpha cages of the FAU250 zeolite: (a) 1 TCP, (b) 2 TCP, (c) 3 TCP molecule(s) per cage at TCP equilibrium concentration equal to (a) 4.6, (b) 77.6 and (c) 77.6 μmol L^{-1}. The characteristic distance between the center of mass of the benzene rings in the TCP molecules is shown as d_1.

shown. When 1 TCP molecule was adsorbed in the alpha cage, TCP preferably excluded the water molecules in between and was arranged close to the wall of the cage (Figure 5.6a). In the alpha cages with 2 or 3 adsorbed TCP molecules, less water molecules were adsorbed and the TCP molecules obtained a parallel configuration, with benzene rings facing each other (Figures 5.6b and 5.6c).

To obtain further information about the structure of adsorbed molecules in the framework, the radial distribution function (RDF) was calculated [76]. The RDF defines the relative probability of finding a particle at distance r from another tagged particle.

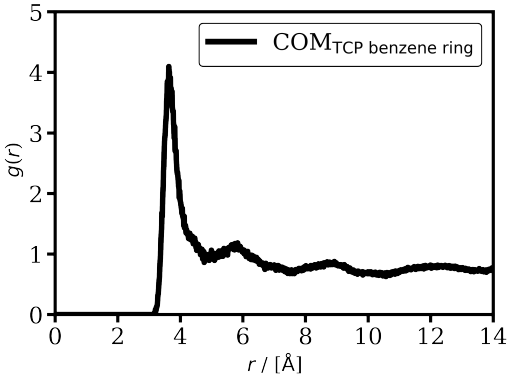

Figure 5.7: Radial distribution function (RDF) for the centers of mass of benzene rings in TCP molecules adsorbed on FAU250 at a TCP equilibrium concentration equal to 77.6 μmol L^{-1}. The characteristic distance between two benzene rings is indicated by the first peak of the RDF around r = 3.7 Å.

In Figure 5.7, the RDF between the center of mass of benzene rings on the FAU250 framework at TCP equilibrium concentration of 77.6 µmol L^{-1} is shown. From Figure 5.7, it is observed that the characteristic distance between two TCP molecules was ~3.7 Å, which is a typical packing distance between π - π stacked aromatic groups (3.4 Å - 3.8 Å). This is in line with literature [319, 320] as TCP molecules in aqueous solutions could experience $\pi - \pi$ interactions, as a form of lateral interactions in the alpha cages. The lateral interaction considerably promoted TCP adsorption at the transition stage (Figure 5.5), and led to the S-shaped adsorption isotherm. This finding is in line with the work of Walton *et al.* [124]. who attributed the steps in the adsorption isotherms for CO_2 on metal-organic frameworks to the sudden clustering of CO_2 molecules in the pores.

π- π interactions can occur between two TCP molecules originating from the unlocalized electrons of the benzene rings. The C – C π electrons of TCP molecules could shift from the center of the benzene ring due to electron donating of hydroxyl groups and electron withdrawing of chlorine atoms to the conjugated π electron. Thus, two TCP molecules could form a π - π interaction with an offset stacked conformation other than a perfect face-to-face alignment, as clearly shown from the simulation snapshots in Figure 5.6. In this conformation, most of the surface of TCP molecules were covered by each other and the π - π interaction between TCP molecules is expected to be strong [321]. Although there is no explicit term to account for the π- π interactions in the force fields used, the use of fixed-point charges can reproduce these interactions [322, 323] as shown by the characteristic distances and orientation of the TCP molecules in Figures 5.6 and 5.7.

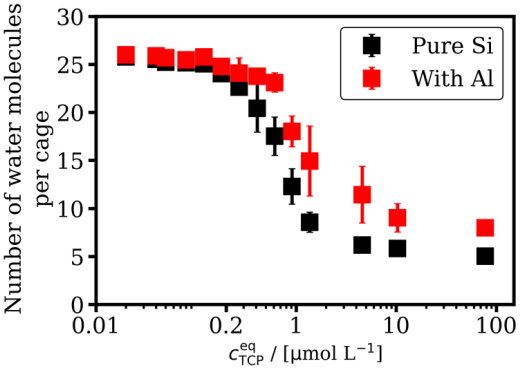

Figure 5.8: Number of adsorbed water molecules in the alpha cages of FAU250 zeolite with and without Al. The black and red color indicate the pure Si and Al containing alpha cages.

5.3.3. EFFECT OF WATER ADSORPTION ON THE OCCURRENCE OF S-SHAPED ADSORPTION ISOTHERMS AND TCP ADSORPTION

In Figure 5.8, the number of adsorbed water molecules in alpha cages of FAU250 is plotted as a function of the equilibrium concentration of TCP. Figure 5.8 shows that the number of water molecules in the alpha cages of FAU250 decreased with equilibrium concentration of TCP. Al-containing cages had a higher number of adsorbed water molecules than the cages without Al. At higher equilibrium concentrations (> 77 µmol L^{-1}), about 8 water molecules per cage were adsorbed in the alpha cages with Al atom, while approximately 5 molecules per cage were adsorbed in the alpha cages without Al atom. Compared to water adsorption in sodalite cages (0 – 3 water molecules per cage, Figure 5.10), more water molecules were adsorbed in alpha cages (8 – 25 water molecules per cage, Figure 5.8). This can be attributed to the much less space inside sodalite cages than alpha cages [309].

The arrangements of the adsorbed water and TCP molecules in the Al- containing alpha cages are shown in Figure 5.9. The distance between hydrogen atoms from water and the oxygen atoms of zeolites, which are connected to Al atom, was computed to be 1.7 Å. In the Al-containing alpha cages with one TCP molecule adsorbed, a total number of 19 water molecules were adsorbed (Figure 5.9a), while 10 water molecules were adsorbed in the alpha cages with 2 adsorbed TCP molecules (Figure 5.9b). In the non Al-containing alpha cages, however, 14 water molecules were co-adsorbed along with one TCP molecule, and 3 water molecules were co-adsorbed along with two TCP molecules (Figure 5.6). This is in line with the results presented in Figure 5.9, where it is shown that more water molecules were adsorbed in the alpha cages with Al. The Al-containing alpha cages with 3 adsorbed TCP molecules were not found in the simulation box, since water molecules hinder the TCP adsorption due to the limited space

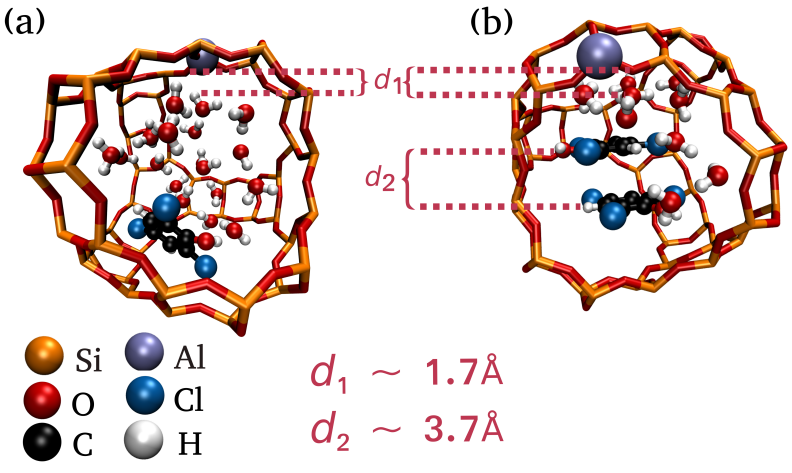

Figure 5.9: The arrangements of TCP and water molecules in Al containing alpha cages of the FAU250 zeolite. (a) 1 TCP molecule per cage at the equilibrium concentration equal to 4.6 µmol L^{-1} (b) 2 TCP molecules per cage at the equilibrium concentration equal to 77.6 μmol L^{-1}.

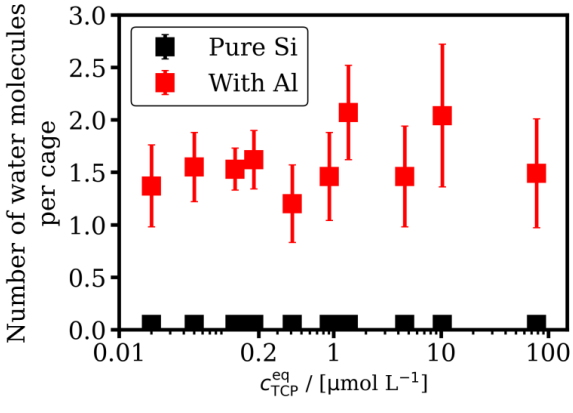

Figure 5.10: Number of adsorbed water molecules in the pure Si and Al containing sodalite cages of the FAU250 zeolite. The black and red colors indicate the pure Si and Al containing sodalite cages.

in the alpha cages.

In Figure 5.10, the number of adsorbed water molecules in sodalite cages of FAU250 zeolites is shown as a function of the equilibrium concentration of TCP. It can be observed that the adsorption of water in the sodalite cages is not affected by the equilibrium concentration of TCP. The sodalite cages with Al atom had an average number of approximately 1.5 water molecules per cage with a variation from 1 to 2 water molecules per cage, while the sodalite cages without Al atom exhibited almost no ability for water adsorption.

The RDF between the hydrogen atom from water and the oxygen atom connected

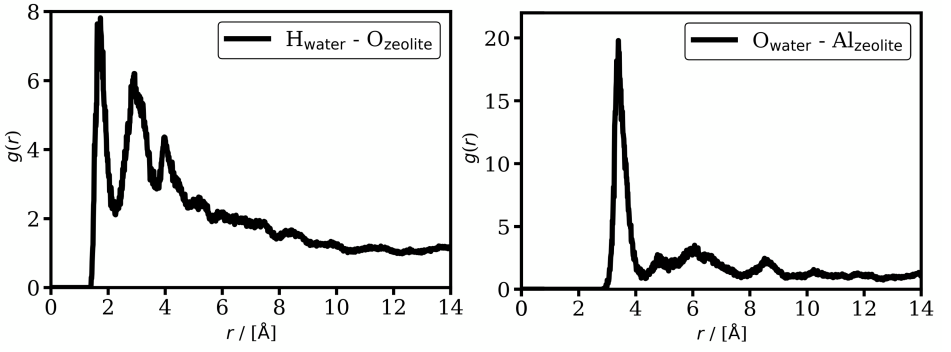

Figure 5.11: Radial distribution function (RDF) for (a) the H atoms of water with the O atoms connected to Al in the FAU250 zeolite; (b) the O atom of water with Al atoms of the FAU250 zeolite at TCP equilibrium concentration equal to 77.6 μmol L^{-1}.

to Al atom of FAU250 zeolites was calculated to determine the structure of adsorbed water molecules on FAU250 zeolite. As shown in Figure 5.11a, one peak is observed at the distance of 1.7 Å, which is the typical H-bond length [324]. Thus, we can safely conclude that water molecules were being adsorbed on FAU-type zeolites by forming H-bonds with the framework. Narasimhan *et al.* [312] indicated that the existence of water clusters could weaken the interaction of water molecules with zeolites, as well as the interaction of OMPs with zeolites, which, however, would strengthen the interactions between OMPs and water. The two wide peaks at distances of 2.9 Å and 4.0 Å shown in Figure 5.11a, indicate that water molecules which do not form H- bonds with the FAU-type zeolite formed water clusters.

As shown in Figure 5.11b, the RDF between the O atom of the adsorbed water molecules and Al atom of the zeolite framework has a strong peak at distance of approximately 3.4 Å. Bolis *et al.* [325] suggested that water molecules were adsorbed on zeolites by interacting with the –Si-O-Si- groups of zeolites. The distance of 3.4 Å between Al atom of zeolites and water molecules, shown in Figure 5.11b, clearly indicate that there was an additional driving force for water adsorption on the alpha cages (Figure 5.8) and sodalite cages (Figure 5.10) of the FAU-type zeolite. The additional driving forces from Al atoms might cause an extra number of water molecules to be adsorbed in the alpha cages (Figure 5.8) and sodalite cages (Figure 5.10). Due to the additional water adsorption on Al atom, FAU-type zeolite with higher Al content (lower Si/Al ratio) had a lower TCP adsorption loading and less pronounced S- shaped adsorption isotherms (Figures 5.3 and 5.4). Zhang *et al.* [301] studied TCP adsorption on FAU-type zeolites with Si/Al ratio 30 and observed no plateau from the adsorption isotherm, which confirms the finding in the present chapter.

The alpha cages of FAU-type zeolites with large pore opening and inner sizes pro-

vided the basic conditions for the accommodation of multiple TCP molecules and their lateral interaction in the presence of water molecules, which was crucial for the occurrence of the S-shaped adsorption isotherms. In the zeolite frameworks with channels, the adsorbed OMPs preferred to be located in the channels and channel intersections, whereas water molecules preferably adsorbed in the vicinity of the OMP molecules [311, 326, 327]. Due to the hindering of water molecules, the lateral interaction of adsorbed OMP molecules would be negligible. Therefore, the S-shaped adsorption isotherm was not observed in previous literature, which studied OMP adsorption on zeolites frameworks with channels, *e.g.* BEA- and MFI-type zeolites [328–330].

5.4. CONCLUSIONS

In batch adsorption experiments of TCP in high-silica FAU-type zeolites, S-shaped adsorption isotherms were observed. To the best of our knowledge, this the first time that an S-shaped adsorption isotherm has been reported for the adsorption of OMPs on high-silica zeolites. In this chapter, MC simulations were used to explain the mechanism of S- shaped adsorption isotherms of TCP adsorption on high-silica FAU-type zeolites. It was shown that the occurrence of S-shaped adsorption isotherms can be attributed to the lateral interactions of TCP, *e.g.*, the π- π interactions. The alpha cages of FAU-type zeolites provided a possible accommodation for multiple TCP molecules as a potential condition of lateral interactions of TCP. Water molecules were adsorbed in the sodalite cages and alpha cages of FAU-type zeolites by forming H-bonds with the framework of zeolites. Compared to the non-Al containing alpha cages, more water molecules were stably adsorbed as water clusters in the alpha cages of FAU-type zeolites with high Al content. An additional amount of adsorbed water molecules in Al-containing alpha cages could inhibit TCP adsorption and could prevent the occurrence of an S-shaped adsorption isotherm. FAU-type zeolites with higher Si/Al ratio, therefore, have evident S-shaped adsorption isotherms, and, meanwhile, achieved higher TCP adsorption loadings compared to FAU-type zeolites with lower Si/Al ratios. MC simulation has shown to be a powerful tool to study the adsorption of OMPs in water, thereby supporting experimental results. Performing MC simulation will further allow investigating the adsorption mechanisms of OMP adsorption from the view of molecular interaction between OMPs, OMP and adsorbents as well as water and adsorbents. The unfavourable adsorption of OMPs have been widely observed for OMP adsorption on solid adsorbents. The low adsorption capacity would be followed by a steep increase of OMP adsorption capacity at a certain equilibrium concentration, showing the typical feature of S-shaped isotherms. This chapter suggests that the increase in the OMP adsorption capacity was caused by the interaction between OMPs. Except for the π- π interactions between TCP molecules in this chapter, various types

of OMP interactions such as formation of hydrogen bonds, ionic interactions, formation of host-guest systems *etc.* might exist as driving forces for OMP adsorption, since the physicochemical properties of OMPs also vary.

6

INCLUSION COMPLEXATION OF ORGANIC MICROPOLLUTANTS WITH β-CYCLODEXTRIN

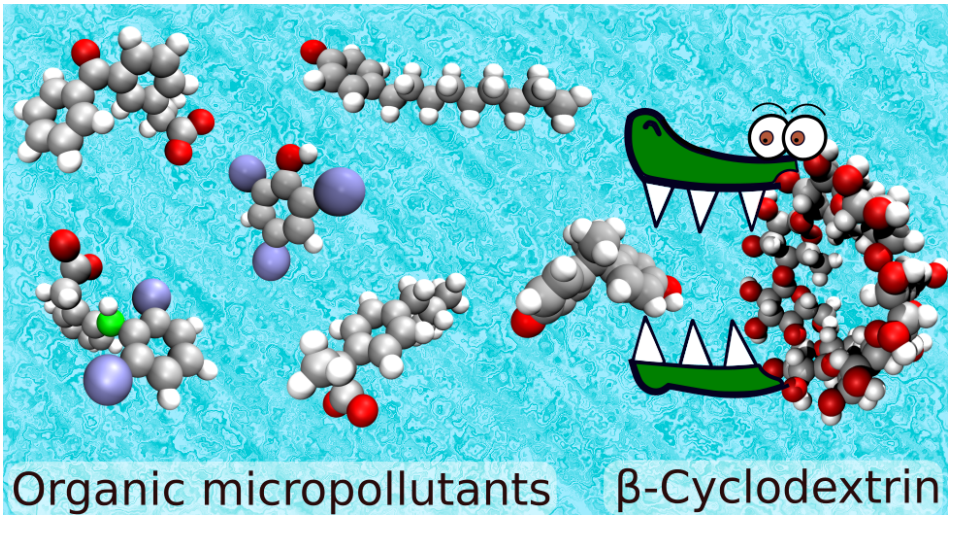

This chapter is based on the following publication: M. Erdős, R. Hartkamp, T. J. H. Vlugt, and O. A. Moultos, Inclusion complexation of organic micropollutants with β-cyclodextrin, *Journal of Physical Chemistry B* **124**, 1218 (2020).

6.1. INTRODUCTION

Industrial, agricultural, and domestic activities give rise, directly or indirectly, to water contamination with a wide variety of harmful organic compounds [331]. Thousands of organic micropollutants (OMPs) of different origin and type, *e.g.* industrial chemicals, pesticides, pharmaceuticals, personal-care products, human hormones, detergents, as well as their transformation products, are ubiquitously detected in surface and ground waters [332–338]. Despite their relatively low concentration, ranging from a few picograms to several micrograms per liter, many of those OMPs raise to significant environmental and toxicological concerns [339, 340]. Due to the large physicochemical diversity of OMPs, and their low concentrations, conventional water and wastewater treatment processes (*e.g.*, coagulation, flocculation, sedimentation, sand filtration) achieve a poor removal efficiency, essentially allowing many harmful OMPs to survive and find their way into the urban water cycle [341–345]. Several techniques for the efficient removal of OMPs have been developed, including oxidation, catalytic degradation, membrane filtration, and adsorption [346–351]. Adsorption based technologies are considered promising due to their simplicity, low operational cost and versatility through adsorbent selection. To this end, novel porous materials that can be tailor-designed have emerged as promising candidates for water treatment [352].

Porous polymer adsorbents exhibit distinct advantages compared to zeolites, silica and activated carbons, such as high surface area, long-term physicochemical stability in water, low weight, mechanical flexibility, cost-efficiency, good selectivity, fast adsorption kinetics, large capacity, and easy preparation and regeneration [353–358]. The numerous available molecular building blocks [356] of porous polymers allows for the synthesis of a wide variety of adsorbents, having diverse structures and functions.

One promising building block is β-Cyclodextrin (βCD). In recent years, βCD based polymers with enhanced adsorption kinetics, high removal capacity of OMPs and uptake rates have been synthesized [359–363]. These polymers can capture a wide variety of OMPs, even at trace concentrations, via various mechanisms such as inclusion complexation, hydrogen bonding, electrostatic and hydrophobic interactions [363, 364]. As it is far from trivial to determine the contribution of each mechanism only based on experimental measurements, the exact physical-chemistry via which the polymer captures the various types OMPs (*e.g.*, polar, non-polar) is still not completely understood [364]. Previous studies have suggested that the inclusion complex formation of OMPs with the βCD building blocks of the polymer is one of the major mechanism for capturing the OMPs [364].

Recently, computational studies testing various force field combinations for the inclusion complexation of different guest molecules with β-CD have been reported

[365–367]. Henriksen and Gilson [365] computed the binding free energies and binding enthalpies of 21 guest molecules with β-CD using four different water models and two charge derivation methods, and compared with the available experiments. Molecules with three types of functional groups (i.e., ammoniums, alcohols, carboxylates) attached to linear, aliphatic scaffolds, and phenyl groups were studied. It was shown that the combination of the AM1-BCC/q4md-CD force field [368, 369] for the host, the AM1-BCC/GAFF force field for the guest [314, 368], and TIP3P [294] for water produced the lowest deviation from experimental binding free energies, having a root mean square error (RMSE) = 3.35 kJ mol^{-1}. This force field combination, however, yielded a poor prediction of the binding enthalpy, deviating from experimental measurements by approximately a factor of 2. In the same study, significant variations in the computed free energies and enthalpies were obtained by using the q4md-CD (host) [369], RESP/GAFF (guest) [314] and different water force fields (i.e., TIP3P [294], TIP4Pew [295] and SPC [315]).

Tang and Chang [366] reported computations of the binding free energy, binding enthalpy and binding entropy of three aliphatic alcohols, methyl-butyrate, aspirin, 1-naphthyl-ethanol and 2-naphthyl-ethanol with β-CD. Two different force fields, i.e., GAFF [314] and q4md-CD [369], were used for the host (β-CD), while the RESP/GAFF [314] force field was used for the guest, and the TIP3P for water. It was shown that the calculated binding free energies are in a reasonable quantitative agreement with the respective experiments, having RMSE= 1.5 – 1.6 kcal mol^{-1}. Based on the these results, it is evident that no available force field combination is able to reproduce both the experimental binding free energies and binding enthalpies within the error of the experimental measurements for a wide variety of molecule types. More discussion on the inclusion complexation of CDs with guest molecules for food, pharmaceutical and separation technology applications can be found in the relevant literature *e.g.*, anthracene [370], isoflavones [371–373], octyl glycoside [374], ionic liquids [375], chalcone [376], glycyrrhizic acid [377]. Some studies focus on the investigation of inclusion complex formation of widely used drug molecules (*e.g.* ketoprofen [378, 379], ibuprofen [378, 380, 381], lidocaine [382], naproxen [378]) with β-CD. To the best of our knowledge, there is no comprehensive study on the inclusion complex formation of OMPs with β-CD, although this mechanism is one of the most important for the capturing capability of β-CD polymers [360, 364].

In this chapter, a representative set of OMPs is selected based on the measured occurrences of the compound in surface and ground waters [336, 338], and the directives by the European Union (EU) [383, 384]. The priority substance list, i.e., directives 2000/60/EC and 2008/105/EC, which contains substances presenting a significant risk to the environment [383], and the surface water Watch List [384], which contains sub-

stances posing possible health risks, were considered. The selected compounds are listed in Figure 6.1a. Bisphenol A (BPA) is an endocrine disruptor frequently detected in waters. Due to BPA's potential risk for public health it also appears on the priority substance list published by the EU [384]. Diclofenac is a non-steroidal anti-inflammatory drug which is listed as an emerging contaminant by the EU Watch list [383]. 4-nonylphenol (NP) is an endocrine disruptor which is detected at high concentration in the aquatic environment and listed on the priority substance list published by the EU [384]. 2,4,6-trichlorophenol (TCP) is a compound used as a pesticide and wood preservative. TCP is frequently detected in the aquatic environment and listed as carcinogen [385]. Ibuprofen and ketoprofen are non-steroidal anti-inflammatory drugs which are frequently detected in surface and ground waters [336, 338] due to their widespread use.

The purpose of this chapter is to provide the necessary physical insight into the inclusion complexation of β-CD with OMPs by performing MD simulations with the well-established Attach-Pull-Release method of Henriksen *et al.* [386]. To characterize the inclusion complex formation, the binding free energy, binding enthalpy and the average number of hydrogen bonds between the β-CD, OMPs and water are calculated. The binding enthalpy is further decomposed into several contributions, i.e., intramolecular, Lennard-Jones and electrostatic. The choice of force fields used in this chapter was based on the work by Henriksen and Gilson [365] and Yin *et al.* [367] where the inclusion complexation of β-CD with a wide and diverse range of guest molecules has been studied. The obtained binding free energies for all studied OMPs are in a reasonable agreement with the experimental results. Two different binding orientations, shown in Figure 6.1b, are discussed. It is shown that based on the obtained results, the contribution of the different interactions can be established and differences in binding strength can be explained. The remainder of this chapter is structured as follows. In Section 6.2, the details about the calculation of the binding free energy and enthalpy are explained. In Section 6.3, the results of the binding free energy, enthalpy and entropy calculations are presented and discussed for all OMPs.

6.2. SIMULATION METHODOLOGY AND COMPUTATIONAL DETAILS

All simulations were carried out using the GROMACS2018.2 software package [387]. The bonded and non-bonded force field parameters of β-CD, OMPs, sodium and chloride were taken from the q4md-CD [369], General AMBER (GAFF) [314] and Joung-Cheatham force fields [388], respectively. For the representation of water, two models were used: the TIP3P [294] and Bind3P [367]. Bind3P is a water force field, developed recently by Yin *et al.* [367], who refitted the Lennard-Jones size and energy pa-

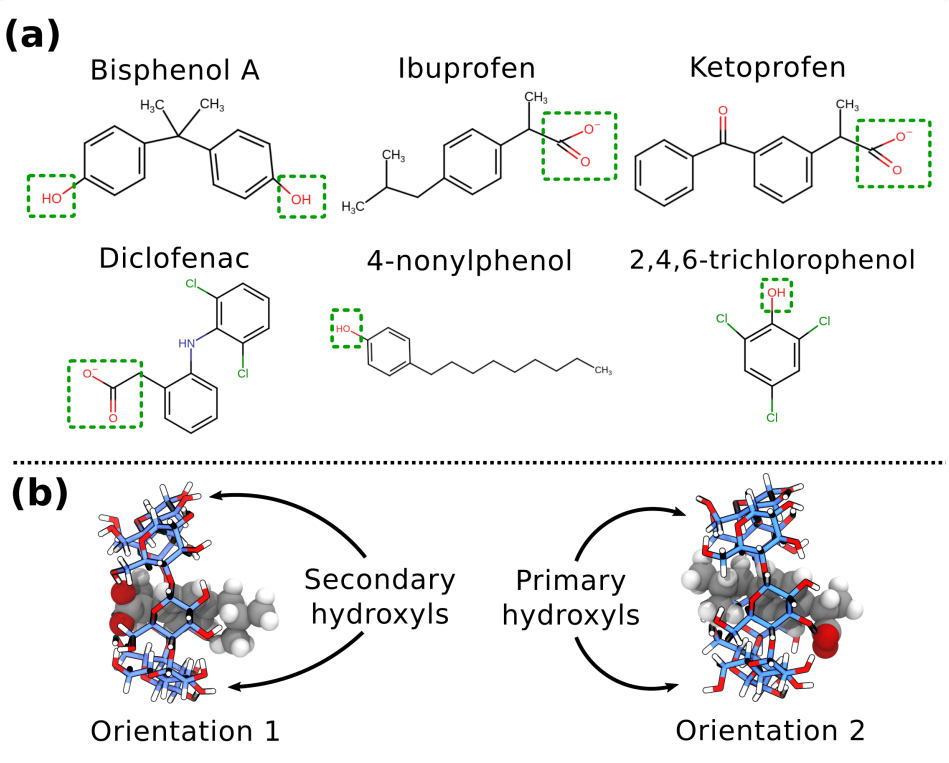

Figure 6.1: (a) The organic micopollutants (OMPs) studied in this work, and (b) schematic illustrations of the different binding orientations. The main functional group of each molecule is indicated by a green rectangle. The orientations are defined based on the position of the main functional group. Orientation 1 refers to the binding orientation in which the main functional group of the molecule is near the primary hydroxyl groups (small rim) of cyclodextrin. Orientation 2 refers to the binding orientation in which the main functional group of the molecule is near the secondary hydroxyl groups (large rim) of cyclodextrin.

rameters of the TIP3P force field to better match the experimental host-guest binding data [367]. In this chapter, the Bind3P water model is used because it is specifically fitted to reproduce experimental host-guest data. Simulations with the TIP3P water model are also performed since this model is widely used along with GAFF. The partial charges of β-CD, water, sodium and chloride are taken from the original publications [294, 367, 369, 388]. The partial charges for all OMPs were computed with Restrained Electrostatic Potential (RESP) at the 6-31G* level of theory, using the R.E.D III.52 script [389] with the Gaussian09 RevB.01 software package [390]. GROMACS parameter files containing all force field parameters are provided in the Supporting Information of Ref. [391]. The nonbonded interactions were truncated at 9.0 Å and analytic tail corrections are applied in the computation of the energies and pressures. The long range elec-

trostatic interactions are taken into account by using the Particle-Mesh Ewald (PME) method [392]. The stochastic leap-frog algorithm is used to integrate the equation of motion with a timestep of 2 fs. The scheme followed in all simulations is as follows: Initially, the energy of the system is minimized using the steepest descent method. Consequently, equilibration runs were performed for (i) 50 ps in the NVT ensemble at a temperature of 50 K, (ii) 1 ns in the NVT ensemble with a temperature ramping from 50 K to 300 K, and (iii) 2 ns in the NPT ensemble at 300 K and 1 bar. The production runs were carried out in the NPT ensemble at the same temperature and pressure, regulated using the Langevin thermostat [393] and Berendsen barostat [394].

To calculate the binding free energy of the selected OMPs with β-CD, the Attach-Pull-Release (APR) method [386] was used. A detailed description of the APR method can be found in the study reported by Henriksen *et al.* [386]. The binding enthalpies of the OMPs with β-CD was calculated with the solvent-balance method [395]. The errors in the binding free energies are calculated by the used built-in GROMACS tools [387]. The errors in the binding enthalpies are calculated with the block average method [396]. The details on the implementation of the APR and the solvent-balance method are reported in Sections A.1 and A.2 of the Appendix.

It is important to note that several orientations of the OMPs can contribute to the binding free energy and enthalpy with β-CD [365, 386]. In experiments, these binding orientations occur naturally, and therefore the measurements of the binding free energies and enthalpies do not explicitly distinguish between the different orientations. In this chapter, the combined binding free energies and enthalpies for two different binding orientations are calculated for all OMPs. The orientations are shown in Figure 6.1b. The approach for calculating the combined binding free energies and enthalpies are presented in Section A.3 of the Appendix. In experimental studies, the binding constant, K_a, or the dissociation constant, $K_d = 1/K_a$, of the host-guest complex is reported. The binding constant is a special type of equilibrium constant which is related to the concentration of the complex, the free host and the free guest in the solution [397]. To compare experimental and simulation results, the binding free energy of the guest can be calculated from the binding/dissociation constant (K_d in units of mol/L) using [398]:

$$\Delta G_{\text{combined}} = RT \ln \frac{K_d}{c^\circ} \tag{6.1}$$

where $\Delta G_{\text{combined}}$ is the combined free energy of the different orientations, R is the universal gas constant, T is temperature, and c° is the standard reference concentration ($c^\circ = 1$ mol/L).

6.3. RESULTS AND DISCUSSION

6.3.1. BINDING FREE ENERGY

In Figure 6.2, the experimentally measured and the computed binding free energies of the OMPs with β-CD using the q4md-CD/GAFF/TIP3P and q4md-CD/GAFF/Bind3P force field combinations are shown. It can be observed that the experimentally measured binding free energies for specific OMPs varies between studies. This may be due to the different experimental conditions or measurement techniques applied in these studies. In Figure 6.2, three sets of experimental results are presented for the binding free energy of ketoprofen with β-CD. In the study reported by Waters *et al.* [399], the binding free energy was measured by isothermal titration calorimetry (ITC). In the studies by Felton *et al.* [378] and Rozou *et al.* [400] phase solubility measurements were performed. It can be seen that despite using the same measurement technique the reported binding free energies by Felton *et al.* and Rozou *et al.* differ by c.a. 2.5 kJ mol^{-1}. The most probable cause of this discrepancy is that in the measurements of Felton *et al.* [378], no buffer is applied to keep the pH of the solution constant, while in the study by Rozou *et al.* [400] a phosphate buffer is applied. It has been shown that due to the competition of the ions and guest molecules for the cavity, the type and concentration of the applied buffer affects the binding affinity of guest molecules with β-CD [401, 402] and other host molecules (*e.g.*, curcurbit[7]uril, octa-acid) [403]. The measurements by Waters *et al.* [399] and Rozou *et al.* [400] are at the same conditions (*e.g.*, type of buffer, temperature), but use different measurement techniques. Thus, the discrepancy between the reported experimental studies may be attributed to the different techniques. To quantitatively compare the binding affinity of different guest molecules with β-CD, experiments at the same conditions and using the same technique should be carried out. To the best of our knowledge, a systematic study reporting the experimentally measured binding free energies of all selected OMPs with β-CD is lacking.

The binding free energy measurements by Pellegrino Vidal *et al.* [404] are shown in Figure 6.2. It can be seen that BPA forms a more stable complex with β-CD than NP ($\Delta G_{\text{binding}}$ is equal to -27.68 kJ mol^{-1} and -22.13 kJ mol^{-1}, respectively). Our calculations of the binding free energies predict the same trend of binding affinity for these molecules. Interestingly, the experimentally measured binding free energy of BPA with the β-CD based polymer reported by Alsbaiee *et al.* [360], $\Delta G_{\text{binding}}$=-27.26 kJ mol^{-1}, is very close to the calculated binding free energy of BPA with just the β-CD using the Bind3P water model, $\Delta G_{\text{binding}}$=-28.63 kJ mol^{-1}. The computed value is almost identical with the experimentally reported binding free energy of BPA with β-CD ($\Delta G_{\text{binding}}$=-27.68 kJ mol^{-1}) [404]. Mironov *et al.* [405] reported the binding free energy of diclofenac and ibuprofen, measured both by affinity capillary electrophoresis

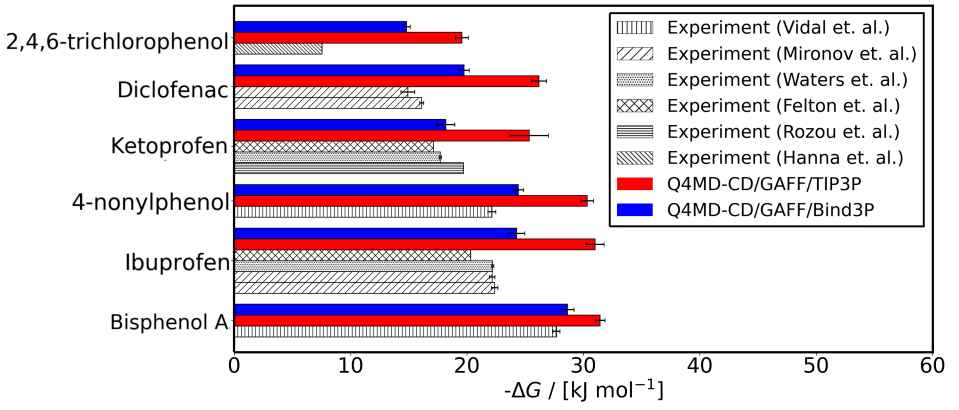

Figure 6.2: Computed and experimentally measured binding free energies of bisphenol A, ibuprofen, 4-nonylphenol, ketoprofen, diclofenac and 2,4,6-trichlorophenol (TCP) molecules with β-CD. The columns in red and blue represent the calculated binding free energies using the q4md-CD/GAFF/TIP3P [294, 314, 369] and q4md-CD/GAFF/Bind3P [314, 367, 369] force field combinations, respectively. The columns with the black-and-white patterns represent the experimental data which is taken from the following sources: Pellegrino Vidal *et al.* [404], Mironov *et al.* [405], Waters *et al.* [399], Felton *et al.* [378], Rozou *et al.* [400], and Hanna *et al.* [406].

coupled with mass spectrometry (CE-MS) and with UV detection (CE-UV) techniques. Both experimental techniques predict that ibuprofen has a more negative binding free energy than diclofenac. This indicates that ibuprofen forms a more stable inclusion complex with β-CD than diclofenac. The same trend is observed from the MD calculations using both water force fields. The experimental measurements by Felton *et al.* [378] and Waters *et al.* [399] for ketoprofen and ibuprofen, are also shown also in Figure 6.2. In both studies it was found that ibuprofen has a more negative binding free energy with β-CD than ketoprofen, indicating that ibuprofen forms a more stable inclusion complex than ketoprofen. Our MD simulations are in-line with these experimental findings. It is important to note here that since the experiments are performed at different conditions and with varying techniques, an exact quantitative comparison of the computed and experimentally measured binding free energies cannot be carried out for the selected OMPs. From the qualitative point of view, the computed binding free energies, using both TIP3P and Bind3P water force fields, follow the trend of the experiments, i.e., MD simulations can predict which OMPs form more stable inclusion complexes with β-CD. The calculated binding free energies of all OMPs using the Bind3P water force field show a slight overestimation compared to the corresponding experimental value but are still in a reasonable agreement, having RMSE= 3.5 kJ mol^{-1}, which corresponds to a deviation of 24%. Consistently, with the findings by Henriksen and Gilson [365], our MD results for the binding free energies using the TIP3P water force field considerably overestimate the experimental measurements by ca. 59%.

6.3.2. BINDING ENTHALPY

The computed binding enthalpies of the OMPs with β-CD are shown in Figure 6.3, along with the respective experimental results obtained from the literature [399, 400, 406–409]. Available experimental binding enthalpies for the selected compounds are more scarce compared to binding free energies. Experimentally measured binding enthalpies for NP and TCP with β-CD are not available in the literature. The only available binding enthalpies of ketoprofen and ibuprofen are from the study by Waters *et al.* [399], who performed measurements using ITC [399]. In Figure 6.3, both the experimental and MD results show that the binding of ketoprofen ($\Delta H^{\text{ketoprofen}}_{\text{Bind3P}}$=-27.22 kJ mol^{-1}, $\Delta H^{\text{ketoprofen}}_{\text{TIP3P}}$=-32.98 kJ mol^{-1}, $\Delta H^{\text{ketoprofen}}_{\text{Experiment}}$=-16.00 kJ mol^{-1}) is more exothermic than the binding of ibuprofen ($\Delta H^{\text{ibuprofen}}_{\text{Bind3P}}$=-25.28 kJ mol^{-1}, $\Delta H^{\text{ibuprofen}}_{\text{TIP3P}}$=-30.10 kJ mol^{-1}, $\Delta H^{\text{ibuprofen}}_{\text{Experiment}}$=-14.60 kJ mol^{-1}). Similarly to the binding free energy results, the computed binding enthalpies follow the trend of the experimental measurements, which is $\Delta H^{\text{BisphenolA}} < \Delta H^{\text{Ketoprofen}} < \Delta H^{\text{Diclofenac}} \sim \Delta H^{\text{Ibuprofen}} < \Delta H^{4-\text{Nonylphenol}} < \Delta H^{2,4,6-\text{Trichlorophenol}}$. As can be seen in Figure 6.3, the computed binding enthalpies using the Bind3P water force field are systematically closer to the experiments compared to simulations using TIP3P. This finding is in agreement with Yin *et al.* [367], who performed binding free energy and enthalpy computations using TIP3P and Bind3P force fields for 21 β-CD-guest pairs. Based on our comparison of the experimental and computed binding free energies and enthalpies it can be concluded that MD simulation techniques have the potential to predict the binding affinity of OMPs with β-CD. The quantitative predictive power of the method is expected to improve even more with the development of improved force fields, which can be developed considering also the binding thermodynamics data [365].

To obtain a better understanding of the binding mechanism, the contribution of different interactions is investigated. The binding enthalpy is decomposed to three contributions: (1) intramolecular (bonded, intramolecular LJ and electrostatic interactions), (2) intermolecular Lennard-Jones, and (3) intermolecular electrostatic interactions. In Figure 6.4, the decomposition of the computed enthalpies using the Bind3P water force field is shown for all studied OMPs. Computations considering both binding orientations are shown (representations of the two orientations are shown in Figure 6.1b). As can be seen in Figure 6.4, for all OMPs studied and for both binding orientations, the Lennard-Jones and electrostatic contributions are negative, which means that these interactions are favorable for the inclusion complex formation. The binding is hindered by the intramolecular interactions (positive energy) for almost all OMPs, except for ketoprofen. The main opposing terms in the intramolecular contribution are the 1-4 interactions, which mainly originate from the conformational change of the host upon binding. For the case of orientation 1 of ketoprofen, the 1-4 electrostatic

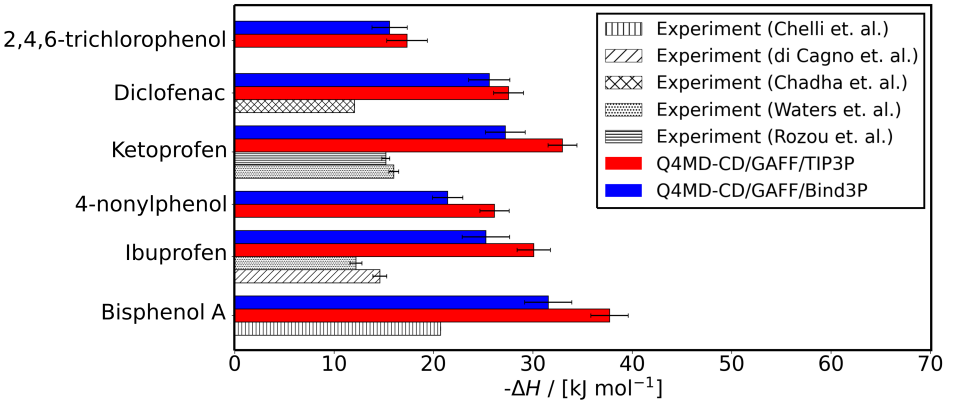

Figure 6.3: Computed and experimentally measured binding enthalpies of bisphenol A, ibuprofen, 4-nonylphenol, ketoprofen, diclofenac and 2,4,6-trichlorophenol (TCP) molecules with β-CD. The columns in red and blue represent the calculated binding enthalpies using the q4md-CD/GAFF/TIP3P [294, 314, 369] and q4md-CD/GAFF/Bind3P [314, 367, 369] force field combinations, respectively. The columns with black-and-white patterns represent the experimental data which is taken from from the following sources: Chelli *et al.* [407], di Cagno *et al.* [408], Chadha *et al.* [409], Waters *et al.* [399], and Rozou *et al.* [400].

term becomes favorable and results in a negative intramolecular contribution to the binding.

To further investigate the role of the different intramolecular contributions, the position of the carboxyl oxygens relative to the primary and secondary rim of the β-CD is investigated for both orientations of ibuprofen and ketoprofen (Figure 6.5). In Figure 6.5c-f, the distances of the carboxylic oxygens from the center of mass of the primary or secondary oxygens of β-CD are shown for both orientations of ibuprofen and ketoprofen. In orientation 1, the carboxyl group of ketoprofen shows a preference for a tighter binding to the primary rim of β-CD than ibuprofen (Figure 6.5c). The tighter binding of the carboxyl oxygen at the narrower rim provides the possibility for the oxo group to form hydrogen bonds with the oxygen atoms at the wider rim of the β-CD (see Figure 6.5c-d). In orientation 2, the carboxyl oxygen of ketoprofen shows a slight preference compared to ibuprofen towards the solvent which brings the oxo group closer to the oxygens of the wider rim of β-CD (Figure 6.5e-f). The binding configuration of ketoprofen results in favorable host configurations most probably due to the stabilizing effects of the hydrogen bonds between the host and guest molecules. The stabilizing effects of the hydrogen bonds formed between ketoprofen and β-CD are also discussed in the study reported by Guzzo *et al.* [379]. In that study, the inclusion complexation of ketoprofen with β-CD is investigated both by performing Nuclear Magnetic Resonance (NMR) measurements and MD simulations.

Although the contributions from Lennard-Jones and electrostatic interactions are favorable for the binding of all studied guest molecules, the relative magnitude of the

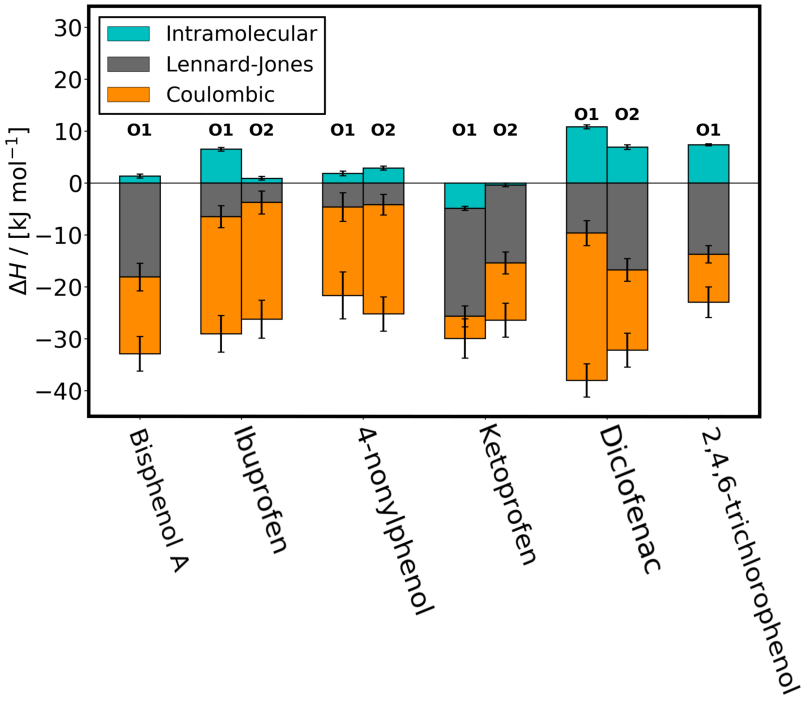

Figure 6.4: The computed enthalpy decomposition of the binding orientations for bisphenol A, ibuprofen, 4-nonylphenol, ketoprofen, diclofenac and 2,4,6-trichlorophenol (TCP) molecules with β-CD. The O1 and O2 labels indicate orientations 1 and 2, respectively. The intramolecular (bonded, 1-4 LJ and 1-4 Coulomb terms) is shown in cyan, the Lennard-Jones contribution in gray, and the electrostatics contribution in orange. The bars representing the contributions of the different interaction types are stacked on each other.

two contributions can differ regardless of the polarity or the protonation state of the OMP. The binding enthalpy can be decomposed into two terms, namely, the host-guest and the desolvation. The host-guest term accounts for the intermolecular host-guest interactions and for the change of enthalpy due to conformational changes of the host and guest upon binding. The desolvation term represents the effects due to the binding of the guest molecule. This term comprises of the interaction change between host-water, guest-water and water-water upon binding. In Figure 6.6, the decomposed enthalpies into the host-guest and desolvation terms, for orientation 1 and 2 are shown for all studied OMPs. Since all desolvation terms are positive (i.e, inclusion complexation is hindered) and all host-guest terms are negative (inclusion complexation is favored), the negative value of the desolvation term ($-\Delta H_{\text{desolvation}}$) is shown in Figure 6.6 to make the comparison to the host-guest term more representative. For orientation 1, the LJ interactions are the dominant contribution to the host-guest term for all OMPs except for ketoprofen. The LJ contribution scales with the number of atoms contribut-

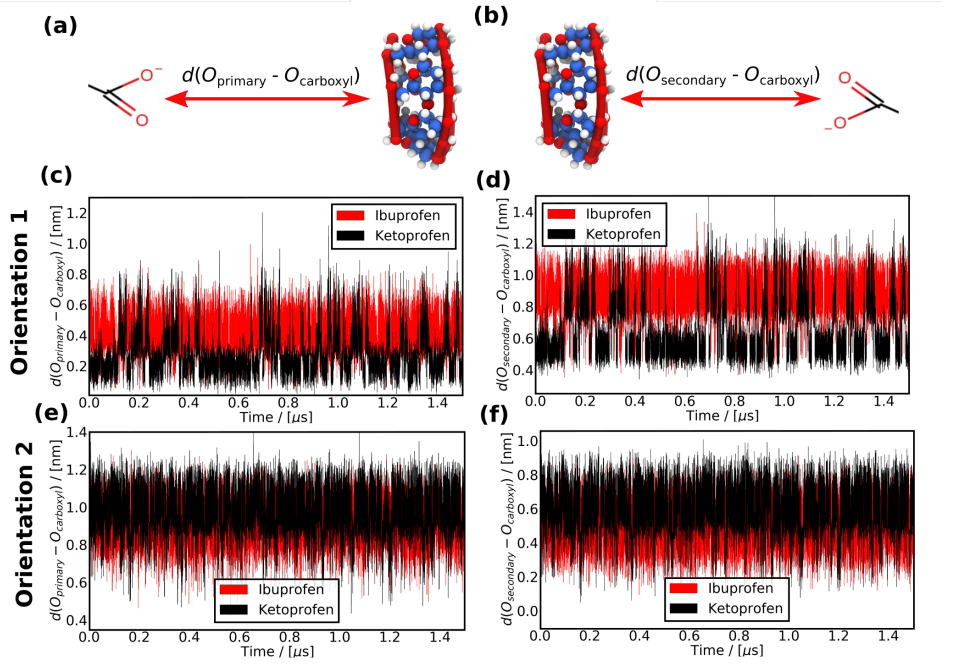

Figure 6.5: The distance of the carboxylic oxygens from the center of mass of the primary or secondary hydroxyl groups of the β-CD for both orientations of ketoprofen and ibuprofen. In subfigures (a) and (b), the schematic representations of the distances of the carboxylic oxygens from the center of mass of the primary and secondary hydroxyl groups are shown, respectively. In subfigures (c) and (d), the distances between the carboxylic oxygens and the center of mass of the primary and secondary hydroxyl groups are shown for Orientation 1, respectively. In subfigures (e) and (f), the distances between the carboxylic oxygens and the center of mass of the primary and secondary hydroxyl groups are shown for Orientation 2, respectively.

ing to the formation of the inclusion complex. By comparing the LJ contributions of the two orientations, it can be seen that the LJ terms are slightly larger for orientation 1. This difference can be attributed to the stronger interactions of the OMPs with the atoms in the narrow rim of the β-CD. In Figure 6.6, it can be observed that the electrostatic interactions become dominant in the host-guest term for both orientations of ketoprofen, and for orientation 2 of diclofenac and ibuprofen. The major role of the electrostatic interactions in the host-guest term is caused by the hydrogen bond formation of the OMPs with β-CD as it will be discussed in the following paragraph.

In Figure 6.6, it can be observed that both the LJ and electrostatic contributions of the desolvation term show the same trend as for the host-guest term. Orientation 1 has a larger LJ contribution to the desolvation term than orientation 2. This means that more atoms are involved in the complex formation and lose interactions with water upon binding in orientation 1.

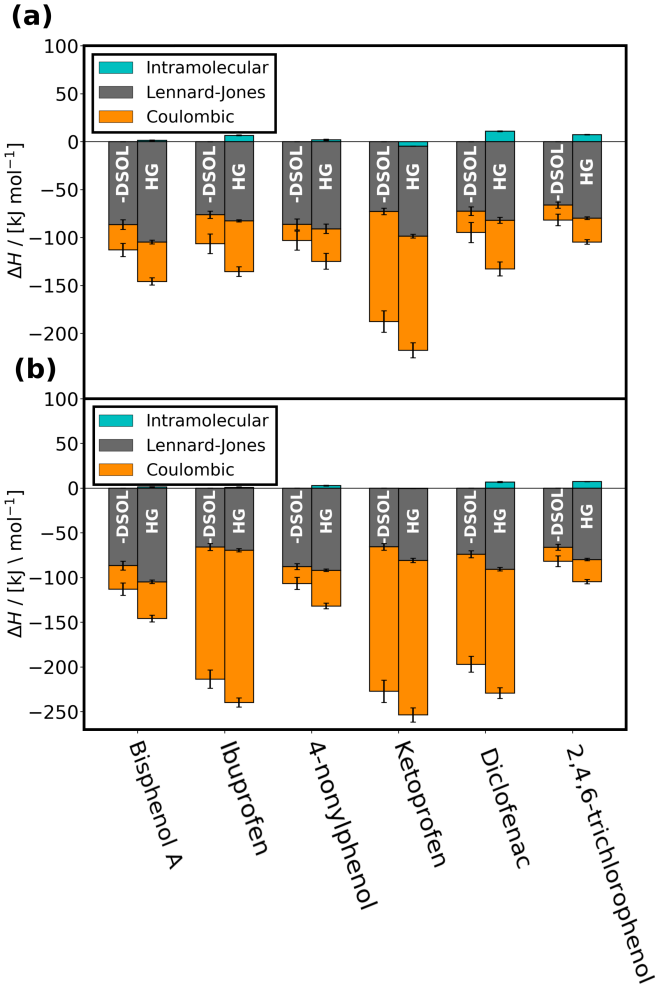

Figure 6.6: The contributions of the host-guest interactions and desolvation effects to the binding enthalpy for (a) orientation 1 and (b) orientation 2 of all studied OMPs. Since the host-guest and desolvation terms have opposite signs, the negative value of the desolvation term ($-\Delta H_{\text{desolvation}}$) is shown. The intramolecular (bonded, 1-4 LJ and 1-4 Coulomb terms) is shown in cyan, the Lennard-Jones contribution in gray and the electrostatics contribution in orange. The bars representing the contributions of the different interaction types are stacked on each other. The -DSOL and HG labels indicate the desolvation and host-guest terms, respectively.

6.3.3. HYDROGEN BONDING

In Figure 6.7, the number of hydrogen bonds between the solvent-guest and host-guest molecules are shown. In all simulations, the criterion for the formation of a hydrogen bond is a cut-off distance of 3.5 Å between the donor and acceptor atoms, and a cut-off angle of 30° between the donor-hydrogen-acceptor atoms [369, 410, 411]. From

Figure 6.7, it can be observed that the guest loses hydrogen bonds with the solvent upon binding to the β-CD. For example ibuprofen (in orientation 2) loses c.a. 2 hydrogen bonds with the solvent upon binding to β-CD. The host also loses interactions with the solvent upon the binding of the guest molecule. The free host forms ca. 33 hydrogen bonds with the solvent. The host may lose some of these hydrogen bonds upon forming an inclusion complex with an OMP. For example, β-CD loses ca. 3 of these hydrogen bonds in the binding with ketoprofen in orientation 1. All data on hydrogen bonding are listed in Table S3 in the Supporting Information of Ref. [391]. The loss of these hydrogen bonds plays a dominant role in determining the magnitude of the electrostatic contribution of the desolvation term. The more hydrogen bonds are lost between the host, guest and the solvent the greater the electrostatic contribution in the desolvation term. The net change in the number of hydrogen bonds upon the binding of the OMP is shown in Table S3 in the Supporting Information of Ref. [391]. As can be seen in Figure 6.7, BPA, NP and TCP molecules practically do not form hydrogen bonds with β-CD (orange part of the bars). The absence of hydrogen bonds results in considerably lower electrostatic contributions to the host-guest and desolvation terms, as discussed earlier and as can be explicitly seen in Figure 6.6. Ibuprofen and diclofenac form fewer hydrogen bonds in orientation 1 than in orientation 2. In orientation 2, the OMPs can form more hydrogen bonds with β-CD due to the more accessible OH groups and less steric hindrance which can lead to a more stable inclusion complex. Due to the positions of the oxo and carboxyl groups in the ketoprofen molecule, it can form almost the same amount of hydrogen bonds in both binding orientations. This indicates that the dominant electrostatic contribution in the host-guest term (see Figure 6.6) is caused by the hydrogen bond formation between the guest and host molecules.

In the study reported by Brown *et al.* [412], experimental measurements of the inclusion complex formation of ibuprofen with permethylated-β-CD (PMβ-CD) were reported. It was found that in the stable inclusion complex, the isobutyl group of ibuprofen lies in the cavity. The carboxyl group forms a hydrogen bond with the methoxy group of the wider rim (orientation 2), which evidently contributes to the stability of the inclusion complex. This finding is in line with our simulation results, which show that the binding of ibuprofen in orientation 2 is more stable than in orientation 1 (see Table S2 in the Supporting Information of Ref. [391]). Brown *et al.* [412], also reports detailed structural properties of the ibuprofen-PMβ-CD inclusion complex, some of which are comparable with our simulation results. The radius of the heptagon, which is the distance of the O4 oxygens from the center of mass of the seven O4 atoms in the CD (see Figure 6.8), is 4.99 Å in the PMβ-CD, and on average 4.93±0.3 Å in our simulations. This shows that the cavity size of the CDs in the experiment and in sim-

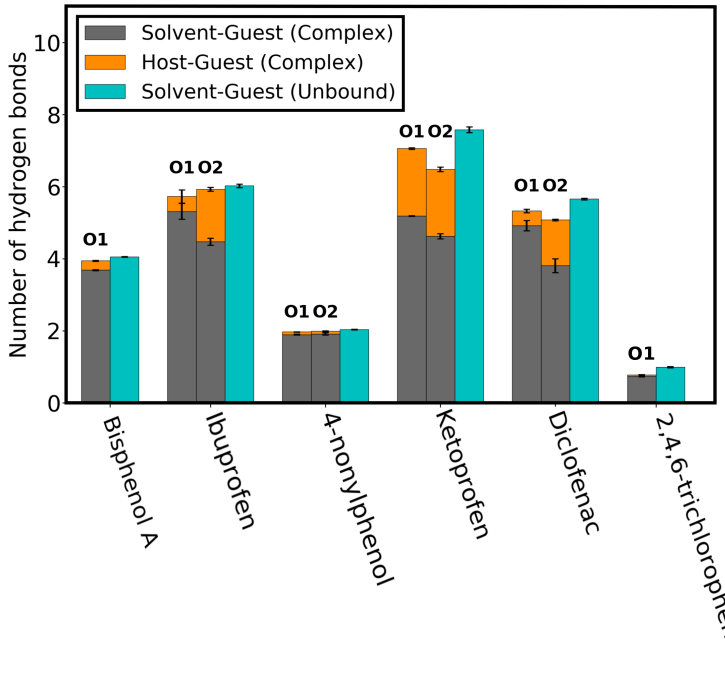

Figure 6.7: The average number of hydrogen bonds formed between: the solvent and the free guest (cyan), the host and the guest (orange), and the solvent and guest in the inclusion complex (grey). The bars representing the number of hydrogen bonds between the different molecule types are stacked on each other. The O1 and O2 labels indicate orientations 1 and 2, respectively.

ulations are equal within the uncertainties of the computation. The glycosidic oxygen angle, which is the angle between the O4 oxygens of the residues of the CDs (see Figure 6.8b), is found to be 127.4 degrees for the PMβ-CD and 127.15±1.64 degrees in our simulations. The agreement in the glycosidic oxygen angles suggest that the shape of the host cavity is not influenced by the functionalization of the β-CD. The number of intramolecular hydrogen bonds in the experiments of PMβ-CD is found to be 7. In our simulation the β-CD forms ca. 6 intramolecular hydrogen bonds. These findings suggest that the configuration of the β-CD and PMβ-CD is similar in the inclusion complex with ibuprofen.

Braga *et al.* [413] performed measurements to investigate the 1:2 ibuprofen-β-CD inclusion complex. The two β-CDs in the complex are linked by the formation of hydrogen bonds between the secondary hydroxyl groups of the wider rim. Braga *et al.* [413] found that in the stable 1:2 inclusion complex the carboxyl group of the ibuprofen protrudes from the smaller rim of the β-CD. In our study on the 1:1 inclusion complex, this configuration of ibuprofen can be identified as orientation 1 and our findings indicate that this orientation is less stable compared to orientation 2. This

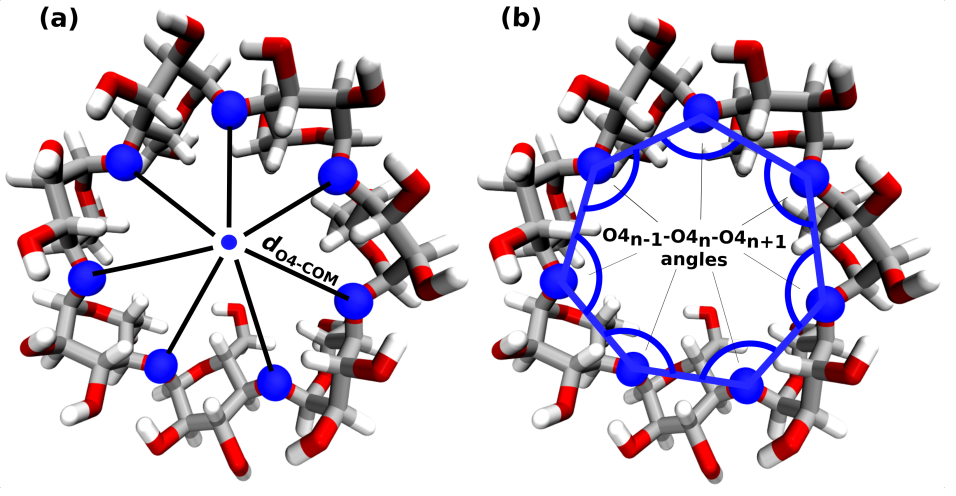

Figure 6.8: Schematic representation of the (a) distance of the O4 oxygens from the centre of mass of the seven O4 atoms in the βCD and the (b) angle between the O4 oxygens of the residues of the βCD. The O4 oxygens are shown in blue. In our simulations, the average of the d_{O4-COM} distances and $O4_{n-1}$-$O4_n$-$O4_{n+1}$ angles are found to be 4.93±0.3 Å and 127.15±1.64 degrees, respectively.

disagreement with the experiments can be most probably attributed to the fact that ibuprofen in the 1:2 complex cannot form hydrogen bonds with the wider rims of the β-CDs. This shows clearly that the dimerization of the β-CDs has a significant effect on the configuration of the inclusion complex.

6.3.4. BINDING ENTROPY

The binding entropy can be computed by subtracting the calculated binding free energy from the binding enthalpy: $\Delta G = \Delta H - T\Delta S$. The computed binding entropies for all studied OMPs and for both orientations are shown in Figure 6.9. Due to the subtraction between very large numbers, the error propagation results in considerable errors for the binding entropy (σ = 1.9 – 3.4 kJ mol^{-1}). From Figure 6.9, it can be observed that the binding entropies for orientation 2 are smaller than in orientation 1, indicating that orientation 2 is entropically more favorable for the binding. This difference can be possibly explained by the tighter binding of OMPs in orientation 1 which results in a less flexible β-CD. The tighter binding of OMPs is also indicated by the more favorable (i.e., more negative) Lennard-Jones contributions of the host-guest term in orientation 1 than orientation 2 as can be seen in Figure 6.6. This is caused because fewer atoms participate in the inclusion complex formation.

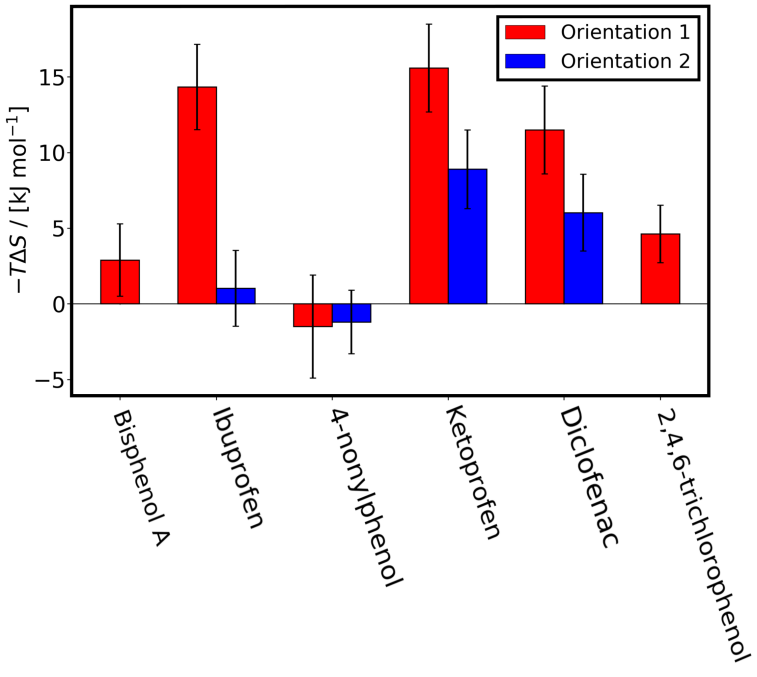

Figure 6.9: The computed binding entropies for orientation 1 (red) and orientation 2 (blue) for all OMPs studied.

6.4. CONCLUSIONS

In this work, the binding free energies and enthalpies of bisphenol A, ibuprofen, ketoprofen, diclofenac, 4-nonylphenol and 2,4,6-trichlorophenol with β-CD are computed by performing force-field based MD simulations. The computed binding free energies using the Bind3P water force field are in a reasonable agreement with the available experimental results. The deviation between the computed and experimentally measured binding enthalpies are found to be considerable. This is in agreement with the findings of Henriksen and Gilson [365]. The computed binding enthalpies are in qualitative agreement with the experimental measurements. To obtain a better understanding of the binding mechanism, the effect of the intramolecular, van der Waals, and electrostatic interactions on the inclusion complex formation is investigated by the decomposition of the binding enthalpy. It is shown that for all studied OMPs, the van der Waals and electrostatic interactions are favourable for the inclusion complex formation but the relative magnitude of the two contributions can differ regardless of the polarity or the protonation state of the OMP. To reveal the effect of the different interactions, the binding enthalpy is decomposed into host-guest and desolvation terms. It is observed that the magnitude of the contribution from the van der Waals

interactions depends on the number atoms participating in the complex formation. It is shown that the hydrogen bond formation of the guest with the solvent and β-CD plays a crucial role in the binding mechanism. Our findings show that MD simulations using the APR method [386] can provide important physical insight into the inclusion complex formation of β-CD with OMPs. Inclusion complexation is suggested to be one of the main mechanisms via which β-CD-based polymers capture OMPs, thus our findings can be used for the design and optimization of these materials.

7

DIFFUSIVITIES OF CYCLODEXTRINS AND OF THE β-CYCLODEXTRIN:IBUPROFEN INCLUSION COMPLEXES IN AQUEOUS SOLUTIONS

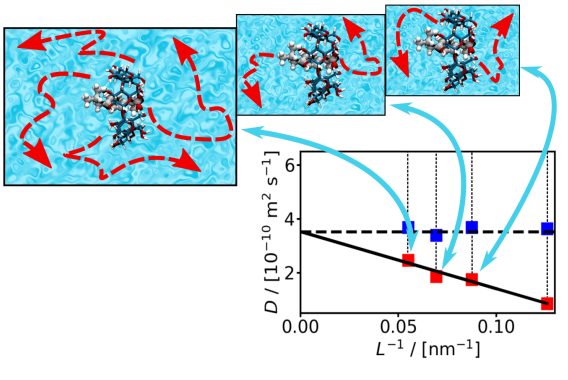

This chapter is based on the following publication: M. Erdős, M. Frangou, T. J. H. Vlugt, and O. A. Moultos, Diffusivity of α-, β-, γ-cyclodextrin and the inclusion complex of β-cyclodextrin: Ibuprofen in aqueous solutions; A Molecular Dynamics simulation study, *Fluid Phase Equilibria* **528**, 112842 (2021).

7.1. INTRODUCTION

In most of the studies concerning cyclodextrins (CDs), the stability of the CD inclusion complex with specific guest molecules are studied by using either experimental or simulation techniques [60, 364, 377, 379, 382, 397, 414–417]. Although in various applications of CDs such as controlled drug-delivery [414, 418–420] mass transport can play an important role, it has not been as widely studied as the binding properties of the inclusion complexes.

To the best of our knowledge, there are only two studies reporting diffusion coefficients of CDs calculated using MD simulations to date. Naidoo *et al.* [421] performed pulse-field-gradient spin-echo nuclear magnetic resonance (PGSE NMR) measurements and MD simulations to determine the diffusion coefficients of α-, β-, and γ-CDs. In that study, the CSFF and SPC/E force fields for the CDs and water were used, respectively. The diffusion coefficients of the CDs were measured at 1 mM concentration in D_2O. Naidoo *et al.* [421] concluded that considering the different solvents used in the simulations and experiments, the simulation results are in a good agreement with the measurements. Tang and Chang [366] presented an MD simulation approach for calculating the binding free energy of host-guest complexes based on the diffusion coefficients of the host and the guest. Using this approach, Tang and Chang computed binding free energies of seven different guest molecules with β-CD using the q4md-CD/GAFF/TIP3P combination of force fields.

In this chapter, a comprehensive study of the diffusivity of CDs in aqueous solutions is reported. Such a study is largely lacking and is important for not only supplementing and further guiding experiments, but also for providing the necessary molecular understanding for the design and/or optimization of applications in which mass transport is crucial, *e.g.*, controlled drug delivery. As it has been shown that the effect of the system size on the computation of self-diffusivity can be significant in MD simulations [422, 423], the effect of the system size on the self-diffusion of CDs is investigated. To model CDs, we use the q4md-CD force field which has been shown to be very accurate in predicting the crystal properties of CDs [369]. Since it has been shown in literature that the choice of force field to represent the solvent has a significant effect on the computed transport properties of the solutes [424–426], the diffusion coefficient of CDs are calculated using four different water force fields. After identifying the best performing solute (i.e. water) force field, the effect of NaCl concentration on the diffusion of CDs is also investigated using two different NaCl force fields. Finally, as a model system for a drug-delivery application, the diffusion coefficient of the ibuprofen:β-CD inclusion complex is computed.

The remainder of this chapter is structured as follows. The following section con-

tains details about the force fields and the MD simulation scheme used. In Section 7.3, the effect of the system size is investigated, the computed self-diffusion coefficients of CDs in different aqueous solutions are presented, and the diffusion of the ibuprofen:β-CD inclusion complex is discussed. The conclusions of this chapter are provided in Section 7.4.

7.2. METHODOLOGY

7.2.1. FORCE FIELDS

All bonded and non-bonded force field parameters of CDs were taken from the q4md-CD force field [369]. Water was modelled using TIP3P [294], SPC/E [315] and TIP4P/2005 [295] force fields, as well as Bind3P [367]. For all water-ion simulations, TIP4P/2005 [295] was used combined with the Joung and Cheatham [388, 427] (JC) and the Madrid-2019 force fields [428] for Na^+ and Cl^-. This choice was based on the recent study by Döpke *et al.* [429] who investigated the performance of different ion force fields combined with the TIP4P/2005 force field in reproducing experimental properties of salt solutions such as diffusion coefficients, ion hydration free energies and hydration radius. The JC force field has full ionic charges (i.e., +1, -1) while the Madrid-2019 force field has scaled atomic charges (i.e., +0.85, -0.85). The Madrid-2019 [428] force field uses specific terms for the Lennard-Jones interactions between the ions and water molecules instead of the general combining rules. Ibuprofen is represented as a fully flexible molecule using the General AMBER force field [314]. The partial charges of Ibuprofen are computed with the Restrained Electrostatic Potential (RESP) method at the 6-31G* level of theory, using the R.E.D III.52 script [389] with the Gaussian09 RevB.01 software package [390]. To check the reliability of the derived charges, the electrostatic potentials (ESPs) generated by the fitted charges and DFT at the 6-31G* level are compared. The relative root mean square between the ESPs in atomic units are found to be smaller than 0.02. The derived charges correspond to the simulation of a molecule at 0 K in vacuum. This approach is used since it is the recommended charge derivation method for the GAFF force field [314]. Recently, Schauperl *et al.* [430] reported the RESP2 method in which the partial charges are calculated from a combination of gas- and aqueous-phase charges. Schauperl *et al.* showed that RESP2 charges are more accurate than the traditional RESP in reproducing experimentally measured properties (*e.g.* hydration free energy, heats of vaporization) of organic liquids [430]. The Lennard-Jones and electrostatic interactions are truncated at 9 Å. Analytic tail corrections are included in the pressure and energy calculations. The Particle-Mesh Ewald (PME) method [392] is used for the long range electrostatic interactions. In all simulations, fixed atomic charges are used and polarization effects are neglected according to the original parametrization of the used force fields. All force field parameters are

reported in the Supporting Information of Ref. [431] in the form of Gromacs parameter files.

7.2.2. SIMULATION DETAILS

MD simulations using the GROMACS2018.2 [387] software package were performed for the diffusivity computations, while LAMMPS (version 16 Feb. 2016) [432] was used for computing viscosities. To integrate the equation of motion, the leap-frog algorithm with 2 fs timestep is used. The initial configurations are obtained by solvating a CD molecule in water. For the aqueous electrolyte systems, additional water molecules are used for the solvation of the CD molecule, and afterwards these are randomly replaced by the appropriate number of Na^+ and Cl^- ions. All initial configurations are created using the built-in GROMACS tools [387]. In this chapter, the same equilibration scheme is followed as in Chapter 6. The temperature is regulated using the modified velocity rescaling thermostat of GROMACS [433], which is able to properly reproduce the canonical ensemble. The coupling constant used in the thermostat is 0.1 ps. The pressure was regulated using the Parrinello-Rahman barostat [434] with a coupling constant of 2 ps. In all simulations, unless stated otherwise, a CD molecule is solvated in 3 000 water molecules.

Self-diffusion coefficients, $D_{i,\text{self}}$, are calculated using the Einstein relation [77]:

$$D_{i,\text{self}} = \frac{1}{6N_i t}\left\langle \sum_{j=1}^{N_i} \left(\mathbf{r}_{j,i}(t) - \mathbf{r}_{j,i}(0)\right)^2 \right\rangle \tag{7.1}$$

where t is the time, N_i is the number of molecules of type i, and $\mathbf{r}_{j,i}$ is the position vector of the jth molecule of species i. The brackets $\langle ... \rangle$ represent an ensemble average. $D_{i,\text{self}}$ is computed by the slope and intercept of the long-time mean squared displacement (MSD) curve at time-scales where the slope of MSD as a function of time is 1 in a log-log plot [77, 435]. Because of the use of one solute molecule and the slow dynamics of CDs due to their size, long MD simulations in the range of 600 ns - 1 µs were needed for obtaining a linear regime with slope equal to 1 in the log-log MSD vs time curve. The self-diffusion coefficients reported in this work are calculated as the average of four independent simulations starting from different initial configurations. Each initial configuration was created by carrying out the equilibration procedure using different random seeds. Each MD simulation was carried out on 12 - 24 CPUs, achieving a performance of 100 - 160 ns/day.

Due to the long range interactions and hydrodynamic effects between the molecules, self-diffusion coefficients computed from MD simulations depend on the size of the simulation box [81, 423, 436–439]. Yeh and Hummer [436] derived an analytic correction term which should be added to the self-diffusivities computed in MD

simulations to obtain the self-diffusion coefficients in the thermodynamic limit [436] (D^{∞}_{self}). The YH correction term is:

$$D^{\text{YH}}_{\text{self}} = \frac{\xi k_B T}{6\pi\eta L} \tag{7.2}$$

where ξ is a constant equal to 2.837297 (for 3D periodic systems), L is the size of the simulation box, and η is the shear viscosity of the solvent computed from MD simulations. It is important to note here that viscosities exhibit no finite-size effects [438]. The viscosity of water and of aqueous electrolyte solutions required for correcting our diffusivity results are not available for all the force fields used and all conditions considered in this chapter. To this purpose, the shear viscosities of all systems are calculated using the OCTP plugin [435] in LAMMPS, an easy-to-use tool which computes transport properties on-the-fly during the simulation. The reported viscosities are calculated as the average of four independent 20 ns long simulations. All details about the OCTP plugin can be found in the original paper [435]. All self-diffusivities reported in this work are corrected for system size effects using Eq. 7.2, unless it is stated otherwise. The computed viscosities for all systems are listed in Tables A.11 and A.12 of the Appendix. In this work, the statistical error in the self-diffusion coefficients and viscosities are calculated as the standard deviation of the mean from the four independent simulations.

7.3. RESULTS AND DISCUSSION

7.3.1. SYSTEM SIZE EFFECTS

The effect of the system size on the diffusivity of pure fluids or mixtures computed with MD simulations has been investigated in detail by several authors [81, 422, 436, 437, 440]. In Figure 7.1, the computed self-diffusion coefficients of β-CD with and without the YH correction at 298.15 K are shown as a function of the simulation box length. The TIP4P/2005 water force field is used. As expected, the finite size self-diffusivities scale linearly with the size of the simulation box, and thus, the application of the YH correction yields the self-diffusivity value in the thermodynamic limit. However, it is important to note that the magnitude of the required correction is substantial. As shown in Figure 7.1, by using 1500 water molecules the computed self-diffusion coefficient (i.e. 1.9×10^{-10} m^2 s^{-1}) is almost equal to the required correction (i.e. 1.8×10^{-10} m^2 s^{-1}). Celebi *et al.* [423] derived a relation between the self diffusion coefficient and finite size self-diffusion coefficient computed from MD simulations. In the relation, the ratio of the effective hydrodynamic radius of the solute and the length of the simulation box is considered. For smaller systems the correction is even higher. For a system size of 500 water molecules, the YH correction is approximately 76% of the final self-

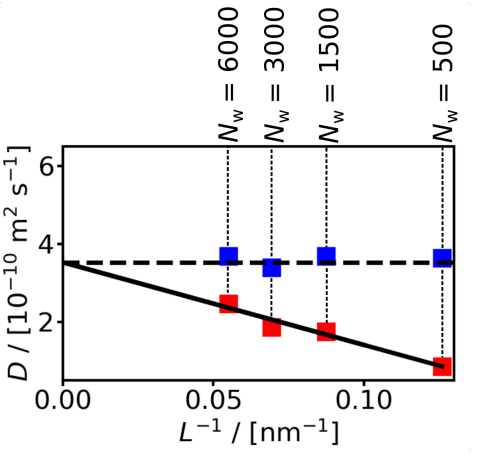

Figure 7.1: The computed self-diffusion coefficients of β-CD as a function of the inverse of the simulation box length at T = 298.15 K and P = 1 bar. The symbols in red and blue colors indicate the calculated self-diffusion coefficients without and with using the YH correction [436], respectively. N_w denotes the number of water molecules used in the simulation. For modelling the β-CD and water the q4md-CD [369] and TIP4P2005 [295] force fields were used, respectively. The maximum statistical error in the computed self-diffusion coefficients is 10%. The error bars are smaller than the symbol size.

diffusion coefficient value. In the study by Moultos *et al.* [422], the effect of the system size on the self-diffusion coefficient of pure CO_2 and CH_4 was studied. The authors show that the magnitude of the YH correction for these systems ranges from ca. 6 to 15% of the final self-diffusion coefficient, depending on the system size. For the systems investigated in this chapter, in which the size of the solute is considerably larger than the size of the solvent (i.e. CDs in water), correcting the self-diffusion coefficient of the solute for system size effects is absolutely crucial because the correction term can be in many cases larger than the computed diffusivity value in MD. Similarly to the results obtained for the β-CD, the required system size correction for the α- and γ-CDs is also substantial as shown in Figures A.3 and A.4 of the Appendix. Hereafter, all of the reported self-diffusion coefficients in tables and figures are corrected for system size effects using using Equation 7.2.

7.3.2. EFFECT OF THE FORCE FIELD ON THE DIFFUSIVITY OF CYCLODEXTRINS IN WATER

In Figure 7.2, the computed and experimentally measured self-diffusion coefficients of the α-, β-, and γ-CDs in water are shown as a function of temperature for the range 298.15 - 312.15 K at a pressure equal to 1 bar. The experimental results are taken from the studies of Ribeiro *et al.* [441–443]. As can be seen, by using the SPC/E and TIP4P/2005 water models the computed self-diffusion coefficients are in a reasonable agreement with the experimental results. The self-diffusion coefficients predicted us-

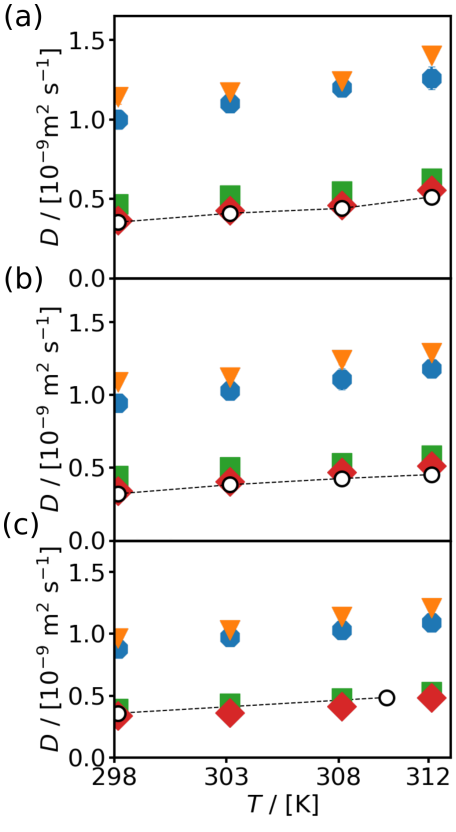

Figure 7.2: Computed self-diffusion coefficients of (a) α-CD, (b) β-CD and (c) γ-CD as a function of temperature at P = 1 bar. The symbols in blue, orange, green, and red colors indicate the use of the TIP3P [294], Bind3P [367], SPCE [315], and TIP4P2005 [295] force fields for water, respectively. The self-diffusivities are corrected for finite size effects using Eq. 2. The experimentally measured self-diffusion coefficients are shown with open black symbols [441–443]. The maximum statistical error in the computed self-diffusion coefficients is 10%. The error bars are smaller than the symbol size.

ing the TIP4P/2005 water force field are the most accurate, showing a mean average deviation from the experimental measurements equal to ca. 8 %. From Figure 7.2, it can be also observed that when the TIP3P and Bind3P water force fields are used, the predicted diffusivities are higher than the experimental measurements by a factor of 3 to 4, for the whole temperature range. In the case of TIP3P water model, this overestimation is expected since the predicted diffusivity and viscosity of pure water with this model are substantially over- and underestimated, respectively [444]. The Bind3P force field was recently developed by Yin *et al.* [367], who refitted the Lennard-Jones size and energy parameters of the TIP3P water model to better predict the experimentally measured binding free energies and enthalpies of host-guest systems. It was shown that compared to TIP3P, the Bind3P force field systematically improves the prediction

of the experimental binding free energies and enthalpies of CDs with different guest molecules [367]. To the best of our knowledge, transport properties for the Bind3P water model are not reported in literature, and thus it is not known how accurately this new force field is in predicting transport properties of pure water. In Table A.11 of the Appendix, it can be seen that the viscosity of pure water calculated with TIP3P is on average 12% higher than with Bind3P. This relatively small difference in viscosities justifies the similar poor performance of the two force fields in predicting the diffusivity of the CDs in water. In general, it is evident that the predicted self-diffusion coefficients of the CDs strongly depend on the accuracy of the force field used for modelling the solvent (i.e. water). This finding is in-line with the literature reporting MD simulations of self-diffusivity in aqeuous solutions [422, 424].

To obtain a better understanding of the effect of the water force fields on the physical properties of the CDs which can influence the diffusion, the average number of water molecules residing in the cavity of the CD during the diffusion process, the number of intra- and intermolecular hydrogen bonds between the CD and water, and the size of the small and large rims of the CDs are studied. The rims refer to the two openings in the CD molecule as can be seen in Figure 6.1b. In Figure 7.3, the average number of hydrogen bonds formed between the water molecules and the α-, β-, and γ-CD are shown as a function of temperature for the four water force fields used. The hydrogen bond analysis is carried out by using the built-in hbond GROMACS tool with the same criteria as in Chapter 6.The difference in the average number of intermolecular hydrogen bonds formed using the different force fields is lower or equal to one in all cases investigated. In Figure A.5 of the Appendix, the average number of intramolecular hydrogen bonds between the hydroxyl groups of the α-, β-, and γ-CD is shown when using the four different water force fields. Similarly to the intermolecular hydrogen bonds, there is no significant difference observed. Thus, the significant difference between the self-diffusion coefficients computed by using the different water models is not reflected in the number of inter- or intramolecular hydrogen bonds in the system.

In Figure A.6 of the Appendix, the average number of water molecules residing inside the cavity of the α-, β-, and γ-CDs are shown as a function of temperature. Since the number of water molecules inside the cavity of the CDs continuously changes as the CD diffuses (i.e., water molecules continuously entering and leaving the cavity), the number of water molecules is calculated as a time average. In the studies by Cézard *et al.* [369], Rodriguez *et al.* [445], and Shikata *et al.* [446] the residence time of water molecules in the CD cavity was investigated by MD simulations and experimental techniques. Both the computed and the measured residence times are in the range of 20 - 75 ps. This shows that the water molecules are continuously flowing in and out of the CD cavity with no stable water clusters being formed. In this chapter, a water

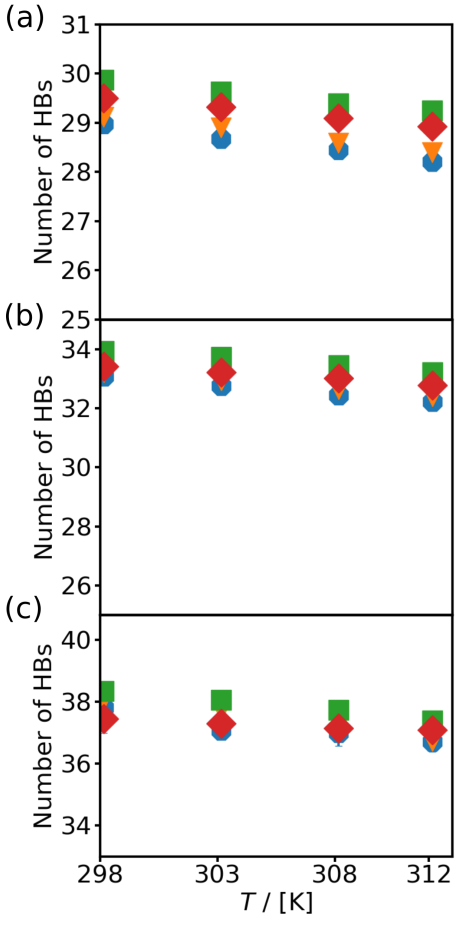

Figure 7.3: The average number of hydrogen bonds (HBs) formed between the (a) α-CD, (b) β-CD and (c) γ-CD with water as a function of temperature at P = 1 bar. The symbols in blue, orange, green, and red colors indicate the use of TIP3P [294], Bind3P [367], SPC/E [315], and TIP4P/2005 [295] water force fields, respectively. The maximum statistical error in the computed number of HBs is 10%. The error bars are smaller than the symbol size.

molecule is considered to be inside the cavity of the α-, β-, and γ-CD if the distance between the centers of mass of the CD and the water is smaller than 0.34, 0.4, and 0.46 nm, respectively. This definition is adapted from the work of Zhang *et al.* [410]. Similarly to our findings for hydrogen-bonding, the average number of water molecules inside the cavity of the CDs predicted by using the different water models is almost identical. The rim sizes of the CDs do not show any significant difference for the different tested force fields. This is shown in Figures A.7 and A.8 of the Appendix, the diameter of the upper and lower rim of the α-, β- and γ-CDs are shown as a function

of temperature.

From the analysis presented above, it is evident that the shape and size of the CDs is almost unaffected by the choice of the force field of the solvent. Moreover, the large differences in the self-diffusion coefficients predicted by using different water models (see Figure 7.2) are not reflected in the number of hydrogen bonds (see Figure 7.3) or in the number of water molecules residing in the CD cavity (see Figure A.6 of the Appendix). These findings strongly suggest that the observed differences in the self-diffusion coefficients of the CDs are mainly caused by the ability of the various water force fields to accurately predict the density and transport coefficients of the pure solvent. Thus, it is not surprising that the force field combination q4md-CD/TIP4P/2005 yields the most accurate results for the diffusivity of CDs in water, since TIP4P/2005 predicts the relevant properties of pure water very accurately [295, 444].

7.3.3. EFFECT OF NACL CONCENTRATION

Since in most applications CDs are dissolved in aqueous solutions containing salts, we investigate the effect of NaCl concentration in water on the diffusion of CDs using two different ion force fields (i.e. JC and Madrid-2019) combined with the TIP4P/2005 water force field. The TIP4P/2005 force field was chosen since it was found to be the most accurate one combined with the q4md-CD force field (see Figure 7.2). The two ion force fields are selected based on the study by Döpke *et al.* [429] who showed that the JC and Madrid-2019 ion force fields combined with TIP4P/2005 can reproduce properties including ion hydration free energy, hydration radius reasonably well. In Figure 7.4, the computed self-diffusion coefficients of the α-, β-, and γ-CDs in the aqueous electrolyte solutions are shown as a function of the NaCl molarity from 0 up to 1 mol L^{-1} at 298.15 K. The diffusivity of all CDs decreases with the increase in NaCl concentration, regardless of the ion force field used. This is most likely caused by the preferential interaction of the ions with the hydroxyl groups of the CDs altering their hydration shell. Moreover, the viscosity of the solvent increases with the NaCl concentration (see Table A.12 of the Appendix), which also contributes to the slower diffusion of the CDs. In Figure 7.4, it can also be observed that for NaCl molarities up to 0.4 mol L^{-1}, both ion force fields yield the same self-diffusivities (within the statistical uncertainty) for all three CDs. For higher ion concentrations (i.e., M_{NaCl} >0.6 mol L^{-1}) , the computed self-diffusion coefficients of α- and β-CD using the two different ion force fields start to deviate from each other, showing that simulations using the Madrid-2019 force field always predict higher values. The difference between the two force field combinations becomes smaller as the size of the CD molecule increases (i.e from α to γ). In the case of γ-CD, both force fields practically predicts the same diffusion coefficients (see Figure 7.4c).

To obtain a better understanding of the cause for these differences, the radial dis-

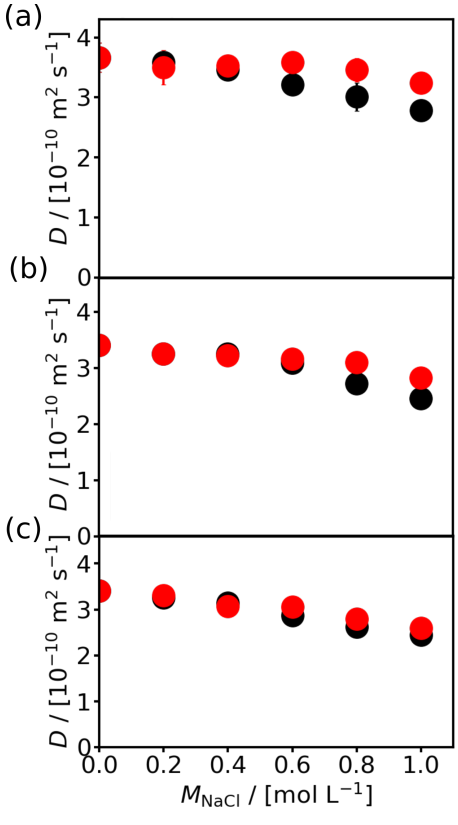

Figure 7.4: The computed self-diffusion coefficients of (a) α-CD, (b) β-CD and (c) γ-CD as a function of NaCl molarity at T = 298.15 K and P = 1 bar. The symbols in black and red colors indicate the use of JC [388] and Madrid-2019 [428] NaCl force fields, respectively. For water the TIP4P2005 [295] water force field is used. The self-diffusivities are corrected for finite size effects using Eq. 2. The maximum statistical error in the computed self-diffusion coefficients is 10%. The error bars are smaller than the symbol size.

tribution functions (RDFs) of the Na^+ and Cl^- ions in respect to the center of mass of the CDs are calculated. Since the highest difference in the diffusion coefficients occurs at the highest NaCl concentration, we calculate the RDFs for the simulations at M_{NaCl} =1.0 mol L^{-1}. In Figures 7.5a, b, and c, the radial distribution function of the α-, β-, and γ-CDs with the Cl^- ions are shown for the JC and Madrid-2019 force fields for M_{NaCl} =1.0 mol L^{-1}. JC Cl^- ions have a slightly higher affinity to interact with the CDs, expressed by a higher first peak on the RDF, than the ions modelled using the Madrid-2019 force field. Figures 7.5b and c show that for the β- and γ-CDs a small peak appears at very short distances (ca. at d =1.5 Å) if the Madrid-2019 force field is used. These peaks suggest that, although it is rare, the Cl^- ions can enter into the cavity of the CDs during the simulation. In Figures 7.5d, e, and f, the radial distribution function of α-, β- and γ-CDs with Na^+ ions are shown for the two force field combina-

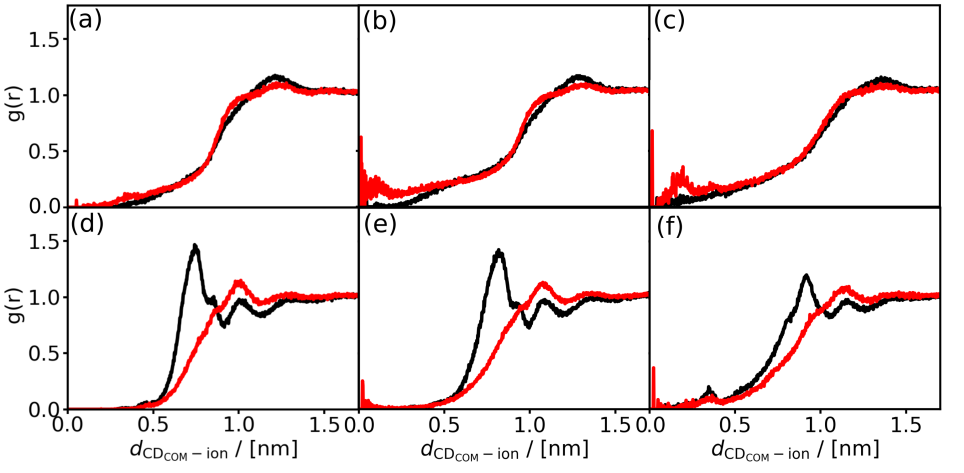

Figure 7.5: Radial distribution functions for the distance between the center of mass of the α-, β- and γ-CDs and the Na^+ and Cl^- ions at T = 298.15 K and P = 1 bar. (a), (b) and (c) subfigures show the RDFs of the Cl^- ions with the α-, β- and γ-CDs (from left to right). (d), (e) and (f) subfigures show the RDFs of the Na^+ ions with the α-, β- and γ-CDs (from left to right). The black and red colors indicate the use of JC [388] and Madrid-2019 [428] ion force fields, respectively. For water the TIP4P/2005 [295] water force field is used.

tions, at M_{NaCl} =1.0 mol L^{-1}. Na^+ ions modelled with the JC force field have a higher affinity to interact with the CDs compared with the Madrid-2019 Na^+ ions. The difference between the height of the peaks in the RDFs is decreasing as the CDs get larger. This means that the affinity of Na^+ ions to interact with the CDs becomes more similar. These findings explain the differences in the computed self-diffusivities caused by the size of the CD and the use of the different ion force fields shown in Figure 7.4.

In Figure 7.6, density contour plots of water, sodium, and chloride around the α-, β-, and γ-CDs are shown. The contour surfaces show the locations where the density of the compound is equal to the set contour level. The contour levels of water, Na^+, and Cl^- are 1.05, 1.5 and 1.3 times the bulk densities of the corresponding compounds, respectively. In-line with the RDFs shown in Figure 7.5, Na^+ ions modelled with the JC force field (see Figures 7.6a, c and e) occupy a larger area around the CDs (corresponding to higher peaks in the RDF) than the Na^+ using the Madrid-2019 force field (see Figures 7.6b, d and f). From the contour plots it can also be seen that the preferred location of the Na^+ ions is near the hydroxyl groups of the larger rim of the CDs when the JC force field is used. When the Madrid-2019 model (see Figures 7.6b, d and f), Na^+ ions are located further from the center of mass of the CDs but still lie in the vicinity of the hydroxyl groups of the large rims. Cl^- ions, regardless of the ion force field used, are always located outside of the CD, close to the center of the large rim.

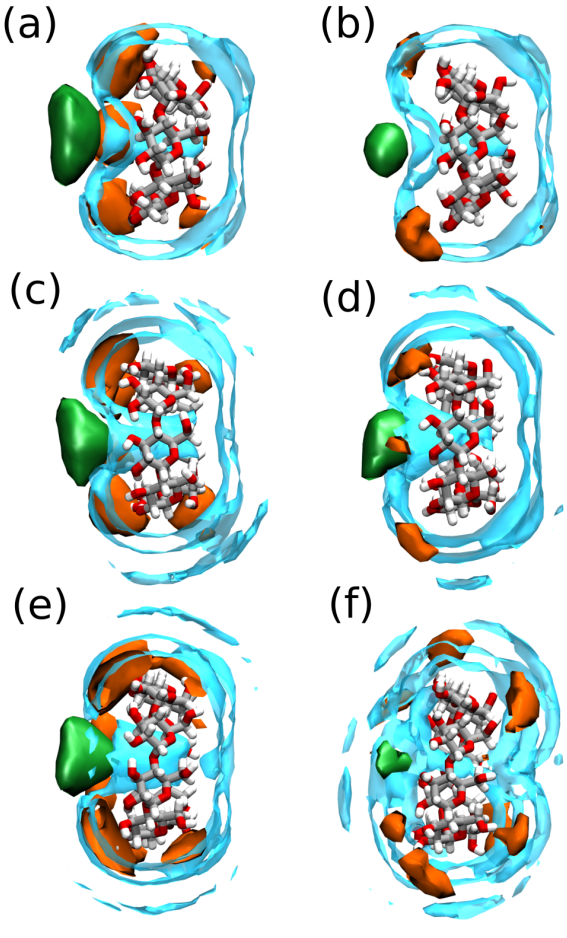

Figure 7.6: Density contour plots of water and NaCl around the CDs at T = 298.15 K, P = 1 bar and M_{NaCl} =1.0 mol L^{-1}. (a) and (b) show the density contour plots around the α-CD. (c) and (d) show the density contour plots around the β-CD. (e) and (f) show the density contour plots around the γ-CD. For the contour plots on the left side of the figure, i.e. (a) (c) and (e), the JC [388] force field is used. For the contour plots on the right side of the figure, i.e. (b) (d) and (f), the Madrid-2019 [428] force field is used. The TIP4P/2005 [295] force field was used to model water. The green, orange, and blue colors indicate the Cl^{-}, Na^{+} and water, respectively.

7.3.4. DIFFUSION OF THE β-CD:IBUPROFEN INCLUSION COMPLEX

Ibuprofen is an anti-inflammatory drug which is widely used worldwide for treating fever, pain and inflammation [447]. Due to its common use, ibuprofen is also a frequently detected contaminant in surface and ground waters [332, 333, 335, 448]. Since β-CD can be potentially used both as a drug delivery agent [57, 58, 61] and in waste water treatment applications [360–362], the mass transport of β-CD:Ibuprofen inclusion complex is an important aspect in both applications. In our MD simulations, the

Table 7.1: Computed self-diffusion coefficients of the βCD:Ibuprofen inclusion complex (the two orientations can be seen in Figure 6.1b) and free βCD in water at T = 298.15 K and P = 1 bar. The q4md-CD [369] force field was used for modelling the β-CDs, the TIP4P2005 [295] for water, and the General AMBER force field [314] was used for ibuprofen. The self-diffusivities are corrected for finite size effects using Eq. 7.2. σ is the error estimate in D with a 95% confidence interval.

	D / $[10^{-10}\mathrm{m}^2\ \mathrm{s}^{-1}]$	σ / $[10^{-10}\mathrm{m}^2\ \mathrm{s}^{-1}]$
βCD:Ibuprofen (orientation 1)	3.3	0.1
βCD:Ibuprofen (orientation 2)	3.20	0.04
Free βCD	3.50	0.05

two possible orientations of ibuprofen inside the β-CD cavity are considered. In Orientation 1, the carboxyl group of ibuprofen is located near the small rim of the β-CD. In Orientation 2, the ibuprofen molecule is rotated by 180 degrees to place the carboxyl group near the large rim of the β-CD. A schematic representation of the orientations is shown in Figure 6.1b. The computed self-diffusion coefficients of the β-CD:Ibuprofen inclusion complex for the two orientations, and the free β-CD at 298.15 K are shown in Table 7.1. The values of the self-diffusivities of the two inclusion complexes are very close to each other (i.e. within 5%), and ca. 5-10% lower than the one of free β-CD.

Although no experimental measurements or molecular simulation computations of the self-diffusivity of the β-CD:Ibuprofen inlcusion complex in aqeous solution are reported, Santos *et al.* [418] presented Taylor dispersion experiments for the free β-CD and the β-CD:caffeine inclusion complex. These experiments revealed that the diffusivity of the free β-CD is only slightly higher than the one of β-CD:caffeine inclusion complex (3.17×10^{-10} m^2 s^{-1} and 3.05×10^{-10} m^2 s^{-1}, respectively). Santos *et al.* [418] concluded that the inclusion complex has practically the same diffusivity with the free β-CD. The authors justified this finding by the fact that caffeine molecule is fully included in the cavity of the β-CD. Although these experiments were carried out using a different guest molecule compared to this chapter, a comparison between the two can be justified because the size of caffeine is comparable to the size of ibuprofen. As shown in Table 7.1, the molecular simulation results are in full agreement with the experimental findings, showing no significant difference in the diffusivity of the free β-CD with the inclusion complex in water. In Figure A.9 of the Appendix, the RDFs of water in respect to the free β-CD and the inclusion complex in both orientations are shown. In the case of free β-CD, the RDF peak at a distance of approx. 2 Å indicates that water molecules enter the cavity, however, in the case of the inclusion complex, no peak in the RDF is observed. This means that ibuprofen fully occupies the cavity of the β-CD preventing water molecules from entering.

7.4. CONCLUSIONS

In this work, the self-diffusion coefficients of α-, β-, γ-CDs and the β-CD:Ibuprofen inclusion complex in aqueous solutions are computed by means of MD simulation and compared with the respective experimental measurements. The effect of the system size on the self-diffusion of CDs is investigated. It is shown that the YH correction can be 76% of the final self-diffusion coefficient value. This suggests that the use of system size corrections for mixtures with compounds which are considerably different in size is absolutely necessary even if relatively large system sizes are used in the MD simulations. The self-diffusion coefficients of the native CDs in water are computed using four different water force fields at temperatures ranging from 298.15 to 312.15 K, at a pressure of 1 bar. The q4md-CD force field by Cézard *et al.* [369] was used to model CDs. We found that by using the TIP4P/2005 force field, the experimentally measured self-diffusion coefficients can be computed very accurately. The physical properties of CDs which can influence their diffusivity, such as the number of hydrogen bonds formed within the CDs and between the CDs and water, the average number of water molecules in the cavity of the CDs, and the size of the lower and upper rims of the CDs are also investigated to obtain a better understanding of effect of the water force field on these properties. Our results show that the effect of the water force field on these properties is almost negligible. This suggests that the large differences in the predicted self-diffusion coefficients are not caused by structural differences (such as the size and shape) of the CDs when different water force fields are used but mainly depend on the performance of these force fields in predicting the density and transport properties of the pure solvent. To reveal the effect of the salt concentration of the solvent on the diffusion of CDs, the self-diffusion coefficient of the three native CDs with two different ion force fields are computed as a function of the NaCl concentration at 298.15 K and 1 bar. It was found that the diffusivity of all CDs decreases with the increasing NaCl concentration, regardless of the ion force field. It is also shown that the Na^+ ion modelled by the JC force field has a higher affinity toward the CDs than the Madrid-2019 force field. This difference is likely the reason of the slower diffusivity of the α- and β-CDs when the JC force field is used. Finally, as a model system for drug delivery and also for waster treatment application of β-CD, the diffusion of the β-CD:Ibuprofen inclusion complex in water is studied. It is shown that self-diffusion coefficient of the inclusion complex is approximately 5-10% lower than the free β-CDs. The similar diffusivity of the inclusion complex and free β-CD is most likely caused by the nearly full inclusion of ibuprofen in the cavity of the β-CD. Our findings indicate that MD simulations can provide reasonable predictions for supporting experiments, and the necessary molecular level understanding which is useful for industrially relevant applications of CDs.

8

CONCLUSIONS

Molecular simulation can be a powerful tool for discovering new or identifying already existing materials which can contribute to the improvement of specific applications, and for obtaining detailed molecular understanding of phenomena at the molecular scale. In this thesis, specific applications of porous materials are studied using molecular simulations. The pressure of a nanoconfined fluid is one of the most important thermodynamic properties needed for an accurate description of, for example, the flow rate and diffusion coefficient of fluids in porous materials. The main difficulty of the pressure calculation arises from the ambiguous definition of the pressure tensor inside porous materials due to the presence of curved surfaces and confinement effects. In Chapter 2, the pressure of fluids in nanoporous materials is investigated based on the theory reported by Galteland *et al.* [147]. In this approach, two different pressures are needed to account for confinement effects in nanoporous materials: the differential pressure P, and the integral pressure $\hat{p}$. By definition, the differential pressure does not depend on the size of the system while the integral pressuree does. The differential and integral pressures are different for small systems and become equal in the thermodynamic limit. It is shown that the difference between the computed differential and integral pressures for all studied cases approaches 0 with the size of the pore approaching infinity. This finding shows that the theory proposed by Galteland *et al.* [147] holds in physical systems. Since the pressure inside the pores influences the transport properties of the fluid, a related quantity, the ratio of driving force for mass transport, $\frac{\mathrm{d}\langle\hat{p}\rangle}{\mathrm{d}P}$, is also investigated. The term $\frac{\mathrm{d}\langle\hat{p}\rangle}{\mathrm{d}P}$ is the ratio of the pressure gradient for mass transport in the bulk phase, $\frac{\mathrm{d}P}{\mathrm{d}L}$, and in the confined space, $\frac{\mathrm{d}\langle\hat{p}\rangle}{\mathrm{d}L}$, which is referred to as the ratio of driving forces for mass transport in this thesis. It is shown that the ratio of driving forces for mass transport in the bulk and in the confined fluid con-

siderably deviates from 1 for small pore sizes which indicates that the approximation $\hat{p} \approx P$ does not hold on the nanoscale. Our findings and the findings of Galteland *et al.* [147] and Rauter *et al.* [174] indicate that the integral pressure should be incorporated in the modeling fluids in nanopores. For example, the different pressures should be considered in the Navier-Stokes equation during the modeling of a fluid flow through a nanopore. Besides testing theories, molecular simulations can be also used to identify new materials to improve the performance of specific applications. In Chapters 3 and 4, two computational screening studies of Metal-Organic Frameworks (MOFs) and zeolites are presented for adsorption driven chillers (ACs) and high-pressure H_2 drying applications, respectively. In Chapter 3, 12 MOF structures are identified from 2 930 already synthesized frameworks as promising candidates for AC application. The deliverable working capacities of these MOFs are considerably higher (> 0.6 ml ml^{-1}) than the previously reported highest value in literature (~ 0.45 ml ml^{-1}) [148]. To the best of our knowledge, these materials have not been considered before for AHP/ACs applications. Based on the obtained results, using the identified frameworks the efficiency of AC devices can be significantly improved. Since several assumptions are used in the simulations *e.g.* perfect crystal structures, rigid frameworks *etc.*, the efficiency of the selected materials should be confirmed by experimental measurements. In Chapter 4, it is shown that zeolites with the lowest possible Si/Al ratio are ideal for high-pressure H_2 drying applications. Based on this finding, 218 zeolites with the lowest possible Si/Al ratio are studied for this application. Zeolites which can be used to dry up to 8 000 times their own volume of H_2 gas are identified based on the molecular simulation results. This indicates that zeolites with high Al content are potential candidates for high-pressure H_2 drying applications. To date, most types of zeolites have not been synthesized with the highest possible Al content [283]. This shows that the development of new synthetic pathways allowing for the creation of zeolites with high Al content would be beneficial for high-pressure H_2 drying. The findings of these two studies show that computational screening of porous materials can be used to provide fundamental guidance for experimental and computational investigations of MOFs and zeolites for specific applications. Besides looking for better performing structures from a large pool of candidates, the efficiency of applications can also be improved by understanding the involved processes and fine tuning of current materials. In case of porous materials, most of the physico-chemical phenomena occur inside pores, therefore, obtaining a molecular level understanding of the involved processes by using only experimental techniques can be challenging. In Chapters 5-7, zeolites and cyclodextrins (CDs) are studied to obtain a molecular level understanding on the physico-chemical phenomena involved during the removal of organic micropollutants (OMPs) from waste water using these materials. In Chapter 5, the adsorp-

tion mechanism leading to the experimentally observed unexpected S-shaped adsorption isotherm of 2,4,6-trichlorophenol (TCP) on high-silica FAU-type zeolites is investigated. The adsorption mechanism is identified and the findings suggest that the experimentally measured S-shaped adsorption isotherm occurs due to the π - π stacking of the TCP molecules inside the alpha cage of the FAU-type zeolite. The alpha cages of FAU-type zeolites provided a possible accommodation for multiple TCP molecules as a potential condition of lateral interactions of TCP. The results indicate that lateral interactions between adsorbates can be expected on structures with pores that can accommodate several adsorbate molecules. This observation might be used in the design of new materials for waste water treatment applications. In Chapters 6 and 7, the inclusion complex formation of 6 OMPs with β-CD and the diffusivity of α-, β-, γ-CD, and the β-CD:ibuprofen inclusion complexes in aqueous solutions are investigated. It is found that the computed binding free energies and binding enthalpies of the inclusion complexes, and self-diffusion coefficients of CDs are in reasonable agreement with experimental measurements. The inclusion complex formation is suggested to be one of the main mechanisms via which β-CD-based polymers capture OMPs. This indicates that the methods used in our study can provide valuable insight for the design and optimization of these materials. The reasonable prediction of the diffusivity of CDs and its inclusion complexes with ibuprofen indicate that MD simulations can be used to support experiments, and provide the necessary molecular level understanding which is useful for industrially relevant applications of CDs. Regarding molecular simulations for porous materials, one of the most important areas on which future research should focus is the more detailed description of frameworks. In most studies of porous materials, the polarizability and flexibility of the framework are neglected which may have a significant effect on the thermodynamical properties of the system. The reason to adopt these assumptions is twofold. First, including the flexibility and polarizability of the framework in simulations is computationally expensive. Second, there are only a limited number of available models which can account for the flexibility or polarizability of a framework. Usually these models are specifically derived for certain systems and cannot be used for others. With the continuously increasing computational capacity and with the appearance of new methods in force field development such as machine learning and artificial intelligence, it is possible that these assumptions will no longer be needed in future studies. Alternatively, molecular systems can be described with more computationally expensive and accurate methods, for example ab initio, density function theory etc. instead of classical force fields. With the continuous increase in computational capacity, ab initio based molecular simulations (*e.g.* ab initio molecular dynamics) will probably become more widespread.

APPENDIX

Table A.1: Force field parameters (Lennard-Jones parameters) used for the MOF framework atoms from Chapter 3. The partial charges of the atoms are taken from the CIFs reported in the DDEC database [208].

Atom	$\frac{\epsilon}{k_B}$ / [K]	σ / [Å]		Atom	$\frac{\epsilon}{k_B}$ / [K]	σ / [Å]
Ag	18.11	2.80		Mo	28.18	2.72
Al	156.00	3.91		N	38.95	3.26
As	206.34	3.70		Na	251.63	2.80
Au	19.63	2.93		Nb	29.70	2.82
B	47.81	3.58		Nd	5.03	3.19
Ba	183.19	3.30		Ne	21.14	2.89
Be	42.77	2.45		Ni	7.55	2.52
Bi	260.69	3.89		Np	9.56	3.05
Br	186.19	3.52		O	48.16	3.03
C	47.86	3.47		P	161.03	3.70
Ca	25.16	3.09		Pb	333.67	3.83
Cd	114.73	2.54		Pr	5.03	3.21
Ce	6.54	3.17		Pt	40.26	2.45
Cl	142.56	3.52		Pu	8.05	3.05
Co	7.05	2.56		Rb	20.13	3.67
Cr	7.55	2.69		Re	33.22	2.63
Cs	22.65	4.02		Rh	26.67	2.61
Cu	2.52	3.11		Ru	28.18	2.64
Dy	3.52	3.05		S	173.11	3.59
Er	3.52	3.02		Sb	225.95	3.94
F	36.48	3.09		Sc	9.56	2.94
Fe	6.54	2.59		Se	216.41	3.59
Ga	208.84	3.90		Si	156.00	3.80
Gd	4.53	3.00		Sm	4.03	3.14
Ge	201.31	3.80		Sn	276.80	3.98
H	7.65	2.85		Sr	118.27	3.24
He	10.90	2.64		Te	200.28	3.98
Hf	36.24	2.80		Th	13.09	3.03
Hg	193.76	2.41		Ti	8.55	2.83
Ho	3.52	3.04		Tm	3.02	3.01
I	256.67	3.70		U	11.07	3.03
In	301.43	3.98		V	8.05	2.80
K	17.61	3.40		W	33.72	2.73
La	8.56	3.14		Y	36.24	2.98
Li	12.58	2.18		Yb	114.75	2.99
Lu	20.63	3.24		Zn	62.40	2.46
Mg	55.86	2.69		Zr	34.72	2.78
Mn	6.54	2.64				

Table A.2: Force field parameters (Lennard-Jones parameters and partial charges) used for methanol and ethanol [213] in Chapter 3.

Atom type	$\frac{\epsilon}{k_B}$ / [K]	σ / [Å]	q / [e]
CH_3	98	3.75	0.265
CH_2	46	3.95	0.265
O	93	3.02	-0.70
H	0.5	0.5	0.435

Table A.3: The calculated saturation vapor pressures of methanol and ethanol as used in Chapter 3, as a function temperature. The vapor pressures are calculated using the Antoine equation [225, 226].

T / [K]	P_0^{methanol} / [kPa]	P_0^{ethanol} / [kPa]
288	9.79	4.28
290	10.94	4.85
292	12.21	5.48
294	13.60	6.18
296	15.13	6.96
298	16.81	7.82
300	18.64	8.77
302	20.63	9.82
304	22.81	10.97
306	25.18	12.25
308	27.75	13.65
310	30.55	15.18
312	33.58	16.86
314	36.86	18.69
316	40.40	20.70
318	44.24	22.88
320	48.37	25.26

Table A.4: Summary of structural analysis of the best 12 structures with ethanol from Chapter 3 including largest cavity diameter (LCD), pore limiting diameter (PLD), helium void fraction (ϕ_{He}), volumetric surface area (VSA), cluster type, ligands, coordination, functional groups, dimensionality, presence of coordinatively unsaturated sites (CUS) and the references (Ref.) to the original publications reporting the MOF structures.

Name	Common name	Ref.	PLD / Å	LCD / Å	Φ / -	VSA / m^2 cm^{-3}	α^a / -	ΔW_{del}	Cluster-type	Ligand 1	Ligand 2	Coordination	Functional groups	CUS	Dim.
ANUGIA	UMCM-152	[235]	6.76	13.85	0.86	2137	0.04	0.558	$[Cu_2]^{4+}$	$[H_7C_14O_4]^{4-}$	-	CL(1)	-	Yes	3D
RUVKAV	PCN-46	[234]	7.15	11.95	0.83	2149	0.04	0.594	$[Cu_2]^{4+}$	$[H_6C_20O_8]^{4-}$	-	CL(1)	-	Yes	3D
FUNBOG	-	[237]	11.01	12.59	0.78	1962	0.05	0.544	$[Zn_2]^{4+}$	$[H_16C_34O_8Br_2]^{4-}$	$[H_8C_10N_4]$	CL(1)L(2)	(C)-Br	No	3D
IYIHUU	-	[449]	10.44	11.84	0.73	1892	0.05	0.447	$[Zn_2]^{4+}$	$[H_16C_34O_8Br_2]^{4-}$	$[H_10C_16N_2]$	CL(1)L(2)	(C)-Br	No	3D
ZECKOJ	-	[450]	7.76	10.01	0.74	2140	0.05	0.472	$[Cu_2]^{4+}$	$[H_6C_6O_2N_2]^{2-}$	-	C(L1)2	-	Yes	3D
FUNCEX	-	[237]	12.48	13.22	0.81	1873	0.07	0.294	$[Zn_2]^{4+}$	$[H_16C_34O_8Br_2]^{4-}$	$[H_8C_12N_6]$	CL(1)L(2)	(C)-Br	No	3D
IRMOF-6	IRMOF-6	[240]	6.71	15.04	0.77	2079	0.07	0.426	$[Zn_4O]^{6+}$	$[H_6C_10O_4]^{2-}$	-	CL(1)3	-	No	3D
XEBHOC	Cu_2(TCPPDA)	[238]	9.91	12.08	0.86	2170	0.07	0.646	$[Cu_2]^{4+}$	$[H_20C_34O_8N_2]^{4-}$	-	CL(1)	-	Yes	3D
FEFDEB	DMOF-1-bpdc	[451]	11.61	13.11	0.76	1873	0.08	0.54	$[Zn_2]^{4+}$	$[H_8C_14O_4]^{2-}$	$[H_12C_6N_2]$	CL(1)2L(2)	-	No	3D
PEVQEO	IRMOF-1	[240]	7.95	14.86	0.84	2184	0.08	0.638	$[Zn_4O]^{6+}$	$[H_4C_8O_4]^{2-}$	-	CL(1)3	-	No	3D
HAFTOZ	-	[239]	7.52	15.37	0.81	2005	0.1	0.606	$[Ni_8]^{12+}$	$[H_6C_15N_6]^{2-}$	-	CL(1)6	-	No	3D
GUNFAW01	-	[241]	7.34	9.61	0.74	2301	0.23	0.653	$[CrMn]^{5+}$	$[C_2O_4]^{2-}$	-	CL(1)3	-	Yes	3D

^{a} - α represents the relative pressure value where the loading is equal to the half of the possible maximum loading of the structure.

The pore limiting diameter (PLD), largest cavity diameter (LCD), and volumetric surface area (VSA) are calculated using the Zeo++ software package [223, 224]. The helium void fraction of the structures are calculated with Widom test particle insertion method implemented in the RASPA software package [90]. The deliverable working capacity (ΔW_{del}) is calculated as the difference in loadings before and after the adsorption step.

Table A.5: Lennard-Jones parameters and atomic charges used in Chapter 4. $Oa_{Zeolite}$ represents the oxygen atoms of the zeolite connected to an Al atom, $O_{Zeolite}$ represents the oxygen atoms of the zeolite connected to only Si atoms, O_{water} is the oxygen atom of the water molecule, L_{water} is dummy atom of the TIP5P/Ew water model [285], H_{water} is the hydrogen atom of the water molecule [97].

Atom type	$\frac{\epsilon}{k_B}$ / [K]	σ / [Å]	Atomic charge	Ref.
$Si_{Zeolite}$	0	0	0.786	[87]
$Al_{Zeolite}$	0	0	0.486	[87]
$O_{Zeolite}$	0	0	-0.393	[87]
$Oa_{Zeolite}$	0	0	-0.414	[87]
O_{water}	89.52	3.10	0	[285]
L_{water}	0	0	-0.241	[285]
H_{water}	0	0	0.241	[285]
$Na_{Zeolite}$	251.78	3.14	0.383	[87]
H_{H_2}	36.73	2.96	0	[97]

Table A.6: Lennard-Jones parameters for the interaction between specific interaction sites used in Chapter 4. $Oa_{Zeolite}$ represents the oxygen atoms of the zeolite connected to an Al atom, $O_{Zeolite}$ represents the oxygen atoms of the zeolite connected to only Si atoms, O_{water} is the oxygen atom of the water molecule, L_{water} is dummy atom of the TIP5P/Ew water model [285], H_{H_2} is the interaction site of the one-site hydrogen model [97].

Site 1	Site 2	$\frac{\epsilon}{k_B}$ / [K]	σ / [Å]	Ref.
H_{H_2}	$Si_{Zeolite}$	28.26	1.85	[97]
H_{H_2}	$Al_{Zeolite}$	26.51	1.99	4
H_{H_2}	$O_{Zeolite}$	66.06	2.89	[97]
H_{H_2}	$Oa_{Zeolite}$	66.06	2.89	4
H_{H_2}	$Na_{Zeolite}$	220	3	4
$O_{Zeolite}$	$Na_{Zeolite}$	33	3.2	[87]
$O_{Zeolite}$	O_{water}	13.71	3.38	[87]
$Oa_{Zeolite}$	$Na_{Zeolite}$	23	3.4	[87]
$Oa_{Zeolite}$	O_{water}	13.71	3.38	[87]
$Na_{Zeolite}$	O_{water}	75	2.39	[87]

Table A.7: Fugacity coefficients of water and H_2 in the infinitely diluted water/H_2 mixture at 400 and 875 bar used for Chapter 4. The coefficients were calculated by performing CFC simulations in the NPT ensemble [89, 292]. Fugacity coefficients of bulk H_2 reported in the NIST reference fluid thermodynamic and transport properties (REFPROP) database [452] at P = 400 and 875 bar, and T = 310 K.

Component	Fugacity coefficient		Source
	P = 400 bar	P = 875 bar	
Water	1.10	1.46	[289]
Hydrogen	1.26	1.68	[289]
Hydrogen	1.27	1.70	REFPROP [452]

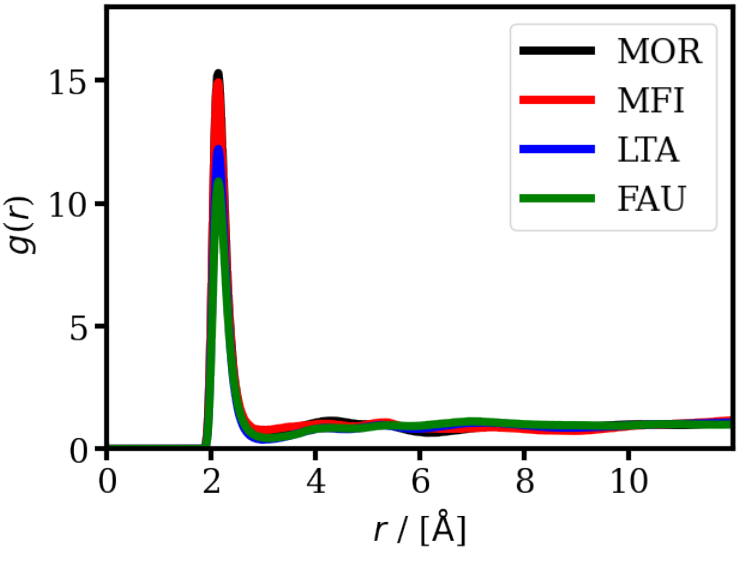

Figure A.1: Radial distribution functions for the oxygen atoms of the water molecules and the Na^+ cations on MOR- (black), MFI- (red), LTA- (blue), and FAU-type (green) zeolites with the lowest Si/Al ratio at $P = 875$ bar, $T = 310$ K, and $y_{H_2O} = 12.3$ ppm (molar) for Chapter 4. The computed loading of each component and the Si/Al ratio of each zeolite type are listed in the Supporting Information of Ref. [289].

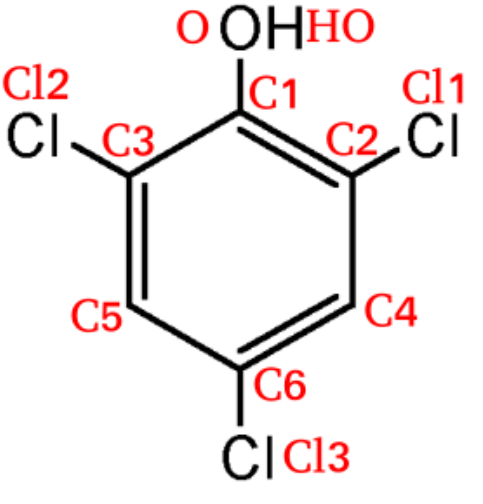

Figure A.2: Representation of the 2,4,6-trichlorophenol molecule used in Chapter 5. The atom names are shown in red.

Table A.8: Lennard-Jones parameters and atomic charges used in Chapter 5. Atom names are shown in Figure A.2 for TCP. The force field parameters of TCP, water, zeolite are taken from the GAFF [314], SPC/E [315], and ClayFF [316], respectively.

Molecule	Atom name	Atom type	$\frac{\epsilon_{ii}}{k_B}$ / [K]	σ_{ii} / [Å]	q_i / [e$^-$]
2,4,6-trichlorophenol	C1	CA	43.277	3.4	0.543841
	C2	CA	43.277	3.4	-0.246516
	C3	CA	43.277	3.4	-0.246516
	C4	CA	43.277	3.4	0.073606
	C5	CA	43.277	3.4	0.073606
	C6	CA	43.277	3.4	-0.143285
	O	O	105.877	3.066	-0.524338
	Cl1	CL	85.547	3.475	-0.051323
	Cl2	CL	85.547	3.475	-0.051323
	Cl3	CL	85.547	3.475	-0.083382
	H1	HA	7.55	2.6	0.141479
	H2	HA	7.55	2.6	0.141479
	H3	HO	0	0	0.372672
Water	O	OW	78.208	3.166	-0.8476
	H	HOW	0	0	0.4238
Zeolite	Si	SI	0	3.302	2.1
	Al	AL	0	3.302	1.575
	OSi	OSI	78.2	3.166	-1.05
	OAl	OAL	78.2	3.166	-1.16875
	Na	NA	65.5	2.35	1

Table A.9: Bond angle bending parameters for all angle types used in Chapter 5. The force field parameters of TCP and water, are taken from the GAFF [314] and SPC/E [315] force fields, respectively.

Molecule	Bond	K_θ / [K rad^2]	θ_0 / [degrees]
2,4,6-trichlorophenol	CA-CA-CA	33806.3	120.00
	CA-O-CA	35149.9	120.00
	CA-CA-CL	31662.6	120.00
	CA-CA-HA	24386.0	120.00
	CA-O-HO	24582.3	109.47
Water	HW-OW-HW	fixed	109.47

Table A.10: Dihedral angle torsion parameters for all dihedral type used in Chapter 5. The force field parameters of TCP are taken from the GAFF [314] force field.

Molecule	Dihedral angle	a_0 / [kJ mol^{-1}]	a_1 / [-]	δ / [degrees]
2,4,6-trichlorophenol	CA-CA-CA-CA	15.166	2	180
	CA-CA-O-HO	3.765	2	180
	CA-CA-CA-CL	4.6	2	180
	CA-CA-O-CA	4.6	2	180
	CA-CA-CA-HA	4.6	2	180

A.1. ATTACH-PULL-RELEASE (APR) METHOD

A short description of the Attach-Pull-Release method used in Chapter 6 for the calculation of binding free energies the selected OMPs with βCD [386] is provided here. In this method, the calculation of the binding free energy is divided into four parts. In the first part (attachment phase), thermodynamic integration is performed to measure the amount of work needed for transferring the host-guest complex to a reference state from its equilibrium configuration. In the second part (pulling phase), the reference state is taken as the initial configuration, and the guest molecule is pulled out of the host to a distance at which the host-guest interactions vanish. In the third part (detachment phase), a thermodynamic integration is performed, starting from the final configuration of the second part, to measure the amount of work which is needed to remove the restraints imposed on the host molecule. In the final part, the rest of the imposed restraints are accounted for using a semi-analytical expression and the amount of work needed to transfer the guest to standard conditions is calculated. The binding free energy can be calculated by combining all of the components of the work obtained from the four parts. The detailed description of the APR method can be found in the study by Henriksen et al. [386]. The same terminology is used in this work as in the original publication of the method. In the the attachment phase, the distance/angle restraints between the OMP and the anchor (λ_p), and the dihedral restraints of the βCD (λ_c) are gradually turned on over 53 simulation windows from $\lambda_p, \lambda_c = 0$ to $\lambda_p, \lambda_c = 1$. The λ values are uniformly distributed over the 53 simulation windows. The final force constant for the distance restraint at $\lambda_p = 1$ is $k_{\text{dist-OMP}} = 8368$ kJ mol^{-1} nm^{-2} and for the angle restraints the final force constant is $k_{\text{ang-OMP}} = 836.8$ kJ mol^{-1} rad^{-2}. The force constant of the dihedral restraints at $\lambda_c = 1$ is $k_{\text{ang-}\beta\text{CD}} = 50.316$ kJ mol^{-1} rad^{-2}. The free energy difference is calculated by using the built-in BAR module in GROMACS [387] which is based on the Bennett's acceptance ratio method [453].

In the pulling phase, all of the restraints are fully turned on and the equilibrium distance between the OMP and the anchor is varied from 6 Å to 24 Å over 73 simulation windows which entails a 0.25 Å difference between two adjacent simulation windows. The free energy difference of the pulling phase is calculated using the built-in WHAM module in GROMACS [387] which is based on the weighted histogram analysis method. The uncertainties are calculated using the bootstrapping method built-in to the WHAM module [454].

In the detachment phase, the dihedral restraints of the βCD are turned off using the same methodology as in the attachment. This stage consisted of 53 simulation windows with a uniformly distributed λ_c from 1 to 0. The free energy difference is calculated the using the built-in BAR module in GROMACS which is based on the Ben-

nett's acceptance ratio method.

In all simulations the system consists of a βCD, an OMP, 3 anchor atoms, 6000 water molecules, 6 pairs of sodium chloride and the necessary amount of sodium to make the system charge neutral.

A.2. SOLVENT BALANCE METHOD

A short description of the Solvent balance method used for the calculation of binding enthalpies of the selected OMPs with βCD [395] in Chapter 6 is provided here. In this method, four separate simulations are carried out and the binding enthalpy is calculated based on the potential energies of the four systems. To obtain the binding enthalpy, it is necessary to simulate the following distinct systems: (1) the host-guest complex in the solvent, (2) the free host in the solvent, (3) the free guest in the solvent, and (4) the pure solvent. The trajectories produced in the simulations (1), (2), (3), and (4) are referred to as (SOLV), (HOST), (GUEST), and (COMP) trajectories. In these simulations, no restraints are used. In all simulations 3000 water molecules, 3 pairs of ions (sodium chloride) and the necessary amount of sodium ions to make the system charge neutral are used. All MD simulations are performed for 1.5 μs and the averages are calculated from that trajectory. For more details and discussion of the theoretical background of this method the reader is referred to the study by Fenley *et al.* [395].

The enthalpy decomposition followed a similar methodology as presented by Tang et. al. [366]. The decomposed enthalpy terms are defined as follows:

$$\Delta H_{\text{host-guest}} = \langle E_{\text{host-guest}}\rangle_{\text{COMP}} - \langle E_{\text{host}}\rangle_{\text{HOST}} - \langle E_{\text{guest}}\rangle_{\text{GUEST}} \tag{A.1}$$

$$\Delta H_{\text{host configuration}} = \langle E_{\text{host}}\rangle_{\text{COMP}} - \langle E_{\text{host}}\rangle_{\text{HOST}} \tag{A.2}$$

$$\Delta H_{\text{guest configuration}} = \langle E_{\text{guest}}\rangle_{\text{COMP}} - \langle E_{\text{guest}}\rangle_{\text{GUEST}} \tag{A.3}$$

$$\Delta H_{\text{solute intermolecular}} = \langle E_{\text{host-guest}}\rangle_{\text{COMP}} - \langle E_{\text{host}}\rangle_{\text{COMP}} - \langle E_{\text{guest}}\rangle_{\text{COMP}} \tag{A.4}$$

$$\Delta H_{\text{desolvation}} = \Delta H_{\text{host-solvent}} + \Delta H_{\text{guest-solvent}} + \Delta H_{\text{solvent-solvent}} \tag{A.5}$$

$$\Delta H_{\text{host-solvent}} = \left(\langle E_{\text{solvent-host}}\rangle_{\text{COMP}} - \langle E_{\text{solvent}}\rangle_{\text{COMP}} - \langle E_{\text{host}}\rangle_{\text{COMP}}\right) \tag{A.6}$$

$$- \left(\langle E_{\text{solvent-host}}\rangle_{\text{HOST}} - \langle E_{\text{solvent}}\rangle_{\text{HOST}} - \langle E_{\text{host}}\rangle_{\text{HOST}}\right) \tag{A.7}$$

$$\Delta H_{\text{guest-solvent}} = \left(\langle E_{\text{solvent-guest}}\rangle_{\text{COMP}} - \langle E_{\text{solvent}}\rangle_{\text{COMP}} - \langle E_{\text{guest}}\rangle_{\text{COMP}}\right) \tag{A.8}$$

$$- \left(\langle E_{\text{solvent-guest}}\rangle_{\text{GUEST}} - \langle E_{\text{solvent}}\rangle_{\text{GUEST}} - \langle E_{\text{guest}}\rangle_{\text{GUEST}}\right) \tag{A.9}$$

$$\Delta H_{\text{solvent-solvent}} = \langle E_{\text{solvent}}\rangle_{\text{COMP}} + \langle E_{\text{solvent}}\rangle_{\text{solvent}} - \langle E_{\text{solvent}}\rangle_{\text{HOST}} - \langle E_{\text{solvent}}\rangle_{\text{GUEST}} \tag{A.10}$$

Here the $\langle E_{\text{solvent}}\rangle_{\text{COMP}}$, $\langle E_{\text{host}}\rangle_{\text{COMP}}$, $\langle E_{\text{guest}}\rangle_{\text{COMP}}$, $\langle E_{\text{host-guest}}\rangle_{\text{COMP}}$ are the av-

erage potential energies of the solvent, the βCD, the OMP, and the βCD-OMP complex in the (COMP) simulation trajectory, respectively. The $\langle E_{\text{solvent}}\rangle_{\text{HOST}}$, $\langle E_{\text{host}}\rangle_{\text{HOST}}$, $\langle E_{\text{solvent-host}}\rangle_{\text{HOST}}$ terms are representing the average potential energies of the solvent, the βCD, and the host+solvent together in the (HOST) trajectory. The $\langle E_{\text{solvent}}\rangle_{\text{GUEST}}$, $\langle E_{\text{guest}}\rangle_{\text{GUEST}}$, $\langle E_{\text{solvent-guest}}\rangle_{\text{GUEST}}$ terms are representing the average potential energies of the solvent, the OMP, and the guest+solvent together in the (GUEST) trajectory.

A.3. COMBINED BINDING FREE ENERGY AND ENTHALPY CALCULATION

In Chapter 6, computed and experimentally measured binding free energies and binding enthalpies are compared. Since several binding orientations can contribute to the binding of OMPs with β-CD, the predicted binding free energies and binding enthalpies are calculated by combining the results from several binding orientations. The following equation is used to obtain the binding free energy based on the different binding orientations [386]:

$$\Delta G_{\text{combined}} = -RT \ln \sum_{n=1}^{N_m} e^{-\frac{\Delta G_n}{RT}} \tag{A.11}$$

where $\Delta G_{\text{combined}}$ is the combined free energy of the different orientations, R is the universal gas constant, T is temperature, N_m is the total number of different binding orientations, and ΔG_n is the binding free energy of binding orientation n. The symbol Δ indicates the difference between two states of the system, namely, the state in which the OMP is in the bulk phase and the state in which the OMP forms an inclusion complex with the βCD. Similarly, the combined binding enthalpy, $\Delta H_{\text{combined}}$, is calculated using [386]:

$$\Delta H_{\text{combined}} = \frac{\sum_{n=1}^{N_m} \Delta H_n e^{-\frac{\Delta G_n}{RT}}}{\sum_{n=1}^{N_m} e^{-\frac{\Delta G_n}{RT}}} \tag{A.12}$$

where ΔH_n is the binding enthalpy of binding orientation n.

Table A.11: Computed shear viscosities (η) of water for four different water force fields for temperatures from 298.15 K to 312.15 K and at P = 1 bar for Chapter 7. The numbers in the brackets indicate the uncertainty (one standard deviation) in the last digit.

T / [K]	η_{TIP3P} / [mPa s]	η_{Bind3P} / [mPa s]	$\eta_{\mathrm{SPC/E}}$ / [mPa s]	$\eta_{\mathrm{TIP4P/2005}}$ / [mPa s]
298.15	0.33(2)	0.29(1)	0.72(2)	0.90(4)
303.15	0.31(2)	0.28(1)	0.68(3)	0.81(3)
308.15	0.29(1)	0.26(1)	0.64(3)	0.73(3)
312.15	0.27(1)	0.25(1)	0.59(4)	0.68(4)

Table A.12: Computed shear viscosities (η) of water for different NaCl concentrations using the Joung and Cheatham [388] and the Madrid-2019 [428] force fields at T = 298.15 K and P = 1 bar. For water, the TIP4P/2005 [295] force field is used. The numbers in the brackets indicate the uncertainty (one standard deviation) in the last digit. The reported values are used for Chapter 7.

M / [mol L^{-1}]	$\eta_{\mathrm{Joung\ and\ Cheatham}}$ / [mPa s]	$\eta_{\mathrm{Madrid-2019}}$ / [mPa s]
0.0	0.90(4)	0.90(4)
0.2	0.95(5)	0.95(3)
0.4	0.94(7)	0.95(6)
0.6	0.98(7)	0.98(3)
0.8	1.10(7)	1.02(1)
1.0	1.16(7)	1.06(3)

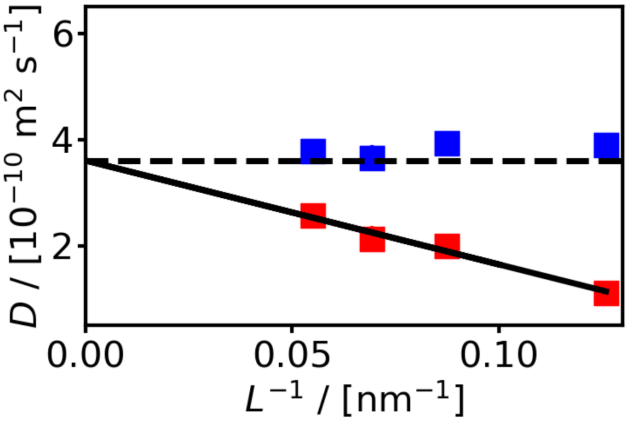

Figure A.3: Computed self-diffusion coefficients of α-CD as a function of the inverse of the simulation box length at T = 298.15 K and P = 1 bar. The symbols in red and blue colors indicate the calculated self-diffusion coefficients without and with using the YH correction [436], respectively. The self diffusion coefficients are calculated using the TIP4P2005 [295] water force field. The error bars are smaller than the symbol sizes.

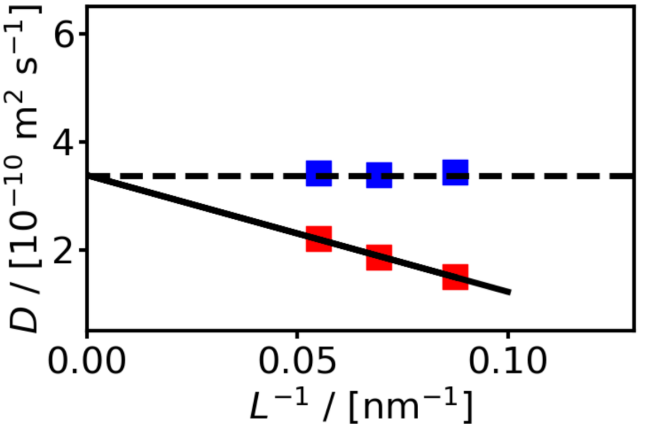

Figure A.4: Computed self-diffusion coefficients of γ-CD as a function of the inverse of the simulation box length at $T = 298.15$ K and $P = 1$ bar. The symbols in red and blue colors indicate the calculated self-diffusion coefficients without and with using the YH correction [436], respectively. The self diffusion coefficients are calculated using the TIP4P2005 [295] water force field. The error bars are smaller than the symbol sizes.

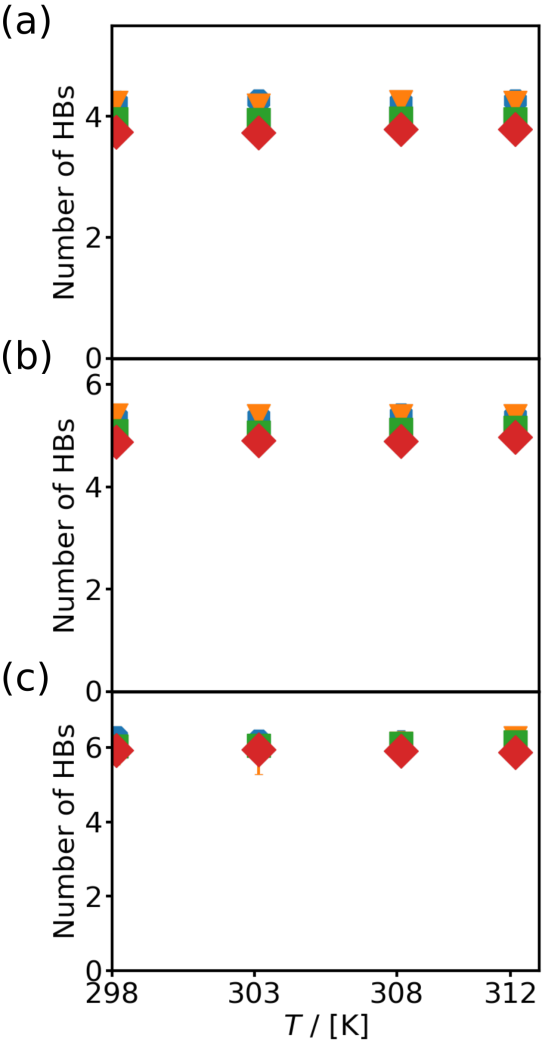

Figure A.5: The average number of intramolecular hydrogen bonds in the (a) α-, (b) β-, and (c) γ-CDs in water as a function of temperature at $P = 1$ bar. The symbols in blue, orange, green, and red colors indicate the average number of hydrogen bonds using the TIP3P [294], Bind3P [367], SPCE [315], and TIP4P2005 [295] force fields, respectively. The error bars are smaller than the symbol sizes.

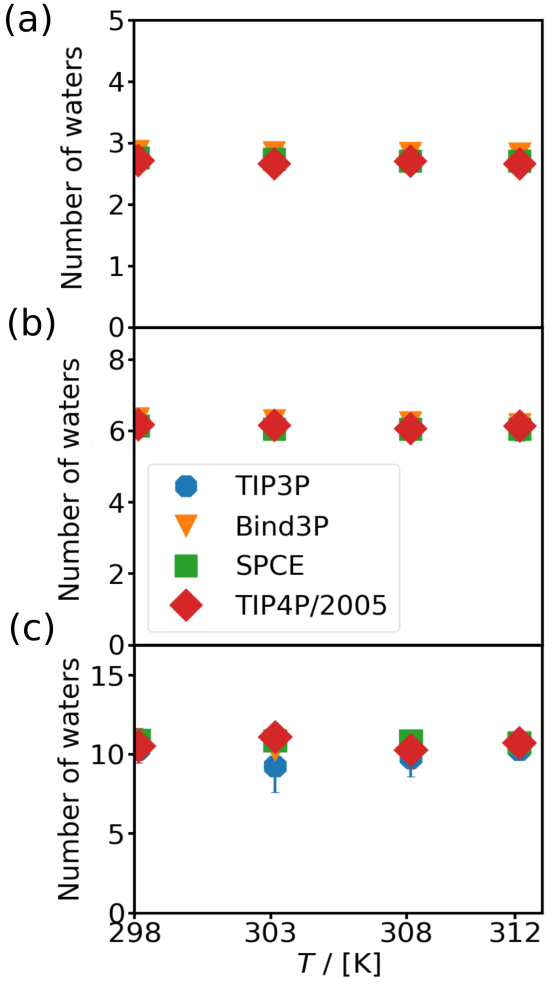

Figure A.6: The average number of water molecules inside the cavity of the (a) α-, (b) β-, and (c) γ-CDs as a function of temperature at $P = 1$ bar. A water molecule is considered to be inside the cavity of the α-, β-, and γ-CD, if the distance between the center of mass of the cyclodextrin and the oxygen of the water molecule is smaller than 0.34, 0.4 and 0.46 nm, respectively. The symbols in blue, orange, green, and red colors indicate the average number of water molecules using the TIP3P [294], Bind3P [367], SPCE [315], and TIP4P2005 [295] force fields, respectively. The error bars are smaller than the symbol sizes.

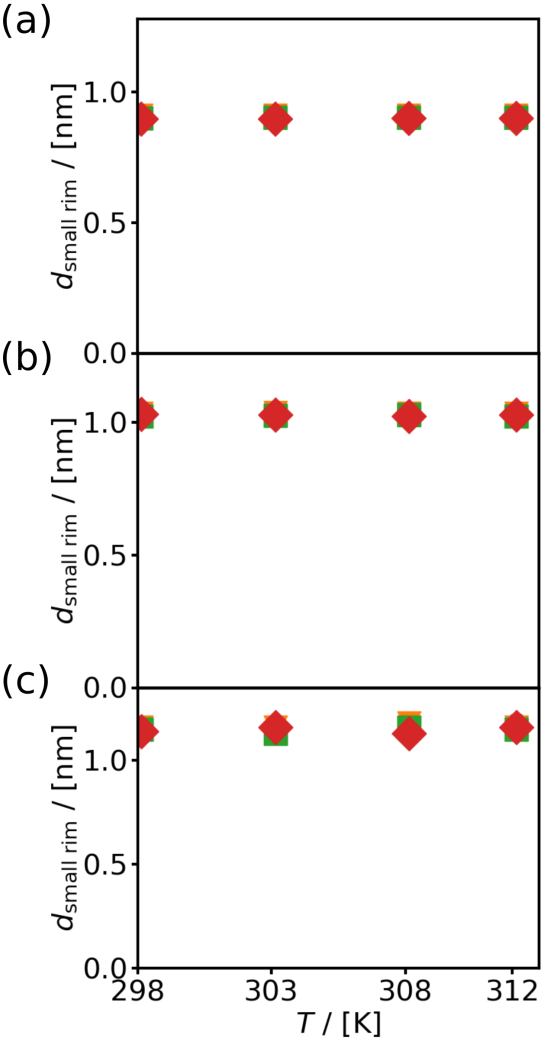

Figure A.7: The diameter of the large rim of (a) α-, (b) β-, and (c) γ-CDs as a function of temperature at $P = 1$ bar. The large diameter is defined as the distance between the geometrically opposite C6 atoms of CDs. A schematic representation of the cyclodextrin is shown in Figure 6.1 where the large rim is indicated by the secondary hydroxyls. The symbols in blue, orange, green, and red colors indicate the average diameter using the TIP3P [294], Bind3P [367], SPCE [315], and TIP4P2005 [295] force fields, respectively. The error bars are smaller than the symbol sizes.

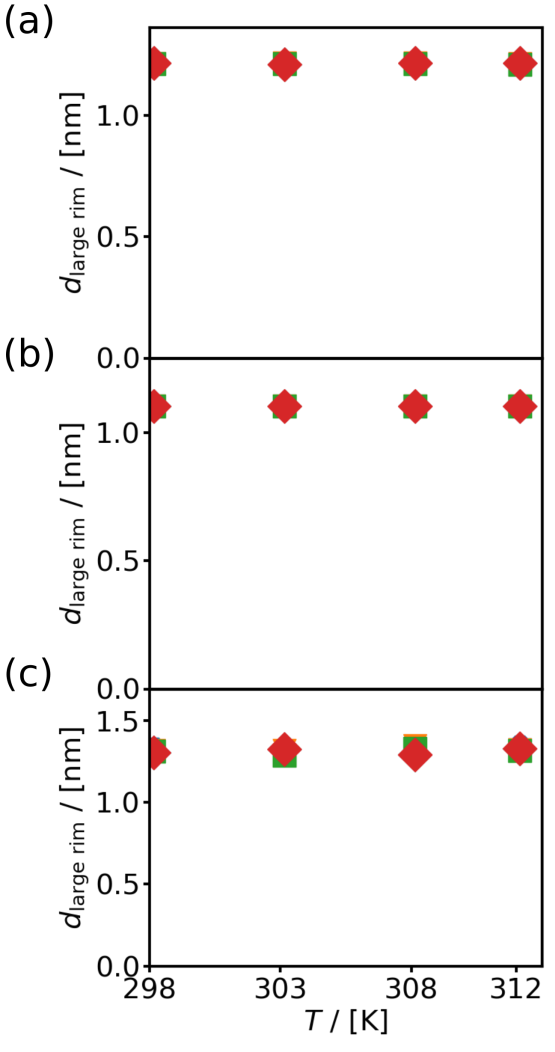

Figure A.8: The diameter of the small rim of (a) α-, (b) β-, and (c) γ-CDs as a function of temperature at $P = 1$ bar. The small diameter is defined as the distance between the geometrically opposite C2 atoms of CDs. A schematic representation of the cyclodextrin is shown in Figure 6.1 where the large rim is indicated by the primary hydroxyls. The symbols in blue, orange, green, and red colors indicate the average diameter using the TIP3P [294], Bind3P [367], SPCE [315], and TIP4P2005 [295] force fields, respectively. The error bars are smaller than the symbol sizes.

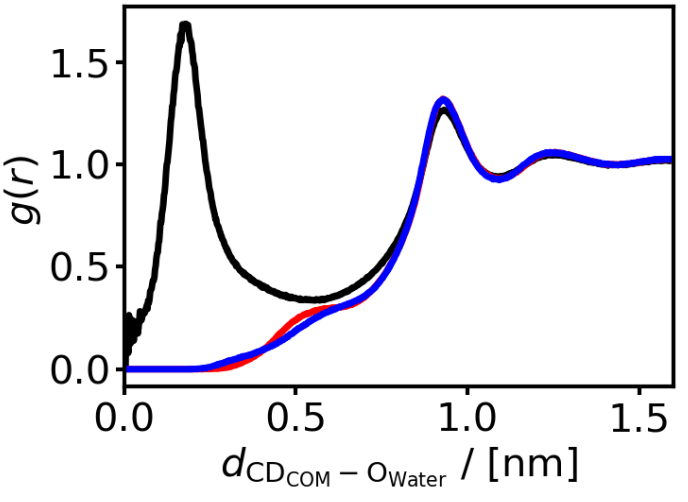

Figure A.9: Radial distribution functions for the distance between the center of mass of the β-CD and the oxygen atom of the water molecules at $T = 298.15$ K and $P = 1$ bar. The black, red and blue colors indicate the systems with a free β-CD, with an ibuprofen:β-CD inclusion complex in orientation 1 (see Figure 6.1), and with an ibuprofen:β-CD inclusion complex in orientation 2 (see Figure 6.1), respectively. For water, the TIP4P/2005 [295] water force field is used.

REFERENCES

[1] N. Jiang, M. Erdős, O. A. Moultos, R. Shang, T. J. H. Vlugt, S. G. Heijman, and L. C. Rietveld, *The adsorption mechanisms of organic micropollutants on high-silica zeolites causing s-shaped adsorption isotherms: An experimental and Monte Carlo simulation study,* Chemical Engineering Journal **389**, 123968 (2020).

[2] N. Jiang, R. Shang, S. G. Heijman, and L. C. Rietveld, *High-silica zeolites for adsorption of organic micro-pollutants in water treatment: A review,* Water Research **144**, 145 (2018).

[3] M. W. Ackley, S. U. Rege, and H. Saxena, *Application of natural zeolites in the purification and separation of gases,* Microporous and Mesoporous Materials **61**, 25 (2003).

[4] D. de Ridder, J. Verberk, S. Heijman, G. Amy, and J. van Dijk, *Zeolites for nitrosamine and pharmaceutical removal from demineralised and surface water: Mechanisms and efficacy,* Separation and Purification Technology **89**, 71 (2012).

[5] J.-R. Li, R. J. Kuppler, and H.-C. Zhou, *Selective gas adsorption and separation in metal-organic frameworks,* Chemical Society Reviews **38**, 1477 (2009).

[6] U. Mueller, M. Schubert, F. Teich, H. Puetter, K. Schierle-Arndt, and J. Pastré, *Metal-organic frameworks - prospective industrial applications,* Journal of Materials Chemistry **16**, 626 (2006).

[7] F. Di Renzo, *Zeolites as tailor-made catalysts: Control of the crystal size,* Catalysis Today **41**, 37 (1998).

[8] J. Weitkamp, *Zeolites and catalysis,* Solid State Ionics **131**, 175 (2000).

[9] W. Hölderich and H. van Bekkum, *Chapter 16 "Zeolites in organic syntheses",* in *Introduction to Zeolite Science and Practice,* Studies in Surface Science and Catalysis, Vol. 58, edited by H. van Bekkum, E. Flanigen, and J. Jansen (Elsevier, 1991) pp. 631 – 726.

[10] S. Kitagawa, R. Kitaura, and S.-I. Noro, *Functional porous coordination polymers,* Angewandte Chemie - International Edition **43**, 2334 (2004).

[11] D. I. Tchernev, *Natural Zeolites in Solar Energy Heating, Cooling, and Energy Storage,* Reviews in Mineralogy and Geochemistry **45**, 589 (2001).

[12] K. Johannes, F. Kuznik, J.-L. Hubert, F. Durier, and C. Obrecht, *Design and characterisation of a high powered energy dense zeolite thermal energy storage system for buildings,* Applied Energy **159**, 80 (2015).

[13] Y. I. Aristov, *Novel materials for adsorptive heat pumping and storage: Screening and nanotailoring of sorption properties,* Journal of Chemical Engineering of Japan **40**, 1242 (2007).

[14] S. K. Henninger, F. Jeremias, H. Kummer, and C. Janiak, *MOFs for use in adsorption heat pump processes,* European Journal of Inorganic Chemistry , 2625 (2012).

[15] N. E. R. Zimmermann and M. Haranczyk, *History and utility of zeolite framework-type discovery from a data-science perspective,* Crystal Growth & Design **16**, 3043 (2016).

[16] P. G. Boyd, Y. Lee, and B. Smit, *Computational development of the nanoporous materials genome,* Nature Reviews Materials **2**, 17037 (2017).

[17] W. J. Mortier and R. A. Schoonheydt, *Surface and solid state chemistry of zeolites,* Progress in Solid State Chemistry **16**, 1 (1985).

[18] C. Baerlocher and L. McCusker, *Database of zeolite structures,* Available at http://www.iza-structure.org/databases/ (accessed at 2021.11.20).

[19] M. Treacy and M. Foster, *Hypothetical zeolite database,* Available at http://www.hypotheticalzeolites.net/ (accessed at 2020.01.15).

[20] Y. Lee, S. D. Barthel, P. Dłotko, S. M. Moosavi, K. Hess, and B. Smit, *High-throughput screening approach for nanoporous materials genome using topological data analysis: Application to zeolites,* Journal of Chemical Theory and Computation **14**, 4427 (2018).

[21] D. J. Earl and M. W. Deem, *Toward a database of hypothetical zeolite structures,* Industrial & Engineering Chemistry Research **45**, 5449 (2006).

[22] M. E. DAVIS, *Zeolites and molecular sieves : not just ordinary catalysts,* Industrial & Engineering Chemistry Research **30**, 1675 (1991).

[23] S. Abate, K. Barbera, G. Centi, P. Lanzafame, and S. Perathoner, *Disruptive catalysis by zeolites,* Catal. Sci. Technol. **6**, 2485 (2016).

[24] Y. Li and J. Yu, *Emerging applications of zeolites in catalysis, separation and host-guest assembly,* Nature Reviews Materials **In Press** (2021), 10.1038/s41578-021-00347-3.

[25] E.-P. Ng and S. Mintova, *Nanoporous materials with enhanced hydrophilicity and high water sorption capacity,* Microporous and Mesoporous Materials **114**, 1 (2008).

[26] A. García-Sánchez, C. O. Ania, J. B. Parra, D. Dubbeldam, T. J. H. Vlugt, R. Krishna, and S. Calero, *Transferable force field for carbon dioxide adsorption in zeolites,* Journal of Physical Chemistry C **113**, 8814 (2009).

[27] M. Khalid, G. Joly, A. Renaud, and P. Magnoux, *Removal of phenol from water by adsorption using zeolites,* Industrial & Engineering Chemistry Research **43**, 5275 (2004).

[28] L. Li, Q. Wang, H. Liu, T. Sun, D. Fan, M. Yang, P. Tian, and Z. Liu, *Preparation of spherical mordenite zeolite assemblies with excellent catalytic performance for dimethyl ether carbonylation,* ACS Applied Materials & Interfaces **10**, 32239 (2018).

[29] S. Wang, P. Bai, Y. Wei, W. Liu, X. Ren, J. Bai, Z. Lu, W. Yan, and J. Yu, *Three-dimensional-printed core–shell structured MFI-type zeolite monoliths for volatile organic compound capture under humid conditions,* ACS Applied Materials & Interfaces **11**, 38955 (2019).

[30] H. Thakkar, S. Eastman, A. Hajari, A. A. Rownaghi, J. C. Knox, and F. Rezaei, *3d-printed zeolite monoliths for CO_2 removal from enclosed environments,* ACS Applied Materials & Interfaces **8**, 27753 (2016).

[31] Y. Quan, S. Li, S. Wang, Z. Li, M. Dong, Z. Qin, G. Chen, Z. Wei, W. Fan, and J. Wang, *Synthesis of chainlike ZSM-5 zeolites: Determination of synthesis parameters, mechanism of chainlike morphology formation, and their performance in selective adsorption of xylene isomers,* ACS Applied Materials & Interfaces **9**, 14899 (2017).

[32] J. Perez-Carbajo, I. Matito-Martos, S. R. G. Balestra, M. N. Tsampas, M. C. M. van de Sanden, J. A. Delgado, V. I. Águeda, P. J. Merkling, and S. Calero, *Zeolites for CO_2–CO–O_2 separation to obtain CO_2-neutral fuels,* ACS Applied Materials & Interfaces **10**, 20512 (2018).

[33] Y. Yu, X. Li, R. Krishna, Y. Liu, Y. Cui, J. Du, Z. Liang, X. Song, and J. Yu, *Enhancing CO_2 adsorption and separation properties of aluminophosphate zeolites by isomorphous heteroatom substitutions,* ACS Applied Materials & Interfaces **10**, 43570 (2018).

[34] A. Itadani, A. Oda, H. Torigoe, T. Ohkubo, M. Sato, H. Kobayashi, and Y. Kuroda, *Material exhibiting efficient CO_2 adsorption at room temperature for concentrations lower than 1000 ppm: Elucidation of the state of barium ion exchanged in an MFI-type zeolite,* ACS Applied Materials & Interfaces **8**, 8821 (2016).

[35] Z. Song, Q. Dong, W. L. Xu, F. Zhou, X. Liang, and M. Yu, *Molecular layer deposition-modified 5A zeolite for highly efficient CO_2 capture,* ACS Applied Materials & Interfaces **10**, 769 (2018).

[36] B. Besser, H. A. Tajiri, G. Mikolajczyk, J. Möllmer, T. C. Schumacher, S. Odenbach, R. Gläser, S. Kroll, and K. Rezwan, *Hierarchical porous zeolite structures for pressure swing adsorption applications,* ACS Applied Materials & Interfaces **8**, 3277 (2016).

[37] Z. Zhu, H. Xu, J. Jiang, H. Wu, and P. Wu, *Hydrophobic nanosized all-silica beta zeolite: Efficient synthesis and adsorption application,* ACS Applied Materials & Interfaces **9**, 27273 (2017).

[38] Q. Al-Naddaf, H. Thakkar, and F. Rezaei, *Novel zeolite-5A@MOF-74 composite adsorbents with core–shell structure for H_2 purification,* ACS Applied Materials & Interfaces **10**, 29656 (2018).

[39] R. Shaw, R. Sharma, S. Tiwari, and S. K. Tiwari, *Surface engineered zeolite: An active interface for rapid adsorption and degradation of toxic contaminants in water,* ACS Applied Materials & Interfaces **8**, 12520 (2016).

[40] K. M. Gupta, Z. Qiao, K. Zhang, and J. Jiang, *Seawater pervaporation through zeolitic imidazolate framework membranes: Atomistic simulation study,* ACS Applied Materials & Interfaces **8**, 13392 (2016).

[41] J. Cai, L. Li, X. Lv, C. Yang, and X. Zhao, *Large surface area ordered porous carbons via nanocasting Zeolite 10X and high performance for hydrogen storage application,* ACS Applied Materials & Interfaces **6**, 167 (2014).

[42] T. Ben, H. Ren, S. Ma, D. Cao, J. Lan, X. Jing, W. Wang, J. Xu, F. Deng, J. Simmons, S. Qiu, and G. Zhu, *Targeted synthesis of a porous aromatic framework with high stability and exceptionally high surface area,* Angewandte Chemie International Edition **48**, 9457 (2009).

[43] P. J. Waller, F. Gándara, and O. M. Yaghi, *Chemistry of covalent organic frameworks,* Accounts of Chemical Research **48**, 3053 (2015).

[44] B. Chen, Z. Yang, Y. Zhu, and Y. Xia, *Zeolitic imidazolate framework materials: recent progress in synthesis and applications,* Journal of Materials Chemistry A **2**, 16811 (2014).

[45] D. Dubbeldam, S. Calero, and T. J. H. Vlugt, *iRASPA: GPU-accelerated visualization software for materials scientists,* Molecular Simulation **44**, 653 (2018).

[46] H.-C. J. Zhou and S. Kitagawa, *Metal-organic frameworks (MOFs),* Chemical Society Reviews **43**, 5415 (2014).

[47] C. V. McGuire and R. S. Forgan, *The surface chemistry of metal-organic frameworks,* Chemical Communications **51**, 5199 (2015).

[48] P. Z. Moghadam, A. Li, S. B. Wiggin, A. Tao, A. G. P. Maloney, P. A. Wood, S. C. Ward, and D. Fairen-Jimenez, *Development of a cambridge structural database subset: A collection of metal-organic frameworks for past, present, and future,* Chemistry of Materials **29**, 2618 (2017).

[49] H. Furukawa, K. E. Cordova, M. O'Keeffe, and O. M. Yaghi, *The chemistry and applications of metal-organic frameworks,* Science **341**, 1230444 (2013).

[50] W. X. Zhang, P. Q. Liao, R. B. Lin, Y. S. Wei, M. H. Zeng, and X. M. Chen, *Metal cluster-based functional porous coordination polymers,* Coordination Chemistry Reviews **293-294**, 263 (2015).

[51] A. W. Thornton, C. M. Simon, J. Kim, O. Kwon, K. S. Deeg, K. Konstas, S. J. Pas, M. R. Hill, D. A. Winkler, M. Haranczyk, and B. Smit, *Materials genome in action: Identifying the performance limits of physical hydrogen storage,* Chemistry of Materials **29**, 2844 (2017).

[52] C. M. Simon, J. Kim, D. A. Gomez-Gualdron, J. S. Camp, Y. G. Chung, R. L. Martin, R. Mercado, M. W. Deem, D. Gunter, M. Haranczyk, D. S. Sholl, R. Q. Snurr, and B. Smit, *The materials genome in action: Identifying the performance limits for methane storage,* Energy and Environmental Science **8**, 1190 (2015).

[53] C. Zhang and W. J. Koros, *Zeolitic imidazolate framework-enabled membranes: Challenges and opportunities,* Journal of Physical Chemistry Letters **6**, 3841 (2015).

[54] R. L. Martin, C. M. Simon, B. Smit, and M. Haranczyk, *In silico design of porous polymer networks: High-throughput screening for methane storage materials,* Journal of the American Chemical Society **136**, 5006 (2014).

[55] Y. Gu, J. Zhao, and J. A. Johnson, *Polymer networks: From plastics and gels to porous frameworks,* Angewandte Chemie International Edition **59**, 5022 (2020).

[56] G. Crini, *Review: A history of cyclodextrins,* Chemical Reviews **114**, 10940 (2014).

[57] G. Crini, S. Fourmentin, È. Fenyvesi, G. Torri, M. Fourmentin, and N. Morin-Crini, *Cyclodextrins, from molecules to applications,* Environmental Chemistry Letters **16**, 1361 (2018).

[58] A. Popielec and T. Loftsson, *Effects of cyclodextrins on the chemical stability of drugs,* International Journal of Pharmaceutics **531**, 532 (2017).

[59] K. A. Connors, *The stability of cyclodextrin complexes in solution,* Chemical Reviews **97**, 1325 (1997).

[60] H. M. C. Marques, *A review on cyclodextrin encapsulation of essential oils and volatiles,* Flavour and Fragrance Journal **25**, 313 (2010).

[61] S. Jacob and A. B. Nair, *Cyclodextrin complexes: Perspective from drug delivery and formulation,* Drug Development Research **79**, 201 (2018).

[62] M. E. Davis and M. E. Brewster, *Cyclodextrin-based pharmaceutics: past, present and future,* Nature Reviews Drug Discovery **3**, 1023–1035 (2004).

[63] F. Hapiot, A. Ponchel, S. Tilloy, and E. Monflier, *Cyclodextrins and their applications in aqueous-phase metal-catalyzed reactions,* Comptes Rendus Chimie **14**, 149 (2011).

[64] F. Hapiot, H. Bricout, S. Menuel, S. Tilloy, and E. Monflier, *Recent breakthroughs in aqueous cyclodextrin-assisted supramolecular catalysis,* Catal. Sci. Technol. **4**, 1899 (2014).

[65] È. Fenyvesi, M. Vikmon, and L. Szente, *Cyclodextrins in food technology and human nutrition: Benefits and limitations,* Critical Reviews in Food Science and Nutrition **56**, 1981 (2016).

[66] A. Ciobanu, D. Landy, and S. Fourmentin, *Complexation efficiency of cyclodextrins for volatile flavor compounds,* Food Research International **53**, 110 (2013).

[67] G. K. Scriba, *Chiral recognition in separation science – an update,* Journal of Chromatography A **1467**, 56 (2016).

[68] Y. Xiao, S.-C. Ng, T. T. Y. Tan, and Y. Wang, *Recent development of cyclodextrin chiral stationary phases and their applications in chromatography,* Journal of Chromatography A **1269**, 52 (2012).

[69] M. W. Deem, R. Pophale, P. A. Cheeseman, and D. J. Earl, *Computational discovery of new zeolite-like materials,* Journal of Physical Chemistry C **113**, 21353 (2009).

[70] D. P. Broom and K. M. Thomas, *Gas adsorption by nanoporous materials: Future applications and experimental challenges,* MRS Bulletin **38**, 412–421 (2013).

[71] S. Brandani, E. Mangano, and L. Sarkisov, *Net, excess and absolute adsorption and adsorption of helium,* Adsorption **22**, 261 (2016).

[72] S. Mintova, J.-P. Gilson, and V. Valtchev, *Advances in nanosized zeolites,* Nanoscale **5**, 6693 (2013).

[73] A. Sayari, *Catalysis by crystalline mesoporous molecular sieves,* Chemistry of Materials **8**, 1840 (1996).

[74] L.-C. Lin, A. Berger, R. Martin, J. Kim, J. Swisher, K. Jariwala, C. Rycroft, A. Bhown, M. Deem, M. Haranczyk, and B. Smit, *In silico screening of carbon-capture materials,* Nature Materials **11**, 633 (2012).

[75] B. Smit and T. L. M. Maesen, *Molecular simulations of zeolites: Adsorption, diffusion, and shape selectivity,* Chemical Reviews **108**, 4125 (2008).

[76] D. Frenkel and B. Smit, *Understanding molecular simulation*, 2nd ed. (Academic Press, London, 2001).

[77] M. P. Allen and D. J. Tildesley, *Computer Simulation of Liquids*, 2nd ed. (Oxford University Press, Oxford, 2017).

[78] M. Tuckerman, *Computer Simulation of Liquids*, 1st ed. (Oxford Graduate Press, Oxford, 2010).

[79] D. Dubbeldam, S. Calero, D. E. Ellis, and R. Q. Snurr, *RASPA: Molecular simulation software for adsorption and diffusion in flexible nanoporous materials,* Molecular Simulation **42**, 81 (2016).

[80] A. F. Voter, *Introduction to the Kinetic Monte Carlo Method*, 1st ed. (Springer, Dordrecht, 2005).

[81] S. H. Jamali, L. Wolff, T. M. Becker, A. Bardow, T. J. H. Vlugt, and O. A. Moultos, *Finite-size effects of binary mutual diffusion coefficients from molecular dynamics,* Journal of Chemical Theory and Computation **14**, 2667 (2018).

[82] M. Erdős, O. Galteland, D. Bedeaux, S. Kjelstrup, O. A. Moultos, and T. J. H. Vlugt, *Gibbs Ensemble Monte Carlo simulation of fluids in confinement: Relation between the differential and integral pressures,* Nanomaterials **10**, 293 (2020).

[83] K. E. Gubbins, Y. Long, and M. Śliwinska Bartkowiak, *Thermodynamics of confined nano-phases,* Journal of Chemical Thermodynamics **74**, 169 (2014).

[84] T. Ikeshoji, B. Hafskjold, and H. Furuholt, *Molecular-level calculation scheme for pressure in inhomogeneous systems of flat and spherical layers,* Molecular Simulation **29**, 101 (2003).

[85] A. Poursaeidesfahani, A. Torres-Knoop, D. Dubbeldam, and T. J. H. Vlugt, *Direct free energy calculation in the Continuous Fractional Component Gibbs ensemble,* Journal of Chemical Theory and Computation **12**, 1481 (2016).

[86] A. Rahbari, J. Brenkman, R. Hens, M. Ramdin, L. J. P. van den Broeke, R. Schoon, R. Henkes, O. A. Moultos, and T. J. H. Vlugt, *Solubility of water in hydrogen at high pressures: A molecular simulation study,* Journal of Chemical & Engineering Data **64**, 4103 (2019).

[87] J. M. Castillo, J. Silvestre-Albero, F. Rodriguez-Reinoso, T. J. H. Vlugt, and S. Calero, *Water adsorption in hydrophilic zeolites: experiment and simulation,* Physical Chemistry Chemical Physics. **15**, 17374 (2013).

[88] J. Kuhn, J. M. Castillo-Sanchez, J. Gascon, S. Calero, D. Dubbeldam, T. J. H. Vlugt, F. Kapteijn, and J. Gross, *Adsorption and diffusion of water, methanol, and ethanol in all-silica DD3R: Experiments and simulation,* Journal of Physical Chemistry C **113**, 14290 (2009).

[89] A. Rahbari, R. Hens, M. Ramdin, O. A. Moultos, D. Dubbeldam, and T. J. H. Vlugt, *Recent advances in the Continuous Fractional Component Monte Carlo methodology,* Molecular Simulation **47**, 804 (2021).

[90] D. Dubbeldam, A. Torres-Knoop, and K. S. Walton, *On the inner workings of Monte Carlo codes,* Molecular Simulation **39**, 1253 (2013).

[91] H. Furukawa, F. Gándara, Y.-B. Zhang, J. Jiang, W. L. Queen, M. R. Hudson, and O. M. Yaghi, *Water adsorption in porous metal–organic frameworks and related materials,* Journal of the American Chemical Society **136**, 4369 (2014).

[92] M. Trzpit, M. Soulard, J. Patarin, N. Desbiens, F. Cailliez, A. Boutin, I. Demachy, and A. H. Fuchs, *The effect of local defects on water adsorption in silicalite-1 zeolite: A joint experimental and molecular simulation study,* Langmuir **23**, 10131 (2007).

[93] C. Brunchi, J. Castillo Sanchez, A. Stankiewicz, H. Kramer, and T. J. H. Vlugt, *Adsorption of volatile organic compounds. Experimental and theoretical study,* Industrial and Engineering Chemistry Research **51**, 16697 (2012).

[94] A. O. Yazaydin, R. Q. Snurr, T.-H. Park, K. Koh, J. Liu, M. D. LeVan, A. I. Benin, P. Jakubczak, M. Lanuza, D. B. Galloway, J. J. Low, and R. R. Willis, *Screening of metal-organic frameworks for carbon dioxide capture from flue gas using a combined experimental and modeling approach,* Journal of the American Chemical Society **131**, 18198 (2009).

[95] T. J. H. Vlugt and M. Schenk, *Influence of framework flexibility on the adsorption properties of hydrocarbons in the zeolite silicalite,* Journal of Physical Chemistry B **106**, 12757 (2002).

[96] S. A. Zygmunt, L. A. Curtiss, L. E. Iton, and M. K. Erhardt, *Computational studies of water adsorption in the zeolite H-ZSM-5,* Journal of Physical Chemistry **100**, 6663 (1996).

[97] K. S. Deeg, J. J. Gutiérrez-Sevillano, R. Bueno-Pérez, J. B. Parra, C. O. Ania, M. Doblaré, and S. Calero, *Insights on the molecular mechanisms of hydrogen adsorption in zeolites,* Journal of Physical Chemistry C **117**, 14374 (2013).

[98] S. Calero, D. Dubbeldam, R. Krishna, B. Smit, T. J. H. Vlugt, J. F. M. Denayer, J. A. Martens, and T. L. M. Maesen, *Understanding the role of sodium during adsorption: A force field for alkanes in sodium-exchanged faujasites,* Journal of the American Chemical Society **126**, 11377 (2004).

[99] C. Wilmer, M. Leaf, C. Lee, O. Farha, B. Hauser, J. Hupp, and R. Snurr, *Large-scale screening of hypothetical metal-organic frameworks,* Nature Chemistry **4**, 83 (2012).

[100] W. Sun, L.-C. Lin, X. Peng, and B. Smit, *Computational screening of porous metal-organic frameworks and zeolites for the removal of SO_2 and no_x from flue gases,* AIChE Journal **60**, 2314 (2014).

[101] I. Erucar and S. Keskin, *Screening metal-organic framework-based mixed-matrix membranes for CO_2/CH_4 separations,* Industrial and Engineering Chemistry Research **50**, 12606 (2011).

[102] Y. G. Chung, P. Bai, M. Haranczyk, K. T. Leperi, P. Li, H. Zhang, T. C. Wang, T. Duerinck, F. You, J. T. Hupp, O. K. Farha, J. I. Siepmann, and R. Q. Snurr, *Computational screening of nanoporous materials for hexane and heptane isomer separation,* Chemistry of Materials **29**, 6315 (2017).

[103] Z. Qiao, C. Peng, J. Zhou, and J. Jiang, *High-throughput computational screening of 137953 metal-organic frameworks for membrane separation of a $CO_2/N_2/CH_4$ mixture,* Journal of Materials Chemistry A **4**, 15904 (2016).

[104] K. M. Jablonka, D. Ongari, S. M. Moosavi, and B. Smit, *Big-data science in porous materials: Materials genomics and machine learning,* Chemical Reviews **120**, 8066 (2020).

[105] Y. J. Colon and R. Q. Snurr, *High-throughput computational screening of metal-organic frameworks,* Chemical Society Reviews. **43**, 5735 (2014).

[106] N. S. Bobbitt, J. Chen, and R. Q. Snurr, *High-throughput screening of metal-organic frameworks for hydrogen storage at cryogenic temperature,* Journal of Physical Chemistry C **120**, 27328 (2016).

[107] D. A. Gomez, J. Toda, and G. Sastre, *Screening of hypothetical metal-organic frameworks for H_2 storage,* Physical Chemistry Chemical Physics **16**, 19001 (2014).

[108] A. Martin-Calvo, J. J. Gutiérrez-Sevillano, I. Matito-Martos, T. J. H. Vlugt, and S. Calero, *Identifying zeolite topologies for storage and release of hydrogen,* Journal of Physical Chemistry C **122**, 12485 (2018).

[109] Y. G. Chung, D. A. Gómez-Gualdrón, P. Li, K. T. Leperi, P. Deria, H. Zhang, N. A. Vermeulen, J. F. Stoddart, F. You, J. T. Hupp, O. K. Farha, and R. Q. Snurr, *In silico discovery of metal-organic frameworks for precombustion CO_2 capture using a genetic algorithm,* Science Advances **2**, e1600909 (2016).

[110] H. Zhang, B. J. Bucior, and R. Q. Snurr, *Molecular modeling of carbon dioxide adsorption in metal-organic frameworks,* Modelling and Simulation in the Science of Micro- and Meso-Porous Materials , 99 (2017).

[111] J. Kim, M. Abouelnasr, L.-C. Lin, and B. Smit, *Large-scale screening of zeolite structures for CO_2 membrane separations,* Journal of the American Chemical Society **135**, 7545 (2013).

[112] B. Liu and B. Smit, *Comparative molecular simulation study of CO_2/N_2 and CH_4/N_2 separation in zeolites and metal-organic frameworks,* Langmuir **25**, 5918 (2009).

[113] I. Matito-Martos, A. Martin-Calvo, J. J. Gutiérrez-Sevillano, M. Haranczyk, M. Doblare, J. B. Parra, C. O. Ania, and S. Calero, *Zeolite screening for the separation of gas mixtures containing SO_2, CO_2 and CO,* Phys. Chem. Chem. Phys. **16**, 19884 (2014).

[114] E. Haldoupis, S. Nair, and D. S. Sholl, *Finding MOFs for highly selective CO_2/N_2 adsorption using materials screening based on efficient assignment of atomic point charges,* Journal of the American Chemical Society **134**, 4313 (2012).

[115] C. Altintas, I. Erucar, and S. Keskin, *High-throughput computational screening of the metal organic framework database for CH_4/H_2 separations,* ACS Applied Materials and Interfaces **10**, 3668 (2018).

[116] A. Energy, US Department of Energy, 2012, http://arpa–e.energy.gov/?q=arpa–e–site–page/view–programs (accessed at 2020.12.20).

[117] Y. G. Chung, E. Haldoupis, B. J. Bucior, M. Haranczyk, S. Lee, H. Zhang, K. D. Vogiatzis, M. Milisavljevic, S. Ling, J. S. Camp, B. Slater, J. I. Siepmann, D. S. Sholl, and R. Q. Snurr, *Advances, updates, and analytics for the computation-ready, experimental metal–organic framework database: Core MOF 2019,* Journal of Chemical & Engineering Data **64**, 5985 (2019).

[118] C. Altintas, G. Avci, H. Daglar, A. Nemati Vesali Azar, I. Erucar, S. Velioglu, and S. Keskin, *An extensive comparative analysis of two MOF databases: high-throughput screening of computation-ready MOFs for CH_4 and H_2 adsorption,* J. Mater. Chem. A **7**, 9593 (2019).

[119] Y. G. Chung, J. Camp, M. Haranczyk, B. J. Sikora, W. Bury, V. Krungleviciute, T. Yildirim, O. K. Farha, D. S. Sholl, and R. Q. Snurr, *Computation-ready, experimental metal–organic frameworks: A tool to enable high-throughput screening of nanoporous crystals,* Chemistry of Materials **26**, 6185 (2014).

[120] Z. Du, G. Manos, T. J. H. Vlugt, and B. Smit, *Molecular simulation of adsorption of short linear alkanes and their mixtures in silicalite,* AIChE Journal **44**, 1756 (1998).

[121] E. J. Maginn, A. T. Bell, and D. N. Theodorou, *Sorption thermodynamics, siting, and conformation of long n-alkanes in silicalite as predicted by configurational-bias Monte Carlo integration,* Journal of Physical Chemistry **99**, 2057 (1995).

[122] B. Smit and J. I. Siepmann, *Computer simulations of the energetics and siting of n-alkanes in zeolites,* Journal of Physical Chemistry **98**, 8442 (1994).

[123] S. Calero and P. Gómez-Álvarez, *On the performance of FAU and MFI zeolites for the adsorptive removal of a series of volatile organic compounds from air using molecular simulation,* Physical Chemistry Chemical Physics **17**, 26451 (2015).

[124] K. Walton, A. Millward, D. Dubbeldam, H. Frost, J. Low, O. Yaghi, and R. Snurr, *Understanding inflections and steps in carbon dioxide adsorption isotherms in metal-organic frameworks,* Journal of the American Chemical Society **130**, 406 (2008).

[125] T. Düren, L. Sarkisov, O. M. Yaghi, and R. Q. Snurr, *Design of new materials for methane storage,* Langmuir **20**, 2683 (2004).

[126] E. Beerdsen, D. Dubbeldam, B. Smit, T. J. H. Vlugt, and S. Calero, *Simulating the effect of nonframework cations on the adsorption of alkanes in MFI-type zeolites,* Journal of Physical Chemistry B **107**, 12088 (2003).

[127] S. Caro-Ortiz, E. Zuidema, M. Rigutto, D. Dubbeldam, and T. J. H. Vlugt, *Effects of framework flexibility on the adsorption and diffusion of aromatics in MFI-type zeolites,* Journal of Physical Chemistry C **124**, 24488 (2020).

[128] J. Perez-Carbajo, D. Dubbeldam, S. Calero, and P. J. Merkling, *Diffusion patterns in zeolite MFI: The cation effect,* Journal of Physical Chemistry C **122**, 29274 (2018).

[129] S. Ban and T. J. H. Vlugt, *Adsorption and diffusion of alkanes in Na-MOR: Modeling the effect of the aluminum distribution,* Journal of Chemical Theory and Computation **5**, 2858 (2009).

[130] D. Dubbeldam, K. S. Walton, T. J. H. Vlugt, and S. Calero, *Design, parameterization, and implementation of atomic force fields for adsorption in nanoporous materials,* Advanced Theory and Simulations **2**, 1900135 (2019).

[131] Z. Chang, D.-H. Yang, J. Xu, T.-L. Hu, and X.-H. Bu, *Flexible metal-organic frameworks: Recent advances and potential applications,* Advanced Materials **27**, 5432 (2015).

[132] J. Zang, S. Nair, and D. S. Sholl, *Prediction of water adsorption in copper-based metal–organic frameworks using force fields derived from dispersion-corrected dft calculations,* Journal of Physical Chemistry C **117**, 7519 (2013).

[133] D. Dubbeldam, S. Calero, T. J. H. Vlugt, R. Krishna, T. L. M. Maesen, E. Beerdsen, and B. Smit, *Force field parametrization through fitting on inflection points in isotherms,* Phys. Rev. Lett. **93**, 088302 (2004).

[134] H. Fang, J. Findley, G. Muraro, P. I. Ravikovitch, and D. S. Sholl, *A strong test of atomically detailed models of molecular adsorption in zeolites using multilaboratory experimental data for CO_2 adsorption in ammonium ZSM-5,* Journal of Physical Chemistry Letters **11**, 471 (2020).

[135] V. Sánchez-Gil, E. G. Noya, J. M. Guil, E. Lomba, and S. Valencia, *Adsorption of argon on pure silica mel. volumetric experiments and grand-canonical Monte Carlo simulations,* Microporous and Mesoporous Materials **222**, 218 (2016).

[136] M. Schenk, B. Smit, T. L. M. Maesen, and T. J. H. Vlugt, *Molecular simulations of the adsorption of cycloalkanes in mfi-type silica,* Phys. Chem. Chem. Phys. **7**, 2622 (2005).

[137] S. Caro-Ortiz, E. Zuidema, D. Dekker, M. Rigutto, D. Dubbeldam, and T. J. H. Vlugt, *Adsorption of aromatics in MFI-type zeolites: Experiments and framework flexibility in Monte Carlo simulations,* Journal of Physical Chemistry C **124**, 21782 (2020).

[138] P. D. Kolokathis, G. Káli, H. Jobic, and D. N. Theodorou, *Diffusion of aromatics in Silicalite-1: Experimental and theoretical evidence of entropic barriers,* The Journal of Physical Chemistry C **120**, 21410 (2016).

[139] A. Schneemann, V. Bon, I. Schwedler, I. Senkovska, S. Kaskel, and R. A. Fischer, *Flexible metal-organic frameworks,* Chemical Society Reviews **43**, 6062 (2014).

[140] J. Heinen and D. Dubbeldam, *On flexible force fields for metal–organic frameworks: Recent developments and future prospects,* WIREs Computational Molecular Science **8**, e1363 (2018).

[141] S. Horike, S. Shimomura, and S. Kitagawa, *Soft porous crystals,* Nature Chemistry **1**, 695–704 (2009).

[142] S. M. J. Rogge, M. Waroquier, and V. Van Speybroeck, *Reliably modeling the mechanical stability of rigid and flexible metal–organic frameworks,* Accounts of Chemical Research **51**, 138 (2018).

[143] S. Bureekaew, S. Amirjalayer, M. Tafipolsky, C. Spickermann, T. K. Roy, and R. Schmid, *MOF-ff - a flexible first-principles derived force field for metal-organic frameworks,* Physica Status Solidi (b) **250**, 1128 (2013).

[144] D. E. Coupry, M. A. Addicoat, and T. Heine, *Extension of the universal force field for metal–organic frameworks,* Journal of Chemical Theory and Computation **12**, 5215 (2016).

[145] L. Vanduyfhuys, S. Vandenbrande, T. Verstraelen, R. Schmid, M. Waroquier, and V. Van Speybroeck, *Quickff: A program for a quick and easy derivation of force fields for metal-organic frameworks from ab initio input,* Journal of Computational Chemistry **36**, 1015 (2015).

[146] J. Heinen, N. C. Burtch, K. S. Walton, and D. Dubbeldam, *Flexible force field parameterization through fitting on the ab initio-derived elastic tensor,* Journal of Chemical Theory and Computation **13**, 3722 (2017).

[147] O. Galteland, D. Bedeaux, B. Hafskjold, and S. Kjelstrup, *Pressures inside a nano-porous medium. the case of a single phase fluid,* Frontiers in Physics **7**, 60 (2019).

[148] B. T. Nguyen, H. L. Nguyen, T. C. Nguyen, K. E. Cordova, and H. Furukawa, *High methanol uptake capacity in two new series of metal–organic frameworks: Promising materials for adsorption-driven heat pump applications,* Chemistry of Materials **28**, 6243 (2016).

[149] Z.-Y. Gu, C.-X. Yang, N. Chang, and X.-P. Yan, *Metal-organic frameworks for analytical chemistry: From sample collection to chromatographic separation,* Accounts of Chemical Research **45**, 734 (2012).

[150] B. Yilmaz and U. Müller, *Catalytic applications of zeolites in chemical industry,* Topics in Catalysis **52**, 888 (2009).

[151] R. Glaser and J. Weitkamp, *The application of zeolites in catalysis,* Springer Series in Chemical Physics **75**, 159 (2004).

[152] M. Erdős, M. F. de Lange, F. Kapteijn, O. A. Moultos, and T. J. H. Vlugt, *In silico screening of metal–organic frameworks for adsorption-driven heat pumps and chillers,* ACS Applied Materials & Interfaces **10**, 27074 (2018).

[153] J. H. Irving and J. G. Kirkwood, *The statistical mechanical theory of transport processes. iv. the equations of hydrodynamics,* Journal of Chemical Physics **18**, 817 (1950).

[154] G. Férey and C. Serre, *Large breathing effects in three-dimensional porous hybrid matter: Facts, analyses, rules and consequences,* Chemical Society Reviews **38**, 1380 (2009).

[155] H. Song, M. Yu, W. Zhu, P. Wu, Y. Lou, Y. Wang, and J. Killough, *Numerical investigation of gas flow rate in shale gas reservoirs with nanoporous media,* International Journal of Heat and Mass Transfer **80**, 626 (2015).

[156] P. Huber, *Soft matter in hard confinement: phase transition thermodynamics, structure, texture, diffusion and flow in nanoporous media,* Journal of Physics: Condensed Matter **27**, 103102 (2015).

[157] B. D. Todd, D. J. Evans, and P. J. Daivis, *Pressure tensor for inhomogeneous fluids,* Phys. Rev. E **52**, 1627 (1995).

[158] J. Walton, D. Tildesley, J. Rowlinson, and J. Henderson, *The pressure tensor at the planar surface of a liquid,* Molecular Physics **48**, 1357 (1983).

[159] E. M. Blokhuis and D. Bedeaux, *Pressure tensor of a spherical interface,* Journal of Chemical Physics **97**, 3576 (1992).

[160] G. M. Wang, E. M. Sevick, E. Mittag, D. J. Searles, and D. J. Evans, *Experimental demonstration of violations of the second law of thermodynamics for small systems and short time scales,* Phys. Rev. Lett. **89**, 050601 (2002).

[161] R. H. Nilson and S. K. Griffiths, *Influence of atomistic physics on electro-osmotic flow: An analysis based on density functional theory,* Journal of Chemical Physics **125**, 164510 (2006).

[162] J. W. Lee, R. H. Nilson, J. A. Templeton, S. K. Griffiths, A. Kung, and B. M. Wong, *Comparison of molecular dynamics with classical density functional and Poisson-Boltzmann theories of the electric double layer in nanochannels,* Journal of Chemical Theory and Computation **8**, 2012 (2012).

[163] M. A. Gjennestad and Øivind Wilhelmsen, *Thermodynamic stability of droplets, bubbles and thick films in open and closed pores,* Fluid Phase Equilibria **505**, 112351 (2020).

[164] T. L. Hill, *Thermodynamics of Small Systems,* 1st ed. (Dover, New York, 1964).

[165] A. Z. Panagiotopoulos, *Direct determination of phase coexistence properties of fluids by Monte Carlo simulation in a new ensemble,* Molecular Physics **61**, 813 (1987).

[166] P. Bai and J. I. Siepmann, *Selective adsorption from dilute solutions: Gibbs ensemble Monte Carlo simulations,* Fluid Phase Equilibria **351**, 1 (2013).

[167] W. Shi and E. J. Maginn, *Continuous Fractional Component Monte Carlo: An adaptive biasing method for open system atomistic simulations,* Journal of Chemical Theory and Computation **3**, 1451 (2007).

[168] C. H. Bennett, *Efficient estimation of free energy differences from Monte Carlo data,* Journal of Computational Physics **22**, 245 (1976).

[169] J. Stecki, *Steele (10-4-3) potential due to a solid wall,* Langmuir **13**, 597 (1997).

[170] G. Jiménez-Serratos, H. Cárdenas, and E. A. Müller, *Extension of the effective solid-fluid steele potential for mie force fields,* Molecular Physics **117**, 3840 (2019).

[171] J. D. Weeks, D. Chandler, and H. C. Andersen, *Role of repulsive forces in determining the equilibrium structure of simple liquids,* Journal of Chemical Physics **54**, 5237 (1971).

[172] B. Smit, *Phase diagrams of Lennard-Jones fluids,* Journal of Chemical Physics **96**, 8639 (1992).

[173] J. J. Potoff and A. Z. Panagiotopoulos, *Critical point and phase behavior of the pure fluid and a Lennard-Jones mixture,* Journal of Chemical Physics **109**, 10914 (1998).

[174] M. T. Rauter, O. Galteland, M. Erdős, O. A. Moultos, T. J. H. Vlugt, S. K. Schnell, D. Bedeaux, and S. Kjelstrup, *Two-phase equilibrium conditions in nanopores,* Nanomaterials **10**, 608 (2020).

[175] International Energy Agency, *World energy outlook 2019,* Available at https://www.iea.org/reports/world-energy-outlook-2019 (accessed at 2021.11.20).

[176] European Comission, *Communication from the commission to the european parliament, the council, the European economic and social committee and the committe of the regions,* Available at https://ec.europa.eu/energy/sites/ener/files/documents/1_EN_ACT_part1_v14.pdf (accessed at 2018-03-22).

[177] M. Isaac and D. P. van Vuuren, *Modeling global residential sector energy demand for heating and air conditioning in the context of climate change,* Energy Policy **37**, 507 (2009).

[178] P. Tatsidjodoung, N. Le Pierrès, and L. Luo, *A review of potential materials for thermal energy storage in building applications,* Renewable and Sustainable Energy Reviews **18**, 327 (2013).

[179] M. Aneke and M. Wang, *Energy storage technologies and real life applications – a state of the art review,* Applied Energy **179**, 350 (2016).

[180] M. J. Moran and H. N. Shapiro, *Fundamentals of Engineering Thermodynamics*, 5th ed. (Wiley, New York, 2006).

[181] W. Wu, B. Wang, W. Shi, and X. Li, *Absorption heating technologies: A review and perspective,* Applied Energy **130**, 51 (2014).

[182] K. Parham, M. Khamooshi, D. B. K. Tematio, M. Yari, and U. Atikol, *Absorption heat transformers - a comprehensive review,* Renewable and Sustainable Energy Reviews **34**, 430 (2014).

[183] C. W. Chan, J. Ling-Chin, and A. P. Roskilly, *A review of chemical heat pumps, thermodynamic cycles and thermal energy storage technologies for low grade heat utilisation,* Applied Thermal Engineering **50**, 1257 (2013).

[184] N. Yu, R. Z. Wang, and L. W. Wang, *Sorption thermal storage for solar energy,* Progress in Energy and Combustion Science **39**, 489 (2013).

[185] Y. I. Aristov, *Challenging offers of material science for adsorption heat transformation: A review,* Applied Thermal Engineering **50**, 1610 (2013).

[186] W. Wongsuwan, S. Kumar, P. Neveu, and F. Meunier, *A review of chemical heat pump technique and applications,* Applied Thermal Engineering **21**, 1489 (2001).

[187] A. Kühn, *Thermally driven heat pumps for heating and cooling,* Ph.D. thesis, Technical University of Berlin (2013).

[188] M. F. de Lange, K. J. F. M. Verouden, T. J. H. Vlugt, J. Gascon, and F. Kapteijn, *Adsorption-driven heat pumps: The potential of metal-organic frameworks,* Chemical Reviews **115**, 12205 (2015).

[189] G. Santori and C. Di Santis, *Optimal fluids for adsorptive cooling and heating,* Sustainable Materials and Technologies **12**, 52 (2017).

[190] M. M. Younes, I. I. El-Sharkawy, A. E. Kabeel, and B. B. Saha, *A review on adsorbent-adsorbate pairs for cooling applications,* Applied Thermal Engineering **114**, 394 (2017).

[191] H.-M. Henning, *Solar assisted air conditioning of buildings - an overview,* Applied Thermal Engineering **27**, 1734 (2007).

[192] H. Demir, M. Mobedi, and S. Ülkü, *A review on adsorption heat pump: Problems and solutions,* Renewable and Sustainable Energy Reviews **12**, 2381 (2008).

[193] S. Kayal, S. Baichuan, and B. B. Saha, *Adsorption characteristics of aqsoa zeolites and water for adsorption chillers,* International Journal of Heat and Mass Transfer **92**, 1120 (2016).

[194] V. D. Ugale and A. D. Pitale, *A review on working pair used in adsorption cooling system,* International Journal of Air-Conditioning and Refrigeration **23**, 1530001 (2015).

[195] V. Brancato, A. Frazzica, A. Sapienza, L. Gordeeva, and A. Freni, *Ethanol adsorption onto carbonaceous and composite adsorbents for adsorptive cooling system,* Energy **84**, 177 (2015).

[196] B. B. Saha, I. I. El-Sharkawy, T. Miyazaki, S. Koyama, S. K. Henninger, A. Herbst, and C. Janiak, *Ethanol adsorption onto metal organic framework: Theory and experiments,* Energy **79**, 363 (2015).

[197] D. Wang, J. Zhang, Q. Yang, N. Li, and K. Sumathy, *Study of adsorption characteristics in silica gel-water adsorption refrigeration,* Applied Energy **113**, 734 (2014).

[198] M. F. de Lange, B. L. Van Velzen, C. P. Ottevanger, K. J. F. M. Verouden, L.-C. Lin, T. J. H. Vlugt, J. Gascon, and F. Kapteijn, *Metal-organic frameworks in adsorption-driven heat pumps: The potential of alcohols as working fluids,* Langmuir **31**, 12783 (2015).

[199] I. Spanopoulos, P. Xydias, C. D. Malliakas, and P. N. Trikalitis, *A straight forward route for the development of metal-organic frameworks functionalized with aromatic-oh groups: Synthesis, characterization, and gas (N_2, Ar, H_2, CO_2, CH_4, NH_3) sorption properties,* Inorganic Chemistry **52**, 855 (2013).

[200] D. Saha and S. Deng, *Ammonia adsorption and its effects on framework stability of MOF-5 and MOF-177,* Journal of Colloid and Interface Science **348**, 615 (2010).

[201] N. C. Burtch, H. Jasuja, and K. S. Walton, *Water stability and adsorption in metal-organic frameworks,* Chemical Reviews **114**, 10575 (2014).

[202] F. Jeremias, D. Fröhlich, C. Janiak, and S. K. Henninger, *Water and methanol adsorption on MOFs for cycling heat transformation processes,* New Journal of Chemistry **38**, 1846 (2014).

[203] H. Sato, K. Watanabe, J. M. H. Levelt Sengers, J. S. Gallagher, P. G. Hill, J. Straub, and W. Wagner, *Sixteen thousand evaluated experimental thermodynamic property data for water and steam,* Journal of Physical and Chemical Reference Data **20**, 1023 (1991).

[204] J. Brown, G. N. and W. T. Ziegler, *Temperature dependence of excess thermodynamic properties of ethanol + n-heptane and 2-propanol + n-heptane solutions,* Journal of Chemical and Engineering Data **24**, 319 (1979).

[205] H. G. Carlson and E. F. Westrum Jr., *Methanol: Heat capacity, enthalpies of transition and melting, and thermodynamic properties from 5-300 k,* Journal of Chemical Physics **54**, 1464 (1971).

[206] R. E. Critoph and Y. Zhong, *Review of trends in solid sorption refrigeration and heat pumping technology,* Proceedings of the Institution of Mechanical Engineers, Part E: Journal of Process Mechanical Engineering **219**, 285 (2005).

[207] D. W. Green and R. H. Perry, *Perry's Chemical Engineers' Handbook*, 8th ed. (McGraw-Hill: New York, 2008).

[208] D. Nazarian, J. S. Camp, and D. S. Sholl, *A comprehensive set of high-quality point charges for simulations of metal–organic frameworks,* Chemistry of Materials **28**, 785 (2016).

[209] T. M. Becker, J. Heinen, D. Dubbeldam, L.-C. Lin, and T. J. H. Vlugt, *Polarizable force fields for CO_2 and CH_4 adsorption in M-MOF-74,* Journal of Physical Chemistry C **121**, 4659 (2017).

[210] T. M. Becker, D. Dubbeldam, L.-C. Lin, and T. J. H. Vlugt, *Investigating polarization effects of CO_2 adsorption in MgMOF-74,* Journal of Computational Science **15**, 86 (2016).

[211] E. W. Lemmon, M. O. McLinden, and D. G. Friend, *"Thermophysical Properties of Fluid Systems" in NIST Chemistry WebBook, NIST Standard Reference Database Number 69*, edited by P. J. Linstrom and W. G. Mallard (National Institute of Standards and Technology, Gaithersburg MD, 20899, 2005).

[212] Z. Liu, L. Herrera, V. T. Nguyen, D. D. Do, and D. Nicholson, *A Monte Carlo scheme based on mid-density in a hysteresis loop to determine equilibrium phase transition,* Molecular Simulation **37**, 932 (2011).

[213] B. L. Eggimann, A. J. Sunnarborg, H. D. Stern, A. P. Bliss, and J. I. Siepmann, *An online parameter and property database for the TraPPE force field,* Molecular Simulation **40**, 101 (2014).

[214] S. L. Mayo, B. D. Olafson, and W. A. Goddard III, *Dreiding: a generic force field for molecular simulations,* Journal of Physical Chemistry **94**, 8897 (1990).

[215] A. K. Rappé, C. J. Casewit, K. S. Colwell, W. A. Goddard III, and W. M. Skiff, *UFF, a full periodic table force field for molecular mechanics and molecular dynamics simulations,* Journal of the American Chemical Society **114**, 10024 (1992).

[216] P. P. Ewald, *Die berechnung optischer und elektrostatischer gitterpotentiale,* Annalen der Physik **369**, 253 (1921).

[217] H. A. Lorentz, *Ueber die anwendung des satzes vom virial in der kinetischen theorie der gase,* Annalen der Physik **248**, 127 (1881).

[218] R. Babarao, S. Dai, and D.-E. Jiang, *Effect of pore topology and accessibility on gas adsorption capacity in zeolitic-imidazolate frameworks: Bringing molecular simulation close to experiment,* Journal of Physical Chemistry C **115**, 8126 (2011).

[219] Y. Gurdal and S. Keskin, *Atomically detailed modeling of metal organic frameworks for adsorption, diffusion, and separation of noble gas mixtures,* Industrial and Engineering Chemistry Research **51**, 7373 (2012).

[220] T. J. H. Vlugt, R. Krishna, and B. Smit, *Molecular simulations of adsorption isotherms for linear and branched alkanes and their mixtures in silicalite,* Journal of Physical Chemistry B **103**, 1102 (1999).

[221] M. G. Martin and J. I. Siepmann, *Novel Configurational-Bias Monte Carlo method for branched molecules. transferable potentials for phase equilibria. 2. united-atom description of branched alkanes,* Journal of Physical Chemistry B **103**, 4508 (1999).

[222] D.-Y. Peng and D. B. Robinson, *A new two-constant equation of state,* Industrial & Engineering Chemistry Fundamentals **15**, 59 (1976).

[223] T. F. Willems, C. H. Rycroft, M. Kazi, J. C. Meza, and M. Haranczyk, *Algorithms and tools for high-throughput geometry-based analysis of crystalline porous materials,* Microporous and Mesoporous Materials **149**, 134 (2012).

[224] R. L. Martin, B. Smit, and M. Haranczyk, *Addressing challenges of identifying geometrically diverse sets of crystalline porous materials,* Journal of Chemical Information and Modeling **52**, 308 (2012).

[225] D. Ambrose and C. Sprake, *Thermodynamic properties of organic oxygen compounds xxv. vapour pressures and normal boiling temperatures of aliphatic alcohols,* Journal of Chemical Thermodynamics **2**, 631 (1970).

[226] C. B. Kretschmer and R. Wiebe, *Liquid-vapor equilibrium of ethanol-toluene solutions,* Journal of the American Chemical Society **71**, 1793 (1949).

[227] B. K. Peterson, K. E. Gubbins, G. S. Heffelfinger, U. Marini, B. Marconi, and F. van Swol, *Lennard-Jones fluids in cylindrical pores: Nonlocal theory and computer simulation,* Journal of Chemical Physics **88**, 6487 (1988).

[228] B. K. Peterson and K. E. Gubbins, *Phase transitions in a cylindrical pore grand-canonical Monte Carlo, mean field theory and the Kelvin equation,* Molecular Physics **62**, 215 (1987).

[229] T. Maris, T. J. H. Vlugt, and B. Smit, *Simulation of alkane adsorption in the aluminophosphate molecular sieve $AlPO_4$-5,* Journal of Physical Chemistry B **102**, 7183 (1998).

[230] D. Ambrose and C. H. S. Sprake, *Thermodynamic properties of organic oxygen compounds xxv. vapour pressures and normal boiling temperatures of aliphatic alcohols,* Journal of Chemical Thermodynamics **2**, 631 (1970).

[231] A. J. Graham, J.-C. Tan, D. R. Allan, and S. A. Moggach, *The effect of pressure on Cu-BTC: Framework compression vs. guest inclusion,* Chemical Communications **48**, 1535 (2012).

[232] L. J. Murray, M. Dinca, J. Yano, S. Chavan, S. Bordiga, C. M. Brown, and J. R. Long, *Highly-selective and reversible O_2 binding in Cr_3(1,3,5-benzenetricarboxylate)$_2$,* Journal of the American Chemical Society **132**, 7856 (2010).

[233] Y. Hu, S. Xiang, W. Zhang, Z. Zhang, L. Wang, J. Bai, and B. Chen, *A new MOF-505 analog exhibiting high acetylene storage,* Chemical Communications , 7551 (2009).

[234] D. Zhao, D. Yuan, A. Yakovenko, and H.-C. Zhou, *A NbO-type metal-organic framework derived from a polyyne-coupled di-isophthalate linker formed in situ,* Chemical Communications **46**, 4196 (2010).

[235] J. Schnobrich, O. Lebel, K. Cychosz, A. Dailly, A. Wong-Foy, and A. Matzger, *Linker-directed vertex desymmetrization for the production of coordination polymers with high porosity,* Journal of the American Chemical Society **132**, 13941 (2010).

[236] L. Ma, A. Jin, Z. Xie, and W. Lin, *Freeze drying significantly increases permanent porosity and hydrogen uptake in 4,4-connected metal-organic frameworks,* Angewandte Chemie - International Edition **48**, 9905 (2009).

[237] O. K. Farha, C. D. Malliakas, M. G. Kanatzidis, and J. T. Hupp, *Control over catenation in metal-organic frameworks via rational design of the organic building block,* Journal of the American Chemical Society **132**, 950 (2010).

[238] D. Sun, Y. Ke, T. M. Mattox, B. A. Ooro, and H.-C. Zhou, *Temperature-dependent supramolecular stereoisomerism in porous copper coordination networks based on a designed carboxylate ligand,* Chemical Communications , 5447 (2005).

[239] E. Quartapelle Procopio, S. Rojas, N. M. Padial, S. Galli, N. Masciocchi, F. Linares, D. Miguel, J. E. Oltra, J. A. R. Navarro, and E. Barea, *Study of the incorporation and release of the non-conventional half-sandwich ruthenium(ii) metallodrug rapta-c on a robust MOF,* Chemical Communications **47**, 11751 (2011).

[240] M. Eddaoudi, J. Kim, N. Rosi, D. Vodak, J. Wachter, M. O'Keeffe, and O. Yaghi, *Systematic design of pore size and functionality in isoreticular MOFs and their application in methane storage,* Science **295**, 469 (2002).

[241] R. Andrés, M. Brissard, M. Gruselle, C. Train, J. Vaissermann, B. Malézieux, J.-P. Jamet, and M. Verdaguer, *Rational design of three-dimensional (3d) optically active molecule-based magnets,* Inorganic Chemistry **40**, 4633 (2001).

[242] Y.-S. Wei, K.-J. Chen, P.-Q. Liao, B.-Y. Zhu, R.-B. Lin, H.-L. Zhou, B.-Y. Wang, W. Xue, J.-P. Zhang, and X.-M. Chen, *Turning on the flexibility of isoreticular porous coordination frameworks for drastically tunable framework breathing and thermal expansion,* Chemical Science **4**, 1539 (2013).

[243] J. Jia, X. Lin, C. Wilson, A. J. Blake, N. R. Champness, P. Hubberstey, G. Walker, E. J. Cussen, and M. Schröder, *Twelve-connected porous metal-organic frameworks with high H_2 adsorption,* Chemical Communications , 840 (2007).

[244] M. Eddaoudi, J. Kim, D. Vodak, A. Sudik, J. Wachter, M. O'Keeffe, and O. M. Yaghi, *Geometric requirements and examples of important structures in the assembly of square building blocks,* Proceedings of the National Academy of Sciences of the United States of America **99**, 4900 (2002).

[245] D. N. Dybtsev, H. Chun, and K. Kim, *Rigid and flexible: A highly porous metal-organic framework with unusual guest-dependent dynamic behavior,* Angewandte Chemie - International Edition **43**, 5033 (2004).

[246] L. Feng, Z. Chen, T. Liao, P. Li, Y. Jia, X. Liu, Y. Yang, and Y. Zhou, *Supramolecular isomerism of metal-organic frameworks derived from a bicarboxylate linker with two distinct binding motifs,* Crystal Growth and Design **9**, 1505 (2009).

[247] T. Kitazawa, S. Nishikiori, and T. Iwamoto, *Three-dimensional framework structures built of heptacyanotricadmate(ii) units providing polyhedral cavities for guests: Classification of the zeolite-like structures,* Journal of the Chemical Society, Dalton Transactions , 3695 (1994).

[248] E. Neofotistou, C. D. Malliakas, and P. N. Trikalitis, *Remarkable structural diversity and single-crystal-to-single-crystal transformations in sulfone functionalized lanthanide MOFs,* CrystEngComm **12**, 1034 (2010).

[249] M. P. Suh, H. J. Park, T. K. Prasad, and D.-W. Lim, *Hydrogen storage in metal-organic frameworks,* Chemical Reviews **112**, 782 (2012).

[250] Z. Liang, J. Du, L. Sun, J. Xu, Y. Mu, Y. Li, J. Yu, and R. Xu, *Design and synthesis of two porous metal-organic frameworks with NBO and AGW topologies showing high CO_2 adsorption capacity,* Inorganic Chemistry **52**, 10720 (2013).

[251] N. M. Padial, E. Quartapelle Procopio, C. Montoro, E. López, J. E. Oltra, V. Colombo, A. Maspero, N. Masciocchi, S. Galli, I. Senkovska, S. Kaskel, E. Barea, and J. A. R. Navarro, *Highly hydrophobic isoreticular porous metal-organic frameworks for the capture of harmful volatile organic compounds,* Angewandte Chemie - International Edition **52**, 8290 (2013).

[252] J. L. C. Rowsell, E. C. Spencer, J. Eckert, J. A. K. Howard, and O. Yaghi, *Chemistry: Gas adsorption sites in a large-pore metal-organic framework,* Science **309**, 1350 (2005).

[253] P. Edwards, V. Kuznetsov, and W. David, *Hydrogen energy,* Philosophical Transactions of the Royal Society A: Mathematical, Physical and Engineering Sciences **365**, 1043 (2007).

[254] K. Mazloomi and C. Gomes, *Hydrogen as an energy carrier: Prospects and challenges,* Renewable and Sustainable Energy Reviews **16**, 3024 (2012).

[255] J. Abe, A. Popoola, E. Ajenifuja, and O. Popoola, *Hydrogen energy, economy and storage: Review and recommendation,* International Journal of Hydrogen Energy **44**, 15072 (2019).

[256] International Energy Agency, *The future of hydrogen,* Available at https://www.iea.org/reports/the-future-of-hydrogen (accessed at 2021.11.20).

[257] G. Gahleitner, *Hydrogen from renewable electricity: An international review of power-to-gas pilot plants for stationary applications,* International Journal of Hydrogen Energy **38**, 2039 (2013).

[258] S. Niaz, T. Manzoor, and A. H. Pandith, *Hydrogen storage: Materials, methods and perspectives,* Renewable and Sustainable Energy Reviews **50**, 457 (2015).

[259] S. A. Singh, K. Vishwanath, and G. Madras, *Role of hydrogen and oxygen activation over pt and pd-doped composites for catalytic hydrogen combustion,* ACS Applied Materials & Interfaces **9**, 19380 (2017).

[260] C. Liu, F. Li, L.-P. Ma, and H.-M. Cheng, *Advanced materials for energy storage,* Advanced Materials **22**, E28 (2010).

[261] H. Ibrahim, A. Ilinca, and J. Perron, *Energy storage systems—characteristics and comparisons,* Renewable and Sustainable Energy Reviews **12**, 1221 (2008).

[262] N. Jia, Y. Liu, L. Wang, P. Chen, X. Chen, Z. An, and Y. Chen, *0.2 V electrolysis voltage-driven alkaline hydrogen production with nitrogen-doped carbon nanobowl-supported ultrafine Rh nanoparticles of 1.4 nm,* ACS Applied Materials & Interfaces **11**, 35039 (2019).

[263] X. Tong, S. Ovtar, K. Brodersen, P. V. Hendriksen, and M. Chen, *A 4 × 4 cm^2 nanoengineered solid oxide electrolysis cell for efficient and durable hydrogen production,* ACS Applied Materials & Interfaces **11**, 25996 (2019).

[264] J. Zheng, X. Liu, P. Xu, P. Liu, Y. Zhao, and J. Yang, *Development of high pressure gaseous hydrogen storage technologies,* International Journal of Hydrogen Energy **37**, 1048 (2012).

[265] J. Adolf, C. H. Balzer, J. Louis, U. Schabla, M. Fischedick, K. Arnold, A. Pastowski, and D. Schüwer, *Energy of the future? : Sustainable mobility through fuel cells and H_2 ; Shell hydrogen study*, Tech. Rep. (Shell Deutschland Oil, Hamburg, 2017).

[266] P. Bouwman, *Electrochemical hydrogen compression (ehc) solutions for hydrogen infrastructure.* Fuel Cells Bulletin **2014**, 12 (2014).

[267] M. Rhandi, M. Trégaro, F. Druart, J. Deseure, and M. Chatenet, *Electrochemical hydrogen compression and purification versus competing technologies: Part I. pros and cons,* Chinese Journal of Catalysis **41**, 756 (2020).

[268] K. Wipke, S. Sprik, J. Kurtz, T. Ramsden, C. Ainscough, and G. Saur, *National fuel cell electric vehicle learning demonstration final report,* (2012).

[269] J. Zou, N. Han, J. Yan, Q. Feng, Y. Wang, Z. Zhao, J. Fan, L. Zeng, H. Li, and H. Wang, *Electrochemical compression technologies for high-pressure hydrogen: Current status, challenges and perspective,* Electrochemical Energy Reviews , 2520 (2020).

[270] HyET Hydrogen BV, Available at https://hyet.nl/hydrogen (2020.12.07).

[271] M. Bampaou, K. D. Panopoulos, A. I. Papadopoulos, P. Seferlis, and S. Voutetakis, *An electrochemical hydrogen compression model,* Chemical Engineering Transactions **70**, 1213 (2018).

[272] International Organization for Standardization, *Hydrogen fuel, product specification, part 2: Proton exchange membrane (pem) fuel cell applications for road vehicles.* Available at www.iso.org/committee/54560/x/catalogue/ (accessed at 2021.11.20).

[273] Y. Ligen, H. Vrubel, and H. Girault, *Energy efficient hydrogen drying and purification for fuel cell vehicles,* International Journal of Hydrogen Energy **45**, 10639 (2020).

[274] A. Rahbari, J. C. Garcia-Navarro, M. Ramdin, L. J. P. van den Broeke, O. A. Moultos, D. Dubbeldam, and T. J. H. Vlugt, *Effect of water content on thermodynamic properties of compressed hydrogen,* Journal of Chemical Engineering Data **66**, 2071 (2021).

[275] S. Sircar, T. Golden, and M. Rao, *Activated carbon for gas separation and storage,* Carbon **34**, 1 (1996).

[276] T. Golden and S. Sircar, *Activated carbon adsorbent for psa driers,* Carbon **28**, 683 (1990).

[277] Y.-K. Seo, J. W. Yoon, J. S. Lee, Y. K. Hwang, C.-H. Jun, J.-S. Chang, S. Wuttke, P. Bazin, A. Vimont, M. Daturi, S. Bourrelly, P. L. Llewellyn, P. Horcajada, C. Serre, and G. Férey, *Energy-efficient dehumidification over hierachically porous metal-organic frameworks as advanced water adsorbents,* Advanced Materials **24**, 806 (2012).

[278] X. Zheng, T. Ge, and R. Wang, *Recent progress on desiccant materials for solid desiccant cooling systems,* Energy **74**, 280 (2014).

[279] P. Gómez-Álvarez and S. Calero, *Insights into the microscopic behaviour of nanoconfined water: host structure and thermal effects,* CrystEngComm **17**, 412 (2015).

[280] J. M. Castillo, D. Dubbeldam, T. J. H. Vlugt, B. Smit, and S. Calero, *Evaluation of various water models for simulation of adsorption in hydrophobic zeolites,* Molecular Simulation **35**, 1067 (2009).

[281] J. Hriljac, M. Eddy, A. Cheetham, J. Donohue, and G. Ray, *Powder neutron diffraction and ^{29}Si mas NMR studies of siliceous zeolite-Y,* Journal of Solid State Chemistry **106**, 66 (1993).

[282] T. Kuroki, N. Sakoda, K. Shinzato, M. Monde, and Y. Takata, *Prediction of transient temperature of hydrogen flowing from pre-cooler of refueling station to inlet of vehicle tank,* International Journal of Hydrogen Energy **43**, 1846 (2018).

[283] K. Muraoka, W. Chaikittisilp, and T. Okubo, *Energy analysis of aluminosilicate zeolites with comprehensive ranges of framework topologies, chemical compositions, and aluminum distributions,* Journal of the American Chemical Society **138**, 6184 (2016).

[284] K. Itabashi, Y. Kamimura, K. Iyoki, A. Shimojima, and T. Okubo, *A working hypothesis for broadening framework types of zeolites in seed-assisted synthesis without organic structure-directing agent,* Journal of the American Chemical Society **134**, 11542 (2012).

[285] S. W. Rick, *A reoptimization of the five-site water potential (TIP5P) for use with Ewald sums,* Journal of Chemical Physics **120**, 6085 (2004).

[286] A. Martin-Calvo, J. B. Parra, C. O. Ania, and S. Calero, *Insights on the anomalous adsorption of carbon dioxide in LTA zeolites,* Journal of Physical Chemistry C **118**, 25460 (2014).

[287] E. García-Pérez, D. Dubbeldam, B. Liu, B. Smit, and S. Calero, *A computational method to characterize framework aluminum in aluminosilicates,* Angewandte Chemie International Edition **46**, 276 (2007).

[288] B. Liu, E. García-Pérez, D. Dubbeldam, B. Smit, and S. Calero, *Understanding aluminum location and non-framework ions effects on alkane adsorption in aluminosilicates: A molecular simulation study,* Journal of Physical Chemistry C **111**, 10419 (2007).

[289] M. Erdős, D. F. Geerdink, A. Martin-Calvo, E. A. Pidko, L. J. P. van den Broeke, S. Calero, T. J. H. Vlugt, and O. A. Moultos, *In silico screening of zeolites for high-pressure hydrogen drying,* ACS Applied Materials & Interfaces **13**, 8383 (2021).

[290] D. H. Olson, *The crystal structure of dehydrated NaX,* Zeolites **15**, 439 (1995).

[291] J. J. Pluth and J. V. Smith, *Accurate redetermination of crystal structure of dehydrated zeolite a. absence of near zero coordination of sodium. refinement of silicon,aluminum-ordered superstructure,* Journal of the American Chemical Society **102**, 4704 (1980).

[292] R. Hens, A. Rahbari, S. Caro-Ortiz, N. Dawass, M. Erdős, A. Poursaeidesfahani, H. S. Salehi, A. T. Celebi, M. Ramdin, O. A. Moultos, D. Dubbeldam, and T. J. H. Vlugt, *BRICK-CFCMC: Open source software for Monte Carlo simulations of phase and reaction equilibria using the Continuous Fractional Component Method,* Journal of Chemical Information and Modeling **60**, 2678 (2020).

[293] H. M. Polat, H. S. Salehi, R. Hens, D. O. Wasik, A. Rahbari, F. de Meyer, C. Houriez, C. Coquelet, S. Calero, D. Dubbeldam, O. A. Moultos, and T. J. H. Vlugt, *New features of the open source Monte Carlo software Brick-CFCMC: Thermodynamic integration and hybrid trial moves,* Journal of Chemical Information and Modeling **61**, 3752 (2021).

[294] W. L. Jorgensen, J. Chandrasekhar, J. D. Madura, R. W. Impey, and M. L. Klein, *Comparison of simple potential functions for simulating liquid water,* Journal of Chemical Physics **79**, 926 (1983).

[295] J. L. F. Abascal and C. Vega, *A general purpose model for the condensed phases of water: TIP4P/2005,* Journal of Chemical Physics **123**, 234505 (2005).

[296] C. Giles, D. Smith, and A. Huitson, *A general treatment and classification of the solute adsorption isotherm. i. theoretical,* Journal of Colloid And Interface Science **47**, 755 (1974).

[297] G. Limousin, J.-P. Gaudet, L. Charlet, S. Szenknect, V. Barthès, and M. Krimissa, *Sorption isotherms: A review on physical bases, modeling and measurement,* Applied Geochemistry **22**, 249 (2007).

[298] V. Inglezakis, S. Poulopoulos, and H. Kazemian, *Insights into the s-shaped sorption isotherms and their dimensionless forms,* Microporous and Mesoporous Materials **272**, 166 (2018).

[299] C. Hinz, *Description of sorption data with isotherm equations,* Geoderma **99**, 225 (2001).

[300] V. Simon, A. Thuret, L. Candy, S. Bassil, S. Duthen, C. Raynaud, and A. Masseron, *Recovery of hydroxycinnamic acids from renewable resources by adsorption on zeolites,* Chemical Engineering Journal **280**, 748 (2015).

[301] Y. Zhang, R. Mancke, M. Sabelfeld, and S.-U. Geißen, *Adsorption of trichlorophenol on zeolite and adsorbent regeneration with ozone,* Journal of Hazardous Materials **271**, 178 (2014).

[302] J. Gao, L. Liu, X. Liu, H. Zhou, S. Huang, and Z. Wang, *Levels and spatial distribution of chlorophenols - 2,4-dichlorophenol, 2,4,6-trichlorophenol, and pentachlorophenol in surface water of china,* Chemosphere **71**, 1181 (2008).

[303] K. Verschueren, *Handbook of Environmental Data on Organic Chemicals*, 5th ed. (Wiley, New York, 2008).

[304] B. Hameed, I. Tan, and A. Ahmad, *Adsorption isotherm, kinetic modeling and mechanism of 2,4,6-trichlorophenol on coconut husk-based activated carbon,* Chemical Engineering Journal **144**, 235 (2008).

[305] D. L. Sparks, *Sorption phenomena on soils*, 2nd ed. (Academic Press, Cambdridge, 2003) pp. 133–186.

[306] A. Yonli, I. Batonneau-Gener, and J. Koulidiati, *Adsorptive removal of α-endosulfan from water by hydrophobic zeolites. an isothermal study,* Journal of Hazardous Materials **203-204**, 357 (2012).

[307] B. Koubaissy, G. Joly, I. Batonneau-Gener, and P. Magnoux, *Adsorptive removal of aromatic compounds present in wastewater by using dealuminated faujasite zeolite,* Industrial and Engineering Chemistry Research **50**, 5705 (2011).

[308] S. Fukahori, T. Fujiwara, R. Ito, and N. Funamizu, *pH-dependent adsorption of sulfa drugs on high silica zeolite: Modeling and kinetic study,* Desalination **275**, 237 (2011).

[309] L. McCusker, D. Olson, and C. Baerlocher, *Atlas of Zeolite Framework Types* (2007).

[310] D. Faux, W. Smith, and T. Forester, *Molecular dynamics studies of hydrated and dehydrated Na^+-zeolite-4A,* Journal of Physical Chemistry B **101**, 1762 (1997).

[311] R. Dejaco, P. Bai, M. Tsapatsis, and J. I. Siepmann, *Adsorptive separation of 1-butanol from aqueous solutions using MFI-and FER-type zeolite frameworks: A Monte Carlo study,* Langmuir **32**, 2093 (2016).

[312] L. Narasimhan, B. Kuchta, O. Schaef, P. Brunet, and P. Boulet, *Mechanism of adsorption of p-cresol uremic toxin into faujasite zeolites in presence of water and sodium cations - a Monte Carlo study,* Microporous and Mesoporous Materials **173**, 70 (2013).

[313] International Energy Agency, *Acd/physchem module, version 5.0.0.184, advanced chemistry development, inc., Toronto, ON, Canada,* www.acdlabs.com (accessed at 2021.11.20.).

[314] J. Wang, R. M. Wolf, J. W. Caldwell, P. A. Kollman, and D. A. Case, *Development and testing of a general amber force field,* Journal of Computational Chemistry **25**, 1157 (2004).

[315] H. J. C. Berendsen, J. R. Grigera, and T. P. Straatsma, *The missing term in effective pair potentials,* Journal of Physical Chemistry **91**, 6269 (1987).

[316] R. Cygan, J.-J. Liang, and A. Kalinichev, *Molecular models of hydroxide, oxyhydroxide, and clay phases and the development of a general force field,* Journal of Physical Chemistry B **108**, 1255 (2004).

[317] L. Narasimhan, P. Boulet, B. Kuchta, O. Schaef, R. Denoyel, and P. Brunet, *Molecular simulations of water and paracresol in MFI zeolite - a Monte Carlo study,* Langmuir **25**, 11598 (2009).

[318] J. Shah, E. Marin-Rimoldi, R. Mullen, B. Keene, S. Khan, A. Paluch, N. Rai, L. Romanielo, T. Rosch, B. Yoo, and E. Maginn, *Cassandra: An open source Monte Carlo package for molecular simulation,* Journal of Computational Chemistry **38**, 1727 (2017).

[319] C. Janiak, *A critical account on n-n stacking in metal complexes with aromatic nitrogen-containing ligands,* Journal of the Chemical Society, Dalton Transactions , 3885 (2000).

[320] C. Martinez and B. Iverson, *Rethinking the term "π-stacking",* Chemical Science **3**, 2191 (2012).

[321] M. Waters, *Aromatic interactions in model systems,* Current Opinion in Chemical Biology **6**, 736 (2002).

[322] C. Ge, J. Du, L. Zhao, L. Wang, Y. Liu, D. Li, Y. Yang, R. Zhou, Y. Zhao, Z. Chai, and C. Chen, *Binding of blood proteins to carbon nanotubes reduces cytotoxicity,* Proceedings of the National Academy of Sciences of the United States of America **108**, 16968 (2011).

[323] G. Zuo, W. Gu, H. Fang, and R. Zhou, *Carbon nanotube wins the competitive binding over proline-rich motif ligand on SH_3 domain,* Journal of Physical Chemistry C **115**, 12322 (2011).

[324] S. Wallwork, *Hydrogen-bond radii,* Acta Crystallographica **15**, 768 (1962).

[325] V. Bolis, C. Busco, and P. Ugliengo, *Thermodynamic study of water adsorption in high-silica zeolites,* Journal of Physical Chemistry B **110**, 14849 (2006).

[326] P. Boulet, L. Narasimhan, D. Berg'e-Lefranc, B. Kuchta, O. Schäf, and R. Denoyel, *Adsorption into the MFI zeolite of aromatic molecule of biological relevance. investigations by Monte Carlo simulations,* Journal of Molecular Modeling **15**, 573 (2009).

[327] E. Güvenç and M. Ahunbay, *Adsorption of methyl tertiary butyl ether and trichloroethylene in MFI-type zeolites,* Journal of Physical Chemistry C **116**, 21836 (2012).

[328] J. Reungoat, J. S. Pic, M. H. Manéro, and H. Debellefontaine, *Adsorption of nitrobenzene from water onto high silica zeolites and regeneration by ozone,* Separation Science and Technology **42**, 1447 (2007).

[329] L. Damjanović, V. Rakić, V. Rac, D. Stošić, and A. Auroux, *The investigation of phenol removal from aqueous solutions by zeolites as solid adsorbents,* Journal of Hazardous Materials **184**, 477 (2010).

[330] R. Gonzalez-Olmos, F.-D. Kopinke, K. Mackenzie, and A. Georgi, *Hydrophobic Fe-zeolites for removal of MTBE from water by combination of adsorption and oxidation,* Environmental Science & Technology **47**, 2353 (2013).

[331] R. P. Schwarzenbach, B. I. Escher, K. Fenner, T. B. Hofstetter, C. A. Johnson, U. von Gunten, and B. Wehrli, *The challenge of micropollutants in aquatic systems,* Science **313**, 1072 (2006).

[332] A. Verliefde, E. Cornelissen, G. Amy, B. van der Bruggen, and H. van Dijk, *Priority organic micropollutants in water sources in Flanders and the Netherlands and assessment of removal possibilities with nanofiltration,* Environmental Pollution **146**, 281—289 (2007).

[333] R. Loos, G. Locoro, S. Comero, S. Contini, D. Schwesig, F. Werres, P. Balsaa, O. Gans, S. Weiss, L. Blaha, M. Bolchi, and B. M. Gawlik, *Pan-European survey on the occurrence of selected polar organic persistent pollutants in ground water,* Water Research **44**, 4115 (2010).

[334] R. Hut, N. van de Giesen, and C. J. Houtman, *Medicinal footprint of the population of the rhine basin,* Environmental Research Letters **8**, 044057 (2013).

[335] E. Vulliet and C. Cren-Olivé, *Screening of pharmaceuticals and hormones at the regional scale, in surface and groundwaters intended to human consumption,* Environmental Pollution **159**, 2929 (2011).

[336] Y. Luo, W. Guo, H. H. Ngo, L. D. Nghiem, F. I. Hai, J. Zhang, S. Liang, and X. C. Wang, *A review on the occurrence of micropollutants in the aquatic environment and their fate and removal during wastewater treatment,* Science of The Total Environment **473-474**, 619 (2014).

[337] Y. Yang, Y. S. Ok, K.-H. Kim, E. E. Kwon, and Y. F. Tsang, *Occurrences and removal of pharmaceuticals and personal care products (ppcps) in drinking water and water/sewage treatment plants: A review,* Science of The Total Environment **596-597**, 303 (2017).

[338] J. C. Sousa, A. R. Ribeiro, M. O. Barbosa, M. F. R. Pereira, and A. M. Silva, *A review on environmental monitoring of water organic pollutants identified by EU guidelines,* Journal of Hazardous Materials **344**, 146 (2018).

[339] M. Macova, S. Toze, L. Hodgers, J. F. Mueller, M. Bartkow, and B. I. Escher, *Bioanalytical tools for the evaluation of organic micropollutants during sewage treatment, water recycling and drinking water generation,* Water Research **45**, 4238 (2011).

[340] C. Stamm, K. Räsänen, F. Burdon, F. Altermatt, J. Jokela, A. Joss, M. Ackermann, and R. Eggen, *Chapter four - unravelling the impacts of micropollutants in aquatic ecosystems: Interdisciplinary studies at the interface of large-scale ecology,* in *Large-Scale Ecology: Model Systems to Global Perspectives,* Advances in Ecological Research, Vol. 55, edited by A. J. Dumbrell, R. L. Kordas, and G. Woodward (Academic Press, 2016) pp. 183 – 223.

[341] P. E. Stackelberg, J. Gibs, E. T. Furlong, M. T. Meyer, S. D. Zaugg, and R. L. Lippincott, *Efficiency of conventional drinking-water-treatment processes in removal of pharmaceuticals and other organic compounds,* Science of The Total Environment **377**, 255 (2007).

[342] R. Loos, R. Carvalho, D. C. António, S. Comero, G. Locoro, S. Tavazzi, B. Paracchini, M. Ghiani, T. Lettieri, L. Blaha, B. Jarosova, S. Voorspoels, K. Servaes, P. Haglund, J. Fick, R. H. Lindberg, D. Schwesig, and B. M. Gawlik, *EU-wide monitoring survey on emerging polar organic contaminants in wastewater treatment plant effluents,* Water Research **47**, 6475 (2013).

[343] J. Margot, L. Rossi, D. A. Barry, and C. Holliger, *A review of the fate of micropollutants in wastewater treatment plants,* Wiley Interdisciplinary Reviews: Water **2**, 457 (2015).

[344] R. L. Oulton, T. Kohn, and D. M. Cwiertny, *Pharmaceuticals and personal care products in effluent matrices: A survey of transformation and removal during wastewater treatment and implications for wastewater management,* Journal of Environmental Monitoring **12**, 1956 (2010).

[345] R. P. Schwarzenbach, T. Egli, T. B. Hofstetter, U. von Gunten, and B. Wehrli, *Global water pollution and human health,* Annual Review of Environment and Resources **35**, 109 (2010).

[346] G. Crini and E. Lichtfouse, *Advantages and disadvantages of techniques used for wastewater treatment,* Environmental Chemistry Letters **17**, 145 (2019).

[347] M. Luan, G. Jing, X. Xu, B. Hou, Y. Wang, and D. Meng, *A review: Wet oxidation and catalytic wet oxidation of industrial wastewater,* Recent Patents on Chemical Engineering **6**, 79 (2013).

[348] M. Shannon, P. Bohn, M. Elimelech, J. Georgiadis, B. Marīas, and A. Mayes, *Science and technology for water purification in the coming decades,* Nature **452**, 301 (2008).

[349] U. Gaya and A. Abdullah, *Heterogeneous photocatalytic degradation of organic contaminants over titanium dioxide: A review of fundamentals, progress and problems,* Journal of Photochemistry and Photobiology C: Photochemistry Reviews **9**, 1 (2008).

[350] T. Cath, A. Childress, and M. Elimelech, *Forward osmosis: Principles, applications, and recent developments,* Journal of Membrane Science **281**, 70 (2006).

[351] P. Sun, T. Meng, Z. Wang, R. Zhang, H. Yao, Y. Yang, and L. Zhao, *Degradation of organic micropollutants in UV/NH_2Cl advanced oxidation process,* Environmental Science & Technology **53**, 9024 (2019).

[352] I. Ali and V. Gupta, *Advances in water treatment by adsorption technology,* Nature Protocols **1**, 2661 (2007).

[353] A. Trewin and A. I. Cooper, *Porous organic polymers: Distinction from disorder?* Angewandte Chemie International Edition **49**, 1533 (2010).

[354] A. Thomas, *Functional materials: From hard to soft porous frameworks,* Angewandte Chemie International Edition **49**, 8328 (2010).

[355] W. Zhang, B. Aguila, and S. Ma, *Retraction: Potential applications of functional porous organic polymer materials,* Journal of Materials Chemistry A **5**, 18896 (2017).

[356] L. Tan and B. Tan, *Hypercrosslinked porous polymer materials: design, synthesis, and applications,* Chemical Society Reviews **46**, 3322 (2017).

[357] R. Sawicki and L. Mercier, *Evaluation of mesoporous cyclodextrin-silica nanocomposites for the removal of pesticides from aqueous media,* Environmental Science & Technology **40**, 1978 (2006).

[358] F. Zhao, E. Repo, D. Yin, Y. Meng, S. Jafari, and M. Sillanpää, *Edta-cross-linked β-cyclodextrin: An environmentally friendly bifunctional adsorbent for simultaneous adsorption of metals and cationic dyes,* Environmental Science & Technology **49**, 10570 (2015).

[359] D. Alzate-Sánchez, Y. Ling, C. Li, B. Frank, R. Bleher, D. Fairbrother, D. Helbling, and W. Dichtel, *β-cyclodextrin polymers on microcrystalline cellulose as a granular media for organic micropollutant removal from water,* ACS Applied Materials and Interfaces **11**, 8089 (2019).

[360] A. Alsbaiee, B. Smith, L. Xiao, Y. Ling, D. Helbling, and W. Dichtel, *Rapid removal of organic micropollutants from water by a porous β-cyclodextrin polymer,* Nature **529**, 190 (2016).

[361] J. Wang, X. Wang, and X. Zhang, *Cyclic molecule aerogels: a robust cyclodextrin monolith with hierarchically porous structures for removal of micropollutants from water,* Journal of Materials Chemistry A **5**, 4308 (2017).

[362] Y. Ling, M. J. Klemes, L. Xiao, A. Alsbaiee, W. R. Dichtel, and D. E. Helbling, *Benchmarking micropollutant removal by activated carbon and porous β-cyclodextrin polymers under environmentally relevant scenarios,* Environmental Science & Technology **51**, 7590 (2017).

[363] Z. Wang, P. Zhang, F. Hu, Y. Zhao, and L. Zhu, *A crosslinked β-cyclodextrin polymer used for rapid removal of a broad-spectrum of organic micropollutants from water,* Carbohydrate Polymers **177**, 224 (2017).

[364] N. Morin-Crini, P. Winterton, S. Fourmentin, L. D. Wilson, Éva Fenyvesi, and G. Crini, *Water-insoluble β-cyclodextrin–epichlorohydrin polymers for removal of pollutants from aqueous solutions by sorption processes using batch studies: A review of inclusion mechanisms,* Progress in Polymer Science **78**, 1 (2018).

[365] N. M. Henriksen and M. K. Gilson, *Evaluating force field performance in thermodynamic calculations of cyclodextrin host–guest binding: Water models, partial charges, and host force field parameters,* Journal of Chemical Theory and Computation **13**, 4253 (2017).

[366] Z. Tang and C. A. Chang, *Binding thermodynamics and kinetics calculations using chemical host and guest: A comprehensive picture of molecular recognition,* Journal of Chemical Theory and Computation **14**, 303 (2018).

[367] J. Yin, N. M. Henriksen, H. S. Muddana, and M. K. Gilson, *Bind3P: Optimization of a water model based on host–guest binding data,* Journal of Chemical Theory and Computation **14**, 3621 (2018).

[368] A. Jakalian, D. B. Jack, and C. I. Bayly, *Fast, efficient generation of high-quality atomic charges. AM1-BCC model: Ii. parameterization and validation,* Journal of Computational Chemistry **23**, 1623 (2002).

[369] C. Cézard, X. Trivelli, F. Aubry, F. Djedaini-Pilard, and F. Dupradeau, *Molecular dynamics studies of native and substituted cyclodextrins in different media: 1. charge derivation and force field performances,* Physical Chemistry Chemical Physics **13**, 15103 (2011).

[370] X. Zhu, G. Wu, and D. Chen, *Molecular dynamics simulation of cyclodextrin aggregation and extraction of anthracene from non-aqueous liquid phase,* Journal of Hazardous Materials **320**, 169 (2016).

[371] H. Zhang, C. Ge, D. van der Spoel, W. Feng, and T. Tan, *Insight into the structural deformations of beta-cyclodextrin caused by alcohol cosolvents and guest molecules,* Journal of Physical Chemistry B **116**, 3880 (2012).

[372] H. Zhang, T. Tan, C. Hetényi, Y. Lv, and D. van der Spoel, *Cooperative binding of cyclodextrin dimers to isoflavone analogues elucidated by free energy calculations,* Journal of Physical Chemistry C **118**, 7163 (2014).

[373] H. Zhang, T. Tan, C. Hetényi, and D. van der Spoel, *Quantification of solvent contribution to the stability of noncovalent complexes,* Journal of Chemical Theory and Computation **9**, 4542 (2013).

[374] A. Pineiro, X. Banquy, S. Pérez Casas, E. Tovar, A. García, A. Villa, A. Amigo, A. E. Mark, and M. Costas, *On the characterization of host-guest complexes: Surface tension, calorimetry, and molecular dynamics of cyclodextrins with a non-ionic surfactant,* Journal of Physical Chemistry B **111**, 4383 (2007).

[375] R. Semino and J. Rodríguez, *Molecular dynamics study of ionic liquids complexation within β-cyclodextrins,* Journal of Physical Chemistry B **119**, 4865 (2015).

[376] M. I. Sancho, S. Andujar, R. D. Porasso, and R. D. Enriz, *Theoretical and experimental study of inclusion complexes of β-cyclodextrins with chalcone and 2,4-dihydroxychalcone,* Journal of Physical Chemistry B **120**, 3000 (2016).

[377] M. Oda and M. Kuroda, *Molecular dynamics simulations of inclusion complexation of glycyrrhizic acid and cyclodextrins (1:1) in water,* Journal of Inclusion Phenomena and Macrocyclic Chemistry **85**, 271 (2016).

[378] L. A. Felton, C. Popescu, C. Wiley, E. X. Esposito, P. Lefevre, and A. J. Hopfinger, *Experimental and computational studies of physicochemical properties influence nsaid-cyclodextrin complexation,* AAPS PharmSciTech **15**, 872 (2014).

[379] T. Guzzo, W. Mandaliti, R. Nepravishta, A. Aramini, E. Bodo, I. Daidone, M. Allegretti, A. Topai, and M. Paci, *Conformational change in the mechanism of inclusion of ketoprofen in β-cyclodextrin: NMR spectroscopy, ab initio calculations, molecular dynamics simulations, and photoreactivity,* Journal of Physical Chemistry B **120**, 10668 (2016).

[380] J. Škvára and I. Nezbeda, *Molecular dynamics study of racemic mixtures: Solutions of ibuprofen and β-cyclodextrin in methanol,* Journal of Molecular Liquids **265**, 791 (2018).

[381] R. Wang, H. Zhou, S. W. I. Siu, Y. Gan, Y. Wang, and D. Ouyang, *Comparison of three molecular simulation approaches for cyclodextrin-ibuprofen complexation,* Journal of Nanomaterials **2015**, 8 (2015).

[382] L. M. Pinto, M. B. de Jesus, E. de Paula, A. C. Lino, J. B. Alderete, H. A. Duarte, and Y. Takahata, *Elucidation of inclusion compounds between β-cyclodextrin/local anaesthetics structure: a theoretical and experimental study using differential scanning calorimetry and molecular mechanics,* Journal of Molecular Structure: THEOCHEM **678**, 63 (2004).

[383] European Commission, *Development of the first watch list under the environmental quality standards directive,* Available at http://publications.jrc.ec.europa.eu/repository/bitstream/JRC95018/lbna27142enn.pdf (accessed at 2021.11.20).

[384] European Comission, *Directive of the European parliament ad of the council amending directives 2000/60/ec and 2008/105/ec as regards priority substances in the field of water policy,* Available at https://eur-lex.europa.eu/legal-content/EN/TXT/PDF/?uri=CELEX:52011PC0876&from=EN (accessed at 2021.11.20).

[385] J. Huff, *Long-term toxicology and carcinogenicity of 2,4,6-trichlorophenol,* Chemosphere **89**, 521 (2012).

[386] N. M. Henriksen, A. T. Fenley, and M. K. Gilson, *Computational calorimetry: High-precision calculation of host–guest binding thermodynamics,* Journal of Chemical Theory and Computation **11**, 4377 (2015).

[387] M. J. Abraham, T. Murtola, R. Schulz, S. Páll, J. C. Smith, B. Hess, and E. Lindahl, *Gromacs: High performance molecular simulations through multi-level parallelism from laptops to supercomputers.* SoftwareX **1-2**, 19 (2015).

[388] I. S. Joung and T. E. Cheatham, *Determination of alkali and halide monovalent ion parameters for use in explicitly solvated biomolecular simulations,* Journal of Physical Chemistry B **112**, 9020 (2008).

[389] F.-Y. Dupradeau, A. Pigache, T. Zaffran, C. Savineau, R. Lelong, N. Grivel, D. Lelong, W. Rosanski, and P. Cieplak, *The R.E.D. tools: advances in RESP and ESP charge derivation and force field library building,* Physical Chemistry Chemical Physics **12**, 7821 (2010).

[390] M. J. Frisch, G. W. Trucks, H. B. Schlegel, G. E. Scuseria, M. A. Robb, J. R. Cheeseman, J. A. Montgomery, Jr., T. Vreven, K. N. Kudin, J. C. Burant, J. M. Millam, S. S. Iyengar, J. Tomasi, V. Barone, B. Mennucci, M. Cossi, G. Scalmani, N. Rega, G. A. Petersson, H. Nakatsuji, M. Hada, M. Ehara, K. Toyota, R. Fukuda, J. Hasegawa, M. Ishida, T. Nakajima, Y. Honda, O. Kitao, H. Nakai, M. Klene, X. Li, J. E. Knox, H. P. Hratchian, J. B. Cross, V. Bakken, C. Adamo, J. Jaramillo, R. Gomperts, R. E. Stratmann, O. Yazyev, A. J. Austin, R. Cammi, C. Pomelli, J. W. Ochterski, P. Y. Ayala, K. Morokuma, G. A. Voth, P. Salvador, J. J. Dannenberg, V. G. Zakrzewski, S. Dapprich, A. D. Daniels, M. C. Strain, O. Farkas, D. K. Malick, A. D. Rabuck, K. Raghavachari, J. B. Foresman, J. V. Ortiz, Q. Cui, A. G. Baboul, S. Clifford, J. Cioslowski, B. B. Stefanov, G. Liu, A. Liashenko, P. Piskorz, I. Komaromi, R. L. Martin, D. J. Fox, T. Keith, M. A. Al-Laham, C. Y. Peng, A. Nanayakkara, M. Challacombe, P. M. W. Gill, B. Johnson, W. Chen, M. W. Wong, C. Gonzalez, and J. A. Pople, *Gaussian 09, revision B.01,* (2016).

[391] M. Erdős, R. Hartkamp, T. J. H. Vlugt, and O. A. Moultos, *Inclusion complexation of organic micropollutants with β-cyclodextrin,* Journal of Physical Chemistry B **124**, 1218 (2020).

[392] T. Darden, D. York, and L. Pedersen, *Particle Mesh Ewald: An N*log*(N) method for Ewald sums in large systems*. Journal of Chemical Physics. **98**, 10089 (1993).

[393] N. Goga, A. J. Rzepiela, A. H. de Vries, S. J. Marrink, and H. J. C. Berendsen, *Efficient algorithms for Langevin and DPD dynamics*. Journal of Chemical Theory and Computation **8**, 3637 (2012).

[394] H. J. C. Berendsen, Postma, J. P. M., A. DiNola, and J. R. Haak, *Molecular dynamics with coupling to an external bath*. Journal of Chemical Physics **81**, 3684 (1984).

[395] A. T. Fenley, N. M. Henriksen, H. S. Muddana, and M. K. Gilson, *Bridging calorimetry and simulation through precise calculations of cucurbituril–guest binding enthalpies,* Journal of Chemical Theory and Computation **10**, 4069 (2014).

[396] H. Flyvbjerg and H. G. Petersen, *Error estimates on averages of correlated data,* Journal of Chemical Physics **91**, 461 (1989).

[397] E. D. Valle, *Cyclodextrins and their uses: a review,* Process Biochemistry **39**, 1033 (2004).

[398] H.-X. Zhou and M. K. Gilson, *Theory of free energy and entropy in noncovalent binding,* Chemical Reviews **109**, 4092 (2009).

[399] L. J. Waters, S. Bedford, G. M. Parkes, and J. Mitchell, *Influence of lipophilicity on drug–cyclodextrin interactions: A calorimetric study,* Thermochimica Acta **511**, 102 (2010).

[400] S. Rozou, S. Michaleas, and E. Antoniadou-Vyza, *Study of structural features and thermodynamic parameters, determining the chromatographic behaviour of drug-cyclodextrin complexes,* Journal of chromatography. A **1087**, 86—94 (2005).

[401] K. Mochida, A. Kagita, Y. Matsui, and Y. Date, *Effects of inorganic salts on the dissociation of a complex of β-cyclodextrin with an azo dye in an aqueous solution,* Bulletin of Chemical Society of Japan **46**, 3703 (1973).

[402] I. Terekhova, E. Chibunova, R. Kumeev, and G. Alper, *Cyclodextrin–benzoic acid binding in salt solutions: Effects of biologically relevant anions,* Carbohydrate Polymers **110**, 472 (2014).

[403] D. L. Mobley and M. K. Gilson, *Predicting binding free energies: Frontiers and benchmarks,* Annual Review of Biophysics **46**, 531 (2017).

[404] R. B. Pellegrino Vidal, G. A. Ibañez, and G. M. Escandar, *Spectrofluorimetric study of phenolic endocrine disruptors in cyclodextrin media,* Royal Society of Chemistry Advances **5**, 20914 (2015).

[405] G. G. Mironov, J. Logie, V. Okhonin, J. B. Renaud, P. M. Mayer, and M. V. Berezovski, *Comparative study of three methods for affinity measurements: Capillary electrophoresis coupled with uv detection and mass spectrometry, and direct infusion mass spectrometry,* Journal of The American Society for Mass Spectrometry **23**, 1232 (2012).

[406] K. Hanna, C. de Brauer, and P. Germain, *Solubilization of the neutral and charged forms of 2,4,6-trichlorophenol by β-cyclodextrin, methyl-β-cyclodextrin and hydroxypropyl-β-cyclodextrin in water,* Journal of Hazardous Materials **100**, 109 (2003).

[407] S. Chelli, M. Majdoub, M. Jouini, S. Aeiyach, F. Maurel, K. I. Chane-Ching, and P.-C. Lacaze, *Host–guest complexes of phenol derivatives with β-cyclodextrin: an experimental and theoretical investigation,* Journal of Physical Organic Chemistry **20**, 30 (2007).

[408] M. di Cagno, P. C. Stein, N. Skalko-Basnet, M. Brandl, and A. Bauer-Brandl, *Solubilization of ibuprofen with β-cyclodextrin derivatives: Energetic and structural studies,* Journal of Pharmaceutical and Biomedical Analysis **55**, 446 (2011).

[409] R. Chadha, N. Kashid, A. Kumar, and D. V. S. Jain, *Calorimetric studies of diclofenac sodium in aqueous solution of cyclodextrin and water-ethanol mixtures,* Journal of Pharmacy and Pharmacology **54**, 481 (2002).

[410] H. Zhang, T. Tan, W. Feng, and D. van der Spoel, *Molecular recognition in different environments: β-cyclodextrin dimer formation in organic solvents,* Journal of Physical Chemistry B **116**, 12684 (2012).

[411] F. W. Starr, J. K. Nielsen, and H. E. Stanley, *Hydrogen-bond dynamics for the extended simple point-charge model of water,* Phys. Rev. E **62**, 579 (2000).

[412] G. R. Brown, M. R. Caira, L. R. Nassimbeni, and B. van Oudtshoorn, *Inclusion of ibuprofen by heptakis(2,3,6-tri-o-methyl)-β-cyclodextrin: An x-ray diffraction and thermal analysis study,* Journal of inclusion phenomena and molecular recognition in chemistry **26**, 281 (1996).

[413] S. S. Braga, I. S. Gonçalves, E. Herdtweck, and J. J. C. Teixeira-Dias, *Solid state inclusion compound of s-ibuprofen in β-cyclodextrin: structure and characterisation,* New J. Chem. **27**, 597 (2003).

[414] J. Gebhardt and N. Hansen, *Calculation of binding affinities for linear alcohols to α-cyclodextrin by twin-system enveloping distribution sampling simulations,* Fluid Phase Equilibria **422**, 1 (2016).

[415] G. Raffaini and F. Ganazzoli, *A molecular dynamics study of the inclusion complexes of C_{60} with some cyclodextrins,* Journal of Physical Chemistry B **114**, 7133 (2010).

[416] T. Moufawad, L. Moura, M. Ferreira, H. Bricout, S. Tilloy, E. Monflier, M. Costa Gomes, D. Landy, and S. Fourmentin, *First evidence of cyclodextrin inclusion complexes in a deep eutectic solvent,* ACS Sustainable Chemistry & Engineering **7**, 6345 (2019).

[417] C. Delitala, B. Marongiu, B. Pittau, and S. Porcedda, *Thermodynamic studies on water-β-cyclodextrin-surfactant ternary systems,* Fluid Phase Equilibria **126**, 257 (1996).

[418] C. I. A. V. Santos, A. C. F. Ribeiro, and M. A. Esteso, *Drug delivery systems: Study of inclusion complex formation between methylxanthines and cyclodextrins and their thermodynamic and transport properties,* Biomolecules **9**, 196 (2019).

[419] A. Ribeiro and M. Esteso, *Transport properties for pharmaceutical controlled-release systems: A brief review of the importance of their study in biological systems,* Biomolecules **8**, 178 (2018).

[420] A. C. Ribeiro, C. I. Santos, V. M. Lobo, A. M. Cabral, F. J. Veiga, and M. A. Esteso, *Diffusion coefficients of the ternary system (2-hydroxypropyl-β-cyclodextrin+caffeine+water) at T=298.15K,* Journal of Chemical Thermodynamics **41**, 1324 (2009).

[421] K. J. Naidoo, J. Y.-J. Chen, J. L. M. Jansson, G. Widmalm, and A. Maliniak, *Molecular properties related to the anomalous solubility of β-cyclodextrin,* Journal of Physical Chemistry B **108**, 4236 (2004).

[422] O. A. Moultos, Y. Zhang, I. N. Tsimpanogiannis, I. G. Economou, and E. J. Maginn, *System-size corrections for self-diffusion coefficients calculated from molecular dynamics simulations: The case of CO_2, n-alkanes, and poly(ethylene glycol) dimethyl ethers,* Journal of Chemical Physics **145**, 074109 (2016).

[423] A. T. Celebi, S. H. Jamali, A. Bardow, T. J. H. Vlugt, and O. A. Moultos, *Finite-size effects of diffusion coefficients computed from molecular dynamics: a review of what we have learned so far,* Molecular Simulation **47**, 831 (2021).

[424] O. A. Moultos, I. N. Tsimpanogiannis, A. Z. Panagiotopoulos, and I. G. Economou, *Atomistic molecular dynamics simulations of CO_2 diffusivity in H_2O for a wide range of temperatures and pressures,* Journal of Physical Chemistry B **118**, 5532 (2014).

[425] O. A. Moultos, I. N. Tsimpanogiannis, A. Z. Panagiotopoulos, J. P. M. Trusler, and I. G. Economou, *Atomistic molecular dynamics simulations of carbon dioxide diffusivity in n-hexane, n-decane, n-hexadecane, cyclohexane, and squalane,* Journal of Physical Chemistry B **120**, 12890 (2016).

[426] K. D. Papavasileiou, L. D. Peristeras, A. Bick, and I. G. Economou, *Molecular dynamics simulation of pure n-alkanes and their mixtures at elevated temperatures using atomistic and coarse-grained force fields,* Journal of Physical Chemistry B **123**, 6229 (2019).

[427] G. A. Orozco, O. A. Moultos, H. Jiang, I. G. Economou, and A. Z. Panagiotopoulos, *Molecular simulation of thermodynamic and transport properties for the H_2O+NaCl system,* Journal of Chemical Physics **141**, 234507 (2014).

[428] I. M. Zeron, J. L. F. Abascal, and C. Vega, *A force field of Li^+, Na^+, K^+, Mg^{2+}, Ca^{2+}, Cl^-, and SO_4^{2-} in aqueous solution based on the TIP4P/2005 water model and scaled charges for the ions,* Journal of Chemical Physics **151**, 134504 (2019).

[429] M. F. Döpke, O. A. Moultos, and R. Hartkamp, *On the transferability of ion parameters to the TIP4P/2005 water model using molecular dynamics simulations,* Journal of Chemical Physics **152**, 024501 (2020).

[430] M. Schauperl, P. Nerenberg, H. Jang, L.-P. Wang, C. Bayly, D. Mobley, and M. Gilson, *Non-bonded force field model with advanced restrained electrostatic potential charges (RESP2),* Communications Chemistry **3** (2020).

[431] M. Erdős, M. Frangou, T. J. H. Vlugt, and O. A. Moultos, *Diffusivity of α-, β-, γ-cyclodextrin and the inclusion complex of β-cyclodextrin: Ibuprofen in aqueous solutions; a molecular dynamics simulation study,* Fluid Phase Equilibria **528**, 112842 (2021).

[432] S. Plimpton, *Fast Parallel Algorithms for Short-Range Molecular Dynamics,* Journal of Computational Physics **117**, 1 (1995).

[433] G. Bussi, D. Donadio, and M. Parrinello, *Canonical sampling through velocity rescaling,* Journal of Chemical Physics **126**, 014101 (2007).

[434] M. Parrinello and A. Rahman, *Polymorphic transitions in single crystals: A new molecular dynamics method,* Journal of Applied Physics **52**, 7182 (1981).

[435] S. H. Jamali, L. Wolff, T. M. Becker, M. de Groen, M. Ramdin, R. Hartkamp, A. Bardow, T. J. H. Vlugt, and O. A. Moultos, *OCTP: A tool for on-the-fly calculation of transport properties of fluids with the order-n algorithm in LAMMPS,* Journal of Chemical Information and Modeling **59**, 1290 (2019).

[436] I.-C. Yeh and G. Hummer, *System-size dependence of diffusion coefficients and viscosities from molecular dynamics simulations with periodic boundary conditions,* Journal of Physical Chemistry B **108**, 15873 (2004).

[437] B. Dünweg and K. Kremer, *Molecular dynamics simulation of a polymer chain in solution,* Journal of Chemical Physics **99**, 6983 (1993).

[438] S. H. Jamali, R. Hartkamp, C. Bardas, J. Söhl, T. J. H. Vlugt, and O. A. Moultos, *Shear viscosity computed from the finite-size effects of self-diffusivity in equilibrium molecular dynamics,* Journal of Chemical Theory and Computation **14**, 5959 (2018).

[439] S. H. Jamali, A. Bardow, T. J. H. Vlugt, and O. A. Moultos, *Generalized form for finite-size corrections in mutual diffusion coefficients of multicomponent mixtures obtained from equilibrium molecular dynamics simulation,* Journal of Chemical Theory and Computation **16**, 3799 (2020).

[440] T. J. dos Santos, C. R. Abreu, B. A. Horta, and F. W. Tavares, *Self-diffusion coefficients of methane/n-hexane mixtures at high pressures: An evaluation of the finite-size effect and a comparison of force fields,* Journal of Supercritical Fluids **155**, 104639 (2020).

[441] A. C. F. Ribeiro, A. J. M. Valente, C. I. A. V. Santos, P. M. R. A. Prazeres, V. M. M. Lobo, H. D. Burrows, M. A. Esteso, A. M. T. D. P. V. Cabral, and F. J. B. Veiga, *Binary mutual diffusion coefficients of aqueous solutions of α-cyclodextrin, 2-hydroxypropyl-α-cyclodextrin, and 2-hydroxypropyl-β-cyclodextrin at temperatures from (298.15 to 312.15) K,* Journal of Chemical & Engineering Data **52**, 586 (2007).

[442] A. C. F. Ribeiro, D. G. Leaist, M. A. Esteso, V. M. M. Lobo, A. J. M. Valente, C. I. A. V. Santos, A. M. T. D. P. V. Cabral, and F. J. B. Veiga, *Binary mutual diffusion coefficients of aqueous solutions of β-cyclodextrin at temperatures from 298.15 to 312.15 K,* Journal of Chemical & Engineering Data **51**, 1368 (2006).

[443] A. C. F. Ribeiro, C. I. A. V. Santos, A. J. M. Valente, O. S. Ascenso, V. M. M. Lobo, H. D. Burrows, A. M. T. D. P. V. Cabral, F. J. B. Veiga, C. Teijeiro, and M. A. Esteso, *Some transport properties of γ-cyclodextrin aqueous solutions at (298.15 and 310.15) K,* Journal of Chemical & Engineering Data **53**, 755 (2008).

[444] I. N. Tsimpanogiannis, O. A. Moultos, L. F. M. Franco, M. B. de M. Spera, M. Erdős, and I. G. Economou, *Self-diffusion coefficient of bulk and confined water: a critical review of classical molecular simulation studies,* Molecular Simulation **45**, 425 (2019).

[445] J. Rodriguez, D. Hernán Rico, L. Domenianni, and D. Laria, *Confinement of polar solvents within β-cyclodextrins,* Journal of Physical Chemistry B **112**, 7522 (2008).

[446] T. Shikata, R. Takahashi, and Y. Satokawa, *Hydration and dynamic behavior of cyclodextrins in aqueous solution,* Journal of Physical Chemistry B **111**, 12239 (2007).

[447] K. D. Rainsford, *Ibuprofen: pharmacology, efficacy and safety,* Inflammopharmacology **17**, 275 (2009).

[448] R. Loos, B. M. Gawlik, G. Locoro, E. Rimaviciute, S. Contini, and G. Bidoglio, *EU-wide survey of polar organic persistent pollutants in European river waters,* Environmental Pollution **157**, 561 (2009).

[449] C. Y. Lee, Y.-S. Bae, N. C. Jeong, O. K. Farha, A. A. Sarjeant, C. L. Stern, P. Nickias, R. Q. Snurr, J. T. Hupp, and S. T. Nguyen, *Kinetic separation of propene and propane in metal-organic frameworks: Controlling diffusion rates in plate-shaped crystals via tuning of pore apertures and crystallite aspect ratios,* Journal of the American Chemical Society **133**, 5228 (2011).

[450] E. Quartapelle Procopio, T. Fukushima, E. Barea, J. A. R. Navarro, S. Horike, and S. Kitagawa, *A soft copper(ii) porous coordination polymer with unprecedented aqua bridge and selective adsorption properties,* Chemistry - A European Journal **18**, 13117 (2012).

[451] P. V. Dau, M. Kim, S. J. Garibay, F. H. L. Münch, C. E. Moore, and S. M. Cohen, *Single-atom ligand changes affect breathing in an extended metal-organic framework,* Inorganic Chemistry **51**, 5671 (2012).

[452] E. W. Lemmon, M. L. Huber, and M. O. McLinden, *NIST reference fluid thermodynamic and transport properties - REFPROP,* NIST standard reference database **23**, v7 (2002).

[453] C. H. Bennett, *Efficient estimation of free energy differences from Monte Carlo data,* Journal of Computational Physics **22**, 245 (1976).

[454] J. S. Hub, B. L. de Groot, and D. van der Spoel, *g_wham—a free weighted histogram analysis implementation including robust error and autocorrelation estimates,* Journal of Chemical Theory and Computation **6**, 3713 (2010).

SUMMARY

In this thesis, molecular simulations of porous materials are performed, ranging from testing theories using simple models to predicting thermodynamic properties of realistic complex systems. Porous materials such as zeolites, MOFs, and cyclodextrins (CDs) are studied for waste water treatment and energy related applications. The purpose of the presented studies is twofold: (1) identify the best performing materials for a specific application from a large pool of structures, (2) obtain molecular insight into the molecular level phenomena involved in a specific application. These studies aim to provide guidance for experimentalist in finding new, better performing materials, and a more detailed understanding of the involved phenomena. In Chapter 1, the importance of porous materials and the role of molecular simulations in the discovery of new types of porous materials are discussed. In Chapter 2, a theoretical concept based on Hill's thermodynamics [164] for calculating the pressure of nanoconfined fluids is presented. In this approach, two different pressures are defined to take into account the smallness of the system: the so-called differential and the integral pressures. The effect of several factors contributing to the confinement of fluids in nanopores are investigated: the pore geometry, fluid-wall interactions, and the differential pressure of the bulk fluid phase. It is shown that the differential and integral pressures are different for small pores and become equal for very large pores. Since the pressure inside the pores influences the transport properties of the fluid, a related quantity, the ratio of driving force for mass transport, $\frac{\mathrm{d}\langle\hat{p}\rangle}{\mathrm{d}P}$, is also investigated. The term $\frac{\mathrm{d}\langle\hat{p}\rangle}{\mathrm{d}P}$ is the ratio of the pressure gradient for mass transport in the bulk phase, $\frac{\mathrm{d}P}{\mathrm{d}L}$, and in the confined space, $\frac{\mathrm{d}\langle\hat{p}\rangle}{\mathrm{d}L}$, which is referred to as the ratio of driving forces for mass transport in this thesis. It is found that for small pore sizes (i.e. pore size $< 5\sigma_{\mathrm{fluid}}$) the ratio of the two driving forces considerably deviates from 1. Our findings as well as the findings of Galteland *et al.* [147], and Rauter *et al.* [174] imply that the integral pressure should be incorporated in the computation of thermodynamic properties of fluids in nanopores. In Chapter 3, a computational screening of 2930 experimentally synthesized Metal-Organic Frameworks (MOFs) is carried out to find the best performing structures for adsorption driven cooling (AC) applications with methanol and ethanol as working fluids. The most promising MOFs are selected based on the working capacity of the structures and the location of the adsorption step (if present), which can be related to the applicable operational conditions in AC. Due to the possibility of reversible pore condensation (first-order phase transition), the mid-density scheme [212] is used to efficiently and accurately determine the location of the adsorption step. At the end of

the screening procedure, from the original 2930 structures, six MOFs with high deliverable working capacities (~0.6 ml working fluid per 1 ml structure) and diverse adsorption step locations are selected for both adsorbates. Since the highest experimentally measured deliverable working capacity to date for MOFs with methanol is ca. 0.45 ml ml^{-1}, the selected six structures show the potential to improve the efficiency of ACs. In Chapter 4, a computational screening study using MC simulations is carried out to identify potential zeolite frameworks for the drying of high-pressure H_2 gas. We show that the Si/Al ratio and adsorption selectivity have a negative correlation. 218 zeolites available in the database of the International Zeolite Association are considered in the screening. We computed adsorption selectivities for water of each zeolite from high pressure H_2 gas (P = 300-900 bar) with a water content close to saturation. It is shown that due to the formation of water clusters, the water content in high-pressure H_2 gas has a significant effect on the selectivity of zeolites with helium void fractions larger than 0.1. At each operating condition, the 5 most promising zeolites are identified based on the adsorption selectivity, the pore limiting diameter, and the volume of H_2 gas that can be dried by 1 dm^3 of zeolite. It is shown that at low water content, structures with helium void fractions smaller than 0.07 are preferred. The structures identified for high water content have helium void fractions larger than 0.26. The proposed zeolites can be used to dry 400 to 8 000 times their own volume of H_2 gas depending on the operating conditions. Our findings strongly indicate that zeolites are potential candidates for the drying of high-pressure H_2 gas. In Chapter 5, MC simulations are performed to understand the adsorption mechanism of 2,4,6-trichlorophenol (TCP) on high-silica zeolites causing the experimentally observed S-shaped adsorption isotherm. It is found that the π - π interactions between TCP molecules give rise to the adsorption of multiple TCP molecules per alpha cage of FAU-type zeolite, and thus causing an S-shaped adsorption isotherm. As the Al content of the zeolite increases, the steep increase in the amount of adsorbed TCP molecules (S-shape) becomes less pronounced since the preferential adsorption of water hinders the adsorption of TCP. In Chapters 6 and 7, the inclusion complex formation of organic micropollutants (OMPs) with β-cyclodextrin (CD) and the diffusivity of α-, β-, γ-CD, and the β-CD:ibuprofen inclusion complexes are investigated. In this thesis, CDs are studied since these are the main building blocks of recently reported CD-based polymers which show promising characteristics for waste water treatment applications. As a first step towards the modeling of CD based polymers, the thermodynamic and transport properties of CDs and their inclusion complexes are studied. In Chapter 6, the inclusion complex formation of OMPs with β-CD in an aqueous solution is investigated by using the well-established Attach-Pull-Release method [386] in force field based Molecular Dynamics simulations. A representative set of OMPs is selected based on

the measured occurrences in surface and ground waters and the directives published by the European Union. To characterize the formation of inclusion complex, the binding free energies, enthalpies and entropies are computed and compared to experimental values. It is shown that computations using the q4md-CD/GAFF/Bind3P force field combination yield binding free energies that are in reasonable agreement with the experimental results for all OMPs studied. Inclusion complexation is suggested to be one of the main mechanisms via which β-CD-based polymers capture OMPs. Our findings can be used for the design and optimization of these materials. In Chapter 7, a comprehensive simulation study on the diffusion of the native α-, β- and γ-CDs in aqueous solutions is carried out using Molecular Dynamics simulations. The effect of the system size on the computed self-diffusivities is investigated and it is found that the required finite-size correction can be as much as 75% of its final value. The effect of the water force field is examined and it is shown that the q4md-CD/TIP4P/2005 force field combination predicts the experimentally measured self-diffusion coefficients of CDs very accurately. The self-diffusion coefficients of the three native CDs were also computed for aqueous-NaCl solutions using the Joung and Cheatham (JC) and the Madrid-2019 force fields. It is found that Na^+ ions have higher affinity towards the CDs when the JC force field is used and for this reason the predicted diffusivity of CDs is lower compared to simulations using the Madrid-2019 force field. The diffusion of the β-CD:ibuprofen inclusion complex in water is studied, as a model system for drug delivery and wastewater treatment applications. It is shown that the inclusion complex and the free β-CD have almost equal self-diffusion coefficients which is in excellent agreement with the experimental findings. Our analysis revealed that this is most likely caused by the almost full inclusion of ibuprofen in the cavity of β-CD.

SAMENVATTING

In dit proefschrift worden moleculaire simulaties van poreuze materialen beschreven, variërend van het testen van theorieën met behulp van eenvoudige modellen tot het voorspellen van thermodynamische eigenschappen van realistische complexe systemen. Poreuze materialen zoals zeolieten, Metal Organic Frameworks (MOFs) en cyclodextrines (CDs) werden bestudeerd voor afvalwaterbehandeling en energie-gerelateerde toepassingen. Het doel van het onderzoek in dit proefschrift is tweeledig: (1) identificeer de best presterende materialen voor een specifieke toepassing uit een grote groep van structuren, (2) inzicht verkrijgen in de verschijnselen op moleculair niveau die van belang zijn voor een specifieke toepassing. Dit onderzoek heeft tot doel om suggesties voor experimentatoren aan te reiken bij het vinden van nieuwe, beter presterende materialen, en het verkrijgen van een gedetailleerd begrip van de betrokken verschijnselen. In hoofdstuk 1 wordt het belang van poreuze materialen en de rol van moleculaire simulaties bij de ontdekking van nieuwe poreuze materialen besproken. In hoofdstuk 2 wordt een theoretisch concept gebaseerd op op Hill's thermodynamica [164] voor het berekenen van de druk van nano-confined vloeistoffen gepresenteerd. Om rekening mee te houden de kleinheid van het systeem worden er twee drukken gedefinieerd: de zogenaamde differentiële en de integrale druk. Het effect van verschillende factoren die bijdragen aan de confinement van vloeistoffen in nanoporiën zijn onderzocht: de poriegeometrie, vloeistof-wandinteracties en het drukverschil met de bulkvloeistoffase. Er wordt aangetoond dat de differentiële en integrale druk verschillend zijn voor kleine poriën en gelijk zijn voor zeer grote poriën. Omdat de druk binnen in poriën de transporteigenschappen van de vloeistof beïnvloedt, onderzoeken we een gerelateerde hoeveelheid, namelijk de verhouding van de drijvende krachten voor massatransport, $\frac{\mathrm{d}\langle\hat{p}\rangle}{\mathrm{d}P}$. De term $\frac{\mathrm{d}\langle\hat{p}\rangle}{\mathrm{d}P}$ is de verhouding van de drukgradiënt voor massatransport in de bulkfase $\frac{\mathrm{d}P}{\mathrm{d}L}$ en in confinement $\frac{\mathrm{d}\langle\hat{p}\rangle}{\mathrm{d}L}$, en daarom noemen we deze term de verhouding van drijvende krachten voor massatransport. Het blijkt dat voor kleine poriegroottes (d.w.z. poriegrootte < 5 maal de molecuulgrootte) de verhouding van de twee drijvende krachten aanzienlijk afwijkt van 1. Onze bevindingen impliceren dat de integrale druk moet worden gebruikt voor de berekening van thermodynamische eigenschappen van vloeistoffen in nanoporiën. Dit is in overeenstemming met onderzoek van Galteland *et al.* [147] en Rauter *et al.* [174]. In hoofdstuk 3 wordt met computersimulaties een screening van 2 930 experimenteel gesynthetiseerde MOFs uitgevoerd om de best presterende structuren te vinden voor adsorptie-gedreven koeling met methanol en ethanol als werkvloeistoffen. De meest

veelbelovende MOFs worden geselecteerd op basis van de werkcapaciteit en de locatie van de adsorptiestap (indien aanwezig). Deze grootheden kunnen gerelateerd worden aan de operationele omstandigheden in adsorptie gedreven koeling. Vanwege de mogelijkheid van reversibele poriecondensatie (eerste-orde faseovergang), wordt het zogenaamde mid-density-schema [212] gebruikt om de locatie van de adsorptiestap efficiënt en nauwkeurig te bepalen. Uit de oorspronkelijke 2 930 structuren zijn uiteindelijk zes MOFs met hoge werkcapaciteiten (ca. 0.6 ml werkvloeistof per 1 ml-structuur) en diverse adsorptiestaplocaties geselecteerd, voor zowel methanol als ethanol als werkvloeistof. Aangezien de hoogste experimenteel gemeten werkcapaciteit tot nu toe voor MOFs met methanol ca. 0.45 ml ml^{-1} is, is het duidelijk dat de geselecteerde zes structuren het potentieel hebben om de efficiëntie van adsorptiegedreven koeling te verbeteren. In hoofdstuk 4 wordt met behulp van Monte Carlo simulaties een screeningstudie uitgevoerd om potentiële zeolieten voor het drogen van waterstof gas onder hoge druk te ontdekken. We laten zien dat de Si/Al-verhouding van het framework en adsorptieselectiviteit een negatieve correlatie hebben. De 218 zeolieten die beschikbaar zijn in de IZA database worden in de screening meegenomen. Voor elk zeoliet hebben we de adsorptieselectiviteit berekend voor water uit waterstof gas onder hoge druk (P = 300-900 bar), voor een watergehalte dat dicht bij de verzadigingswaarde ligt. We hebben aangetoond dat door de vorming van waterclusters in zeolieten het watergehalte in waterstof gas bij hoge druk een significant effect heeft op de adsorptieselectiviteit voor zeolieten met helium void fractions groter dan 0.1. Bij elke bedrijfsconditie worden de 5 meest veelbelovende zeolieten geïdentificeerd op basis van de adsorptieselectiviteit, de poriebeperkende diameter en het volume waterstofgas dat kan worden gedroogd met 1 dm^3 zeoliet. We hebben aangetoond dat bij een laag watergehalte, structuren met helium void fractions kleiner dan 0.07 de voorkeur genieten boven andere zeolieten. De structuren die zijn geïdentificeerd voor een hoog watergehalte hebben helium void fractions die groter zijn dan 0.26. De voorgestelde zeolieten kunnen worden gebruikt om 400 tot 8 000 keer hun eigen volume aan waterstofgas te drogen, afhankelijk van de bedrijfsomstandigheden. Onze bevindingen laten duidelijk zien dat zeolieten potentiële kandidaten zijn voor het drogen van waterstofgas onder hoge druk. In hoofdstuk 5 worden Monte Carlo simulaties uitgevoerd om het adsorptiemechanisme van 2,4,6-trichloorfenol (TCP) in zeolieten met een hoge Si/Al verhouding te begrijpen. We zijn met name geïnteresseerd in het verklaren van de experimenteel waargenomen S-vormige adsorptie isothermen. Het blijkt dat de zogenaamde π- π interacties tussen TCP-moleculen aanleiding geven tot de adsorptie van meerdere TCP-moleculen per alfa-kooi van zeoliet FAU, hetgeen een S-vormige adsorptie-isotherm veroorzaakt. Naarmate het Al-gehalte van het zeoliet toeneemt, wordt de toename van de hoeveelheid geadsorbeerde TCP-

moleculen (S-vorm) minder sterk, aangezien de preferentiële adsorptie van water de adsorptie van TCP belemmert. In hoofdstukken 6 en 7 worden complexen gevormd door organische microverontreinigingen (OMPs) en β-cyclodextrines (β-CDs) onderzocht, alsmede de diffusie van α-, β-, γ-CD en β-CD:ibuprofen inclusie complexen. Deze CDs worden hier bestudeerd omdat dit de belangrijkste bouwstenen zijn van recent gerapporteerde op CDs gebaseerde polymeren. Deze polymeren vertonen veelbelovende eigenschappen voor afvalwaterbehandelingstoepassingen. De thermodynamische en transporteigenschappen van CDs en hun inclusiecomplexen worden in dit proefschrift bestudeerd als eerste stap op weg naar de modellering van op CD gebaseerde polymeren. In hoofdstuk 6 wordt de inclusiecomplexvorming van OMPs met β-CD in een waterige oplossing onderzocht met behulp van de bekende Attach-Pull-Release-methode [386]. Hiervoor gebruiken we Moleculaire Dynamica simulaties met een klassiek krachtenveld. Een representatieve set OMPs werd geselecteerd op basis van metingen aan oppervlakte- en grondwater en de door de Europese Unie gepubliceerde richtlijnen. Om de vorming van een inclusiecomplex te karakteriseren worden verschillen in vrije energie, enthalpie en entropie berekend en vergeleken met experimentele waarden. Berekeningen met behulp van de q4md-CD/GAFF/Bind3P-krachtveldcombinatie leveren verschillen in vrije energie op die redelijk in overeenstemming zijn met experimentele resultaten voor alle onderzochte OMPs. In de literatuur wordt gesuggereerd dat inclusiecomplexatie een van de belangrijkste mechanismen is waarmee op β-CDs gebaseerde polymeren OMPs vangen. Onze bevindingen kunnen worden gebruikt voor het ontwerp en de optimalisatie van deze materialen. In hoofdstuk 7 wordt een uitgebreide studie uitgevoerd naar de diffusie van α-, β- en γ-CDs in waterige oplossingen met behulp van Moleculaire Dynamica simulaties. Het effect van de systeemgrootte op de berekende zelf-diffusiecoëfficiënten is onderzocht. Het blijkt dat de vereiste finite-size correcties tot ca. 75% van de uiteindelijke waarde van de diffusiecoëfficiënt kan zijn. Het effect van het waterkrachtveld wordt onderzocht en er wordt aangetoond dat de q4md-CD/TIP4P/2005 krachtveldcombinatie de experimenteel gemeten zelfdiffusiecoëfficiënten van CDs zeer nauwkeurig voorspelt. De zelf-diffusiecoëfficiënten van de drie CDs werden ook berekend voor waterige NaCl-oplossingen met behulp van de Joung en Cheatham (JC) en de Madrid-2019 krachtvelden. Er is gevonden dat Na+-ionen een hogere affiniteit hebben voor de CDs wanneer het JC-krachtveld wordt gebruikt. Om deze reden is de voorspelde diffusiecoëfficiënt van CDs lager in vergelijking met simulaties met het Madrid-2019-krachtveld. Tevens werd de diffusie van het β-CD:ibuprofen inclusiecomplex in water bestudeerd. We beschouwen dit als een modelsysteem voor toepassing voor medicijnafgifte en afvalwaterbehandeling. We laten zien dat het inclusiecomplex en het vrije (niet-gebonden) β-CD bijna gelijke zelf-diffusiecoëfficiënten hebben, hetgeen

in overeenstemming is met experimenten. Uit onze analyse bleek dat dit hoogstwaarschijnlijk wordt veroorzaakt door de bijna volledige opname van ibuprofen in de holte van β-CD.

CURRICULUM VITÆ

Erdős Máté was born on the 18th of September in 1992 in Gyula, Hungary. In 2011, he started his bachelor studies in chemical engineering on the process technology track at the Budapest University of Technology. During his bachelor he participated in research projects concerning flow-sheet modeling of adsorption and distillation processes in the research group of Prof. Láng Péter. He concluded his bachelor studies with a project on the numerical modeling of nanostructure growth of thin layers on spherical nanoparticles in the research group of Prof. Ruud van Ommen. Subsequently, he started his master studies at Delft University of Technology in the Netherlands as a chemical engineer on the process technology track. After successfully finishing his master studies, he started his PhD studies on 15th of April in 2017 under the supervision of Dr. Othonas A. Moultos and Prof. Thijs J. H. Vlugt. In his PhD, he worked on molecular simulation of porous materials. In this thesis, you can read the details about his work. From January in 2021, he started to work at ChemAxon in Hungary as an application scientist. Currently, he resides in Budapest where he spends his days in happiness with his family.

LIST OF PUBLICATIONS

PUBLICATIONS INCLUDED IN THIS THESIS:

1. M. Erdős, O. Galteland, D. Bedeaux, S. Kjelstrup, O. A. Moultos, and T. J. H. Vlugt, Gibbs ensemble monte carlo simulation of fluids in confinement: Relation between the differential and integral pressures, *Nanomaterials* **10**, 293 (2020).

2. M. Erdős, M. F. de Lange, F. Kapteijn, O. A. Moultos, and T. J. H. Vlugt, In silico screening of metal–organic frameworks for adsorption-driven heat pumps and chillers, *ACS Applied Materials & Interfaces* **10**, 27074 (2018).

3. M. Erdős, D. F. Geerdink, A. Martin-Calvo, E. Pidko, L. J. P. van den Broeke, S. Calero, T. J. H. Vlugt, and O. A. Moultos, In silico screening of zeolites for high-pressure hydrogen drying, *ACS Applied Materials & Interfaces* **13**, 8383 (2021).

4. N. Jiang, M. Erdős, O. A. Moultos, R. Shang, T. J. H. Vlugt, S. G. Heijman, and L. C. Rietveld, The adsorption mechanisms of organicmicropollutants on high-silica zeolites causing s-shaped adsorption isotherms: An experimental and Monte Carlo simulation study, *Chemical Engineering Journal* **389**, 123968 (2020).

5. M. Erdős, R. Hartkamp, T. J. H. Vlugt, and O. A. Moultos, Inclusion complexation of organic micropollutants with β-cyclodextrin, *Journal of Physical Chemistry B* **124**, 1218 (2020).

6. M. Erdős, M. Frangou, T. J. H. Vlugt, and O. A. Moultos, Diffusivity of α-, β-, γ-cyclodextrin and the inclusion complex of β-cyclodextrin: Ibuprofen in aqueous solutions; A Molecular Dynamics simulation study, *Fluid Phase Equilibria* **528**, 112842 (2021).

PUBLICATIONS NOT INCLUDED IN THIS THESIS:

1. I. N. Tsimpanogiannis, O. A. Moultos, L. F. M. Franco, M. B. de M. Spera, M. Erdős, and I. G. Economou, Self-diffusion coefficient of bulk and confined water: a critical review of classical molecular simulation studies, *Molecular Simulation* **45**, 425 (2019).

2. M. T. Rauter, O. Galteland, M. Erdős, O. A. Moultos, T. J. H. Vlugt, S. K. Schnell, D. Bedeaux, and S. Kjelstrup, Two-phase equilibrium conditions in nanopores, *Nanomaterials* **10**, 608 (2020).

3. R. Hens, A. Rahbari, S. Caro-Ortiz, N. Dawass, M. Erdős, A. Poursaeidesfahani, H. S. Salehi, A. T. Celebi, M. Ramdin, O. A. Moultos, D. Dubbeldam, and T. J. H. Vlugt, BRICK-CFCMC: open source software for Monte Carlo simulations of phase and reaction equilibria using the Continuous Fraction Component method, *Journal of Chemical Information and Modeling* **60**, 2678 (2020).

ACKNOWLEDGMENTS

First, I would like to thank my promoter Thijs J. H. Vlugt, and my co-promoter Othonas (Otto) Moultos for all their help and guidance during my PhD. You were always there to discuss science and help with any problems. I am very happy that I had the opportunity to pursue my PhD degree under your supervision. It was a pleasure to work with you both. Besides scientific discussions, I would also like to thank Otto for our discussions on every day life matters which I appreciated very much.

Second, I would like to thank all of my friends and co-workers from the Process & Energy department. Especially, Remco, Max, Sebastian, Alper, Christos, and Metin for creating a fun office environment, out of office activities, adding very "nice" comments, and having interesting discussions. I would also like to thank Seyed, Hirad, Reza, Martijn, Mariette, Julia, Noura, Mahinder, and Ali for all their help and discussions.

Third, I would like to thank Remco Hartkamp, Nan Jiang, Michalis Frangou, Daan F. Geerdink, Signe Kjelstrup, Dick Bedeaux, Olav Galteland, Michael Rauter, Freek Kapteijn, Ana Martin-Calvo, Evgeny Pidko, Sofia Calero, Ran Shang, Bas Heijman, Luuk C. Rietveld, Ioannis N. Tsimpanogiannis, Luis F. M. Franco, Marcella B. de M. Spera, Ioannis G. Economou, Sondre K. Schnell, and David Dubbeldam for all the help, collaboration, and providing opportunities to learn new things.

Fourth, I would like to thank my family for supporting me during my PhD. Especially, my wife, Ági who urged me the most to complete my PhD. :)